Oxygen-ion transport and electrocatalysis in high entropy oxides

TECHNISCHE
UNIVERSITÄT
DARMSTADT

Vom Fachbereich Material- und Geowissenschaften der
Technischen Universität Darmstadt

zur Erlangung des akademischen Titels
Doktor-Ingenieur (Dr.-Ing.)

genehmigte Dissertation von
M. Tech. Mohana Veerraju Kante

1. Gutachten: Prof. Dr. Horst Hahn
2. Gutachten: Prof. Dr. Jan Philipp Hofmann

Darmstadt 2025

Erklärung zur Dissertation

Hiermit versichere ich, dass ich meine Dissertation selbstständig und nur mit den angegebenen Quellen und Hilfsmitteln angefertigt habe. Diese Arbeit hat in gleicher oder ähnlicher Form noch keiner Prüfungsbehörde vorgelegen.

Darmstadt, den

(Mohana Veerraju Kante)

Tag der Prüfung: 15.07.2025

Darmstadt, Technische Universität Darmstadt

Veröffentlichungsjahr der Dissertation auf TUprints: 2025

Bitte zitieren Sie dieses Dokument als:

URN: urn:nbn:de:tuda-tuprints-310320

Abstract

Global average temperatures have been increasing since the onset of the Industrial Revolution, with the most pronounced rise occurring between 2023 and 2024, exceeding 1.5°C above pre-industrial levels. This temperature increase is primarily attributed to the elevated atmospheric concentrations of greenhouse gases, such as CO_2 and CH_4, largely resulting from fossil fuel combustion. To mitigate greenhouse gas emissions, significant research efforts have been devoted to sustainable energy solutions. One widely investigated strategy involves the utilization of renewable energy sources, such as solar and wind, to meet energy demands through efficient energy-to-fuel and fuel-to-energy conversion processes. The development of these technologies necessitates high-performance solar cells, electrolyzers, fuel cells, and batteries, all of which rely on advanced electrolyte and electrode materials. A fundamental challenge in materials science is the design and optimization of materials with superior functional properties to enhance the efficiency, stability, and performance of these energy conversion and storage systems.

High entropy oxides are a new class of promising materials known for their single-phase stability, compositional complexity, and exceptional functional properties. The main objective of the thesis is to explore the potential of high entropy oxides as oxygen ion conductors and electrocatalysts for oxygen evolution reaction. The initial step in assessing these functional properties involves synthesizing the high entropy oxides in various forms, such as powders, pellets, and films. The high entropy oxides are synthesized using mechanochemical synthesis, sol-gel processing, reverse co-precipitation, pulsed laser deposition, and conventional sintering techniques. The fluorite-structured high entropy oxide $(Ce,La,Pr,Sm,Y)O_{2-\delta}$ is considered for comparison. Powders produced using mechanochemical synthesis, sol-gel processing, and reverse co-precipitation consistently exhibit the desired fluorite structure. Likewise, thin films synthesized using the sol-gel process and pulsed laser deposition also maintain the fluorite structure, with pulsed laser deposition allowing the production of films with various morphologies, such as polycrystalline, columnar, and epitaxial. In contrast, pellets synthesized through conventional sintering exhibit a mixture of fluorite and bixbyite structure due to the high sintering temperatures. These techniques are applied to various high entropy oxides to evaluate their potential as oxygen ion conductors and electrocatalysts for the oxygen evolution reaction.

Fluorite- and perovskite-type high entropy oxides are explored as oxygen ion conductors. The oxygen ion conduction is studied for the pellets of these high entropy oxides.

However, the pellets of fluorite structured high entropy oxide - $(Ce,La,Pr,Sm,Y)O_{2-\delta}$ transition to phase mixture of fluorite and bixbyite structure due to high sintering temperatures. In order to prevent the formation of the phase mixture during the sintering, Zr was added at different atomic fractions. Indeed, the fluorite structure is stabilized approximately at 10 at.% of Zr content. Additionally, $(Ce,La,Pr,Sm,Y)_{1-x}Zr_xO_{2-\delta}$ exhibit a homogenous distribution of elements with Pr exhibiting multivalency. As an additional benefit of adding Zr, the ionic conductivity increases with the addition of Zr and reaches a maximum at 8 at.% of Zr and decreases with further addition of Zr. Interestingly, the electronic conductivity in an oxidizing atmosphere expected from a multivalent Pr is suppressed, while high ionic conduction is observed in the fluorite-structured high entropy oxides. The thesis also investigates perovskite-type high entropy oxides, specifically high entropy rare-earth aluminates. Traditional perovskite-structured rare-earth aluminates are known oxygen ion conductors; however, they exhibit p-type electronic conduction in oxidizing environments due to oxygen exchange between the atmosphere and lattice oxygen at high temperatures. High entropy materials, with their elevated configurational entropies, offer stability at high temperatures, suggesting they could reduce unwanted electronic conduction. To explore this phenomenon, high entropy aluminates - $(Gd_{0.2}La_{0.2}Nd_{0.2}Pr_{0.2}Sm_{0.2})_{1-x}Ca_xAlO_3$ are considered. These high entropy aluminates exhibit an orthorhombic perovskite structure with a homogenous distribution of elements, with minor secondary phases appearing at $x = 0.15$ and $x = 0.2$. Conductivity increases with Ca content which peaks at $x = 0.1$ and stays constant with further addition of Ca. At the same time, the p-type conduction typically observed in doped rare-earth aluminates is effectively mitigated. High entropy oxides offer promising potential to constrict the electronic conduction observed in traditional oxygen ion conductors. Furthermore, the conductivities achieved in this research are comparable to the state-of-the-art oxygen ion conductor, yttria-stabilized zirconia.

High entropy materials are promising for developing high-activity electrocatalysts. Their inherent tunability and multiple active sites create opportunities for designing earth-abundant catalytic materials that support energy-efficient electrochemical energy storage. In this thesis, the high entropy perovskite-type oxides are shown to significantly enhance catalytic activity for the oxygen evolution reaction (OER), the kinetically limiting half-reaction in electrochemical energy conversion, including green hydrogen production. Specifically, the catalytic performance of the (001) facet of $La(Cr_{0.2}Mn_{0.2}Fe_{0.2}Co_{0.2}Ni_{0.2})O_{3-\delta}$ was compared to its parent compounds with a single B-site in the ABO_3 perovskite structure. While these single B-site perovskites generally follow expected volcano-type activity trends, the high entropy oxide outperforms all parent compounds, achieving 17 to 680 times higher currents at a fixed

overpotential. Since all samples were grown as epitaxial layers, these results confirm an intrinsic composition-function relationship independent of geometry or surface variability. X-ray photoemission studies reveal a synergistic effect from the simultaneous oxidation and reduction of transition metal cations during intermediate adsorption, highlighting high entropy oxides as a highly attractive class of earth-abundant materials for OER catalysis with activity potential beyond the scaling limits of traditional mono- or bimetallic oxides.

Zusammenfassung

Die globalen Durchschnittstemperaturen sind seit Beginn der industriellen Revolution gestiegen, wobei der stärkste Anstieg zwischen 2023 und 2024 mit mehr als 1,5 °C über dem vorindustriellen Niveau zu verzeichnen ist. Dieser Temperaturanstieg wird in erster Linie auf die erhöhten Konzentrationen von Treibhausgasen wie CO_2 und CH_4 in der Atmosphäre zurückgeführt, die größtenteils aus der Verbrennung fossiler Brennstoffe stammen. Um die Treibhausgasemissionen zu verringern, wurden erhebliche Forschungsanstrengungen auf nachhaltige Energielösungen eingesetzt. Eine weithin untersuchte Strategie ist die Nutzung erneuerbarer Energiequellen wie Sonnen- und Windenergie, um den Energiebedarf durch effiziente Umwandlungsprozesse von Energie in Kraftstoff und von Kraftstoff in Energie zu erzielen. Die Entwicklung dieser Technologien erfordert leistungsstarke Solarzellen, Elektrolyseure, Brennstoffzellen und Batterien, die alle auf fortschrittliche Elektrolyt- und Elektrodenmaterialien angewiesen sind. Eine grundlegende Herausforderung in der Materialwissenschaft ist die Entwicklung und Optimierung von Materialien mit überlegenen funktionellen Eigenschaften, um die Effizienz, Stabilität und Leistung dieser Energieumwandlungs- und Speichersysteme zu verbessern.

Hochentropieoxide (eng. High entropy oxides) sind eine neue Klasse vielversprechender Materialien, die für ihre Einphasenstabilität, ihre komplexe Zusammensetzung und ihre außergewöhnlichen funktionellen Eigenschaften bekannt sind. Das Hauptziel dieser Arbeit ist die Erforschung des Potenzials von Hochentropieoxiden als Sauerstoffionenleiter und Elektrokatalysatoren für Sauerstoffentwicklungsreaktionen. Der erste Schritt zur Bewertung dieser funktionellen Eigenschaften ist die Synthese der Oxide mit hoher Konfigurationsentropie in Form von Pellets und dünne Schichten. Die Hochentropieoxide werden mittels mechanochemisch er Synthese, Sol-Gel-Verfahren, umgekehrte Fällungsreaktion, Laserabscheidung und konventionelle Sintertechniken hergestellt. Das Hochentropieoxid $(Ce,La,Pr,Sm,Y)O_{2-\delta}$ mit Fluoritstruktur wird zum Vergleich herangezogen. Die durch mechanochemischer Synthese, Sol-Gel-Verfahren, umgekehrte Fällungsreaktion hergestellten Pulver weisen durchweg die gewünschte Fluoritstruktur auf. Ebenso behalten dünne Filme, die mit dem Sol-Gel-Verfahren und der Laserabscheidung synthetisiert wurden, die Fluoritstruktur bei, wobei die Laserabscheidung die Herstellung von Filmen mit verschiedenen Morphologien ermöglicht, wie z. B. polykristalline, säulenförmige und epitaktische Morphologien. Im Gegensatz dazu weisen Pellets, die durch konventionelles Sintern hergestellt wurden, aufgrund der hohen Sintertemperaturen eine Mischung aus Fluorit-

und Bixbyitstruktur auf. Diese Techniken werden auf verschiedene Hochentropieoxide angewandt, um ihr Potenzial als Sauerstoffionenleiter und Elektrokatalysatoren für die Sauerstoffentwicklungsreaktion zu bewerten.

Fluorit- und Perowskit-Typ Hochentropieoxide werden als Sauerstoffionenleiter untersucht. Die Sauerstoffionenleitfähigkeit wird an den Pellets dieser Hochentropieoxide untersucht. Die Pellets aus Hochentropieoxiden mit Fluoritstruktur $(Ce,La,Pr,Sm,Y)O_{2-\delta}$ gehen jedoch aufgrund der hohen Sintertemperaturen in eine Bixbyitstruktur über. Um die Bildung der Bixbyitstruktur während des Sinterns der Pellets zu verhindern, wurde Zr in verschiedenen Atomanteilen hinzugefügt. In der Tat wird die Fluoritstruktur bei einem Zr-Gehalt von etwa 10 at.% stabilisiert. Außerdem weisen $(Ce,La,Pr,Sm,Y)_{1-x}Zr_xO_{2-\delta}$ eine homogene Verteilung der Elemente auf, wobei Pr eine Multivalenz aufweist. Als zusätzlicher Vorteil der Zugabe von Zr steigt die ionische Leitfähigkeit mit der Zugabe von Zr und erreicht ein Maximum bei 8 at.% Zr und nimmt mit weiterer Zugabe von Zr ab. Interessanterweise wird die von einem mehrwertigen Pr erwartete elektronische Leitfähigkeit in einer oxidierenden Atmosphäre unterdrückt, während in den Oxiden mit Fluoritstruktur und hoher Entropie eine hohe Ionenleitfähigkeit beobachtet wird. In dieser Arbeit werden auch Oxide mit hoher Entropie vom Perowskit-Typ untersucht, insbesondere Hochentropiealuminate. Herkömmliche Seltenerdaluminate mit Perowskitstruktur sind als Sauerstoffionenleiter bekannt. Sie weisen jedoch in oxidierenden Atmosphären aufgrund des Sauerstoffaustauschs zwischen der Atmosphäre und dem Gittersauerstoff bei hohen Temperaturen eine elektronische Leitung vom p-Typ auf. Materialien mit hoher Entropie bieten mit ihren hohen Konfigurationsentropien Stabilität bei hohen Temperaturen, was darauf hindeutet, dass sie unerwünschte elektronische Leitung reduzieren könnten. Zur Untersuchung dieses Phänomens werden Hochentropiealuminate - $(Gd_{0.2}La_{0.2}Nd_{0.2}Pr_{0.2}Sm_{0.2})_{1-x}Ca_xAlO_3$ - untersucht. Diese Hochentropiealuminate weisen eine orthorhombische Perowskit-Struktur mit einer homogenen Verteilung der Elemente auf, wobei bei $x = 0,15$ und $x = 0,2$ kleinere Sekundärphasen auftreten. Die Leitfähigkeit nimmt mit dem Ca-Gehalt zu, erreicht ihren Höhepunkt bei $x = 0,1$ und bleibt bei weiterer Zugabe von Ca konstant. Gleichzeitig wird die p-Typ-Leitung, die typischerweise in dotierten Seltenerdaluminaten beobachtet wird, wirksam abgeschwächt. Oxide mit hoher Entropie bieten ein vielversprechendes Potenzial, um die elektronische Leitung einzuschränken, die in herkömmlichen Sauerstoffionenleitern beobachtet wird. Darüber hinaus sind die in dieser Forschungsarbeit erzielten Leitfähigkeiten mit dem modernsten Sauerstoffionenleiter, Yttrium-stabilisiertem Zirconiumdioxid, vergleichbar.

Materialien mit hoher Konfigurationsentropie sind vielversprechend für die Entwicklung hochaktiver Elektrokatalysatoren. Diese können je nach Anwendung maßgeschneidert werden und ihre vielzähligen aktiven Stellen eröffnen Möglichkeiten für die Entwicklung katalytischer Materialien mit hoher Verfügbarkeit in der Erdkruste, die eine energieeffiziente elektrochemische Energieumwandlung und -speicherung unterstützen. In dieser Arbeit wird gezeigt, dass die Oxide des Perowskit-Typs mit hoher Entropie die katalytische Aktivität für die Sauerstoffentwicklungsreaktion, die kinetisch begrenzende Halbreaktion bei der elektrochemischen Energieumwandlung, einschließlich der Erzeugung von grünem Wasserstoff, erheblich steigern. Insbesondere wurde die katalytische Leistung der (001)-Facette von $La(Cr_{0.2}Mn_{0.2}Fe_{0.2}Co_{0.2}Ni_{0.2})O_{3-\delta}$ mit der seiner Ausgangsverbindungen mit einer einzelnen B-Gitterposition in der ABO_3-Perowskitstruktur verglichen. Während die Perowskite mit nur einem Element auf der B-Gitterposition im Allgemeinen den erwarteten vulkanartigen Aktivitätstrends folgen, übertrifft das Hochentropieoxid alle Ausgangsverbindungen, indem es bei einer festen Überspannung 17- bis 680-mal höhere Ströme erzielt. Da alle Proben als epitaktische Filme abgeschieden worden sind, bestätigen diese Ergebnisse eine intrinsische Beziehung zwischen Zusammensetzung und Funktion, die unabhängig von Geometrie oder Oberflächenvariabilität ist. Studien mittels Röntgenphotoelektronenspektroskopie zeigen einen synergetischen Effekt durch die gleichzeitige Oxidation und Reduktion von Übergangsmetallkationen während der Zwischenadsorption, wodurch Oxide mit hoher Entropie eine äußerst attraktive Klasse von Materialien für die OER-Katalyse mit einem Aktivitätspotenzial jenseits der Skalierungsgrenzen herkömmlicher mono- oder bi-metallischer Oxide darstellen.

Contents

1 Introduction

1.1 Motivation

The advent of human development has led to a significant carbon footprint, resulting in excess of carbon dioxide in the atmosphere, a major driver of global warming. Over half of the global carbon dioxide emissions stem from the combustion of fossil fuels for energy requirements. To mitigate the climate change caused by the carbon footprint, the United Nations in 2015 set guidelines known as the Paris Agreement regarding the reduction in carbon footprint for countries all over the world. The Paris Agreement aims to achieve a carbon neutral world by the end of 2050. The majority of the global energy requirements are fulfilled by consumption of fossil fuels. In order to achieve carbon neutrality along with sustainable social and ecological growth, it is important to revert the energy needs from the non-renewable energy sources like fossil fuel to renewable energy sources like solar, wind and hydrothermal energies. While renewable energy sources are essential for achieving carbon neutrality, they are not always available. Challenges remain in energy conversion, storage, transportation, and consumption. A potential way for efficient conversion, transportation and consumption is by utilizing green hydrogen. Green hydrogen involves conversion of energy from renewable energy sources to green hydrogen with the help of electrolyzers, transportation of the green hydrogen and reconversion of the green hydrogen to electricity for commercial purposes with help of fuel cells. However, green hydrogen technologies face challenges such as high production costs and energy inefficiencies in cells during reversible conversion, storage, and transportation[1–4]. To enhance the efficiency of electrolyzers and fuel cells, inventing materials with high ionic conductivity for electrolytes and high electrocatalytic activity for electrodes is crucial. One key approach to designing new materials is modifying the composition of a given system—referred to as alloying in metallic systems and doping in non-metallic systems. However, this approach becomes increasingly complex as the number of constituent elements grows. The vast number of possible material combinations in multicomponent systems leads to nearly infinite possibilities, making the search for an optimal composition with the desired functionality a daunting challenge. At the beginning of the 21st century, a new strategy was introduced to explore the vast compositional space of multicomponent systems. This approach focuses on identifying compositions with high configurational entropy greater than 1.5R (where R is the gas constant). The high configurational entropy of these compositions helps thermodynamically

overcome the enthalpic contributions in multicomponent systems at elevated temperatures, leading to the formation of a single-phase material. These materials are termed high entropy materials. Since their introduction in 2005, high entropy materials gained a lot of attention for their four core effects which are high configurational entropy, sluggish diffusion, severe lattice distortion and cocktail effect. The high entropy concept was initially applied to metals, resulting in the development of high entropy alloys. It was later extended to ionic compounds, leading to high entropy oxides, carbides, oxyfluorides, borides, and nitrides, and subsequently to covalently bonded materials, giving rise to high entropy metal-organic frameworks. Among the high entropy materials, high entropy oxides gained attention for their noteworthy functional properties observed for energy applications such as batteries, electro-catalysis, supercapacitors and photo-voltaic applications.

1.2 Objectives

This work explores the novel high entropy oxides with fluorite- and perovskite-type structures as oxygen ion conductors and electrocatalysts for the oxygen evolution reaction. A more detailed overview of the objectives of the research presented in this thesis is as follows:

1) Investigation of different synthesis and processing routes for achieving powders, pellets, and thin films of high entropy oxides.

2) Structural and chemical characterization of the high entropy oxides to investigate the underlying structure, phase purity, chemical homogeneity, and oxidation states of the constituent elements.

3) Exploring the high entropy oxides for their applicability for oxygen ion transport and electrocatalysis for the oxygen evolution reaction.

4) Correlating the structure and valence states to the observed functional properties of these high entropy oxides.

5) Comparison of the functional properties of the high entropy oxides with the functional properties of the corresponding single component oxides and the corresponding state-of-the-art materials.

6) Elucidating the enhanced functional properties in the high entropy oxides compared to single component oxides.

1.3 Outline of the thesis

Chapter 2 discusses the scientific background and has three subsections. **Section 2.1** covers oxygen ion conductors, focusing on their fundamentals and the key criteria that define a good oxygen ion conductor. Additionally, it examines oxygen ion conduction in both fluorite- and perovskite-type oxides. **Section 2.2** of this chapter discusses the electrocatalysis for the oxygen evolution reaction. In this section, the mechanisms for the oxygen evolution reaction on the surface of the catalyst, along with different experimental parameters evaluating the electrocatalytic activity, are discussed. Additionally, the electrocatalytic activity of perovskite-structured oxides and their various activity descriptors available in the literature are discussed. Finally, in the last section - **Section 2.3**, high entropy materials and their four core effects are introduced; subsequently, research on high entropy oxides and their applicability as oxygen ion conductors and electrocatalysts for the oxygen evolution reaction are discussed.

Chapter 3 provides a detailed overview of the characterization techniques employed in this thesis, covering various structural, chemical, and electrochemical methods used to analyze the powders, thin films, and pellets.

Chapter 4 examines the synthesis techniques employed in this thesis to prepare the powders, thin films, and pellets. These methods include reverse co-precipitation, the sol-gel process, mechanochemical synthesis, conventional sintering, and pulsed laser deposition, all tested for fluorite-structured high entropy oxide. This chapter delves deeper into the characterization of samples obtained through these techniques, focusing on variations in structure, crystallite size, morphology, and chemical distribution.

Chapter 5 investigates the oxygen ion conductivity of the high entropy oxides. This chapter has two subsections. **Section 5.1** discusses the investigations on fluorite-type high entropy oxides. The high entropy oxide powders with a composition of $(Ce,La,Pr,Sm,Y)_{1-x}Zr_xO_{2-\delta}$ are synthesized via a mechanochemical route, which are then pressed into pellets and sintered via conventional sintering. The resultant pellets are then characterized structurally and chemically by different characterization techniques, after which the electrochemical or electrical properties of the fluorite-type high entropy oxides are determined. Furthermore, the experimental results are discussed in more detail. **Section 5.2** delves into the investigation of perovskite-type high entropy rare earth aluminates. High entropy oxides with the composition $(Gd,La,Nd,Pr,Sm)_{1-x}Ca_xAlO_3$ with varying amounts of Ca are synthesized by conventional sintering the high entropy oxide powders synthesized via the sol-gel process or Pechini process.

The high entropy rare earth aluminates are then characterized structurally, chemically, and electrically to understand the structure, chemical composition – homogeneity, and oxygen ion conduction, which are further discussed in detail at the end of the section.

Chapter 6 explores the perovskite structured high entropy oxide – La(Co,Cr,Fe,Mn,Ni)O_3 as an electrocatalyst for the oxygen evolution reaction. Electrocatalytic activity is explored for the epitaxial thin films synthesized by pulsed laser deposition. This chapter discusses the structural and chemical characterization of the epitaxial thin films. Furthermore, the catalytic activity of the high entropy oxide is measured and compared to the corresponding single-component oxides. Finally, various advanced characterization techniques explore the possible mechanisms behind the enhanced catalytic activity.

Chapter 7 is the conclusion and outlook of the thesis. All the results and findings, along with possible research opportunities for future investigations, are presented in this chapter.

2   Scientific background

This chapter is divided into three parts. The first part of this chapter includes an introduction to oxygen ion conductors and a brief introduction to the fundamentals, along with a short introduction to fluorite-type and perovskite-type oxygen ion conductors. The second part of the chapter discusses the electrocatalysts for the oxygen evolution reaction along with fundamental mechanisms. This section also explores different experimental parameters characterizing the catalytic activity of catalysts for the oxygen evolution reaction. Furthermore, the perovskite structured oxides as catalysts for oxygen evolution reaction are explored along with various activity descriptors for activity comparison of different perovskite structured oxides. The final section of the chapter explores high entropy oxides and their four core effects, followed by a brief review of studies on oxygen ion conductivity and the electrocatalytic performance of high entropy oxides in the oxygen evolution reaction.

2.1   Oxygen ion conductors

Oxygen ion conductors are materials that transport oxygen ions through their lattices. Oxygen ion conductors have many applications, such as solid oxide fuel cells, solid oxide electrolyzer cells, oxygen sensors, oxygen pumps, and oxygen separation membranes. In all of those applications, the oxygen ion conductor is the electrolyte separating the electrodes. In this section of the thesis, the fundamentals and criteria for a good oxygen ion conductor will initially be discussed, after which the two different structures accommodating oxygen ion conduction and their corresponding advantages and drawbacks will be discussed.

2.1.1   Fundamentals of oxygen ion conductors

An oxygen ion conductor, as an electrolyte, conducts oxygen ions between the electrodes. As a result, the electrolyte or the oxygen ion conductor should exhibit high oxygen ion conduction along with minimal electronic conduction to avoid short circuits in the electrochemical cell. High oxygen ion conductivities in oxygen ion conductors are possible at elevated temperatures (500 – 900 °C). As a result, it has been an exciting endeavor for researchers to find material systems with high oxygen ion conduction at lower operation temperatures (<500 °C). Furthermore, the air electrode in a solid oxide cell is at oxidizing

conditions (1 bar to 10^{-8} bar), whereas the fuel electrode is in reducing conditions (10^{-20} to 10^{-30} bar). Therefore, the electrolyte should exhibit good ionic conduction along with negligible electronic conduction over a wide range of oxygen partial pressure (1 bar to 10^{-30} bar) and lower temperatures (< 500 °C). The total conductivity of the system (σ_t) is the sum of the ionic conductivity (σ_{ion}) and electronic conductivity (σ_{elec}) system and can be written as follows

$$\sigma_t = \sigma_{ion} + \sigma_{elec} \qquad\qquad Eq.\ 2\text{-}1$$

The conductivity of a charge carrier is a result of the movement of the charge carrier under an applied electric field. Consequently, the total conductivity in $Eq.\ 2\text{-}1$ can be written as

$$\sigma_t = c_{ion}q_{ion}\mu_{ion} + c_{elec}q_{elec}\mu_{elec} \qquad\qquad Eq.\ 2\text{-}2$$

where c_{ion} and c_{elec} are the concentrations of the ions and electrons, q_{ion} and q_{elec} are the charges of the ions and electrons and μ_{ion}, μ_{elec} are the mobilities of the ions and electrons. Furthermore, the fraction of conduction of a charge carrier over the total conductivity is often represented by the transference number (t). The transference number of an ion is the fraction of current carried by an ion (i_{ion}) of the total current (i_t). Typically, an electrolyte is operated in the ohmic region in which the resultant current is directly proportional to conductance (G). Consequently, the transference number of ions (t_{ion}) and electrons (t_{elec}) are

$$t_{ion} = \frac{i_{ion}}{i_t} = \frac{G_{ion} \times V}{G_t \times V} = \frac{G_{ion}}{G_t} = \frac{\sigma_{ion}}{\sigma_t} \qquad\qquad Eq.\ 2\text{-}3$$

$$t_{elec} = \frac{\sigma_{elec}}{\sigma_t} \qquad\qquad Eq.\ 2\text{-}4$$

For a good oxygen ion conductor, the total conductivity (σ_t), oxygen ion conductivity (σ_{ion}) as well as the mobility of the oxygen ions (μ_{ion}) should be very high. Conversely, the electronic conductivity (σ_{elec}) and the mobility of the electrons or polarons (μ_{elec}) should be very low. Furthermore, the transference number of oxygen (t_{ion}) should be close to 1.

The ionic conductivity in oxygen ionic conductors occurs via migration of the oxygen ions along the oxygen vacancies. Similarly, small polaron propagation along the multivalent sites under an applied electric field induces electronic conduction. The total conductivity is the sum of both mechanisms. A model for the conduction mechanism for the hopping of the charge carriers will be discussed in the following. For simplicity, a one-dimensional hopping model either along the field direction or against the field direction is assumed. The energy barrier for the charge carrier is higher in one direction and lower in the other direction, depending on the

direction of the electric field (E). The energy for a charge carrier with a charge q is $\left(\Delta g_m - \frac{1}{2}\text{qaE}\right)$ along the electric force and $\left(\Delta g_m + \frac{1}{2}\text{qaE}\right)$ against the electric force, as depicted in *Figure 2-1*. Here a is the jump distance. Consequently, the probability of ion jump (p) along the electric force can be estimated from the Maxwell-Boltzmann statistics, which is

$$p = \exp\left(\frac{-\left(\Delta g_m - \frac{1}{2}qaE\right)}{kT}\right) \qquad \qquad Eq.\ 2\text{-}5$$

here Δg_m is the free energy barrier for migration, k is the Boltzmann constant, and T is the absolute temperature in Kelvin. From *Eq. 2-5*, the jump rate of the ion or polaron along the electric force (Γ_+) can be written as

$$\Gamma_+ = j\exp\left(\frac{-\left(\Delta g_m - \frac{1}{2}qaE\right)}{kT}\right) \qquad \qquad Eq.\ 2\text{-}6$$

here j is the attempt frequency or the vibration frequency of the ion between stable positions. However, the jump rate of the ions or polarons against the electric force (Γ_-) is given by

$$\Gamma_- = j\exp\left(\frac{-\left(\Delta g_m + \frac{1}{2}qaE\right)}{kT}\right) \qquad \qquad Eq.\ 2\text{-}7$$
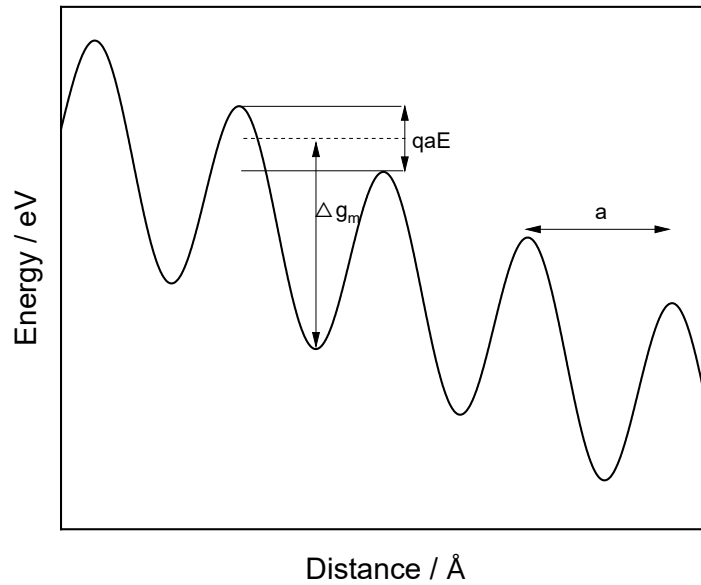

Figure 2-1 The potential energy barrier that needs to be overcome for the migration of ion or polaron under an applied electric field.

The overall jump rate or the velocity (v) of the charge carrier in an applied electric field is the difference of the charge carrier hopping along and against the electric force multiplied by

the jump distance a. Therefore, the velocity of the charge carrier in the direction of the electric force under an applied electric field E from *Eq. 2-6* and *Eq. 2-7* can be written as

$$v = (\Gamma_+ - \Gamma_-)a = ja \left(\exp\left(\frac{-\left(\Delta g_m - \frac{1}{2}qaE\right)}{kT} \right) - \exp\left(\frac{-\left(\Delta g_m + \frac{1}{2}qaE\right)}{kT} \right) \right) \qquad Eq.\ 2\text{-}8$$

$$v = ja \exp\left(\frac{-\Delta g_m}{kT} \right) \left(\exp\left(\frac{qaE}{2kT} \right) - \exp\left(\frac{-qaE}{2kT} \right) \right) \qquad Eq.\ 2\text{-}9$$

qaE is much lower than kT for the applied electric field in conductivity experiments, so

$$\left(\exp\left(\frac{qaE}{2kT} \right) - \exp\left(\frac{-qaE}{2kT} \right) \right) \approx \frac{qaE}{kT} \qquad Eq.\ 2\text{-}10$$

By combining *Eq. 2-9* and *Eq. 2-10*, the velocity of the charge carrier under an applied electric field (E) is

$$v = \frac{jqa^2E}{kT} \exp\left(\frac{-\Delta g_m}{kT} \right) \qquad Eq.\ 2\text{-}11$$

From the velocity of the charge carrier in *Eq. 2-11*, the mobility of the charge carrier ($\mu = \frac{v}{E}$) can be written as

$$\mu = \frac{jqa^2}{kT} \exp\left(\frac{-\Delta g_m}{kT} \right) \qquad Eq.\ 2\text{-}12$$

The mobility of the charge carrier in *Eq. 2-12* is derived under the assumption that the charge carrier is hopping in one dimension. However, the lattice in which the charge carrier is hopping is three-dimensional and in order to account for that, often a geometrical factor (γ) is included in *Eq. 2-12* to give

$$\mu = \frac{\gamma jqa^2}{kT} \exp\left(\frac{-\Delta g_m}{kT} \right) \qquad Eq.\ 2\text{-}13$$

The conductivity of the charge carrier can be estimated and is given by

$$\sigma = cq\mu = \frac{c\gamma jq^2a^2}{kT} \exp\left(\frac{-\Delta g_m}{kT} \right) \qquad Eq.\ 2\text{-}14$$

Furthermore, the free energy barrier for migration of the charge carrier can be further separated into

$$\Delta g_m = \Delta h_m - T\Delta s_m \qquad Eq.\ 2\text{-}15$$

By combining *Eq. 2-14* and *Eq. 2-15* results in

$$\sigma = \frac{c\gamma jq^2 a^2}{kT} \exp\left(\frac{-\Delta h_m}{kT}\right) \exp\left(\frac{\Delta s_m}{k}\right) \qquad\qquad Eq.\ 2\text{-}16$$

The conductivity expression in *Eq. 2-16* resembles the Arrhenius equation which is given by

$$\sigma = \frac{\sigma_o}{T} \exp\left(\frac{-\Delta h_m}{kT}\right) \qquad\qquad Eq.\ 2\text{-}17$$

where
$$\sigma_o = \frac{c\gamma jq^2 a^2}{k} \exp\left(\frac{\Delta s_m}{k}\right) \qquad\qquad Eq.\ 2\text{-}18$$

It is important to note here that the conductivity pre-factor (σ_o) is constant for a given composition. The enthalpy of migration is often termed as activation energy (E_a) for conduction. The activation energy for conduction is calculated by measuring the conductivity at different temperatures and by applying the following expression

$$\ln(\sigma T) = \ln(\sigma_o) - \frac{E_a}{kT} \qquad\qquad Eq.\ 2\text{-}19$$

Therefore, from *Eq. 2-19*, the slope of the plot between $\ln(\sigma T)$ and 1/T provides the activation energy for conduction for a given composition. This method is used for measuring the activation energies of the material systems synthesized in this thesis. A good oxygen ion conductor should have low activation energy for oxygen ion hopping and high activation energy for polaron hopping.

To summarize, the criteria for a good oxygen ion conductor are as follows:

1) The total conductivity should be high with high oxygen ion conductivity along with minimal electronic conductivity at lower temperatures (< 500 °C), wide ranges of oxygen partial pressures (1 bar to 10^{-30} bar).

2) High ionic mobilities along with low electronic mobilities over wide ranges of temperatures (300 to 700 °C) and oxygen partial pressures.

3) The transference number of oxygen ion should be close to 1 ($t_o \approx 1$) over wide ranges of temperature (300 to 700 °C) and oxygen partial pressure (1 bar to 10^{-30} bar).

4) The activation energy of the ion migration should be lower than the activation energy for polaron migration or electron migration.

To enhance oxygen ion conduction, the lattice needs to accommodate the movement of the large oxygen ion through the lattice. Consequently, only a few material systems and structures support oxygen ion conduction. Two of those systems that can accommodate the conduction of

oxygen ions are fluorite-structured oxides and perovskite-structured oxides. These two structures are discussed briefly in the following section.

2.1.2 Fluorite structured oxides

Fluorite-structured oxides are very well known for their oxygen ion conduction since their introduction in the 1900s by Walther Nernst. The fluorite structure exhibits a face-centered cubic (FCC) lattice with cations on the lattice sites and the anions in the tetrahedral voids of the lattice. The stoichiometry of these fluorite-structured oxides is MO_2. The cations in the fluorite structure have an oxidation state of +4 and large ionic radii, allowing the oxygen to occupy the tetrahedral void of the lattice. Examples of cubic fluorite structured oxides include Ceria $(CeO2)$, Uranium dioxide $(UO2)$, and Thorium dioxide (ThO_2). Although Zr is a +4 cation, ZrO_2 exhibits a monoclinic structure and transforms to cubic fluorite above 2300 °C, which is due to the smaller ionic radius of the Zr ion[5]. A stoichiometric fluorite structured oxide does not have any intrinsic oxygen vacancies. To introduce oxygen vacancies, +3 rare earth cations are added into the material systems. The addition of +3 cations like Y and Sc to ZrO_2 not only introduces oxygen vacancies but also stabilizes the cubic fluorite structure at room temperature. Consequently, Y and Sc doped ZrO_2 are popular oxygen ion conductors [5]. Other well-known fluorite structured oxygen ion conductors are doped ceria in which rare earth elements with +3 oxidation states like Gd, and Sm are doped into CeO_2. The electrical conductivity of these fluorite-structured oxides can be seen in *Figure 2-2(a)*[6]. The conductivities of doped zirconia make them suitable as oxygen ion conductors at high operating temperatures (>700 °C), whereas Gd-doped ceria, with higher conductivities than doped zirconia, is suitable for intermediate temperatures (500 - 700 °C). Due to their higher conductivities at lower temperatures, doped ceria has been investigated extensively. Multiple material systems with different rare earth elements as dopants are investigated to find the optimum dopant giving high electrical conductivities. The conductivity of doped ceria vs. the dopant ionic radii is depicted in *Figure 2-2(b)*[6]. Sm doped ceria shows the highest conductivity with Gd doped ceria showing the next best conductivities. The DFT calculations from Andersson *et al.*[7] suggest that co-doping ceria with multiple dopants can be a possible way to increase the conductivity in doped ceria. This possibility of co-doping has been investigated in multiple studies with different results, where some studies show better conductivities and others show inferior conductivities [8–12].

Figure 2-2 (a) Electrical conductivity of fluorite structured oxides plotted by Arrhenius representation and (b) the electrical conductivity of doped ceria with different dopants at 1073 K plotted against the dopant ionic radii [6].

Despite their high conductivities at low temperatures, one of the biggest drawbacks of doped ceria is the electronic conduction observed at different oxygen partial pressures, especially in reducing atmospheres at operating temperatures (500 - 700 °C). Cerium exhibits multivalency in reducing atmospheres, as depicted by the Kroeger Vink equation below

$$2Ce_R^\times + O_O^\times \rightleftharpoons 2Ce_R' + V_O^{\bullet\bullet} + \frac{1}{2}O_2 \qquad \textit{Reaction 2-1}$$

Here $Ce_R^\times$ is Ce^{+4}, $O_O^\times$ is lattice oxygen, Ce_R' is Ce^{+3} and $V_O^{\bullet\bullet}$ is the oxygen vacancy. The presence of multivalent cerium provides a pathway for polaron hopping through the lattice, resulting in an electronic contribution to the total conductivity [13–22]. The electronic conduction arises not only due to a multivalent Ce but also from multivalent dopants like Pr or Tb, resulting in a material with mixed electronic and ionic conduction [13–22]. As a result, doped ceria is explored for applications that require mixed electronic and ionic conduction, e.g., as a barrier layer between electrolyte and electrode.

2.1.3 Perovskite structured oxides

Perovskite-structured oxides are renowned for their exceptional functional properties, including superconductivity, magnetism, ferroelectricity, and oxygen ion conduction, among others. Perovskite oxides have a stoichiometry of ABO_3 with A-site cations on the body center, B-site cations on the corner sites, , and oxygen on the edge center of a unit cell. According to the stoichiometry of the perovskite structure, the total charge on the cations is +6. This is achieved by combining two +3 cations on A and B sites or one +2 cation on A-site and a +4 cation B-site. In some cases, these cations are multivalent like in rare earth transition metal oxides. However, in oxygen ion conductors, as discussed in the ceria-based fluorite structured systems in the previous section, multivalent cations can lead to polaron hopping and, thereby, electronic conduction in the material system. Therefore, perovskite-structured oxides with stable single valent cations are explored for oxygen ion conduction. These material systems contain rare earth cations (R) (+3) on the A-site and Al, In, Ga, and Sc (stable +3 cations) on the B-site. Typically, $RAlO_3$, $RGaO_3$, $RInO_3$, and $RScO_3$ don't have any intrinsic oxygen vacancies. Therefore, cations with lower oxidation states are doped to introduce oxygen vacancies. These dopants usually include alkali earth metals like Mg, Sr, and Ca, which are stable +2 cations. The conductivities of Sr and Mg doped $RAlO_3$, $RGaO_3$, $RInO_3$, and $RScO_3$ vs. inverse temperature are demonstrated in *Figure 2-3(a)*. $La_{0.9}Sr_{0.1}Ga_{0.9}Mg_{0.1}O_3$ shows the highest conductivity with the next best conductivities from $La_{0.9}Sr_{0.1}Al_{0.9}Mg_{0.1}O_3$ and $La_{0.9}Sr_{0.1}Sc_{0.9}Mg_{0.1}O_3$. Furthermore, the conductivity of perovskites over wide ranges of oxygen partial pressures as shown in *Figure 2-3(b)* are constant for $La_{0.9}Sr_{0.1}Ga_{0.9}Mg_{0.1}O_3$, whereas a change in conductivity which is a p-type conduction in the oxidizing regimes in $La_{0.9}Sr_{0.1}Al_{0.9}Mg_{0.1}O_3$, $La_{0.9}Sr_{0.1}Sc_{0.9}Mg_{0.1}O_3$ and $La_{0.9}Sr_{0.1}In_{0.9}Mg_{0.1}O_3$ is observed. This p-type conductivity is a consequence of the surface exchange of the lattice oxygen with atmospheric oxygen, resulting in holes in the system as shown in the following reaction

$$\frac{1}{2}O_2 + V_O^{\bullet\bullet} \leftrightarrow O_O^x + 2h^{\bullet} \qquad \textit{Reaction 2-2}$$

The change in conductivity with oxygen partial pressure in $La_{0.9}Sr_{0.1}Al_{0.9}Mg_{0.1}O_3$, $La_{0.9}Sr_{0.1}Sc_{0.9}Mg_{0.1}O_3$ and $La_{0.9}Sr_{0.1}In_{0.9}Mg_{0.1}O_3$ is observed in oxidizing atmospheres, whereas a constant conductivity is observed under reducing conditions. As a result, $La_{0.9}Sr_{0.1}Ga_{0.9}Mg_{0.1}O_3$ (LSGMO) is a very well-known oxygen ion conductor due to its high oxygen ion conductivity and stability over wide ranges of oxygen partial pressures.
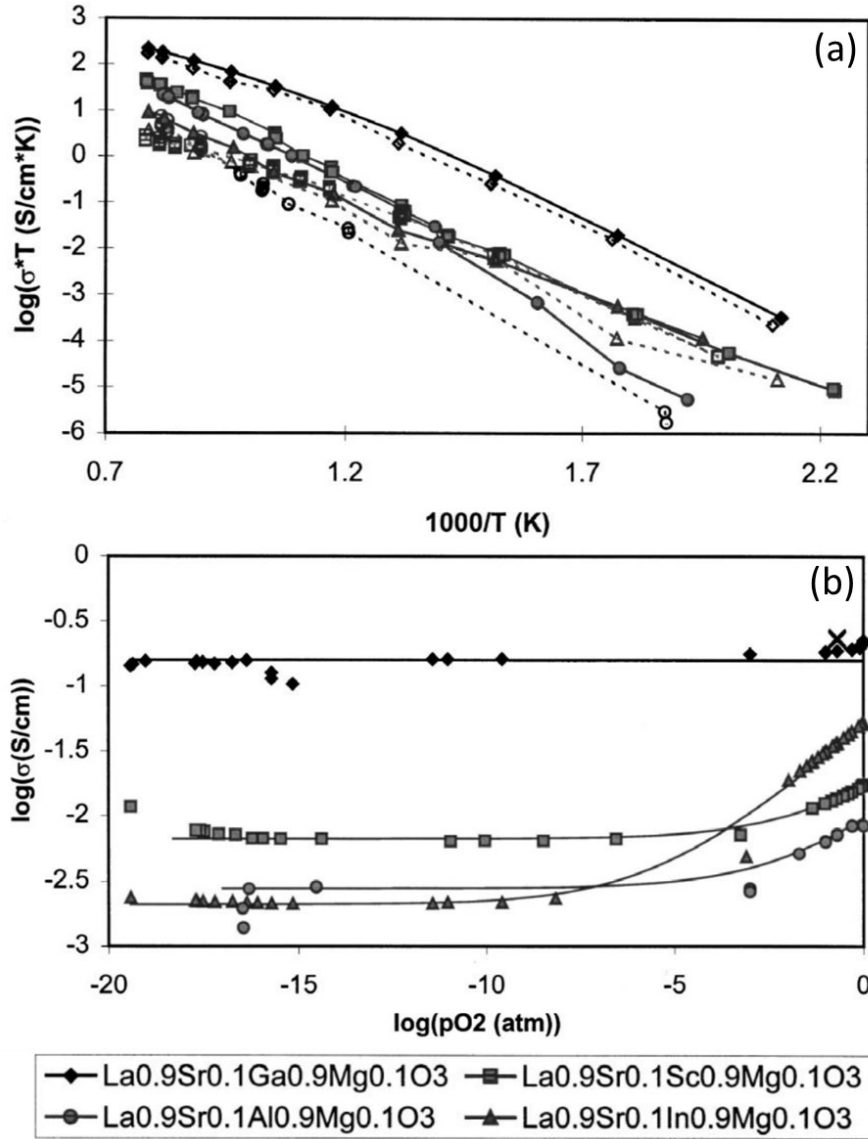
Figure 2-3 (a) The electrical conductivity of the perovskite structured oxide at different temperatures. (b) The electrical conductivity of the perovskite structured oxide at 1000 °C at different oxygen partial pressures [23].

2.2 Electrocatalysis – catalyst for oxygen evolution reaction

An electrolyzer is an electrochemical device that splits water (H_2O) into hydrogen (H_2) and oxygen (O_2) through electrolysis. The oxygen evolution reaction (OER) takes place at the anode, playing a crucial role in the overall efficiency of the process. As a key half-reaction in electrolysis, the kinetics of OER significantly influence the electrolyzer's performance. Thus, developing highly efficient catalysts for the OER at the anode is crucial for enhancing

electrolyzer performance. In this section, we explore the fundamentals of the OER and examine the use of perovskite-structured oxides as OER catalysts.

2.2.1 Fundamentals of the oxygen evolution reaction

Oxygen evolution reaction is a critical electrochemical reaction in which water or oxygen ions are converted into oxygen gas. The reaction mechanisms for OER depend on the electrolyte and are as follows

1) In water-based electrolytes or water electrolysis

$$2H_2O + 4 \times 1.23 \text{ eV} \rightarrow 4H^+ + O_2 + 4e^- \qquad \textit{Reaction 2-3}$$
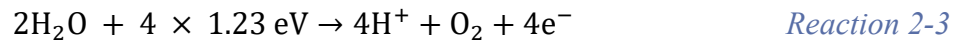
2) In solid oxide electrolytes,

$$2O^{2-} \rightarrow O_2 + 4e^- \qquad \textit{Reaction 2-4}$$

In this thesis, the electrocatalysis for oxygen evolution reaction in oxides was investigated. So hereon, the mechanisms of oxygen evolution reaction in water electrolytes are discussed. Two different reaction mechanisms are suggested in the literature for electron transfer in oxygen evolution reaction for a metal oxide catalyst, which are the conventional adsorbate evolution mechanism (AEM) and lattice oxygen evolution mechanism (LOM). A schematic of both mechanisms is illustrated in *Figure 2-4*. However, both reaction mechanisms involve four important and primary reactions for electron transfer (here * denotes adsorbates) which are as follows

$$H_2O \rightleftharpoons HO^* + H^+ + e^- \; ; \quad \Delta G_1 \qquad \textit{Reaction 2-5}$$

$$HO^* \rightleftharpoons O^* + H^+ + e^- \; ; \; \Delta G_2 \qquad \textit{Reaction 2-6}$$

$$O^* + H_2O \rightleftharpoons HOO^* + H^+ + e^- \; ; \; \Delta G_3 \qquad \textit{Reaction 2-7}$$

$$HOO^* \rightleftharpoons O_2 + H^+ + e^- \; ; \quad \Delta G_4 \qquad \textit{Reaction 2-8}$$
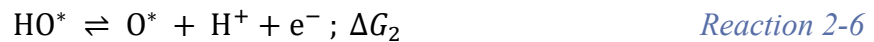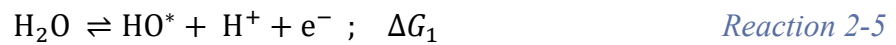
The first reaction mechanism AEM involves the adsorption of the HO^* on the surface of the oxide, which then gets converted to other reaction intermediates as seen from *Reaction 2-5* to *Reaction 2-8* on the surface of the metal oxide. A depiction of the AEM mechanism is depicted in *Figure 2-4(a)*. Whereas in the LOM reaction mechanism, the HO* binds to the lattice oxygen, which forms HOO^* which is then converted to oxygen gas as observed in *Reaction 2-8*. This results in an oxygen vacancy in the system, which is replenished by HO^* in the electrolyte and HO* ➜ O^* as depicted in *Reaction 2-5* and *Reaction 2-9*. In the following step, the oxygen vacancy is replenished and the occupied site can contribute to the next reaction which is *Reaction 2-10*. This reaction mechanism is depicted in *Figure 2-4(b)*. The theoretical standard potential for the oxygen evolution reaction is 1.23 V w.r.t reversible hydrogen electrode (RHE). Consequently, the theoretical Gibbs free energy for the reaction is $\Delta G = -nFE = -4 \times 1.23F \ (where \ F \ is \ a \ Farad)$. In an ideal catalyst, the Gibbs free energies of the intermediate reactions are equal which is $\Delta G_1 = \Delta G_2 = \Delta G_3 = \Delta G_4 = 1.23F$ but in reality $\Delta G_1 \neq \Delta G_2 \neq \Delta G_3 \neq \Delta G_4 \neq 1.23F$. A catalyst is selective for certain reactions resulting in higher ΔG of some reactions than 1.23F, while favored reactions exhibit ΔG smaller than 1.23F. Consequently, an excess potential is necessary for the reaction which is known as overpotential. Moreover, the overpotential of a catalyst depends on the intermediate reaction with the highest free energy. The intermediate reaction with maximum free energy and greater than 1.23F of the ΔG_1, ΔG_2, ΔG_3, ΔG_4 would be the rate limiting step and decides the overpotential.
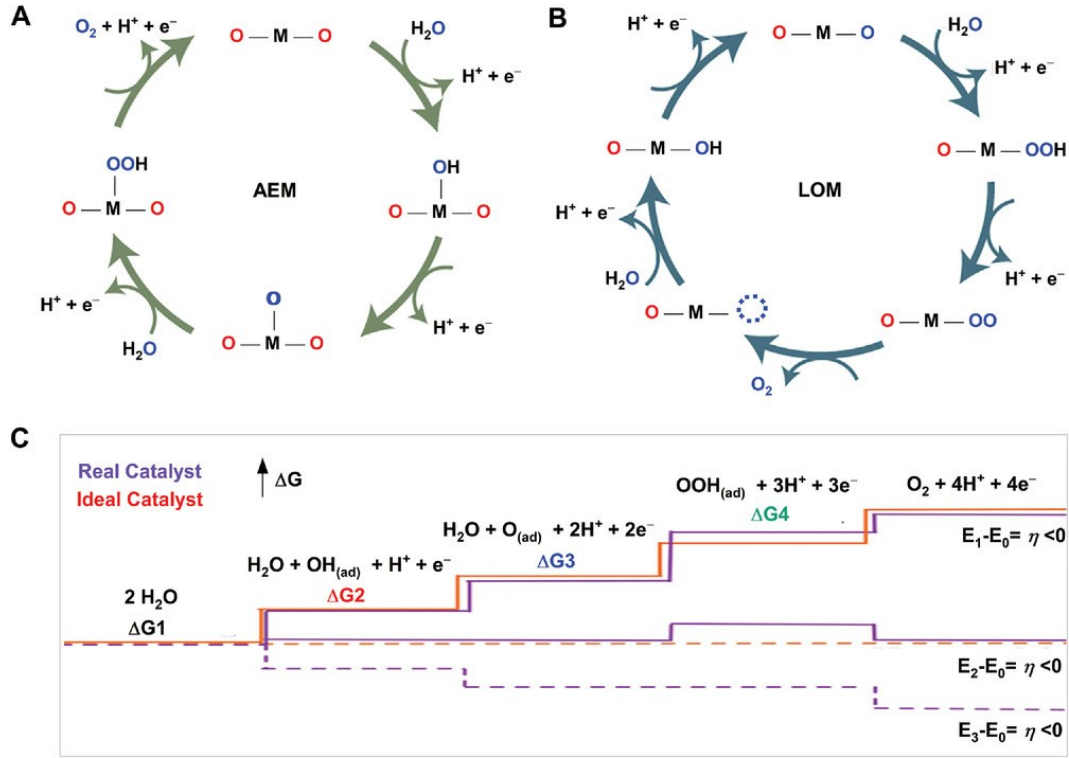
Figure 2-4 (a) Oxygen evolution reaction mechanism by conventional adsorbate evolution mechanism (AEM). (b) Oxygen evolution reaction mechanism by lattice oxygen evolution mechanism (LOM). (c) The Gibbs free energy at zero potential (U = 0) for ideal catalyst and the real catalyst [24].

2.2.2 Experimental parameters representing the catalytic activity of OER

Potential conversion to reversible hydrogen electrode:

A three-electrode setup consisting of working electrode, reference electrode and counter electrode is used to measure the electrocatalytic activity of the catalysts. Different reference electrodes are used in the measurements depending on the pH of the electrolytes as the pH of the solution can affect the potential measured at the reference electrode [25]. As a result, the research community adopts a common standard for representing measured potentials, the reversible hydrogen electrode (RHE), for a systematic comparison among different studies. Therefore, the potential measured at a reference electrode should be converted to RHE. The E_{meas} versus a reference electrode at a given pH can be converted to the potential versus RHE electrode (E_{meas}^{RHE}) with the help of the following expression which is

$$E_{meas}^{RHE} = E_{meas} + E_{RE}^{RHE} + 0.059\,\text{pH} \qquad\qquad \textit{Eq. 2-20}$$

Here E_{RE}^{RHE} is the standard electrode potential of the reference electrode with respect to the reference hydrogen electrode. The solution used in this thesis for electrochemical experiments is 0.1 KOH solution which has pH of 13.

iR compensation:

In an electrochemical cell, the potential drop between working electrode and the reference electrode happens at two regions: 1) the working electrode, due to formation of a double layer and charge transfer resistance, and 2) the electrolyte, due to electrolyte resistance. The measured cell potential simultaneously represents both potential drops. As a result, in order to isolate the potential drop at the electrode, the potential drop due to electrolyte resistance should be subtracted from the total potential drop between the working and reference electrode. The potential drop at the electrode ($E_{electrode}$) can be written as

$$E_{electrode} = E_{meas}^{RHE} - iR_{electrolyte} \qquad \text{Eq. 2-21}$$

where E_{meas}^{RHE} is the measured potential w.r.t the RHE electrode, i is the current and $R_{electrolyte}$ is the electrolyte resistance. The electrolyte resistance is calculated by performing electrochemical impedance spectroscopy on the electrochemical setup. The resistance at higher frequencies corresponds to the electrolyte resistance or the data can be fitted with Randall's circuit to achieve the electrolyte resistance.

The data collected from the potentiostat should be processed according to the aforementioned protocols to facilitate the representation, comparison, and further analysis of the electrochemical properties of the given material.

Overpotential:

The theoretical standard electrode potential of *Reaction 2-3* is 1.23 V versus the reversible hydrogen electrode (RHE). However, in practical applications, the required standard electrode potential is higher than 1.23 eV due to kinetics and potential barriers between the reaction intermediates. Therefore, an excess voltage should be supplied to the reaction to shift the *Reaction 2-3* towards the right at a significant rate. This excess potential or overpotential to achieve a given current density is often considered as one of the parameters depicting catalytic activity of a catalyst. The overpotential (η) required to achieve a given current density can be written as follows

$$\eta = E_{meas}^{RHE} - 1.23 \text{ V} \qquad \qquad \textit{Eq. 2-22}$$

Here E_{meas}^{RHE} is the measured potential at a given current density. Furthermore, current density at a given overpotential is also often used as catalytic activity descriptor of a catalyst. Both current density at a given overpotential and overpotential at a given current density are acceptable ways to compare the catalytic activity of different materials. The most popular way to compare the OER catalytic activity of different catalysts is by comparing the overpotential at a current density of 10 mA cm^{-2}. Lower overpotential values indicate the material's superior catalytic activity.

Tafel plot:

The Tafel plot represents the overpotential vs. the logarithm of current density collected during an electrochemical reaction. It is derived from the Tafel expression which is written as

$$\eta = a + b \log(j) \qquad \qquad \textit{Eq. 2-23}$$

here η is the overpotential, j is the current density, a the Tafel intercept and b the Tafel slope are constants for a given electrochemical reaction which can be further expanded as follows

$$a = \frac{2.303 \text{ R}T \log(j_o)}{\alpha n \text{F}} \qquad \qquad \textit{Eq. 2-24}$$

$$b = \frac{2.303 \text{ R}T}{\alpha n \text{F}} \qquad \qquad \textit{Eq. 2-25}$$

where R is the universal gas constant, F is Faraday's constant, α is charge transfer coefficient, n is the number of electrons transferred during an electrochemical reaction. From *Eq. 2-24*, the slope (b) from the Tafel plot and the charge transfer coefficient are inversely related. As a result, the tafel slope can provide valuable insights into the kinetics of an electrochemical reaction. A good catalyst should have lower Tafel slopes for maximum charge transfer during an electrochemical reaction.

Electrochemical surface area:

Electrochemical surface area is the surface area of the electrode that is catalytically active in an electrochemical reaction. The catalytic performance of a catalyst heavily depends on the electrochemical surface area. The higher the electrochemical surface area, the higher is

the activity of a catalyst. The electrochemical surface area of an electrode (ECSA) can be measured by estimating the double layer capacitance of the electrode (C_{dl}) from either cyclic voltammetry over a potential range in which no faradaic reactions occur or electrochemical impedance spectroscopy.

$$ECSA = \frac{C_{dl}}{C_s} \qquad \textcolor{blue}{Eq.\ 2\text{-}26}$$

Here C_s is the specific capacitance of the electrode. For evaluating the ECSA, the value of the specific capacitance must be known, which is the capacitance of the electrode per unit area. For a new material system, the calculation of ECSA is not straight forward and the specific capacitance should be calculated first in order to accurately determine the ECSA. Therefore, for materials with unknown C_s, it is recommended to compare the double layer capacitances - C_{dl} for the same geometric surface area for a meaningful comparison of active sites on the surface of catalysts.

2.2.3 Perovskite structured oxides and different activity descriptors

Perovskite structured oxides are widely explored as catalysts for the oxygen evolution reaction [24,26–29]. The perovskite structured oxides known for OER catalysis are rare earth transition metal oxides or alkaline earth transition metal oxide (RMO_3). Some good examples of these oxides are $LaMnO_3$, $SrCoO_3$, $LaCuO_3$. However, the active sites contributing to the catalytic activity are the transition metal cations. Therefore, the binding of the adsorbates by the transition metal ion plays a huge role in the OER catalysis. For transition metal cations, the binding ability of the cations decreases from left to right in the periodic table due to the electron-electron repulsion. In *Figure 2-5*, the standard free energy diagram for the OER reaction of the perovskite structured oxide such as $LaMnO_3$ (strong binding), $SrCoO_3$ (medium binding) and $LaCuO_3$ (weak binding) is shown. Contrary to the equal steps of potential - 1.23 V vs. RHE observed in an ideal catalyst, these perovskite structured oxides show nonequal steps of potential for different reaction intermediates. However, the differences between the free energies of HO* and HOO* ($\Delta G_{HOO^*} - \Delta G_{HO^*}$) are constant in all the metal oxide systems with an average value of 3.2 eV compared to 2.46 eV for an ideal catalyst [26]. Even though the $\Delta G_{HOO^*} - \Delta G_{HO^*}$ is constant, ($\Delta G_{HOO^*} - \Delta G_{O^*}$) and ($\Delta G_{O^*} - \Delta G_{HO^*}$) are not constant [26]. These free energy differences can determine the resulting overpotentials. This is evident in the free energy diagrams of the $LaMnO_3$ (strong binding), $SrCoO_3$ (medium binding) and $LaCuO_3$

(weak binding) in Figure 2-5. LaMnO$_3$ has higher ($\Delta G_{HOO^*} - \Delta G_{O^*}$) resulting in high overpotential while ($\Delta G_{HOO^*} - \Delta G_{O^*}$) and ($\Delta G_{O^*} - \Delta G_{HO^*}$) are almost identical for SrCoO$_3$ giving a lower overpotential and in LaCuO$_3$, ($\Delta G_{O^*} - \Delta G_{HO^*}$) is the potential determining step with relatively high overpotential. Hence, Sabatier proposed that the best catalyst in terms of displaying minimum overpotential binds intermediates on its surface neither too strongly nor too weakly [26,30].
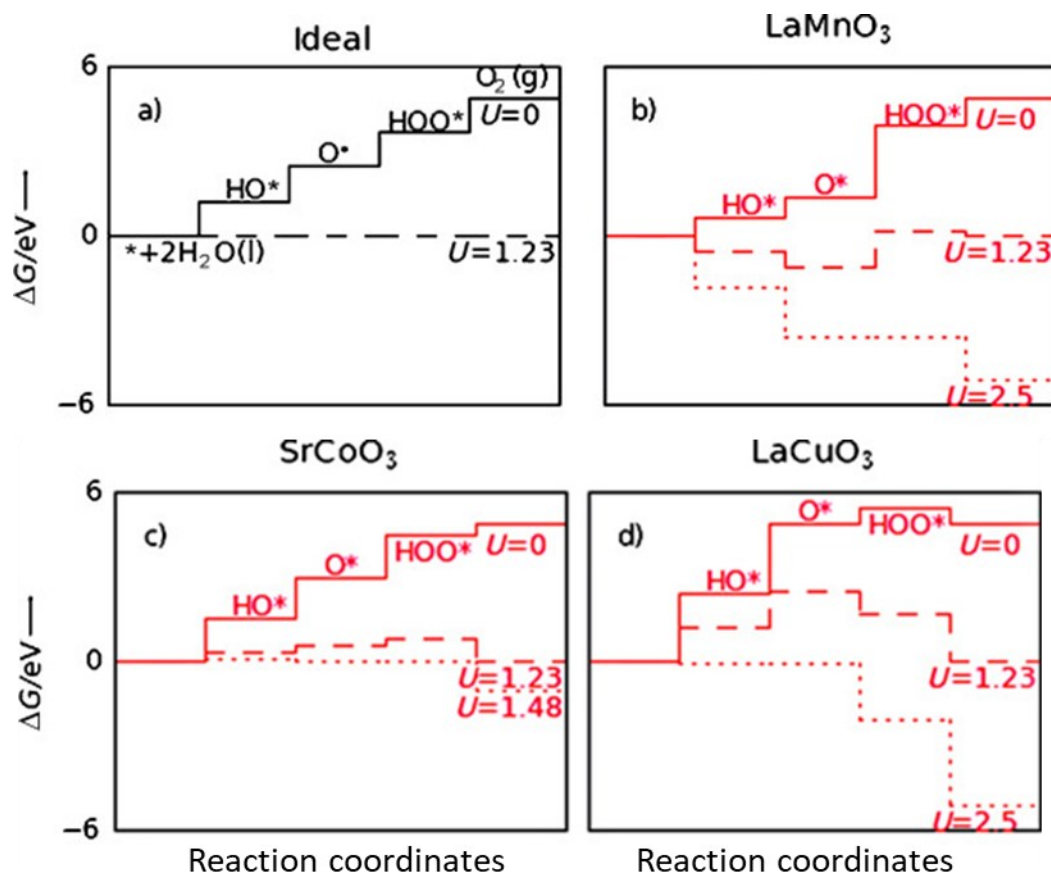
Figure 2-5 Standard free energy diagram for the oxygen evolution reaction of (a) Ideal catalyst, (b) LaMnO$_3$ (b)SrCoO$_3$ (c) LaCuO$_3$ at zero potential, equilibrium potential for each step in an ideal catalyst is 1.23 eV [26].

As the overpotential of catalysts are determined by the ($\Delta G_{O^*} - \Delta G_{HO^*}$) or ($\Delta G_{HOO^*} - \Delta G_{O^*}$) values and as the sum of both free energies is constant, ($\Delta G_{O^*} - \Delta G_{HO^*}$) is often used as activity descriptor in the perovskite structured oxides. The scaling relations with ($\Delta G_{O^*} - \Delta G_{HO^*}$) as activity descriptor are illustrated in *Figure 2-6(a)*. The perovskite oxides on the left side have high ($\Delta G_{HOO^*} - \Delta G_{O^*}$) and O*➔ HOO*is the potential determining step whereas the perovskite oxides on the right of the maximum have high ($\Delta G_{O^*} - \Delta G_{HO^*}$) and HO*➔ O*is the potential determining step. However, at the maximum both ($\Delta G_{O^*} - \Delta G_{HO^*}$) and ($\Delta G_{HOO^*} -$

ΔG_{O^*}) are similar which can be seen as well in *Figure 2-5(b)*. According to Suntivich *et al.*, the e_g orbital occupancy of the transition metal elements on the surface of the perovskite structure influence the OER activity because the e_g orbital of the transition metals directly interacts with adsorbed oxygen intermediates. Hence, the e_g orbital occupancy determines the binding ability of the cation to the adsorbates thereby the overpotentials [31,32]. A volcano type plot is observed for the potential of perovskite oxides vs. e_g orbital occupancy as observed in *Figure 2-6(b)*. Catalysts with a good OER activity are observed when e_g is close to 1. In perovskite structured oxides with strong binding transition metals i.e. transitional metals with low e_g occupancy like $LaCrO_3$, $LaMnO_3$, $LaFeO_3$ and $LaCoO_3$, the OER activity is governed by AEM mechanism, whereas for low binding transition metals with high e_g like $LaNiO_3$ in which oxygen vacancy formation is easier, the OER occurs via LOM mechanism (due to oxygen vacancies) [27]. As a result, the gap between O 2p orbital and Fermi energy level provides a good activity descriptor for OER reaction as the closer the O 2p orbital is to the Fermi energy level, the easier it is to create oxygen vacancies, which are a main prerequisite for the LOM mechanism [31]. Therefore, the difference between O 2p orbital and Fermi energy level is also used as an activity descriptor as seen in *Figure 2-6(c)*. However, if the O 2p orbital is too close to the Fermi energy level then the rapid formation of the oxygen vacancies leads to amorphization on the surface, which decrease the stability and activity of the catalyst.
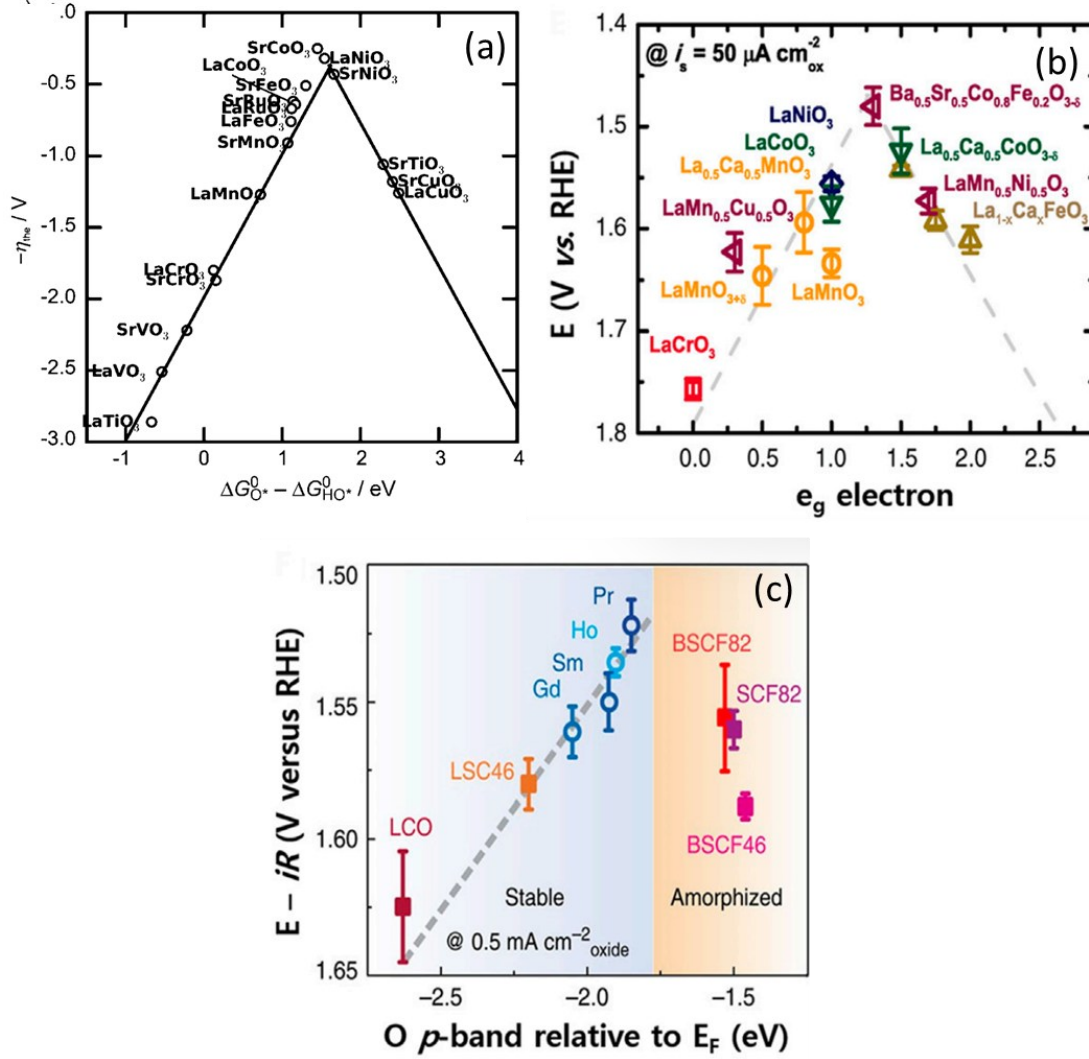
Figure 2-6 Overpotential or potential vs. various activity depictors like (a) (ΔG$_{O*}$ − ΔG$_{HO*}$) (b) e$_g$ electron occupancy and (c) O 2p-band relative to the fermi energy level [26,31,32].

2.3 High entropy materials

In materials science, researchers continually explore diverse compositional spaces to discover materials with exceptional functional properties. However, as the number of constituent elements increases, the compositional space expands exponentially, leaving countless possible compositions yet to be explored. Furthermore, in thermodynamics, the Gibbs phase rule states

$$P = C - F + 1 \qquad\qquad \textit{Eq. 2-27}$$

where P is the number of phases, C is the number of constituents and F are the degrees of freedom. At equilibrium, where $F = 0$, the number of possible phases increases with increasing constituent elements (C+1) which further complicates the possibilities of finding a single-phase system in the vast multicomponent compositional spaces. A new class of materials known as high entropy materials have gained traction in recent years as these are typically single-phase multicomponent compositions with high configurational entropy. Various terms are used to describe high entropy materials. In fact, the first report of high entropy materials was on the alloy with a composition of $Fe_{20}Cr_{20}Mn_{20}Ni_{20}Co_{20}$ by Cantor *et al.* in 2004. These alloys are termed as "equiatomic multicomponent alloys" as the multiple elements are present in equiatomic ratios [33]. Nevertheless, the term "equiatomic multicomponent alloys" can only be used for multicomponent systems in which the constituent elements are in equiatomic ratio. As a results, several other terms like multi-principal element materials, compositionally complex materials, high entropy materials are often used for these materials. Out of all these terms, high entropy material is the popular and most often used term for multicomponent systems with high configurational entropies.

The high entropy term was first introduced by Yeh *et al.* for the single-phase multicomponent systems[34]. The entropy-based classification is according to the Boltzmann equation of entropy which is

$$S_{config} = -R\left(\sum_{i=1}^{N} x_i \ln x_i\right) \qquad \textit{Eq. 2-28}$$

In *Eq. 2-28*, S_{config} is the molar configurational entropy of mixing, R is the universal gas constant, x_i represents the mole fraction of the element and N is the number of constituent elements. Based on *Eq. 2-28*, the multicomponent materials are classified into the following categories

1) Low entropy materials: $S_{config} < 1\,R$

2) Medium entropy materials: $1\,R \leq S_{config} < 1.5\,R$

3) High entropy materials: $S_{config} \geq 1.5\,R$

The configurational entropy of a multicomponent system with n constituent elements (n = 2,3,4,5) is illustrated in *Figure 2-7*. The configurational entropy of the system increases with increasing the number of constituent elements. Moreover, the highest configurational entropy for a given number of constituent elements is achieved when all the constituent elements are in equiatomic ratios. A configurational entropy greater than 1.5 R is achieved in the five component systems, with the highest configurational entropy of 1.61 R at equiatomic

ratio. Consequently, the five component equiatomic compositions are high entropy materials, which ties in with the composition-based terminology. However, in the entropy-based terminology, not only the equiatomic compositions but also all the compositions with configurational entropies greater than 1.5 R are considered high entropy materials. In the case of five component systems, the mole fraction of a constituent element can vary between 0.05 and 0.35 in order to stay in the high entropy regime as demonstrated in *Figure 2-7*. This compositional flexibility of the entropy-based classification is widely accepted and has been adopted by the research community.
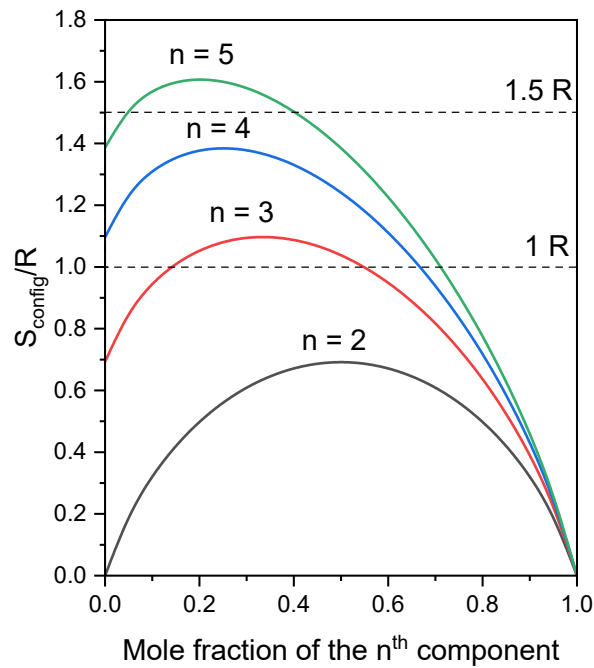
Figure 2-7 Configurational entropy of the multicomponent systems with n elements vs. mole fraction of the nth element, while keeping the rest of the elements equiatomic.

2.3.1 Four core effects

The high entropy materials attracted a lot of attention because of their four core effects resulting from their compositional complexity. These four core effects are:

1) **High entropy effect**: The Gibbs free energy of formation of a single-phase solid solution (ΔG_{mix}) can be written as

$$\Delta G_{mix} = \Delta H_{mix} - T\,\Delta S_{mix} \qquad \text{\textit{Eq. 2-29}}$$

where ΔH_{mix} is the enthalpy of mixing and T is the absolute temperature. If ΔG_{mix} is negative then the multicomponent system is stable as a single crystalline solid solution, whereas if it is positive then the multicomponent system will remix forming multiple phases. The dependency of ΔH_{mix} for a binary system with respect to the mole fraction of the constituent elements is given by

$$\Delta H_{mix} = \beta x_A x_B \qquad\qquad Eq.\ 2\text{-}30$$

where β is a constant, x_A and x_B are mole fractions of constituent elements of the binary system. Depending on the value of β, ΔH_{mix} can either be positive or negative. Consequently, three scenarios are possible depending on the value of ΔH_{mix}, as shown in *Figure 2-8*. In an ideal solid solution, ΔH_{mix} is zero thereby ΔG_{mix} is always negative as $\Delta G_{mix} = -\mathrm{T}\,\Delta S_{mix}$ as depicted in *Figure 2-8(a)*. However, reality is often far from the ideal solid solution. Consequently, ΔH_{mix} is either positive or negative. When the ΔH_{mix} is negative then the Gibbs free energy for mixing or formation of a solid solution is negative as observed in *Figure 2-8(b)* resulting in a single-phase solid solution. When ΔH_{mix} is positive then the Gibbs free energy for mixing is either positive or negative depending on $-\mathrm{T}\,\Delta S_{mix}$ term, which are depicted in *Figure 2-8(c)(d)(e)*. As a result, in material systems with high ΔH_{mix}, increasing the number of elements and temperature can ensure that the $-\mathrm{T}\,\Delta S_{mix}$ can overcome the enthalpic contribution resulting in single phase solid solution. Therefore, the high entropy concept is one of the thermodynamical contributions resulting in the stability of the single-phase solid solution at higher temperatures making it one of the core effects for high entropy materials. Another interesting note is the entropy-based classification originating from this high entropy concept. Although high configurational entropies in multicomponent system can stabilize single-phase solid solutions, a high ΔS_{mix} does not guarantee a single-phase solid solution. The single-phase stability also depends on the ΔH_{mix} and temperature.

2) **Sluggish diffusion:**

Diffusion in materials occurs as atoms jump between neighboring sites, with the free energy of these jumps influenced by the local atomic environment. In multicomponent systems, this energy varies significantly across different local environments compared to binary systems. Some regions exhibit lower energy barriers, while others create high-energy traps, restricting atomic movement. As a result, atoms can become trapped in local energy minima, leading to reduced diffusivity—a phenomenon known as sluggish

diffusion. Sluggish diffusion is thought to influence the nucleation and growth kinetics of diffusion-controlled phase transformations, offering advantages such as higher recrystallization temperatures, reduced grain growth, and increased growth rates. Although this hypothesis remains highly debated, sluggish diffusion is widely acknowledged as a defining trait of high-entropy materials.
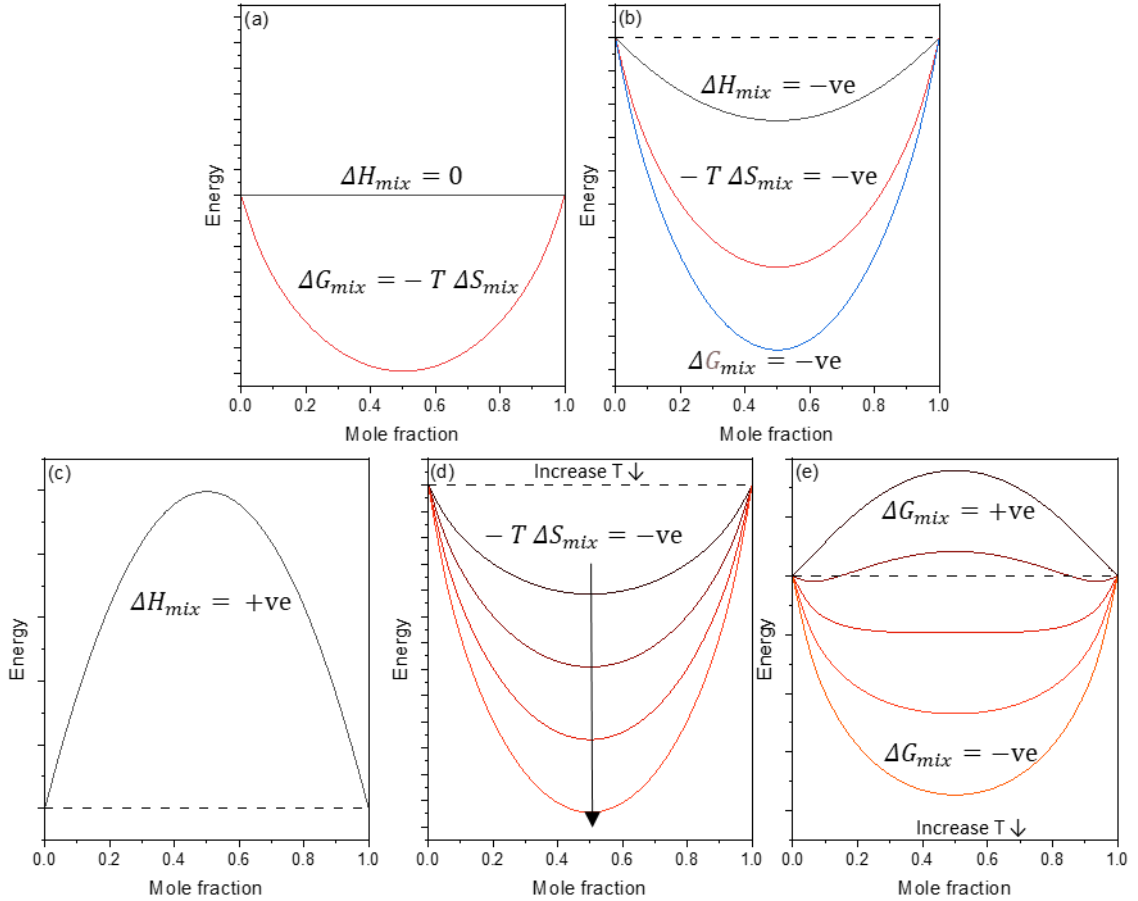
Figure 2-8 (a) The Gibbs free energy, enthalpy and entropy vs. mole fraction in an ideal binary system. (b) The Gibbs free energy, enthalpy and entropy of mixing vs. mole fraction in binary system, where ΔH_{mix} = negative (-ve). The enthalpy (c), entropy (d) and free energy (e) vs. mole fraction in binary system where ΔH_{mix} = positive (+ve).

3) **Severe lattice distortion:**

The constituent elements in the high entropy materials have different atomic or ionic radii even though the elements are selected to have similar atomic or ionic radii. These size differences can cause severe distortion in the lattices which increases with increasing number of constituent elements and the size mismatch among the constituent elements. The severe lattice distortion in high entropy materials has been considered to

impact the mechanical, electrical, and magnetic properties of the high entropy materials [35–38].

4) Cocktail effect:

The properties of materials are a consequence of the interactions between the constituent elements present in the material system. As a result, the presence of multiple elements can lead to complex interactions and synergistic effects, enabling the enhancement of properties that are unattainable in their individual single-component systems. This synergy among different constituent elements is termed cocktail effect. The cocktail effect strongly depends on the composition of the material. Altering the compositions of the high entropy materials, changes the oxidation states and the local chemical environment, which modifies the properties significantly. Therefore, the properties of high entropy materials, owing to the cocktail effect, can be tailored by varying the composition. Hence, the cocktail effect is considered to be one of the core effects of the high entropy materials.

2.3.2 High entropy oxides

High entropy oxides are oxides in which the cation sites are occupied by 5 or more cations in near equiatomic ratio. Considering an oxide $A_xB_yO_z$, the configurational entropy from *Eq. 2-28* can be rewritten as

$$S_{config} = - R \left(x \left(\sum_{i=1}^{N} x_i ln x_i \right)_{A-site} + y \left(\sum_{j=1}^{M} y_j ln y_j \right)_{B-site} + z \left(\sum_{k=1}^{L} z_k ln z_k \right)_{O-site} \right) \qquad Eq.\ 2\text{-}31$$

where x_i, y_j and z_k are the mole fractions of ions present in A-site, B-site and O-site respectively. N and M are the no. of ions present on the A and B-site. L is the no. of ions on the O-site and is 1 for stoichiometric oxides which makes its contribution to configurational entropy zero. However, more often the oxides contain oxygen vacancies which are introduced to increase the functionality. Therefore, considering oxygen vacancies and oxygen sites then the *Eq. 2-31* becomes

$$S_{config} = - R \left(x \left(\sum_{i=1}^{N} x_i ln x_i \right)_{A-site} + y \left(\sum_{j=1}^{M} y_j ln y_j \right)_{B-site} + (z_{Vo} ln z_{Vo} + z_O ln z_O)_{O-site} \right) \qquad Eq.\ 2\text{-}32$$

here z_{Vo} is the mole fraction of oxygen vacancies and z_O is the mole fraction of oxygen vacancies.

High entropy oxides (HEO) were first introduced by Rost *et al.* in 2015 [39]. In the first report of HEO, the authors reported a rock-salt structured high entropy oxide with a composition of $(Co_{0.2},Cu_{0.2},Mg_{0.2},Ni_{0.2},Zn_{0.2})O$. The authors observed the formation of the high entropy oxide to be an endothermic reaction ($\Delta H_{mix} > 0$) resulting in temperature and entropy driven single phase formation, which was proven in the report by investigating the phase purity at different temperatures and configuration entropies (by subsequently decreasing one constituent element). Due to the entropy driven transformation to a single phase at high temperature, $(Co_{0.2},Cu_{0.2},Mg_{0.2},Ni_{0.2},Zn_{0.2})O$ is termed as entropy stabilized oxide. Since then, multiple reports have reported on high entropy oxides with different crystal structures like rock-salt structure [39,40], fluorite structure [41–43], bixbyite structure [43–45], perovskite structure [46,47], spinel structure [48–50] and pyrochlore structure [51–53] to name a few. Among the large number of structures explored for high entropy materials, only a few systems exhibit entropy driven structural transformation. As a result, a new classification of high entropy oxides is introduced, which are entropy stabilized oxides that are essentially systems with entropy driven structural transformations. Although a few high entropy oxides exhibit entropy stabilization of a single-phase structure, most of the high entropy oxides are not solely stabilized by the configurational entropy. It is assumed that these compositions have $\Delta H_{mix} < 0$, making the single-phase structure in these systems stable at all temperatures and configurational entropies. Therefore, all the systems with $S_{config} > 1.5$ R are termed high entropy oxides while the high entropy oxides with temperature and entropy driven single phase formation are termed as entropy stabilized oxides. Since the introduction of high entropy oxides, they have been investigated for countless functional properties. In the following section, the reports investigating the potential of high entropy oxides as oxygen ion conductors and catalyst for OER reaction will be discussed.

2.3.3 High entropy oxides as oxygen ion conductors

Fluorite structured oxides are very well-known oxygen ion conductors. Therefore, researchers have been introducing the high entropy concept into fluorite structured oxides to explore the influence of the four core effects and chemical complexity of high entropy materials on the ionic conductivity of the oxides. The first report on fluorite structured HEOs (F-HEO) was reported by Djenadic *et al.* in 2016 [42]. The authors in the report successfully synthesized fluorite structured high entropy oxide, however, these fluorite structured HEO are observed to change their structure to bixbyite upon heat treatment at 1000 °C. Furthermore, they observed that the stability of the single-phase depends on the content of the +4 cations, in this case Ce^{+4},

rather than the configurational entropy of the system [42]. The single-phase stabilization effect of +4 cations like Ce, Zr on the fluorite structure of the HEO has been observed in multiple reports [42,43,54,55]. Initial investigations of the fluorite structured HEO explored the optical properties. *Sarkar et al.* in 2017 [44] reported an optical band gap of around 2 eV for the fluorite structured HEO even though the rare earth oxides like La_2O_3, Sm_2O_3, CeO_2 exhibit a band gap greater than 3 eV. The drop in band gap in the fluorite HEO is believed to be due to the presence of multivalent Pr in the HEO. Subsequently, many reports investigated the band gap tunability with compositional variation as well as annealing conditions in these fluorites structured high entropy oxides [43,44,54–56]. Not only other elements like Tb which exhibit multivalency have been introduced to tune the band gap of the F-HEO[54,55] but also the annealing atmospheres (H_2, vacuum) are altered to influence the multivalency of elements like Pr, Tb, thereby tuning the band gap of the F-HEO [43,55–57]. In addition to the optical properties of the F-HEO, the conductivity of the F-HEO needs to be explored. A few preliminary studies have investigated the conductivity of the F-HEOs [58–62]. Chen *et al.* in 2018 [58] synthesized a F-HEO with a composition of $(Ce,Zr,Hf,Ti,Sn)O_2$ and measured the electrical conductivity. The electrical conductivity is in the range of semiconductors with an activation energy of 1.43 eV. In the same year Gild *et al.*[60] investigated another set of F-HEO with the compositions $(Hf,Zr,Ce)_x(Y,M)_yO_2$ and $(Hf,Zr,Ce)_x(Yb,M)_yO_2$, where M = La, Ca, Gd, Ti, Mg. The measured activation energies were between 1.1 - 1.3 eV. Multiple F-HEO with varying configurational entropies and varying size mismatch were investigated by Bonnet *et al.*[59] in which they conclude that the configurational entropy does not enhance the conductivity in the compositions investigated and suggest that F-HEO with very low size mismatch might have enhanced conductivity. In a similar study by Zhang *et al.*[61], they have investigated the electrical conductivities of $(Zr,Hf,Pr)_{1-x}(La,Y)_xO_{2-\delta}$ (x = 0.4, 0.5, 0.57) were investigated and an attempt was made by the authors to correlate the size mismatch of the cations and the electrical conductivity among the high entropy oxides. They have observed that the electrical conductivity increases with x, reaches a maximum and decreases with further increasing x. Furthermore, they compare the conductivities of all the above-mentioned high entropy oxides from which they conclude that size mismatch of the cations and the electrical conductivity in the high entropy oxides are not correlated, but rather the conductivity would depend on the composition of the F-HEO. Currently, the conductivities of all the above-mentioned high entropy oxides are lower than the state-of-the-art oxygen ion conductors like YSZ and GDC [61]. However, one of the studies of F-HEO by Dąbrowa *et al.*[62], a F-HEO - $(Ce,La,Pr,Nd,Sm)O_2$ showed conductivities comparable to that of the doped ceria. Nevertheless, these findings are based on initial research, and further

detailed studies are necessary to fully understand the transport properties and oxygen ion conduction in these high entropy oxides.

Another structure discussed in the previous sections that is known for their oxygen ion conduction is perovskite structured rare earth aluminates. The high entropy concept has been introduced to the rare earth aluminates. However, only very few reports exist regarding high entropy rare earth aluminates. These reports investigate the synthesis and applicability of the high entropy rare earth aluminates for high-temperature applications, such as their suitability for thermal barrier coatings, and their high thermal stability and thermal conductivity [63–66]. Although the aluminates show good oxygen ion conduction, the oxygen ion conductivity in high entropy rare earth aluminates are yet to be explored. The first report is a part of this thesis.

2.3.4 High entropy oxides as catalyst for oxygen evolution reaction

Since the introduction of high entropy oxides, one of the most investigated applications for HEO are their catalytic properties for various reactions [67–69]. The first report on catalytic activity of high entropy oxides for oxygen evolution reaction was reported by Wang *et al.*[70]. In this study, the researchers synthesized a single phase spinel structured HEO with a composition of $(Co,Cu,Fe,Mn,Ni)_3O_4$ and particle size of 5 nm. They dispersed the HEO powder on carbon nanotubes (CNT) after which the OER catalytic activity of HEO and HEO+CNT were measured. HEO+CNT showed better catalytic activity than the HEO which was attributed to highly dispersed, active sites, fast charge transfer and excellent electronic conductivity. Furthermore, the OER activity observed was claimed to be higher than for the mixed metal oxides with fewer elements. For HEO+CNT, the observed overpotential at 10 mA cm^{-2} is around 350 mV. The enhanced OER activity was believed to be a result of the diverse valence states of the constituent elements, which can help overcome the kinetic barriers. They conclude that the cations in octahedral voids, which are Co^{+3}, Fe^{+3}, Mn^{+3} and Ni^{+3}, contribute to the adsorption of the intermediates and the cations in tetrahedral voids, which are Cu^{+2}, Co^{+2}, Fe^{+2}, Mn^{+2} and Ni^{+2}, contribute to water splitting. Following this study, several studies emerged on the OER activity of the spinel HEO, which report exceptional OER activity in the spinel HEO than state-of-the-art OER catalyst IrO_2[71–75]. In a systematic study by Abdelhafiz *et al.*[71], the authors synthesized a spinel structured medium entropy oxide - $(Co,Fe,Ni)_3O_4$ to which they systematically add different elements like Cr, V, and Mn to synthesize spinel structured oxides with 4, 5 components. They then measured the OER activity of the corresponding 3, 4, 5 component systems. Among the 3 and 4 component systems they observed the following trend

in the OER activity FeNiCoCr > FeNiCoMn > FeNiCoV > FeNiCo, which suggests that the activity increased with increasing number of components with the system containing Cr having the highest activity. Furthermore, the five component systems with Cr, FeNiCoCrV and FeNiCoCrMn, showed higher activity than the quaternary composition without Cr. However, among the systems with Cr, the activities are in the following order FeNiCoCrV > FeNiCoCr > FeNiCoCrMn. This study indicates the drastic effect of specific elements like Cr, Mn and V on the OER activity. As a result, to understand the effect of Cr on the electronic structure and in turn on the catalytic activity, the authors investigated the oxidation states of active site elements like Ni, Co, Fe with addition of Cr and they observed an increase in the oxidation state of these elements. The authors postulate that the increase in oxidation state of Co, Ni and Fe with addition of Cr can lead to the decrease in 3d orbital level and increase the hybridization of the TM 3d – O 2p orbital, which can enhance the OER activity. The effect of Cr is supported by another study by Hooch Antink *et al.* [73] in which along with Cr, Mo has also been observed to improve the catalytic activity. One more element that has been observed to enhance the OER activity in these spinel HEO is Mg, reported by Stenzel *et al.*[75]. In this study, they observed that addition of Mg into spinel HEO resulted in the formation of multiphase mixture of rock-salt and spinel-type phase which led to an increase in OER activity. Consequently, investigations were conducted on rock-salt structured HEO, which also exhibit promising OER catalytic activities [76,77]. Along with rock-salt and spinel structured HEO, few studies have also reported the OER activity of perovskite structured HEO [78–82]. The first report on the perovskite structured HEO was Nguyen *et al.*[83] in 2021. In the study, the authors investigated the catalytic activity for OER reaction of La(Co,Cr,Fe,Mn,Ni)O$_3$ along with other perovskite-type HEO compositions with each transition metal element on the B-site being doubled. The authors observed the high catalytic activities and durability from La(Co$_2$,Cr,Fe,Mn,Ni)O$_3$ with double Co with the next best activities observed in La(Co,Cr,Fe,Mn,Ni$_2$)O$_3$ and La(Co,Cr$_2$,Fe,Mn,Ni)O$_3$. The overpotential at 10 mA cm^{-2} are around 400 – 500 mV, which is higher than state-of-the-art RuO$_2$ but at higher current densities the perovskite HEO shows lower overpotentials than the RuO$_2$ catalyst. Furthermore, Tafel slopes of the perovskite HEO are lower than RuO$_2$ implying a faster charge transfer making it a better OER catalyst. Following the study by Nguyen *et al.*[83], Sr is doped into the above-mentioned HEO and the catalytic activity of the Sr doped HEO were measured, which decreases the overpotential below 400 mV with even better performances than the undoped counterparts [79–81]. Although there are multiple studies highlighting the enhanced OER catalytic activities of the perovskite HEO, the reason for the enhancement is yet to be confirmed and should be investigated systematically.

3 Characterization techniques

3.1.1 X-ray Diffraction

X-ray diffraction (XRD) is a very well-known technique employed to determine the crystal structure of a material. X-rays have a wavelength in order of the interatomic distances. As a result, when a crystal is irradiated with X-rays, constructive interference can occur over the diffracted beam at certain angles. Based on this principle, Lawrence Bragg and William Henry Bragg came up with an expression which is as follows

$$n\,\lambda = 2d\sin\theta \qquad\qquad \textit{Eq. 3-1}$$

Here λ is the wavelength of X-rays, d is interplanar spacing and θ is the incident angle at which constructive interference happens with the diffracted beam. Constructive interference from various lattice planes leads to a diffraction pattern. Each crystal structure has a unique diffraction pattern, making XRD an effective tool for determining the material's crystal structure. Depending on the form factor of a material, different diffraction techniques are employed in the thesis. The diffraction techniques employed in this thesis are as follows:

1. Powder X-ray diffraction: It is employed for polycrystalline powders. A simple representation of the technique can be seen in *Figure 3-1(a)*. The XRD is measured with a Bruker D8 advance diffractometer. Cu Kα X-ray source irradiates the powder samples, and a LynxEye linear detector collects the diffracted X-rays. The source and detector rotate in Bragg-Brentano geometry, with both the source (incident angle) and the detector (diffracted angle) set at the same angle (θ) relative to the sample stage. The sample position remains fixed. The diffraction intensities at different incident angles (2θ) are measured and plotted. The crystal structure, phase composition, lattice parameters, crystallite size, and micro-strain are determined from the XRD pattern using Rietveld refinement, which is carried out with FullProf software. The instrumental parameters for refinement are obtained from the XRD pattern of the LaB$_6$ standard sample.

2. Grazing incidence X-ray diffraction: This technique is the used for investigating thin films. The diffraction of the thin films is measured by positioning the X-ray source at a fixed low incidence angle (0-5°) while the detector measures the diffracted X-rays at different angles along the goniometer circle as depicted in *Figure 3-1(b)*. The films are

calibrated in the z-direction, sample height, to ensure that the beam irradiates the top surface. For the z-calibration, the source and detector are initially positioned at an angle of 0°. The sample is then moved away from the X-ray beam along the z-direction and gradually repositioned toward the beam to identify the surface of the film. The low incidence angle of X-rays ensures that diffraction only occurs in the film, preventing any diffraction from the substrate.

3. High resolution X-ray diffraction: High-resolution X-ray diffraction (HRXRD) is employed to characterize the structure of epitaxial thin films. Epitaxial films are thin, single-crystalline layers that are deposited onto a single-crystal substrate in such a way that the crystallographic orientation of the film aligns with that of the underlying substrate. This alignment is made possible by carefully selecting a substrate whose lattice constants closely match or, in some cases, are intentionally mismatched to engineer strain. When these films are characterized using high-resolution X-ray diffraction (XRD), they exhibit distinct interference fringes adjacent to the Bragg peaks, known as Laue fringes or Laue oscillations. They arise from the constructive and destructive interference of X-rays diffracted by a limited number of crystallographic planes in the film. The periodic spacing of Laue fringes is inversely related to the thickness of the epitaxial layer as depicted in *Eq 3-2*,

$$t = \frac{2\pi}{\Delta q} = \frac{\lambda}{2(\sin\theta_2 - \sin\theta_1)} \qquad \text{\textit{Eq 3-2}}$$

Where t is the thickness of the film, Δq is scattering vector, λ is the wavelength of the X-rays and θ_2 & θ_1 are the angles of two successive Laue fringes. While the width of the fringes determines the thickness of the film, the intensity, sharpness, and symmetry of the fringes provide insights into the crystallinity of the film. Sharp, well-resolved fringes are indicative of a smooth surface, abrupt interfaces, and a high degree of crystalline perfection throughout the film. On the other hand, fringe patterns that appear damped, blurred, or irregular may point to interface roughness, the presence of dislocations or other crystalline defects, or variations in strain across the film. As such, detailed analysis of Laue fringes in XRD patterns serves as a powerful, non-destructive diagnostic tool for evaluating critical structural parameters of epitaxial films which includes their thickness, crystallinity, interface quality, and strain distribution. Traditional powder diffractometers lack the resolution to detect these oscillations or to resolve the Bragg peak separation between the film and the substrate. Therefore, high-resolution X-ray

diffraction (HRXRD) is designed for the precise structural analysis of epitaxial thin films. High-resolution XRD measurements in this dissertation are performed in a Bruker AXS D8 diffractometer. The diffractometer is equipped with a monochromatic Cu-Kα X-ray source and a Goebel mirror prior to the detector to increase the resolution of the diffractometer. The height is adjusted to align the X-ray beam with the surface, as mentioned in Grazing incidence X-ray diffraction. Next, the stage is tilted between 0 and 0.5 degrees to ensure that the sample surface is parallel to the beam. Once the sample is properly aligned, an omega-2Theta scan is measured.
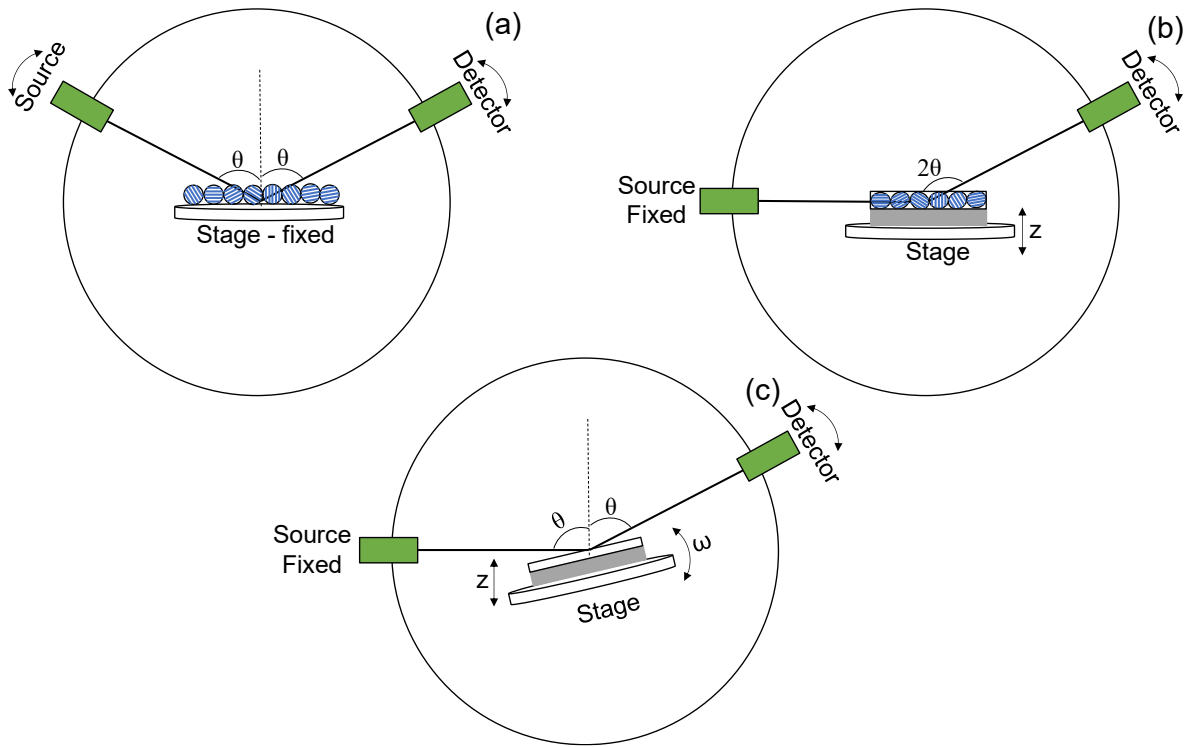
Figure 3-1 Schematic representation of different XRD techniques (a) Powder X-ray diffraction (b) Grazing incidence X-ray diffraction and (c) High resolution X-ray diffraction.

3.1.2 Scanning Electron Microscopy

Scanning Electron Microscopy (SEM) is a technique that uses electrons for imaging. Electrons have a De Broglie wavelength that is smaller than that of visible light, which allows electron microscopes to achieve higher magnifications and resolutions in the order of a few nanometers. In a scanning electron microscope, an electron gun generates primary electrons, and electromagnetic lenses focus these electrons onto the sample. When the primary electrons

interact with the sample, they produce various emissions that provide information about the sample's morphology and chemical composition. The different emissions resulting from the interaction of primary electrons within the penetration volume include the following:

1. Secondary electrons: Secondary electrons are electrons emitted by the inelastic interaction of the primary electrons with the surface atoms. Secondary electrons have very low energy. Consequently, only the secondary electrons originating from the surface of the sample are energetic enough to escape the sample surface, reach the detector. As a result, secondary electrons give information about the morphology of the surface.

2. Back-scattered electrons: The elastic interaction of the primary electron with the atomic nuclei results in back-scattered electrons. Back-scattered electrons are more energetic and emerge from deeper regions than secondary electrons as they result from elastic interactions. The intensity of the back-scattered electrons depends on the atomic number of the atoms. Therefore, back-scattered electrons provide atomic contrast in the SEM images.

3. Characteristic X-rays: Characteristic X-rays are emitted when an electron transitions from an outer shell to an inner shell to fill a vacancy created by the inelastic scattering of the primary electrons. These X-rays are unique to each element. The technique used to analyze elements with characteristic X-rays is called Energy Dispersive X-ray Spectroscopy (EDS). EDS provides elemental maps or chemical distribution of elements, and their corresponding chemical composition.

SEM is measured with a LEO Gemini-1530 scanning electron microscope equipped with an Oxford X-Max^N X-ray detector. The operating voltage, aperture, and working distance are 5 kV, 30 μm, and 5 mm for microscopy, whereas they are 20 kV, 120 μm, and 8.5 mm for EDS.

3.1.3 Transmission Electron Microscopy

Transmission Electron Microscopy (TEM) is a powerful imaging technique that uses a parallel electron beam to pass through an ultra-thin sample, producing highly resolved images down to a few angstroms. TEM provides valuable insights into nanoparticle morphology, local crystal structures, and atomic arrangements.

Scanning Transmission Electron Microscopy (STEM) is a variation of TEM, where a focused electron beam is rastered across the specimen to generate a scanned image. A High-

Angle Annular Dark Field (HAADF-STEM) detector captures electrons scattered at high angles, producing high-Z-contrast images while minimizing diffraction contrast effects.

Energy Dispersive X-ray Spectroscopy (EDS) and Electron Energy Loss Spectroscopy (EELS) are commonly used techniques in TEM for chemical analysis. EDS detects characteristic X-rays emitted when electrons transition to fill vacancies created by inelastic scattering, while EELS measures the energy lost by transmitted electrons due to inelastic interactions. EDS provides valuable insights into chemical composition, elemental distribution at the atomic scale, while EELS delivers information about the valence states of elements.

TEM analysis was conducted using a double aberration-corrected ThermoFisher Themis Z HR-(S)TEM, equipped with a Super-X energy-dispersive X-ray detector and a Gatan GIF Continuum 970 HighRes + K3 IS camera, operating at 300 kV. HAADF-STEM imaging was performed with a beam convergence angle of 30 mrad and a collection angle ranging from 62 to 200 mrad. Both EDS and EELS were acquired in STEM imaging mode. TEM lamellae of the films were extracted using a focused ion beam (FIB) in an FEI Strata 400 system.

3.1.4 Atomic force microscopy

Atomic Force Microscopy (AFM) is a non-optical surface inspection technique that uses an extremely sharp tip to physically probe surface irregularities. An atomic force microscope operates using a cantilever with a sharp tip, which typically has a radius of curvature in the order of a few nanometers. A laser is directed onto the back of the cantilever, and the reflected light is detected by a photodetector. As the sharp tip scans the surface of the sample, variations in surface topography cause the cantilever to deflect. These deflections, caused by interactions between the tip and the surface, lead to changes in the reflected laser signal. This principle allows the AFM to measure surface roughness with high spatial resolution, providing detailed topographical information at the nanoscale.

Atomic force microscopy was measured in a Bruker Dimension ICON (USA). The root mean square roughness of a line profile along the step edge was used to determine the roughness.

3.1.5 UV-Vis spectroscopy

UV-Vis spectroscopy is a technique employed to examine the interaction of a material with both ultraviolet (UV) and visible light. When electromagnetic radiation strikes the sample,

it can be absorbed, reflected, or transmitted. A spectrometer then measures the intensity of absorbed, reflected, or transmitted radiation relative to the incident radiation. This technique is commonly used to determine a optical band gap of materials. In this thesis, reflected radiation is measured to investigate the optical properties of the material. This variation of UV-Vis spectroscopy that measures reflectance is called Diffuse Reflectance Spectroscopy (DRS). The optical band gaps from reflectance data in the thesis are derived using TAUC method using the following expression[84]

$$[F(R_\infty)h\nu]^{1/n} = A(h\nu - E_g)$$

<div align="right">*Eq. 3-3*</div>

Here h is Plank's constant, ν is frequency of the incident beam, E_g is the band gap, A is a constant, n is the parameter dependent on the nature of transition, and $F(R_\infty)$ is reflectance parameter calculated from Kubelka Munk function:

$$F(R_\infty) = \frac{(1-R)^2}{2R}$$

<div align="right">*Eq. 3-4*</div>

where R is reflectance derived from the measurement. The band gap is the x-intercept of the linear portion of the $[F(R_\infty)h\nu]^{1/n}$ vs. $h\nu$. For direct band gap, n = 1/2 is used and for indirect band gap, n = 2 is used.

In this thesis, a Cary 60 UV-Vis spectrometer (Agilent) equipped with a remote fiber optic diffuse reflectance accessory was used to perform UV-Vis spectroscopy. The measurement was conducted between 100 and 1100 nm with speed 600 nm/min.

3.1.6 Raman spectroscopy

Raman Spectroscopy is a technique based on the Raman effect introduced by Sir C.V. Raman. The Raman effect is the phenomenon of inelastic scattering of light by a material. A material absorbs, reflects, or transmits most of the incident light. However, 0.1 to 0.01 % of incident light scatters in all directions. Most of the scattered light is elastically scattered, also known as Rayleigh's scattering, in which the energy of the incident light is equal to the scattered light. Interestingly, there is a one-in-a-million chance that the light scattered will have an energy higher or lower than the incident light. This phenomenon is inelastic scattering or Raman scattering. Raman spectroscopy uses laser light sources in the ultraviolet, visible, and near infrared ranges. These laser light sources excite molecules to higher vibrational energies. If an excited molecule relaxes to the same initial vibrational energy level, then Rayleigh's scattering

(elastic scattering) occurs. However, if the molecules relaxes to a different vibrational energy level than the initial vibrational state, then Raman scattering (inelastic scattering) occurs. Raman spectroscopy provides information about the molecular vibrations, structural transitions, local chemical environments, comparing defect concentrations, electronic and optical properties.

In this thesis, Raman Spectroscopy measurements are conducted using a Renishaw Raman confocal optical microscope with green laser ($\lambda = 532$ nm) and infrared laser ($\lambda = 785$ nm). The measurement was done at 100 to 1000 cm^{-1} for 30 sec and 10 accumulations.

3.1.7 X-ray photoelectron spectroscopy

X-ray Photoelectron Spectroscopy (XPS) is inspired by Einstein's photoelectric effect. The photoelectric effect is the emission of electrons from a material caused by electromagnetic radiation. In XPS, X-rays emit electrons from the surface of the material, and the kinetic energies of the emitted electrons are measured. The energy of X-rays in XPS is converted into the following energies:

1. Binding energy (BE) – The energy required to remove an electron from an atom (binding energy) to Fermi energy level.
2. Work function (W) – The energy required to transfer an electron from the Fermi energy level to vacuum.
3. Kinetic energy (KE) – kinetic energy of the emitted electrons.

According to law of conservation of energy, the energy of X-rays ($h\nu$) is a sum of all the above-mentioned energies.

$$h\nu = BE + W + KE \qquad \qquad Eq.\ 3\text{-}5$$

The binding energy of the electron can be written as

$$BE = h\nu - W - KE \qquad \qquad Eq.\ 3\text{-}6$$

In XPS, a detector measures the kinetic energy of the electrons, and the binding energy is estimated from *Eq. 3-6*. The resultant spectra are created by plotting a graph between the intensity and binding energy. The binding energy of the electron is characteristic of the element and orbital from which it originates. The oxidation states and chemical bonding can

significantly affect the binding energy of electrons. Therefore, XPS spectra provide insights into the oxidation state and chemical bonding of the elements on the surface of the material.

In this thesis, the Omicron XM 1000 MK II X-ray source generates Al K$_\alpha$ X-rays with an energy of 1486.6 eV at an operating voltage of 300 W. The SPECS Phobias 150 spectrometer measures the kinetic energy of the emitted photoelectrons and resulting spectra are analyzed with CASAXPS software.

3.1.8 X-ray absorption spectroscopy

X-ray Absorption Spectroscopy (XAS) involves irradiating a sample with high-energy X-rays and measuring the resulting energy loss. X-rays, typically from a synchrotron source, eject core-shell electrons from atoms, leading to characteristic absorption edges (such as the K-edge or L-edge) in the spectrum. These edges are element specific and provide insights into local atomic environment, and oxidation state.

3.1.9 Density measurements

Density measurements are carried out using Archimedes principle and from the geometry of the material. Archimedes principle was discovered by a Greek mathematician and inventor, Archimedes. Archimedes principle states that any object submerged in a liquid experiences buoyant forces equal to the weight of the liquid displaced, and the volume of the liquid displaced is equal to the volume of the object. As a result, the relative density of an object can be measured using Archimedes principle

$$Weight\ of\ liquid\ displaced = Weight\ of\ object - weight\ of\ object\ in\ liq \qquad Eq.\ 3\text{-}7$$

$$Density\ of\ object = \frac{Weight\ of\ object}{Volume\ of\ object} \qquad Eq.\ 3\text{-}8$$

$$Density\ of\ object = \frac{Weight\ of\ object}{Volume\ of\ liquid\ displaced} \qquad Eq.\ 3\text{-}9$$

$$Density\ of\ object = \frac{Weight\ of\ object}{Weight\ of\ liquid\ displaced \times Density\ of\ the\ Liquid} \qquad Eq.\ 3\text{-}10$$

In this thesis, the weight of the sample is measured in air. Subsequently, the sample is submerged in water, and its weight under water is recorded. The relative densities are then calculated from *Eq. 3-10* by considering the density of water to be 1 g/cc.

The Geometric relative densities are measured by using the dimensions of the sample and weight of the sample (Geometric density).

$$\text{Density of object} = \frac{\text{Weight of object}}{\pi \times r^2 \times h}$$

<div align="right">*Eq. 3-11*</div>

Here r is the radius of the cylindrical pellet, h is the thickness of the cylindrical pellet. The geometric densities account for open and closed pores. However, the relative densities from the Archimedes principle only accounts for closed pores as water can seep into open pores. Therefore, the difference between the relative densities can give a good idea about the open pores present in the system.

3.1.10 Electrochemical Impedance Spectroscopy

Understanding the correlation between voltage and current is crucial in comprehending the functioning of any electrical circuit. The relation is dependent on the type of current that flows through the circuit. For direct current (DC) at equilibrium, potential and current share a direct and proportional relationship for different electrical elements like resistors, capacitors, and inductors. However, the relation between potential and current is more nuanced for alternating current (AC). In AC, the potential difference varies periodically, typically in the form of a sine wave ($V = V_0 \sin(\omega t)$) with an angular frequency of ω. In an ideal resistor,

$$V(t) = I(t)R$$

<div align="right">*Eq. 3-12*</div>

$$V_0 \sin \omega t = I(t)R$$

<div align="right">*Eq. 3-13*</div>

$$I(t) = \frac{V_0}{R} \sin \omega t$$

<div align="right">*Eq. 3-14*</div>

$$I(t) = I_0 \sin \omega t$$

<div align="right">*Eq. 3-15*</div>

From the above expressions, current and potential are directly proportional, and are in phase with each other similar to DC. However, for elements where current and potential exhibit a

phase shift and, therefore, are time-dependent such as capacitor and inductor, the relationship is different. For an ideal capacitor with a capacitance C,

$$I(t) = C \frac{d(V(t))}{dt}$$

Eq. 3-16

$$I(t) = C \frac{d(V_0 \sin \omega t)}{dt}$$

Eq. 3-17

$$I(t) = C\omega V_0 \cos \omega t$$

Eq. 3-18

$$I(t) = I_0 \sin(\omega t + 90)$$

Eq. 3-19

The current in an ideal capacitor lags behind the potential by a phase difference of 90 degrees. In the case of an ideal inductor with an input current ($I(t) = I_0 \sin \omega t$) and inductance L the voltage lags 90 degrees behind the current.

$$V(t) = L \frac{d(I(t))}{dt}$$

Eq. 3-20

$$V(t) = L \frac{d(I_0 \sin \omega t)}{dt}$$

Eq. 3-21

$$V(t) = L\omega I_0 \cos \omega t$$

Eq. 3-22

$$V(t) = V_0 \sin(\omega t + 90)$$

Eq. 3-23

In practice, materials exhibit characteristics that deviate from the ideal behaviors of resistors, capacitors, and inductors, presenting a blend of diverse electrical elements. Consequently, the relationships between current and potential, as well as phase differences, may vary. Impedance is introduced to provide a simplified representation of a material's resistance to an applied voltage or current. Impedance can be written as follows

$$Z = \frac{V(t)}{I(t)}$$

Eq. 3-24

Applying fast Fourier transformation and converting the time regime of potential ($V = V_0 \sin(\omega t)$) to frequency regime gives

$$V = V_0 \exp i(\omega t)$$

Eq. 3-25

and corresponding current response to the alternating current is

$$I = I_0 \exp i(\omega t - \phi)$$ *Eq. 3-26*

here ϕ is the phase difference between current and voltage. The impedance of the corresponding electrical circuit can be written as

$$Z = \frac{V_0 \exp i(\omega t)}{I_0 \exp i(\omega t - \phi)}$$ *Eq. 3-27*

$$Z = \frac{V_0}{I_0} \exp i(\phi)$$ *Eq. 3-28*

$$Z = Z_0(\cos(\phi) + i \sin(\phi)) = \mathrm{Re}(Z') + i \, \mathrm{Im}(Z'')$$ *Eq. 3-29*

The above expression of impedance can be divided into real and imaginary parts. The impedance data is typically represented through Nyquist plots. Nyquist plots is graphical representation between the real and imaginary parts of the impedance. Nyquist plots are fitted with an equivalent circuit that depicts the measuring system appropriately.

In this thesis, electrochemical impedance spectroscopy (EIS) was utilized to test oxygen ion conduction and electrocatalysis. For oxygen ion conduction, EIS was performed from high frequencies (1 MHz) to low frequencies (100 mHz) with a potential amplitude of 500 mV. The impedance to electrical transport in solid electrolytes arises from both the resistance of the electrolyte and the imperfect capacitance associated with the double layer at the interface between the electrolyte and the electrode interface. Typically, an equivalent circuit of resistor (R) and constant phase element (CPE) which serves as imperfect capacitive element in parallel is used to fit the impedance data[85,86]. However, solid electrolytes consist grain and grain boundaries that offer different impedance. As a result, two CPE//R circuits for bulk and grain boundary were considered to fit the impedance data. The CPE fit values were converted to capacitances using the following expression

$$C = (R^{1-n} \times Q)^{\frac{1}{n}}$$ *Eq. 3-30*

here C is capacitance, R is resistance, Q and n are the CPE fit parameters. EIS of the electrolyte was conducted at different temperatures and oxygen partial pressures to derive the activation energies and the conduction nature of the electrolyte. The conductivities were measured in a temperature range of 300 - 800 °C and a pressure range of 1 bar to 5 mbar of oxygen partial

pressure, respectively. Activation energies (E_a) of the electrolyte can be derived with the help of Arrhenius equation:

$$\sigma = \frac{\sigma_0}{T} exp\left(\frac{-E_a}{RT}\right)$$

Eq. 3-31

here σ_0 is the exponential pre-factor of conductivity, R is the universal gas constant, and T is the temperature in Kelvin. Total conductivity was considered for calculating the activation energies. The EIS for electrocatalysis was performed at open-circuit potential with a 10 mV amplitude, and the cell resistance correction (IR correction, typically 45–55 Ω) was determined from the high-frequency intercept of the real impedance.

3.1.11 Cyclic Voltammetry

Cyclic voltammetry (CV) is a versatile technique used to study the oxidation and reduction reactions occurring in an electrochemical cell. In this thesis, CV is utilized to investigate the electro-catalytic activity of oxides. This technique is essential in catalysis as it helps in understanding how effectively a material catalyzes a specific reaction. A setup of the catalytic electrochemical cell is shown in *Figure 3-2*. Typically, an electrochemical cell consists of the following components:

1) Working electrode: The working electrode is the electrode at which the desired reaction occurs in an electrochemical cell. This is the site where electrons are transferred during the reaction, depending on whether the process involves reduction or oxidation.

2) Reference electrode: A reference electrode is an electrode with a well-defined equilibrium potential. The equilibrium potential of a reference electrode should remain constant over the given experimental conditions. The potential measured by the potentiostat during a CV measurement is the potential between the working electrode and the reference electrode. Consequently, the potential plotted in a CV is the working electrode's potential with respect to the reference electrode. Some good examples of a reference electrode are the standard hydrogen electrode, the saturated calomel electrode, and the AgCl/Ag electrode.

3) Counter electrode: The Counter electrode completes an electrical circuit with the working electrode. Counter electrode helps in supplying or receiving current from the working electrode. The reaction at the counter electrode is contrary to the reaction at working electrode. The counter electrode is typically an inert electrode like Pt to avoid any further reactions impeding the CV signal.

4) Electrolyte: Electrolyte is a connecting medium between the electrodes. Electrons from the electrodes generate ions in the electrolyte, which then migrate toward the opposite electrode, maintaining charge neutrality and completing the circuit. A good electrolyte should exhibit high ionic conductivity and remain stable against both oxidation and reduction in the potential range of the experiment.

5) Gas: Gas are supplied to ensure continuous reactant availability, remove gas bubbles, and prevent contamination, thereby enhancing reaction efficiency.

In this thesis, the following components were used for measuring the electro-catalytic activity for oxygen evolution reaction:

1) Working electrode: Epitaxial oxide thin film on a rotating disk electrode.

2) Counter electrode: Platinum.

3) Reference electrode: Hg/HgO.

4) Electrolyte: 0.1 M KOH in water

5) Gas: Oxygen.

Cyclic voltammetry was initially conducted in the pseudocapacitive redox phase change region, specifically between approximately 0.9 and 1.75 V versus RHE. This was done at scan rates ranging from 10 to 500 mV s^{-1}. Following this, the oxygen evolution reaction (OER) testing was performed from 0.9 to 1.9 V versus Hg/HgO at a scan rate of 10 mV s^{-1}.

Figure 3-2 Three electrode setup of electrochemical cell.

4 Synthesis of high entropy oxides

High entropy oxides (HEOs) are complex compounds made up of multiple elements. The synthesis of HEO typically involves mixing the precursors of the constituent elements and then converting the mixture into an oxide. Extensive research has explored various synthesis routes for high entropy oxides. These studies focus on fabricating HEOs in different forms, including powders, pellets, and thin films. Some examples for powder synthesis techniques are reverse co-precipitation, flame spray pyrolysis, nebulized spray pyrolysis, hydrothermal synthesis, solution combustion, mechanochemistry, and sol-gel processes[45,87–91]. Various methods have been investigated for powder synthesis and pellet densification, consisting of conventional sintering, flash sintering, spark plasma sintering, microwave sintering, and reactive flash sintering. [45,91–95]. Thin film synthesis techniques include pulsed laser deposition, sol-gel process, and magnetron sputtering [41,47,96,97]. Various fabrication methods are explored in this thesis to synthesize HEO in different form factors; these are:

1) Reverse co-precipitation synthesis for powders.
2) Mechanochemical synthesis for powders.
3) Sol-gel process for powders and thin films.
4) Pulsed laser deposition for thin films.
5) Conventional sintering for pellets.

In the following sections of this chapter, these synthesis techniques will be discussed in more detail. These methods were applied to synthesize $(Ce,La,Pr,Sm,Y)O_{2-\delta}$ (FHEO), and the resultant samples were characterized both structurally and chemically.

4.1 Powders

4.1.1 Synthesis techniques

Reverse co-precipitation: Reverse co-precipitation (RCP) is a precipitation technique generally utilized to synthesize nanoparticles. In this technique, A precursor solution with a concentration of 0.1 M is prepared by dissolving metal nitrates in water. A strong base - 28% ammonia solution (p^H = 14) is gradually titrated into the precursor solution. The interaction of metal ions with a strong base, like ammonia, leads to the precipitation of the metal hydroxide. A centrifuge separates the precipitates, which are then dried at 80 °C overnight. Further heat treatment of the dried hydroxide precipitate results in the transformation to the desired metal oxide.

$$M(NO_3) + H_2O \xrightarrow{NH_3, P^H = 14} M(OH) \xrightarrow{\Delta} MO$$
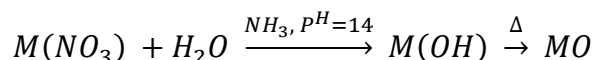
Pechini process (Sol–Gel process): The Pechini process is a versatile technique for synthesizing powders and thin films. It is a variation of the Sol-Gel process. In the Pechini process, metal nitrates are dissolved in water to create a precursor solution. Citric acid is then added to the solution to chelate the metal cations. Subsequently, Ethylene glycol is added to facilitate the polymerization of the chelated metal cations. The resulting solution is aged at 140 °C for a few hours, forming a polyester gel. The gel is dried at 300 °C and sintered at 1250 °C to produce metal oxide powders. In this thesis, the ratio between metal cations, citric acid, and ethylene glycol were 1:1:2 and 1:2:4, and the concentration of metal cations in the solution was 0.2 M.
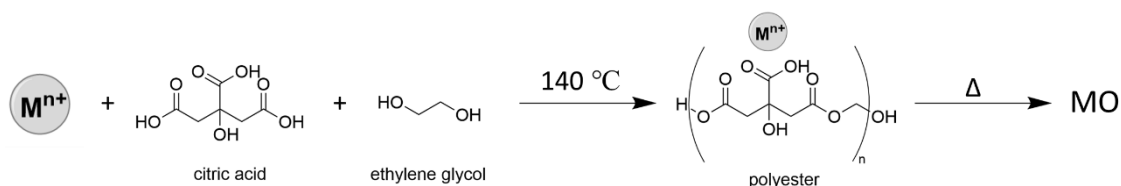
Mechanochemical synthesis: Mechanochemical synthesis involves high-energy ball milling of the constituent metal oxides to create an oxide. A high-energy planetary ball mill (Retsch PM200) mixes the corresponding metal oxides. The high mechanical energy generated by the ball mill induces local heating that facilitates the synthesis of the oxides, resulting in the high entropy oxide. In this thesis, tungsten carbide vials and balls were used. The mass ratio between the precursors and the tungsten carbide balls was kept at 1:50. The ball milling was done at 500 rpm for 48 h to ensure proper mixing with 10 mins mixing and 10 mins rest during the milling.

4.1.2 Structural characterization

The X-ray diffraction (XRD) of the powders is shown in *Figure 4-1*. The X-ray diffraction pattern from *Figure 4-1(a)* suggests the structure is fluorite ($Fm\overline{3}m$). Therefore, the XRD patterns are fitted with the fluorite structure and the Rietveld refinements can be seen in *Figure 4-1(b)*, *Figure 4-1(c)*, and *Figure 4-1(d)*. The XRD pattern of the powder could be fitted with a single-phase fluorite structure. The powder characteristics like lattice parameter and crystallite size are extracted from the Rietveld refinements, which is summarized in *Table 4-1*. Lattice parameters in *Table 4-1* show no significant change. Furthermore, the powders from these synthesis techniques are nanocrystalline with crystallite size in 12 to 20 nm range. The powder synthesis techniques investigated resulted in a single-phase nanocrystalline fluorite structured oxide powder. These powders are used to prepare pellets via conventional sintering.

Table 4-1 Structure, lattice parameter(a), crystallite size of the powders synthesized from corresponding synthesis routes.

Synthesis route	Structure	a (Å)	Crystallite size (nm)
Mechanochemical	$Fm\overline{3}m$	5.43	20.1
Reverse Co-precipitation	$Fm\overline{3}m$	5.48	12
Pechini	$Fm\overline{3}m$	5.48	14
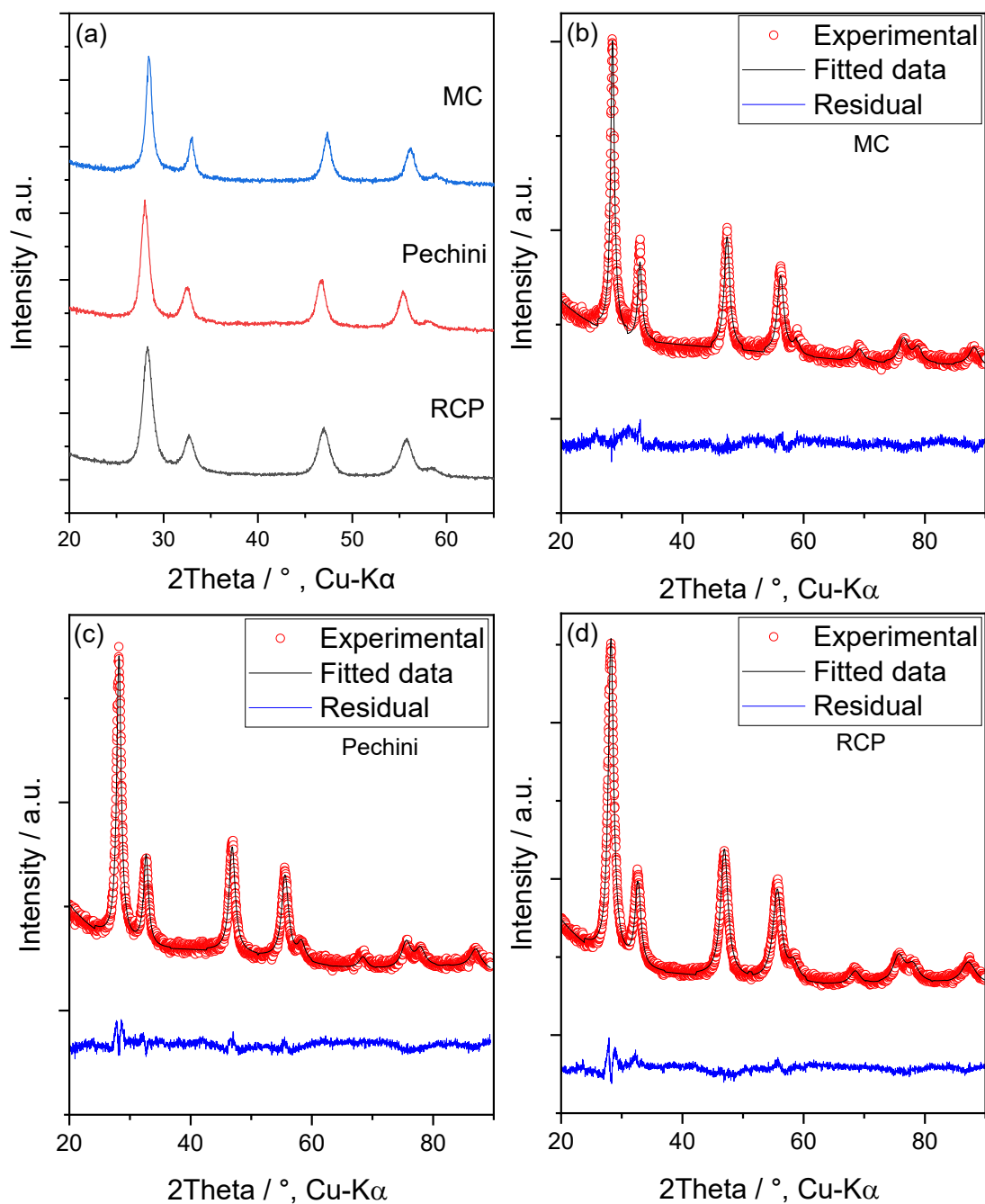
Figure 4-1 (a) X-ray diffraction patterns of powders synthesized by mechanochemical (MC), Pechini, and reverse co-precipitation (RCP) processes. Rietveld refinements of the x-ray diffraction patterns of powders of (b) mechanochemical (MC), (c) Pechini, and (d) reverse co-precipitation (RCP).

4.2 Thin films and pellets

4.2.1 Synthesis techniques

Conventional sintering: The powders synthesized by the above-mentioned techniques are consolidated into cylindrical or disk-like pellets by conventional sintering. Conventional sintering (CS) involves pressing the powders in a uniaxial press and sintering the pellets at high temperatures for densification. In this thesis, pellets were pressed at a pressure of 500 MPa and were sintered at 1400 – 1500 °C for 12 h. The pellets were pressed using a die with a diameter of 8 mm.

Pechini process (Sol–Gel process): The polyester gel obtained from the Pechini process was aged at room temperature for 48 hrs. After aging, the gel was spin-coated onto a Si substrate at a speed of 6000 rpm for 60 s. The coated gel layer was dried on a hot plate at 100 °C. This process of coating and drying was repeated five times. Finally, the films were heat-treated at 750 °C for six hours.

Pulsed Laser Deposition: One of the most prominent techniques to grow thin films is Pulsed Laser Deposition. A schematic representation of the deposition technique is shown in *Figure 4-2*. In pulsed laser deposition (PLD), a high-energy KrF UV-laser (λ = 248 nm) ablates a target made of the desired material onto a heated substrate, depositing the material as a thin film.
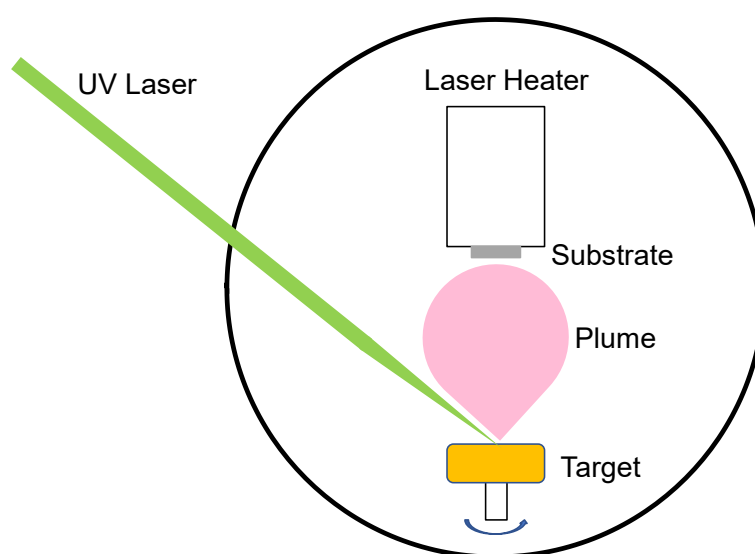
Figure 4-2 Schematic representation of pulsed laser deposition.

The target was synthesized by conventionally sintering powders of $(Ce,La,Pr,Sm,Y)O_{2-\delta}$. These powders were produced using a reverse co-precipitation method. For the conventional sintering process, the powders were pressed into 1-inch pellets using a uniaxial press under a pressure of 400 MPa. Following this, the samples were heat-treated at 1000 °C for 12 hours.

The characteristics of the resulting film depend on several factors, including the laser fluence, deposition temperature, deposition atmosphere, and the type of substrate. Various deposition conditions can be employed to create films with distinct morphologies. As a result, three different samples with three distinct morphologies were synthesized. The deposition conditions for the three different samples are as follows:

1) PLD-Si-1: The samples were deposited on a Si substrate at room temperature with a laser fluence of 1.72 J/cm^2 with a frequency of 2 Hz at an oxygen partial pressure of 0.05 mbar. The deposited films were subsequently heat treated at 750 °C for 15 mins at an oxygen partial pressure of 200 mbar inside the PLD chamber.

2) PLD-Si-2: The samples were deposited on a Si substrate at a temperature of 750 °C with a fluence of 1.72 J/cm^2 with a frequency of 2 Hz at an oxygen partial pressure of 0.05 mbar.

3) PLD-YSZ: The samples were deposited on a YSZ substrate at a temperature of 750 °C with a fluence of 1.72 J/cm^2 with a frequency of 2 Hz at an oxygen partial pressure of 0.05 mbar.

4.2.2 Structural and chemical characterization

The X-ray diffraction patterns of the films and pellets, along with their Rietveld refinements, synthesized in this section are presented in *Figure 4-3* and *Figure 4-4*. The XRD pattern and its refinement of the target and conventionally sintered pellet in *Figure 4-3(a)* and in *Figure 4-4(a) (b)* shows bixbyite structure ($Ia\bar{3}$) even though the powders have a fluorite structure. This structural transition from fluorite to bixbyite in $(Ce,La,Pr,Sm,Y)O_{2-\delta}$ happens above 1000 °C which has been observed in multiple reports[42,44,45,56,98]. The structural transition above 1000 °C occurs due to the ordering of oxygen vacancies along <111> direction. Furthermore, higher sintering temperatures (>1000 °C) are required to achieve high relative densities. However, highly dense thin films can be synthesized without requiring heat treatments above 1000 °C. Consequently, the XRD pattern of thin film synthesized by sol-gel process (heat treated at 750 °C) in *Figure 4-3(a)* shows a fluorite structure which is further supported by the Rietveld refinement in *Figure 4-4(c)*.

The XRD pattern of the samples synthesized by PLD are shown in *Figure 4-3(b)*. The XRD patterns suggest that PLD-Si-1 exhibits a fluorite structure with a polycrystalline morphology. Furthermore, PLD-Si-2 shows only a few peaks of the fluorite structure, suggesting a preferred orientation of the grains. Finally, the XRD pattern of PLD-YSZ shows only the (200) reflection of the FHEO and YSZ, while other reflections are absent, which indicates an epitaxial film on the YSZ substrate. The XRD pattern of the PLD-Si-1 and PLD-Si-2 can be fitted with a single-phase fluorite structure, as observed in *Figure 4-4(d)* and *Figure 4-4(e)*. Moreover, a preferred orientation along <111> direction is used to fit the XRD data of PLD-Si-2 in *Figure 4-4(e)*, indicating a preferred orientation along <111> direction. *Table 4-2* shows the lattice parameter and crystallite size. The conventionally sintered samples (Target and CS) show a bixbyite structure, a superstructure of fluorite structure in which the unit cell is four times that of the fluorite structure, and lattice parameters are twice as large. So, for comparison, the lattice parameters of bixbyite were halved in *Table 4-2*. All the thin films and pellets exhibit a lattice parameter (a or a/2) of 5.4 Å with no significant changes. However, the crystallite sizes differ with the largest ones being observed for the conventionally sintered samples. Typically, conventional sintering involves pressing the nanoparticles together to get sufficient contact between the particles and heat treating the pellets at very high temperatures for densification. In conventional sintering, the temperature is high enough to facilitate densification and grain growth. Grain growth increases the crystallite size as observed in *Table 4-2* for conventionally sintered samples. However, in the case of polycrystalline thin films Pechini and PLD-Si-1, an amorphous layer was initially deposited either by spin coating a precursor gel onto a substrate or laser ablating an oxide material onto a substrate at room temperature. This amorphous layer was then crystallized at 750 °C resulting in a dense crystalline film. Therefore, Pechini and PLD-Si-1 are nanocrystalline and have comparable crystallite sizes. Although PLD-Si-2 was deposited in PLD, they exhibit a polycrystalline thin film with a preferred orientation along <111> direction. The key difference between PLD-Si-1 and PLD-Si-2 in deposition conditions is that the latter is deposited at 750 °C rather than at room temperature. In vapor deposition techniques, depositing films at a temperature in the range of $0.3\,T_m < T < 0.45\,T_m$ (T_m is the melting point of the oxide) results in a columnar or textured growth[99]. The melting point of rare earth oxides is around 2300 - 2500 °C, and the deposition temperature (750 °C) is in the range for columnar growth[100,101]. Subsequently, a columnar growth is observed in PLD-Si-2. PLD-YSZ is an epitaxial film. This is because FHEO and YSZ have the same structure (fluorite) and comparable lattice parameters (FHEO - 5.4 Å and YSZ -

5.2 Å). Furthermore, epitaxial films of ceria-based oxides on YSZ are commonly observed in the literature[102,103]. Therefore, an epitaxial film has been observed in PLD-YSZ.
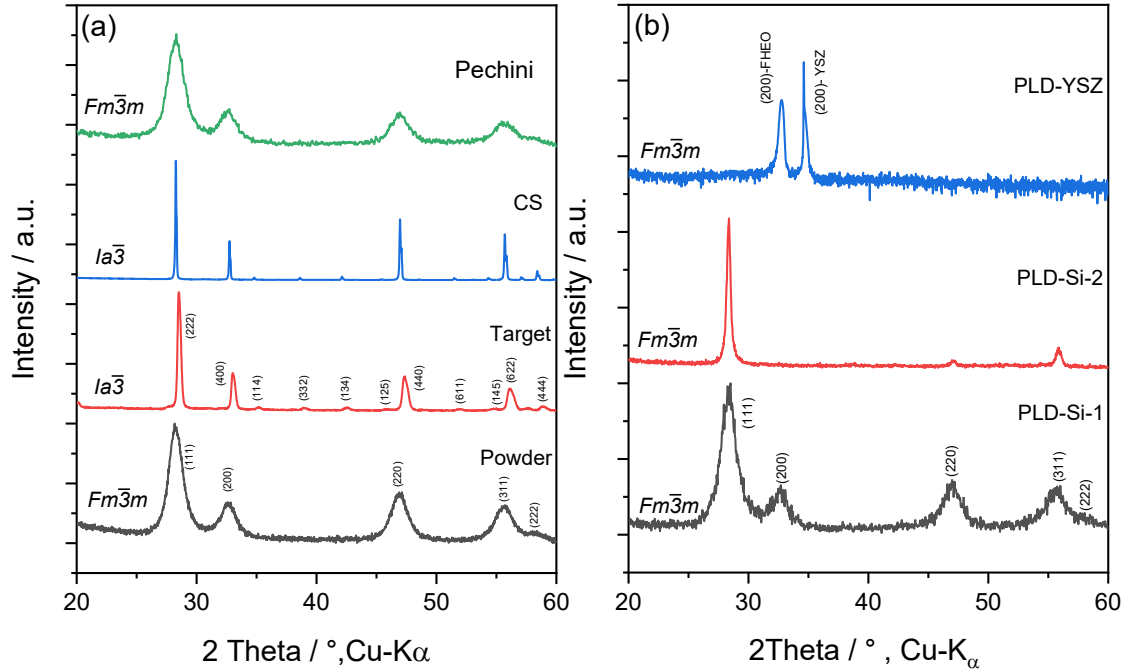
Figure 4-3 (a) X-ray diffraction of powder (reverse co-precipitation), target and pellet (CS) from conventional sintering, thin film from Pechini process (Pechini). (b) X-ray diffraction pattern of thin films from pulsed laser deposition deposited on Si substrate (PLD-Si-1, PLD-Si-2) and on YSZ susbtrate (PLD-YSZ). The XRD of the pellets were measured by powder XRD, the XRD of the films except PLD-YSZ were measured by Grazing incidence XRD, the XRD of PLD-YSZ is measured by high resolution XRD.

Table 4-2 The structure, lattice parameter, crystallite size of the dense materials synthesized by corresponding synthesis technique. For bixbyite structure ($Ia\bar{3}$), the lattice parameter is divided by 2 for a comparison between the structures.

Sample	Synthesis route	Structure	a / a/2 (Å)	Size (nm)
Target	Conventional sintering	$Ia\bar{3}$	5.44	191.3
CS-pellet	Conventional sintering	$Ia\bar{3}$	5.47	250
Pechini	Pechini process	$Fm\bar{3}m$	5.49	7.3
PLD-Si-1-film	Pulsed laser deposition	$Fm\bar{3}m$	5.47	6
PLD-Si-2-film	Pulsed laser deposition	$Fm\bar{3}m$	5.46	21
PLD-YSZ	Pulsed laser deposition	$Fm\bar{3}m$	5.46	-
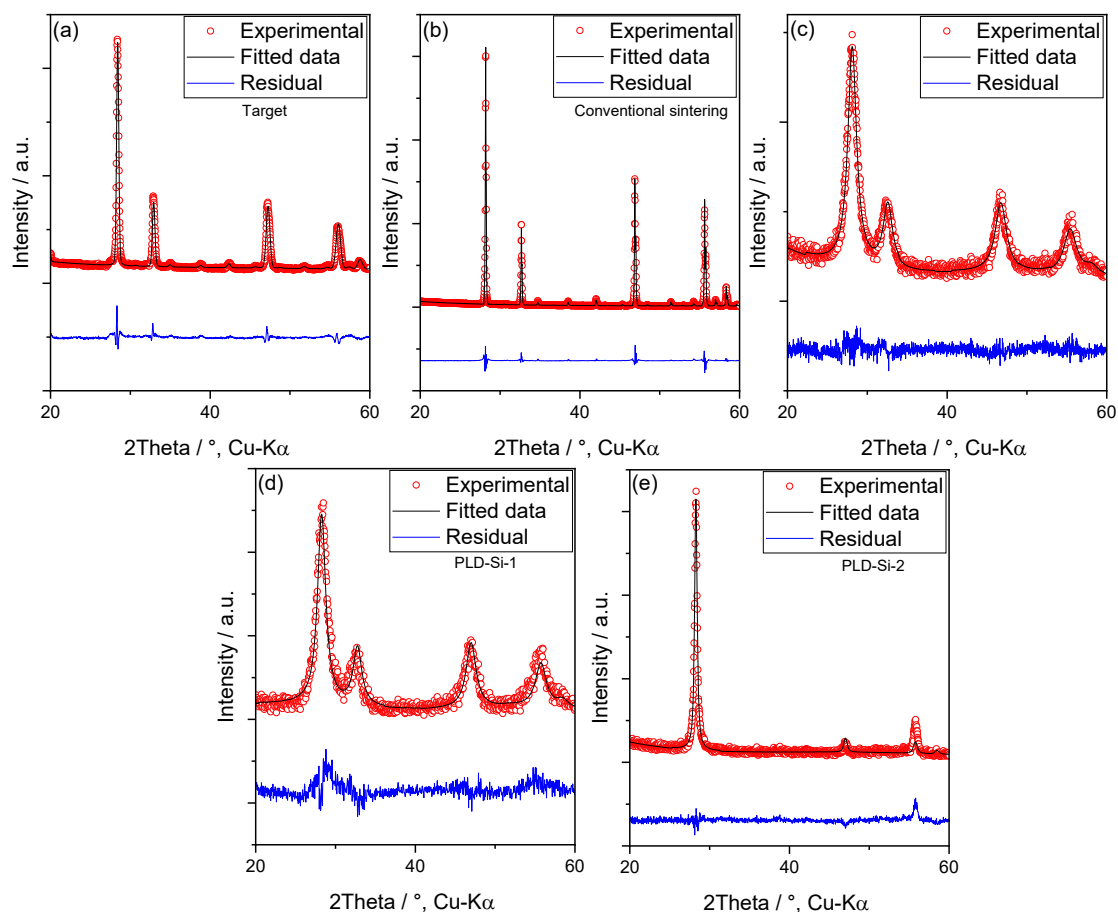
Figure 4-4 Rietveld refinements of (a) Target (b) Conventional sintering (c) Pechini process (d) PLD-Si-1 (e) PLD-Si-2.

Exemplary films and pellets synthesized in this section with different morphologies were selected for further characterization. A polycrystalline morphology film synthesized by the Pechini process (Pechini), columnar and epitaxial film synthesized by PLD (PLD-Si-2 and PLD-YSZ), and the conventional sintered 8 mm pellets (CS) were chosen for further characterization.

The lamellas for transmission electron microscopy (TEM) were extracted from the thin films with a Focused Ion Beam (FIB) system. The TEM images of the lamellas of Pechini, PLD-Si-2, and PLD-YSZ are presented in *Figure 4-5*. The TEM images of Pechini in *Figure 4-5(a)* clearly show a polycrystalline film, and the SAED pattern further confirms the polycrystalline fluorite structure. A closer inspection of the TEM images in *Figure 4-5(a)* is depicted in *Figure 4-5(b)*. It is observed that the crystallite size is way less than 20 nm indicating a nanocrystalline film. These TEM results are in agreement with the XRD results, which suggest a polycrystalline fluorite structured thin film. The energy dispersive X-ray spectroscopy (EDS) maps in *Figure 4-5(c)* show a homogenous distribution of elements on the nanoscale. The XRD data of PLD-Si-2 indicate the presence of columnar grains, which can also be observed in the

TEM images of PLD-Si-2 in *Figure 4-5(d)* and *Figure 4-5(e)*. The SAED patterns show a fluorite structure. It can be seen that the width of the columns is around 20 nm, which is in line with the crystallite size extracted from the XRD pattern in *Table 4-2*. The EDS maps of PLD-Si-2 in *Figure 4-5(f)* show a homogenous distribution of elements on the nanoscale. The TEM images of PLD-YSZ in *Figure 4-5(g)* depict epitaxial growth in *Figure 4-5(h)*. These TEM results of PLD-YSZ align with the XRD results. The EDS maps in *Figure 4-5(i)* show a homogenous distribution of elements on the nanoscale.
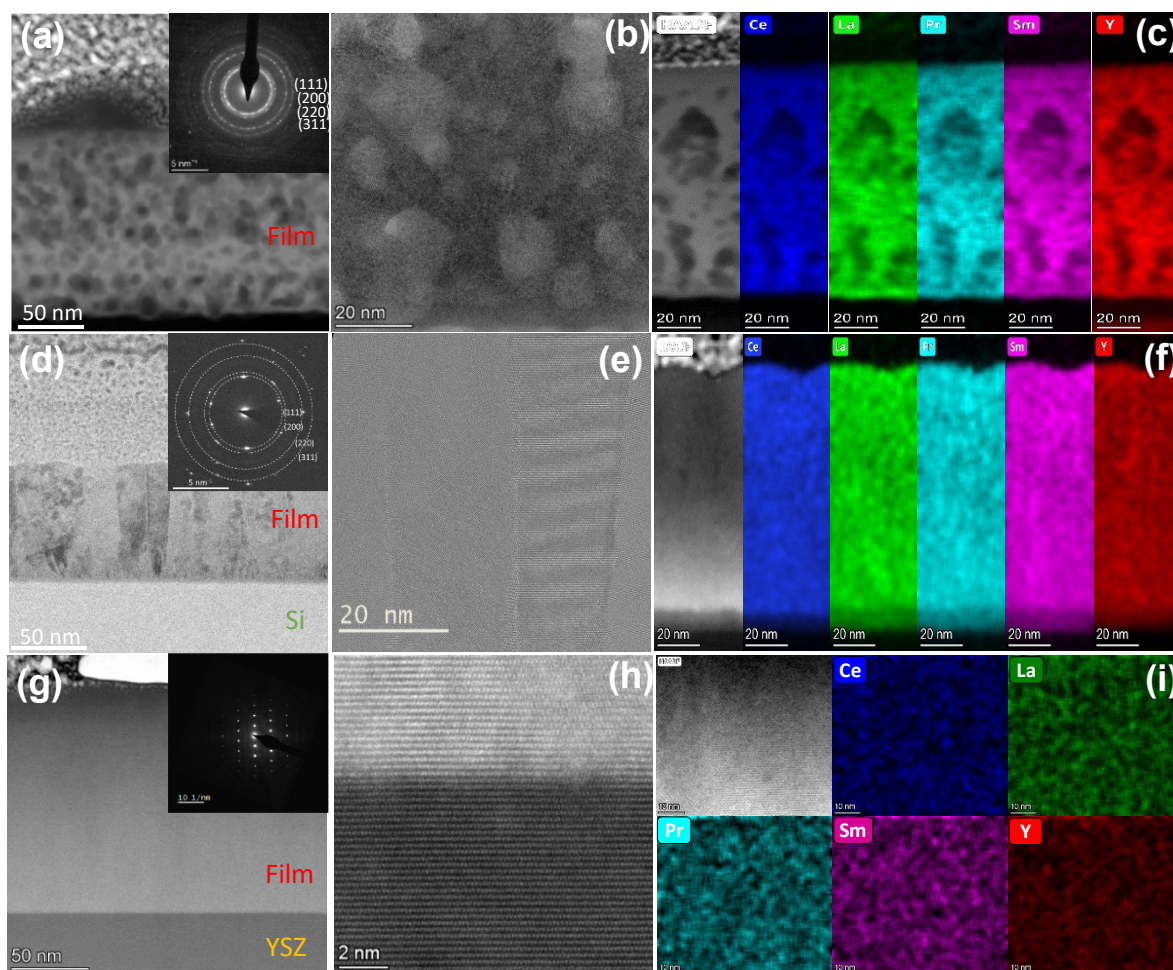
Figure 4-5 (a) The TEM micrograph of Pechini along with the diffraction pattern, (b) Zoomed in TEM micrograph of Pechini, (c) EDS maps of Pechini, (d) The TEM micrograph of PLD-Si-2 along with the diffraction pattern, (e) Zoomed in TEM micrograph of PLD-Si-2, (f) EDS maps of PLD-Si-2, (g) The TEM micrograph of PLD-YSZ along with the diffraction pattern (h) Zoomed in TEM micrograph of PLD-YSZ (i) EDS maps of PLD-YSZ.

The preparation of samples for conducting TEM of the pellets synthesized by conventional sintering (CS) involves crushing the pellets into powders with a pestle and mortar. The TEM was conducted on the powder of the crushed pellets and the TEM data can be seen

in *Figure 4-6*. The TEM micrograph is in *Figure 4-6(a)*. The corresponding SAED patterns in *Figure 4-6(b)* and *Figure 4-6(c)* suggest the presence of both fluorite and bixbyite structures in the system. Although the XRD pattern suggests a single-phase bixbyite structure, TEM data suggest the presence of both fluorite and bixbyite structures. The distinction between the XRD patterns of fluorite and bixbyite structures lies in the small superstructure reflections observed in the bixbyite. Consequently, identifying a mixture of fluorite and bixbyite structures using XRD can be challenging. However, Transmission Electron Microscopy (TEM) can probe the materials locally at higher magnifications, which helps distinguish between the two structures.

The structure of ceria-based systems ($Ce_{1-x}^{+4}R_x^{+3}O_{2-\delta}$) changes from fluorite to bixbyite as the concentration of rare earth cations(x) increases[104–108]. This transformation occurs gradually over a concentration range. At low concentrations, domains of bixbyite cations form around the rare earth cations (R^{+3}). As the concentration increases, these domains grow larger until the material fully transforms into a bixbyite structure at higher rare earth element concentrations[104–109]. Therefore, both fluorite and bixbyite structures can coexist at certain concentrations of rare earth cations (R^{+3}). In FHEO, Ce is +4, Pr is multivalent (+3/+4), while the rest are +3 cations. At high temperatures, Pr^{+4} changes to Pr^{+3} [17,18,21,22,110–112]. This change in oxidation state from +4 to +3 leads to more oxygen vacancies and induces the structural transition from fluorite to a bixbyite structure[42,44,56]. As a result, the XRD pattern of the CS pellet exhibits bixbyite due to the high sintering temperature. However, the transition from fluorite to bixbyite with increasing +3 cation is gradual. As a result, fluorite and bixbyite structures can be present in the CS sample depending on the content of Pr^{+3} or sintering temperature, which is indistinguishable in XRD while detectable in TEM. The EDS maps in *Figure 4-6(d)* clearly show a homogenous distribution of elements on a nanoscale. The chemical compositions from EDS maps are shown in *Table 4-3*. All the elements are close to equiatomic percentage (20 at.%), with Y and Sm slightly higher.
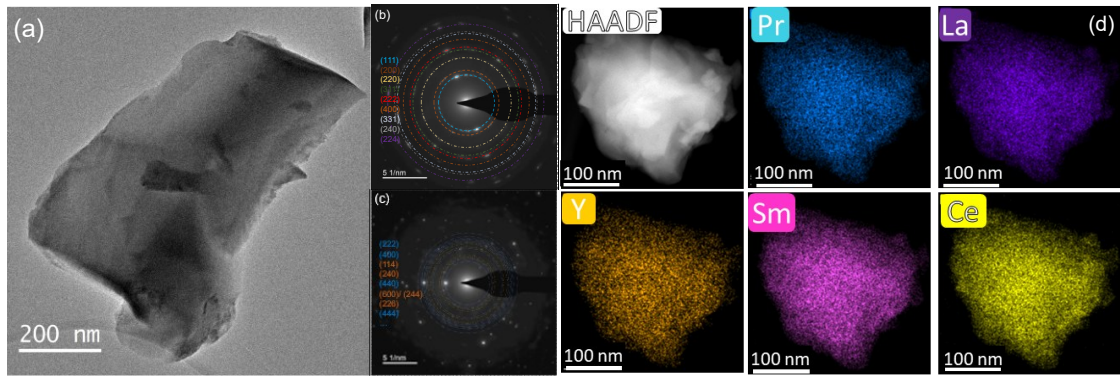
Figure 4-6 (a) TEM micrograph of the powder particle of the crushed pellet, (b) SAED pattern depicting fluorite structure, (c) SAED pattern depicting bixbyite structure, and (d) EDS map of a powder particle of crushed pellet.

Table 4-3 Chemical composition(at %) of Pechini, PLD-Si-2, PLD-YSZ and Pechini from the TEM-EDS maps in Figure 4-5(c, Figure 4-5(f), Figure 4-5(i), and Figure 4-6(d).

Element	Pechini	PLD-Si	PLD-YSZ	CS
Y	21.85	22.89	22.35	23.59
La	18.67	17.58	17.34	17.88
Ce	20.40	19.81	18.70	17.59
Pr	19.16	19.37	19.95	19.09
Sm	19.92	20.36	21.65	21.83

In FHEO - $(Ce,La,Pr,Sm,Y)O_{2-\delta}$, Ce, and Pr are multivalent elements. The oxidation states of these elements can determine the properties of the system. Electron energy loss spectroscopy (EELS) can be a good tool for comparing the oxidation states of the Ce and Pr. EELS was conducted inside the TEM on the same lamellas and powder used for TEM measurement. The EELS spectra of the Ce M edge for CS, PLD-YSZ, PLD-Si-2, and Pechini are illustrated in *Figure 4-7(a)*. The edge positions and intensity ratio (I_{M5}/I_{M4}) of the M_5 and M_4 edges are good indicators to compare the oxidation states[56,113,114]. The edge positions of M edges are close for Pechini, CS, and PLD-YSZ, but the M edge slightly shifts to the right for PLD-Si-2. However, the intensity ratios (I_{M5}/I_{M4}) are identical. These results suggest that Ce has an oxidation state closer to +4, similar oxidations state in Pechini, CS, and PLD-YSZ, and a slightly higher oxidation state in PLD-Si-2[113,114]. The EELS spectra of the Pr M edge for CS, PLD-YSZ, PLD-Si-2, and Pechini are depicted in *Figure 4-7(b)*. Similar to the Ce M edge, the edge positions of M edges are identical for Pechini, CS, and PLD-YSZ but the M edge slightly shifts to the right for PLD-Si-2. Furthermore, the intensity ratios (I_{M5}/I_{M4}) are identical for Pechini, CS, and PLD-YSZ but lower for PLD-Si-2. These results suggest that the oxidation

state of Pr in Pechini, CS, and PLD-YSZ is identical with a slightly higher oxidation state for PLD-Si-2. The intensity ratio (I_{M5}/I_{M4}) for $PrPO_4$ (Pr - +3) is 1.1, while for Pr_6O_{11} (Pr - +3.7) is 1.8 [56,113]. The intensity ratio in this section is between those values, indicating a mixed valency for Pr. Finally, Ce and Pr have similar valence states in Pechini, PLD-Si-2, PLD-YSZ, and CS.
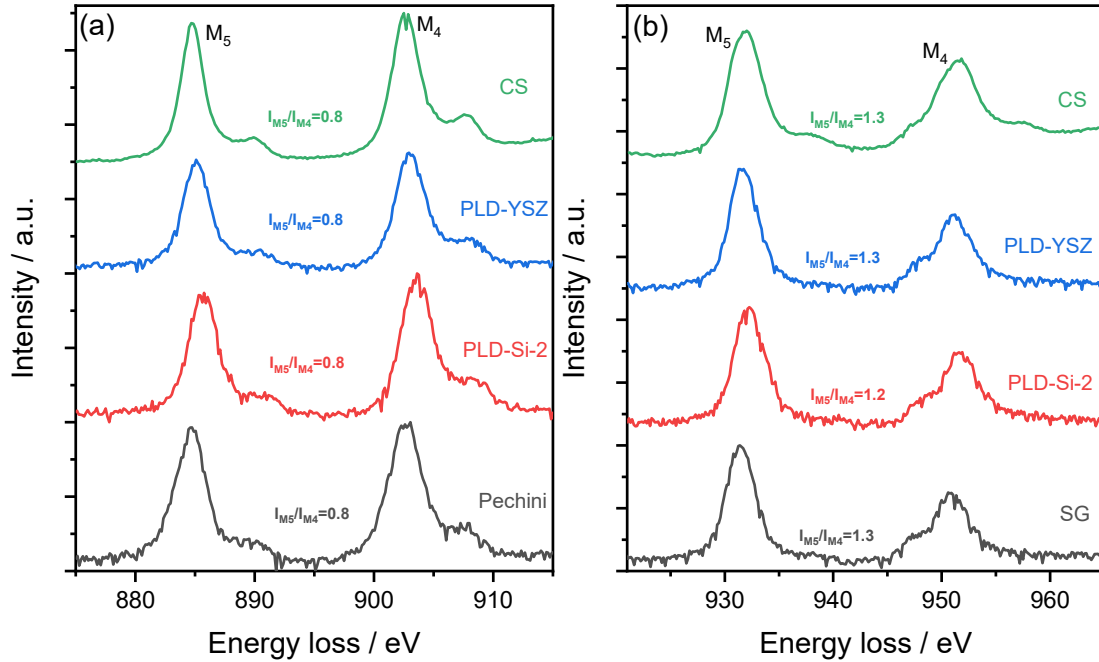
Figure 4-7 Electron energy loss spectra of CS, PLD-YSZ, PLD-Si-2, Pechini at (a) Ce M edge (b) Pr M edge.

4.3 Conclusion

This section explores the synthesis of fluorite structured high entropy oxide - $(Ce,La,Pr,Sm,Y)O_{2-\delta}$. The high entropy oxide is produced in various forms, such as powders, thin films, and pellets employing different synthesis methods.

Powders

In this thesis, powders were synthesized using reverse co-precipitation, Pechini process, and mechanochemical synthesis. Powders obtained by these methods show fluorite structure with a crystallite size of 10 - 20 nm.

Thin films

Thin films were fabricated using Pulsed Laser Deposition and the Pechini process. Thin films deposited using the Pechini process exhibit a fluorite structure with a crystallite size of less than 10 nm. The thin films deposited by PLD show fluorite structure with three different

morphologies: polycrystalline, polycrystalline with texture or columnar and epitaxial films. The oxidation state of Ce is +4, whereas Pr exhibits multivalency. All the elements are distributed homogenously, with nearly equiatomic fractions.

Pellets

Pellets were consolidated by uniaxial pressing and densified using conventional sintering of high entropy oxide powder. The resulting pellets exhibit both fluorite and bixbyite structures, which arise from the high sintering temperatures. Additionally, the pellets have chemical compositions that are nearly equiatomic, with a uniform distribution of elements at the nanoscale.

These synthesis routes are employed to fabricate thin films and pellets, which are then used to examine the oxygen ion conductivity and electrocatalytic activity of high-entropy oxides. The table below discusses some advantages and disadvantages of these fabrication methods.

Table 4-4 Advantages and disadvantages of the sol-gel process, pulsed laser deposition and conventional sintering along with their practical applicability in synthesis of a component in SOC.

Sol-gel process (Pechini)	Pulsed laser deposition	Conventional sintering
Easy to synthesize	Relatively hard to synthesize	Easy to synthesize
Hard to optimize for different compositions	Easier to optimize for different composition	Easier to optimize for different composition
Simple setup and instrumentation	Complicated setup and instrumentation	Simple setup and instrumentation
High temperatures are not necessary	High temperatures are not necessary	High temperatures are required
Temperature sensitive structures can be achieved	Temperature sensitive structures can be achieved	Temperature sensitive structures cannot be achieved
Polycrystalline morphology	Various morphologies are possible	Polycrystalline morphology

5 Electrolytes for solid oxide fuel cells - oxygen ion conductors

5.1 Fluorite-type high entropy oxides - $(Ce,La,Pr,Sm,Y)_{1-x}Zr_xO_{2-\delta}$

Ceria-based ionic conductors are well-known fluorite-structured materials, offering higher conductivities than yttria-stabilized zirconia, as discussed in Chapter 2. However, ceria-based ionic conductors exhibit electronic conduction at different partial pressures of oxygen due to the multivalence of Ce and other multivalent dopants. A good ionic conducting electrolyte should have little to no electronic conduction. The electronic conductivity in the ceria-based ionic conductors can be reduced by reducing the amount of Ce and other multivalent dopants while maintaining the fluorite structure.

$(Ce,La,Pr,Sm,Y)O_{2-\delta}$ is a multicomponent fluorite-structured oxide. In $(Ce,La,Pr,Sm,Y)O_{2-\delta}$, more than 60% of the cations (Pr, La, Sm, Y) have an oxidation state of +3, and the rest of the cations (Ce, some Pr) have an oxidation state of +4. Despite the high concentration of +3 cations, $(Ce,La,Pr,Sm,Y)O_{2-\delta}$ exhibits the fluorite structure (MO_2), a structure where cations have a +4 oxidation state. The presence of a +3 cation in a fluorite structure leads to the formation of oxygen vacancies. Consequently, $(Ce,La,Pr,Sm,Y)O_{2-\delta}$ likely possesses a large oxygen vacancy concentration. However, the structure of $(Ce,La,Pr,Sm,Y)O_{2-\delta}$ changes from fluorite to bixbyite at temperatures above 1000 °C [42]. As a result, the fluorite structure in these high entropy oxides is sensitive to synthesis conditions. To measure the oxygen ion conductivity of the materials, a dense material with high relative

densities is necessary. Traditionally, to investigate the conductivity of the oxides, the oxide powder is pressed and sintered at higher temperatures (>1000 °C) to achieve dense pellets with high relative densities.

One possible way to stabilize the fluorite structure at higher temperatures is by adding a +4 cation into the lattice. In a recent high throughput study by Kumbhakar *et al.*, Zr^{+4} is observed to stabilize the fluorite structure [54]. In this section of the thesis, Zr is doped into $(Ce,La,Pr,Sm,Y)O_{2-\delta}$ at different concentrations. Powders of $(Ce,La,Pr,Sm,Y)_{1-x}Zr_xO_{2-\delta}$ are prepared using mechanochemical synthesis and subsequently pressed into pellets that are sintered at 1400 °C for 12 h. The pellets were structurally, chemically and electrically characterized using the techniques explored in Chapter 3. The pellets are coated with silver electrodes to measure the electrical properties of the pellets. *Table 5-1* summarizes the compositions of Zr doped $(Ce,La,Pr,Sm,Y)O_{2-\delta}$ explored in this section.

Table 5-1 Compositions and corresponding notations of the $(Ce,La,Pr,Sm,Y)_{1-x}Zr_xO_{2-\delta}$

Composition	Notation
$(Ce,La,Pr,Sm,Y)O_{2-\delta}$	$x = 0$
$(Ce,La,Pr,Sm,Y)_{0.95}Zr_{0.05}O_{2-\delta}$	$x = 0.05$
$(Ce,La,Pr,Sm,Y)_{0.92}Zr_{0.08}O_{2-\delta}$	$x = 0.08$
$(Ce,La,Pr,Sm,Y)_{0.9}Zr_{0.1}O_{2-\delta}$	$x = 0.1$
$(Ce,La,Pr,Sm,Y)_{0.84}Zr_{0.16}O_{2-\delta}$	$x = 0.16$
$(Ce,La,Pr,Sm,Y)_{0.7}Zr_{0.3}O_{2-\delta}$	$x = 0.3$

5.1.1 Structural characterization

The structural characterization was done using X-ray Diffraction (XRD) and Transmission Electron Microscopy (TEM). The X-ray diffraction of the powders synthesized via ball milling are shown in *Figure 5-1*. A fluorite structure is observed in the powders irrespective of the Zr content. However, the pellets sintered at 1400 °C exhibit different structures at different Zr content. The XRD was performed on the surface of the pellets and on the crushed pellets to understand their bulk structure. The corresponding XRD patterns can be seen in *Figure 5-1(b)* and *Figure 5-1(c)*. The XRD pattern suggests that a bixbyite structure is observed for $x = 0, 0.05, 0.08$, and the structure transitions to fluorite at $x = 0.1, 0.16$. However, the structure transforms to pyrochlore at $x = 0.3$. The XRD patterns are fitted with these phases

using Rietveld refinement, which are presented in *Figure 5-2*. A single phase fits the XRD patterns of all compositions.

The change in structure from fluorite to bixbyite has been reported in the literature, and the structural transition is a result of the ordering of excess oxygen vacancies (due to $Pr^{+4} \rightarrow Pr^{+3}$) at higher temperatures [104–109,115–117]. As a result, adding Zr (stable +4 cation) decreases the excess oxygen vacancies, stabilizing the fluorite structure at higher temperatures. However, at higher concentrations of Zr, the structure changes to pyrochlore, a structural transition due to the ordering of Zr in the lattice. Bixbyite and pyrochlore phases are superstructures of the fluorite, as observed in *Figure 5-3*. These superstructures originate from either the ordering of oxygen vacancies or the ordering of Zr cations, with the size of the resultant unit cell being eight times larger than that of the unit cell of the fluorite phase. Consequently, the lattice parameter of these superstructures is twice that of the fluorite. Therefore, the lattice parameters of bixbyite and pyrochlore structures are halved to understand the effect of Zr on the lattice. A decrease in the lattice parameters is observed with increasing Zr content, as illustrated in *Figure 5-4.* The decreasing trend is a consequence of the smaller ionic radii of the Zr ion (0.84 Å) when compared to the average ionic radii of Ce, La, Pr, Sm, and Y ions (1.07 Å). As per Vegard`s law, the lattice parameter of a solid solution is the weighted average of the lattice parameter of the corresponding elemental oxides. As a result, the addition of a smaller cation (Zr^{+4}) leads to a decrease in the interplanar spacing of the resultant compositions.
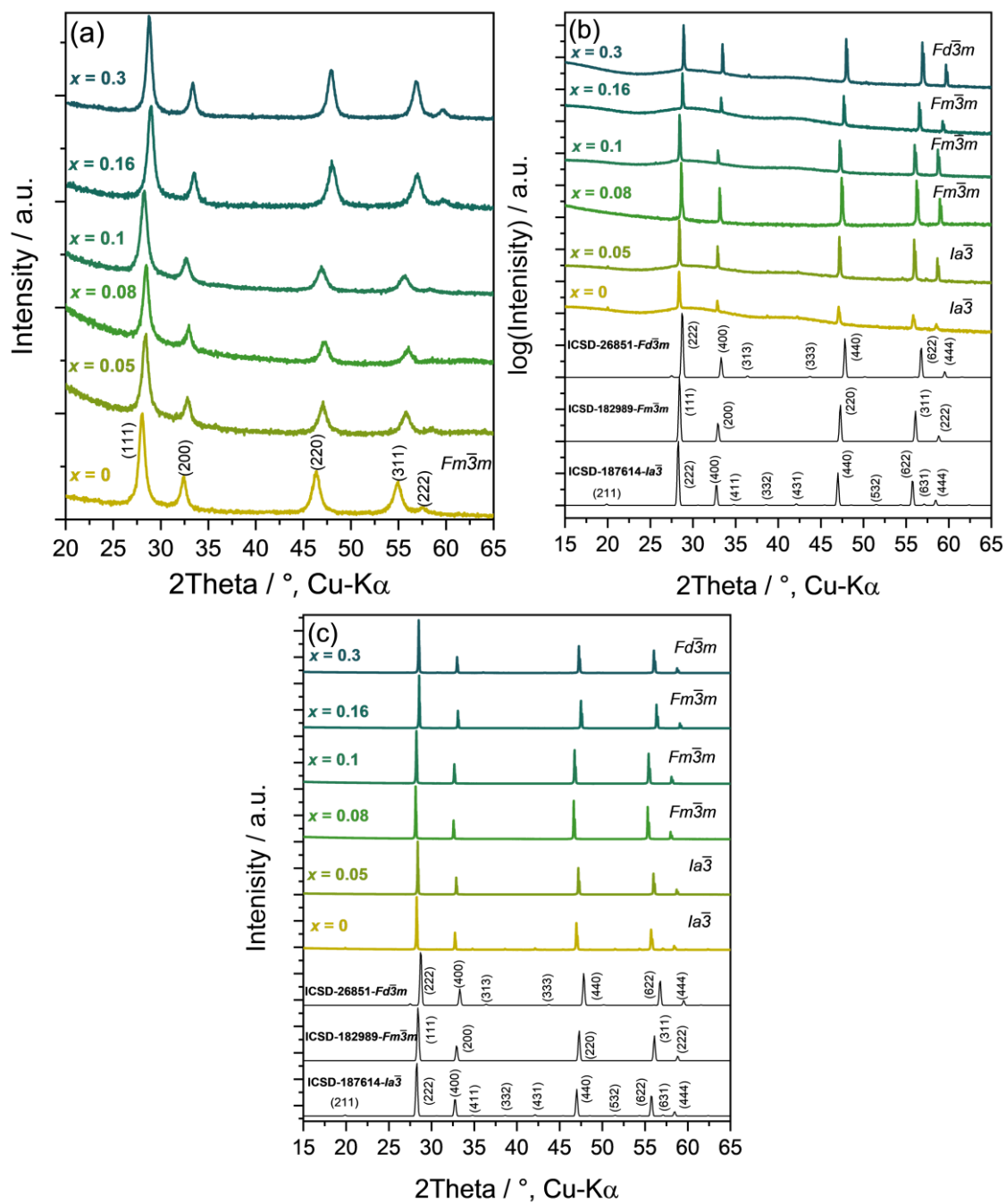
Figure 5-1 The XRD patterns of the (a) powders (b) surface of the pellets (c) crushed pellets of (Ce,La,Pr,Sm,Y)$_{1-x}$Zr$_x$O$_{2-\delta}$ along with the standard XRD-patterns of fluorite(Fm$\overline{3}$m), bixbyite (Ia$\overline{3}$) and pyrochlore (Fd$\overline{3}$m) structures.
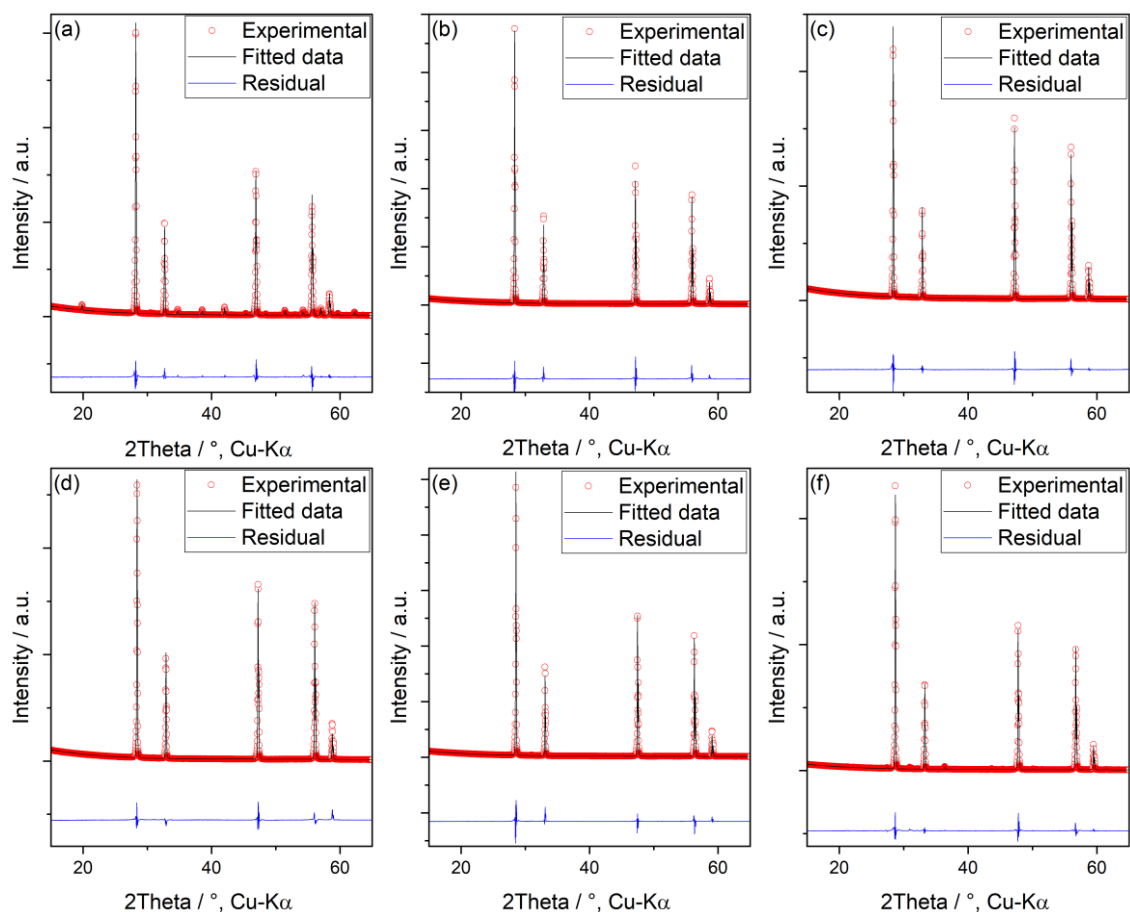
Figure 5-2 Rietveld refinements of the XRD patterns of (Ce,La,Pr,Sm,Y)$_{1-x}$Zr$_x$O$_{2-\delta}$ (a)x = 0, (b) x = 0.05 (b) x = 0.08 (b) x = 0.1 (b) x = 0.16 (b) x = 0.3.
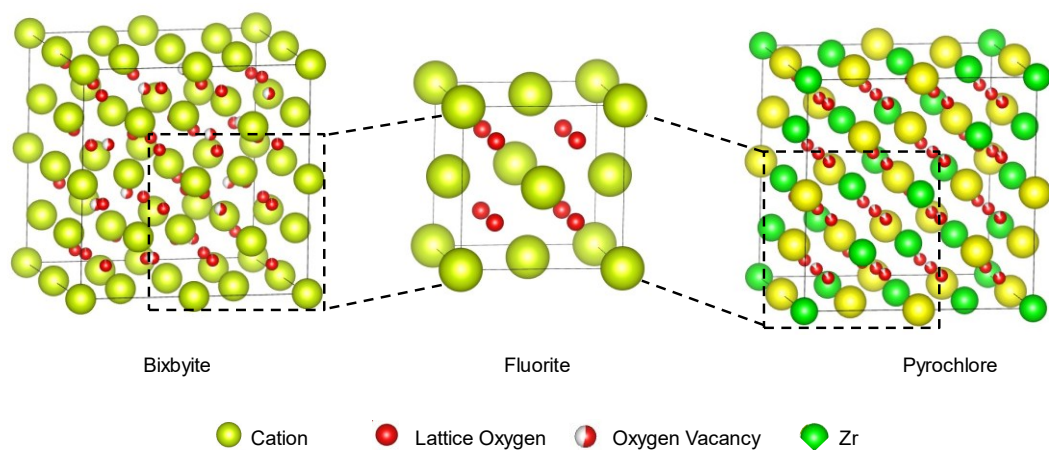
Figure 5-3 Unit cells of the fluorite, bixbyite and pyrochlore structures.
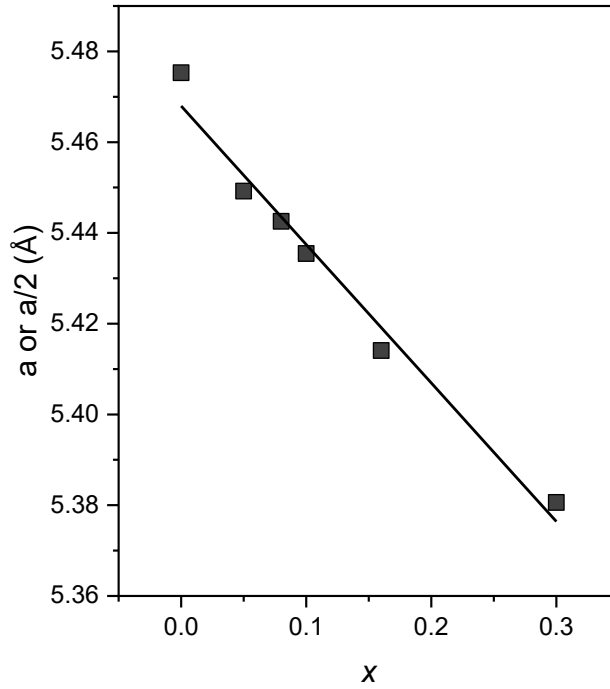
Figure 5-4 Lattice parameter (a) of the fluorite structure and half of lattice parameters (a/2) of the bixbyite and pyrochlore of $(Ce,La,Pr,Sm,Y)_{1-x}Zr_xO_{2-\delta}$ plotted against Zr content (x).

To further explore the crystal structure of $(Ce,La,Pr,Sm,Y)_{1-x}Zr_xO_{2-\delta}$, selected area electron diffraction (SAED) was conducted using TEM. The SAED patterns are shown in *Figure 5-5*. The electron diffraction on $x = 0$ suggests the presence of both fluorite and bixbyite structures, as demonstrated in *Figure 5-5(b)*, and *Figure 5-5(c)*. The SAED patterns of $x = 0.05$ from *Figure 5-5(e)* indicate a fluorite structure. Akin to $x = 0$, both fluorite and bixbyite structures are observed for $x = 0.08$ and are observed in the SAED patterns in *Figure 5-5(g)*, *Figure 5-5(h)*. The SAED patterns for $x = 0$, 0.05, and 0.08 indicate the presence of both fluorite and bixbyite phases. In ceria-based systems, the structure changes from fluorite to bixbyite with increasing concentrations of dopants like Gd and Y[104–108]. However, the transformation from fluorite to bixbyite with increasing dopant concentration happens gradually via the nucleation and growth of bixbyite structure around the dopant (M^{+3}- Gd, Sm, Y) in the fluorite structure [104–109]. As a result, both fluorite and bixbyite structures can be present in the system at certain concentrations of the dopant. However, the XRD pattern of $x = 0$, 0.05, and 0.08 from *Figure 5-1* suggests a single-phase bixbyite structure. Bixbyite is a superstructure of the fluorite, and the difference in the XRD patterns is the small superstructure reflections, which can be identified in the standard XRD pattern from *Figure 5-1(b)* and *Figure 5-1(c)*. Along with the similarities in XRD patterns of fluorite and bixbyite structure, the position of the reflections of the corresponding structures of the same composition are close [42,56]. Therefore, it can be

difficult to accurately distinguish a pure bixbyite phase from a mixture of fluorite and bixbyite structures using XRD. Contrary to XRD, being a bulk technique, electron diffraction, a local technique allows the identification of phase mixtures. Consequently, multiple phases have been identified with the help of TEM or advanced structural characterization techniques like neutron or synchrotron diffraction in some studies of ceria-based systems [104–109]. Nevertheless, in accordance with the XRD data, SAED patterns from *Figure 5-5(i)* and *Figure 5-5(l)* of $x = 0.1$, 0.16 indicates the presence of only a single-phase fluorite structure. As a result, X-ray and electron diffraction suggest that Zr aids in the stabilization of the fluorite structure. However, high concentrations of Zr ($x = 0.3$) lead to the transformation of the fluorite structure to the pyrochlore structure as per the XRD data, and a phase mixture of pyrochlore and fluorite is observed as observed in the SAED patterns in *Figure 5-5(n)* and *Figure 5-5(o)*. The phase mixture arises due to the preferential ordering of Zr ions along <110> direction within Zr-enriched regions.
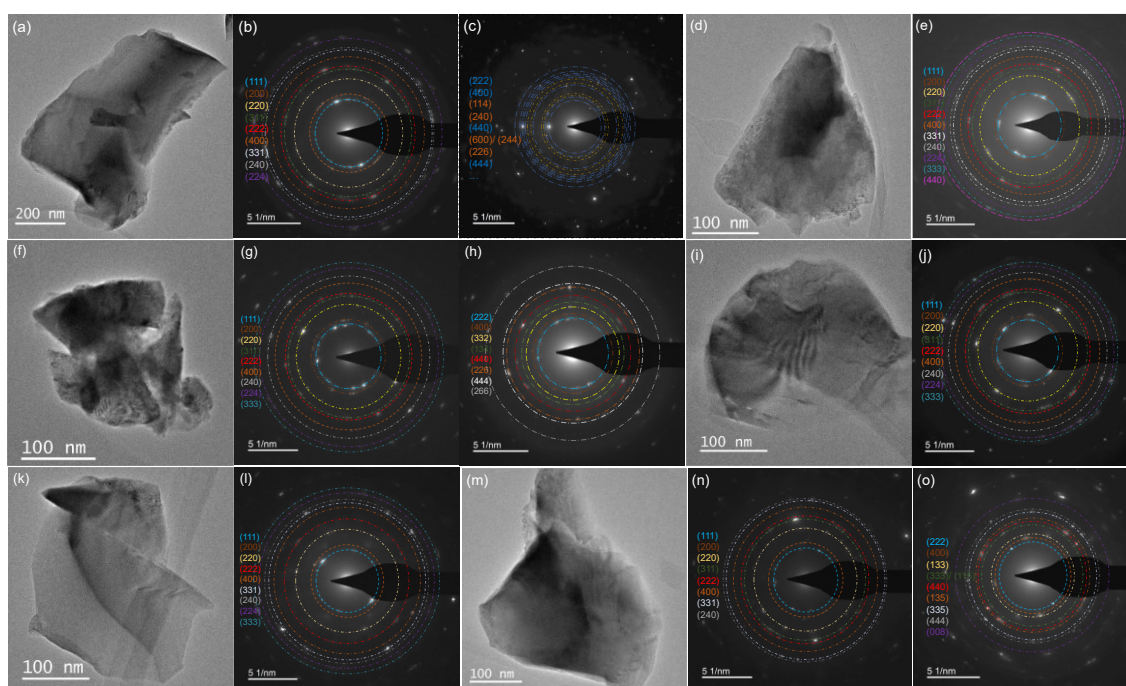
Figure 5-5 The TEM micrograph and the SAED pattern of (Ce,La,Pr,Sm,Y)$_{1-x}$Zr$_x$O$_{2-\delta}$ (a)(b)(c) x = 0 (d)(e) x = 0.05 (f)(g)(h) x = 0.08 (i)(j) x = 0.1 (k)(l) x = 0.16 (m)(n)(o) x = 0.3.

5.1.2 Chemical characterization

The structural characterization techniques indicate a mixture of superstructure phases. This mixture of superstructure phases can depend on the content and the distribution of +3 cations, as any small local segregation can lead to the formation of a bixbyite phase in the vicinity. As a result, the concentration and the distribution of elements in the synthesized systems should be analyzed. To identify the reasons for the existence of two phases, energy dispersive X-ray spectroscopy (EDS) was performed to measure the chemical composition and elemental distribution. It is important to note that among the elements used in this study, Pr exhibits multivalence (+3 and +4). Therefore, the extent of multivalency in Pr is investigated. It is known that multivalency leads to changes in the structure and the conductivity. UV-Vis spectroscopy (UV-vis) and Electron Energy Loss Spectroscopy (EELS) were conducted to understand the valence state of Pr.

The chemical composition and elemental distribution of $(Ce,La,Pr,Sm,Y)_{1-x}Zr_xO_{2-\delta}$ are investigated using SEM on the surface of the pellet at a scale of a few hundred micrometers to study the average chemical composition and elemental distribution, which can be seen in *Figure 5-6(a)* and *Figure 5-6(b)*. The chemical compositions of $(Ce,La,Pr,Sm,Y)_{1-x}Zr_xO_{2-\delta}$ from *Figure 5-6(a)* suggest that Ce, La, Pr, and Sm are equiatomic. However, Y, which was supposed to be equiatomic with Ce, La, Pr, and Sm, is found to be approximately two atomic percent lower. It is important to note that the samples are coated with gold to avoid charging, and EDS was collected at an operating voltage of 20 kV. At 20 kV, the most intense characteristic X-ray peaks of Y, Zr, and Au are L_α – 1.922 eV, L_α – 2.042 eV, and M – 2.048 eV, correspondingly. Consequently, these peaks were used to calculate the compositions of Y and Zr. The similar positions of these peaks can cause discrepancies in determining the composition of these elements. The concentrations of Zr are close to the estimated values from the experiments with a deviation of $\pm$ 2 atomic percent from the expected values. The EDS maps on a micrometer scale suggest that the elements are homogenously distributed with no signs of segregation. As an example, the EDS map of $(Ce,La,Pr,Sm,Y)_{0.92}Zr_{0.08}O_{2-\delta}$ depicting the homogenous distribution of elements is shown in *Figure 5-6(b)*.
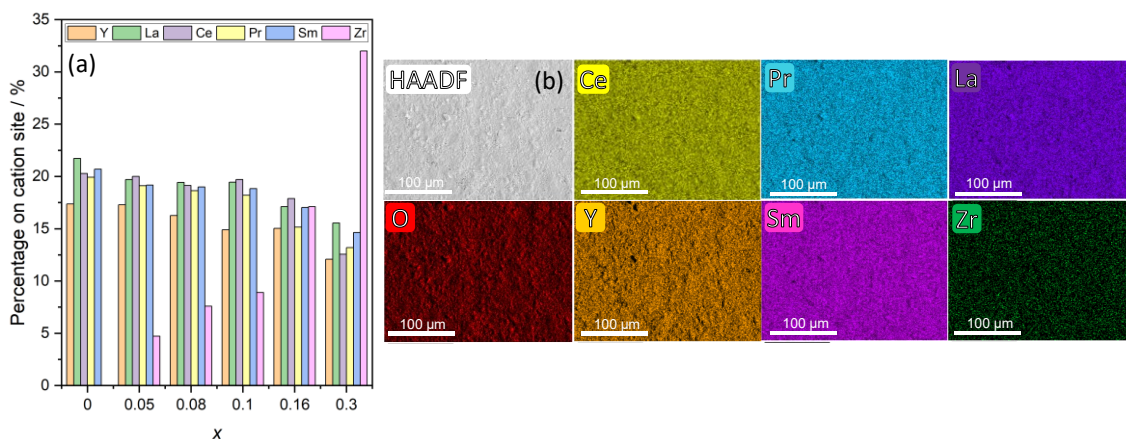
Figure 5-6 (a) Chemical composition of $(Ce,La,Pr,Sm,Y)_{1-x}Zr_xO_{2-\delta}$ with respect to x investigated in SEM (Micrometer scale). (b) Elemental distribution of Ce, La, Pr, Sm, La, Y and Zr in $(Ce,La,Pr,Sm,Y)_{0.92}Zr_{0.08}O_{2-\delta}$ collected by Oxford X-Max^N X-ray detector in a scanning electron microscope (Micrometer scale).

The EDS conducted in the SEM was done on a micrometer scale, which estimates the average chemical composition and bulk elemental distribution. To understand the chemical compositions and elemental distribution on a nanoscale, the pellets are crushed into powders and EDS was conducted using TEM. The chemical compositions obtained from the EDS-TEM suggest equiatomic percentages of Ce, La, Pr, and Sm as seen in *Figure 5-7(a)*. Unlike the case of SEM, these samples were not coated with gold for TEM. As a result, no discrepancies in the concentrations of Y are expected. Nevertheless, Y is slightly higher than the rest of the equiatomic elements, suggesting a slight compositional variation from the nominal values at a nanoscale. These slight compositional variations can contribute to the changes in structural differences observed at a nanoscale in *Figure 5-5*. The concentration of Zr is close to the nominal values with a deviation of ± 2 atomic percent. The EDS-TEM maps suggest that all the elements are homogenously distributed with no apparent signs of segregation of elements, which are presented in *Figure 5-7(b)* for $(Ce,La,Pr,Sm,Y)_{0.92}Zr_{0.08}O_{2-\delta}$.
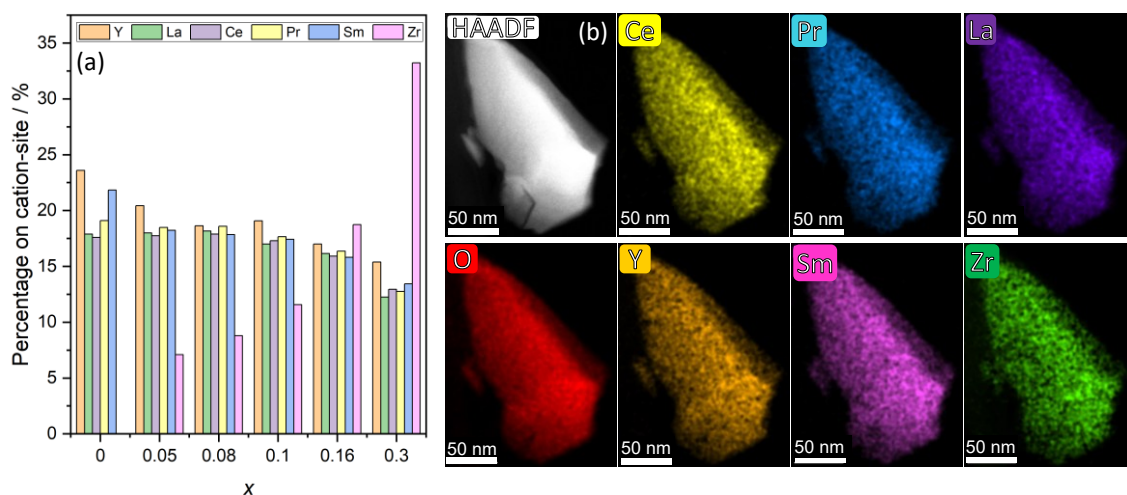
Figure 5-7 (a) Chemical composition of (Ce,La,Pr,Sm,Y)$_{1-x}$Zr$_x$O$_{2-\delta}$ with respect to x investigated in TEM (Nanometer scale). (b) Elemental distribution of Ce, La, Pr, Sm, La, Y and Zr in (Ce,La,Pr,Sm,Y)$_{0.92}$Zr$_{0.08}$O$_{2-\delta}$ collected using a transmission electron microscope (Nanometer scale).

The M edge from EELS data of cerium consists of two edges, M$_5$ at 883 eV and M$_4$ at 901 eV, as depicted in *Figure 5-8(a)*. The M-edge originates from the energy loss due to ionization of electrons in the 3d orbital. The position and intensity ratio of these edges are used as a good indicator of the oxidation state of the element. There is no change in the position and the intensity ratio of the M$_5$ and M$_4$ edges (I$_{M5}$/I$_{M4}$) of Ce in (Ce,La,Pr,Sm,Y)$_{1-x}$Zr$_x$O$_{2-\delta}$ with increasing Zr content, suggesting no change in the oxidation state of Ce with the addition of Zr into the system. The EELS data of standard CeO$_2$ taken from eels.info is included in *Figure 5-8(a)*. It can be seen that the positions of the M edges are very close to standard Ceria (CeO$_2$), and the values of the intensity ratio are the same. As a result, the EELS data suggests that the oxidation state of cerium in (Ce,La,Pr,Sm,Y)$_{1-x}$Zr$_x$O$_{2-\delta}$ is mostly +4 with possibilities of presence of +3 as it is observed in stoichiometric ceria. The M edge of Pr consists of two edges, M$_5$ – 931 eV and M$_4$ – 951 eV, which originates from energy loss due to ionization of the electron in 3d orbital. The EELS spectra of the M-edge of Pr for (Ce,La,Pr,Sm,Y)$_{1-x}$Zr$_x$O$_{2-\delta}$ are shown in *Figure 5-8(b)*. A slight shift in the edge positions towards the left is observed with increasing Zr content, indicating a slight decrease in the oxidation state of Pr with increasing Zr content. Furthermore, the intensity ratio of the M$_5$ and M$_4$ edge slightly increases with increasing Zr content, which further implies a slight decrease in the oxidation state of the Pr with increasing Zr. The M edge of Pr in Pr$_6$O$_{11}$ is added to *Figure 5-8(b)* along with the M edges of (Ce,La,Pr,Sm,Y)$_{1-x}$Zr$_x$O$_{2-\delta}$. The position of the M edge of Pr in Pr$_6$O$_{11}$ is higher than that of the M edges of (Ce,La,Pr,Sm,Y)$_{1-x}$Zr$_x$O$_{2-\delta}$, indicating that the oxidation state to be less

than +3.66 (33% - +3, 66.6% - +4) which is further backed by the higher I_{M5}/I_{M4} observed in $(Ce,La,Pr,Sm,Y)_{1-x}Zr_xO_{2-\delta}$. On closer inspection, in *Figure 5-8(b)*, a shoulder is present at the start of the M_4 edge, which is not present in the M_4 edge of Pr_6O_{11}. This shoulder arises due to the Pr^{+3} present in the system, clearly indicating the presence of Pr^{+3} in $(Ce,La,Pr,Sm,Y)_{1-x}Zr_xO_{2-\delta}$[56,118]. The effective oxidation state of Pr in $(Ce,La,Pr,Sm,Y)_{1-x}Zr_xO_{2-\delta}$ can be roughly estimated from I_{M5}/I_{M4} of $PrPO_4$ (Pr^{+3}) – 1.8 and Pr_6O_{11} $(Pr^{+3.66})$ – 1.1 available in the literature and by assuming a linear relation between I_{M5}/I_{M4} vs. effective oxidation state [118]. According to the presumed linear interpolation, illustrated in *Figure 5-8(c)*, the oxidation of Pr in $(Ce,La,Pr,Sm,Y)_{1-x}Zr_xO_{2-\delta}$ to varying between +3.4 (60% - +3, 40% - +4) and +3.5 (50% - +3, 50% - +4).
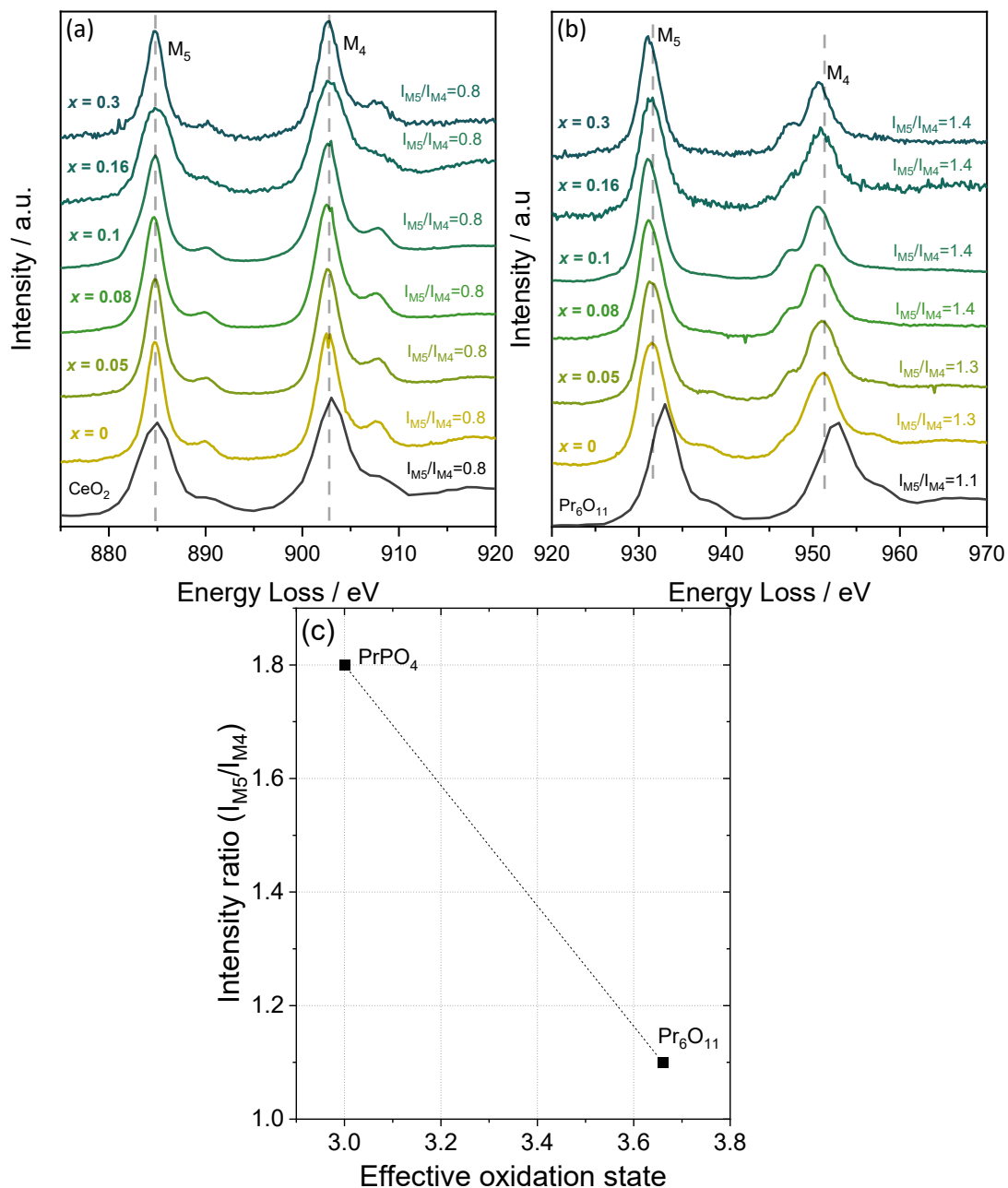
Figure 5-8 Electron energy loss spectra of $(Ce,La,Pr,Sm,Y)_{1-x}Zr_xO_{2-\delta}$ depicting the edges of (a) Ce - M edge (b) Pr – M edge. (c) The intensity ratio of M_5 and M_4 edge for different compositions with different oxidation states namely $PrPO_4$ (+3) and Pr_6O_{11} (+3-33%, +4- 66%, +3.7). The EELS data of CeO_2 and Pr_6O_{11} are from eels.info.

However, the presence of Pr^{+4} still needs to be confirmed. One possible way to identify the presence of Pr^{+4} in this system is by investigating the optical properties, as the presence of Pr^{+4} can significantly affect the band gap [44,56,119]. The optical band gaps were calculated by extracting the TAUC plots from UV-Vis spectra. The TAUC plots of $(Ce,La,Pr,Sm,Y)_{1-x}Zr_xO_{2-\delta}$ are presented in *Figure 5-9(a)*, and band gaps of less than 2 eV are observed. The band gap of

rare earth oxides is between the 5d orbital of the rare earth element and the oxygen 2p orbital, around 5 eV, as illustrated in *Figure 5-9(b)*. However, in the presence of Pr, the band gap is between Pr 4f and O 2p orbitals. A simple representation of the band structure of rare earth oxide due to the presence of Pr is presented in *Figure 5-9(b)*. The energy of the Pr 4f orbital depends on the oxidation state of Pr. Therefore, the band gap can change significantly depending on the oxidation state of Pr. It has been observed that the presence of Pr^{+4} reduces the band gap to below 2 eV [44,56,119]. Consequently, the band gaps of $(Ce,La,Pr,Sm,Y)_{1-x}Zr_xO_{2-\delta}$ indicate the presence of Pr^{+4}, as seen in *Figure 5-9*.
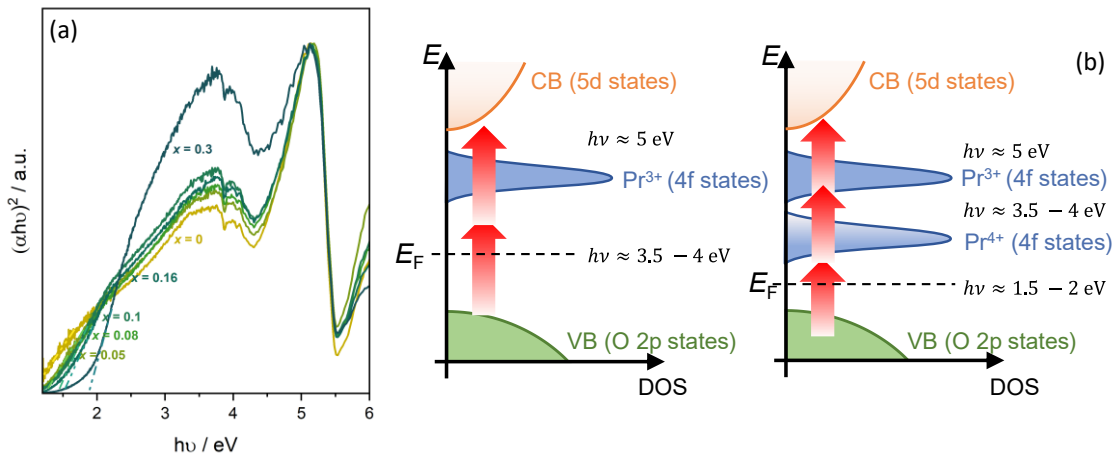
Figure 5-9 (a) TAUC plots extracted from the UV-vis spectra of $(Ce,La,Pr,Sm,Y)_{1-x}Zr_xO_{2-\delta}$. (b) Simple representation of band structure of Pr containing ceria systems.

5.1.3 Morphology and pellet density

The conduction mechanism in the grains and grain boundaries are different, with the grain boundaries usually having higher resistivity to ion migration [120,121]. Therefore, it is vital to investigate the grain size and morphology of the pellets to understand the conduction mechanisms. Some characteristic surface morphologies investigated using SEM are shown in *Figure 5-10*. The grain size of the pellets is in the order of micrometers. It can be observed in *Figure 5-10* that the grain size increases with increasing Zr content, reaching the largest grain size of approximately 5 microns at $x = 0.1$, and then decreases with further addition of Zr.
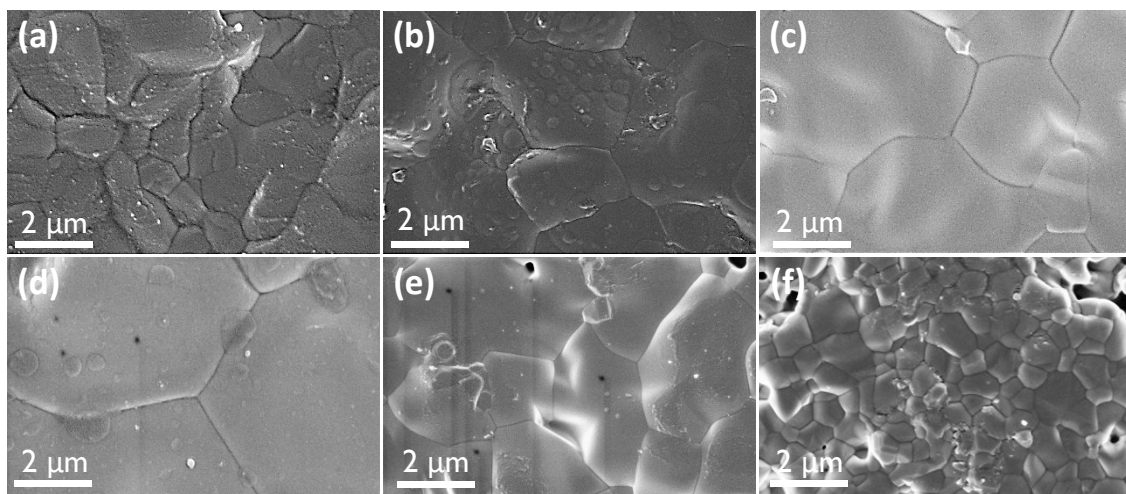
Figure 5-10 SEM micrographs of the surface of the pellets of (Ce,La,Pr,Sm,Y)$_{1-x}$Zr$_x$O$_{2-\delta}$ with (a) x = 0 (b) x = 0.05 (c) x = 0.08 (d) x = 0.1 (e) x = 0.16 (f) x = 0.3.

An important criterion for the anticipated use as oxygen ion conductors for solid electrolytes in solid oxide cells is high relative density with no open pores throughout the pellet to avoid intermixing of the gases between the electrodes. Therefore, the geometric relative density and relative density from Archimedes principle of the pellets were determined, summarized in *Table 5-2*. The geometric densities are around 85-95 %TD, and the Archimedes relative densities vary between 91-98 %TD (TD is theoretical density). The geometric densities account for both closed and open pores in the pellet. However, Archimedes method only accounts for the closed pores as the water can penetrate the open pores, thereby not contributing to the volume of water displaced by the pellet. As a result, the difference between the geometric and Archimedes density can be used as a good indicator of open porosity. The lowest difference is observed in *x* = 0.1 and *x* = 0.3, while the highest difference is observed for *x* = 0.05 and *x* = 0.16. Furthermore, the values of Archimedes relative densities of 91- 98% from *Table 5-2* suggest the presence of closed porosity in the pellets. The closed porosity can be observed in the cross-section images of the pellets in *Figure 5-11*. While the closed porosity is not relevant for gas intermixing, open and continuous pores are detrimental, and further optimization of the sintering procedure is needed to reduce the open porosity in some of these compositions. However, there is no indication that the open pores are continuous and connecting both sides of the solid electrolyte.

Table 5-2 The geometric and Archimedes relative densities along with the difference in relative densities of the (Ce,La,Pr,Sm,Y)$_{1-x}$Zr$_x$O$_{2-\delta}$

Composition	Geometric density (% TD)	Archimedes density (% TD)	Difference (% TD)
x = 0	95	98	3
x = 0.05	89	97	8
x = 0.08	87	92	5
x = 0.1	92	92	0
x = 0.16	86	93	7
x = 0.3	91	91	0
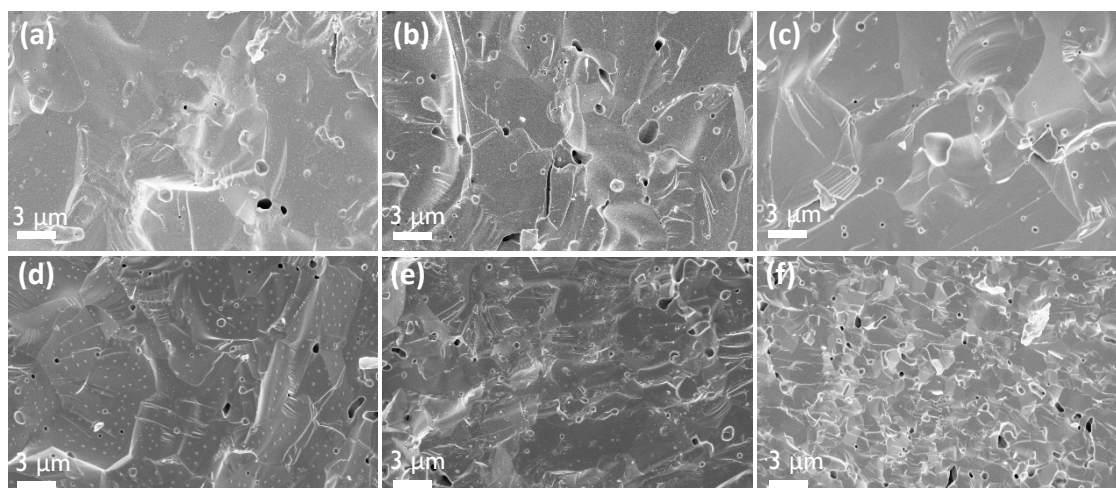
Figure 5-11 SEM micrographs of the cross section of the pellets of (Ce,La,Pr,Sm,Y)$_{1-x}$Zr$_x$O$_{2-\delta}$ with (a) x = 0 (b) x = 0.05 (c) x = 0.08 (d) x = 0.1 (e) x = 0.16 (f) x = 0.3.

5.1.4 Conductivity studies

The conductivity of the pellets was measured using Electrochemical Impedance Spectroscopy (EIS). Silver electrodes are coated on both sides of the pellets for EIS measurements. EIS was performed on (Ce,La,Pr,Sm,Y)$_{1-x}$Zr$_x$O$_{2-\delta}$ in a temperature range of 300 - 750 °C and in an oxygen partial pressure range of 5 mbar to 1 bar. The impedance spectra of (Ce,La,Pr,Sm,Y)$_{0.95}$Zr$_{0.05}$O$_{2-\delta}$ at 300 °C, 400 °C and 600 °C are displayed in *Figure 5-12*. It can be observed that the spectra consist of one big semicircle along with a small semicircle at very

low frequencies. A parallel equivalent circuit of capacitance and resistance can represent a semicircular EIS Nyquist plot. However, on closer inspection, the EIS data observed in *Figure 5-12* is a suppressed semicircle, typically fitted with a combination of constant phase element (CPE) and resistance[122]. As a result, the EIS spectra were fitted with the equivalent circuit consisting of two CPE//R elements in series to each other, as illustrated in *Figure 5-12(a)*. The resultant values of the CPE and resistances from the fit are shown in *Table 5-3*. The values of capacitance calculated from the fit results of the CPE elements using *Eq. 3-30* and respective resistance R suggest that the first big semicircles are in the order of capacitances observed in solid electrolytes, while the small semicircle at very low frequencies matches the capacitances of electrode/electrolyte interface [85,123]. The semicircle gradually vanishes with increasing temperature as observed in *Figure 5-12(b)* and *Figure 5-12(c)*. As a result, fitting the high temperature EIS spectra becomes complicated. Therefore, the total conductivities are considered. The intersection of the EIS data with Z_{Re}-axis at very low frequencies was considered to be the total resistance of the system.
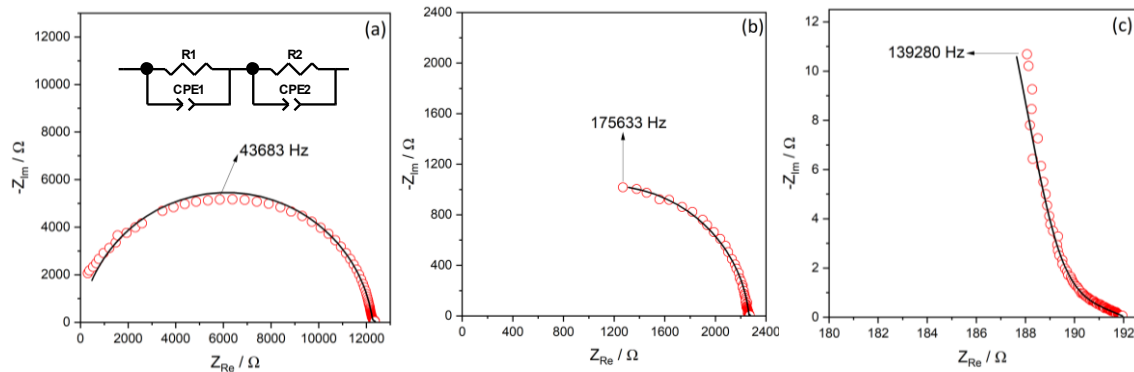
Figure 5-12 Electrochemical impedance spectroscopy of (Ce,La,Pr,Sm,Y)$_{0.95}$Zr$_{0.05}$O$_{2-\delta}$ along with fits (a) 300 °C (b) 400 °C (c) 600 °C.

Table 5-3 *The CPE parameters, resistances, capacitances of the fit of impedance spectra of x = 0.05 at 300, 400, 600 °C from Figure 5-12. The table includes the contributor corresponding to the element.*

Comp	Values	300 ˚C	400 ˚C	600 ˚C	Contributor
1	$Q1(F/s^{(1-\alpha)})$	$8.63 \cdot 10^{-10}$	$8.23 \cdot 10^{-10}$		Electrolyte
	$\alpha1(°)$	0.925	0.94		
	R1(ohm)	12225	2264	190.4	
	C(F)	$3.41 \cdot 10^{-10}$	$3.55 \cdot 10^{-10}$		
2	$Q2(F/s^{(1-\alpha)})$	$2.9 \cdot 10^{-5}$	$4.4 \cdot 10^{-5}$	$6.21 \cdot 10^{-3}$	Electrode/Electrolyte interface
	$\alpha2(°)$	0.806	1	0.615	
	R2(ohm)	136	25.87	1.4	
	C(F)	$7.46 \cdot 10^{-6}$	$4.4 \cdot 10^{-5}$	$3.18 \cdot 10^{-4}$	

The conductivities of the $(Ce,La,Pr,Sm,Y)_{1-x}Zr_xO_{2-\delta}$ at different temperatures can be seen in Figure 5-13. Arrhenius plot of the conductivity data can be fitted with a single straight line as depicted in *Figure 5-13(a)*. The activation energies derived from the fits are in the legend of the Arrhenius plot in *Figure 5-13(a)*. The activation energies are in the range of 0.64 - 0.71 eV. The conductivity of $(Ce,La,Pr,Sm,Y)_{1-x}Zr_xO_{2-\delta}$ increases initially with the addition of Zr, followed by a maximum at $x = 0.05$, after which the conductivity decreases with further addition of Zr. In traditional oxygen ion conductors like YSZ, the conductivity increases with the addition of the dopant, reaching a maximum at a certain concentration, and a reduction is observed with further addition of the dopant[5,116,120,124–126]. The observed decrease in conductivity in these systems may be attributed to complex defect interactions and grain sizes. A detailed discussion of these defect interactions will follow in the next section of this chapter. Additionally, it is important to note that the oxygen-ion conductivity is influenced by grain size, as grain boundaries in many cases contribute to higher resistance[121]. Consequently, the conductivities of samples with compositions x = 0.16 and x = 0.3 are lower than those of the other compositions due to their smaller grain sizes.
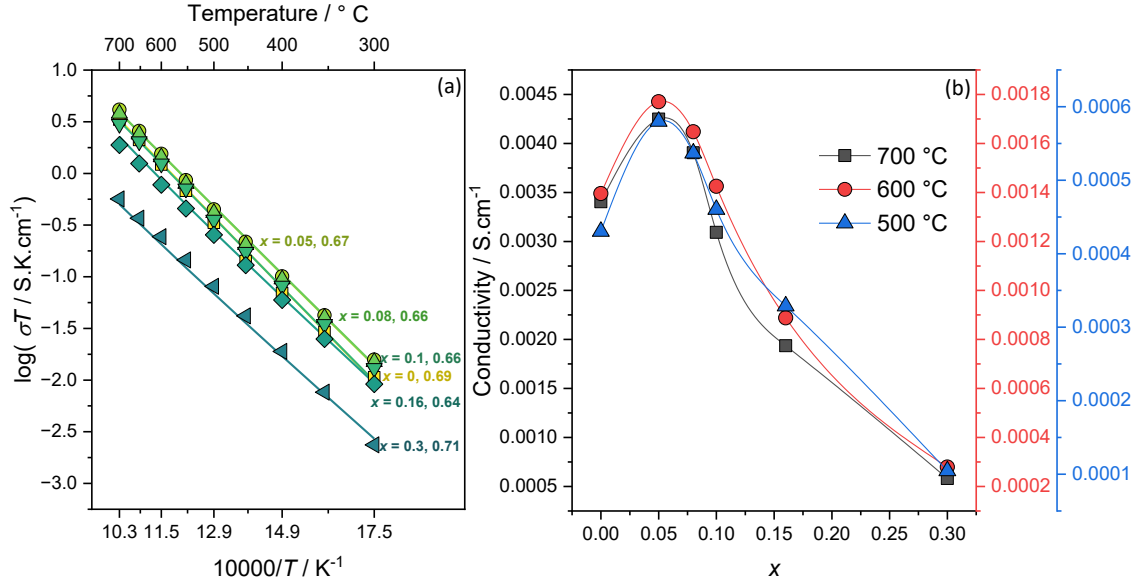
Figure 5-13 (a) Arrhenius plot of the total conductivities of (Ce,La,Pr,Sm,Y)$_{1-x}$Zr$_x$O$_{2-\delta}$ along with the activation energies (eV) extracted from Eq. 2-19.   (b) Conductivity of (Ce,La,Pr,Sm,Y)$_{1-x}$Zr$_x$O$_{2-\delta}$ vs. Zr content (x) at 500, 600 and 700 °C.

The conductivities of (Ce,La,Pr,Sm,Y)$_{1-x}$Zr$_x$O$_{2-\delta}$ are measured at different partial pressures of oxygen ($p(O_2)$) and temperatures, as shown in *Figure 5-14*. The changes in conductivity with $p(O_2)$ are minimal in (Ce,La,Pr,Sm,Y)$_{1-x}$Zr$_x$O$_{2-\delta}$ at various temperatures, with slopes less than 1/12, which is highly desirable for an oxygen ion conductor. On closer inspection, the conductivity slightly increases with decreasing $p(O_2)$ for $x = 0$, $x = 0.05$, $x = 0.08$ and $x = 0.1$. Whereas, a decreasing trend is observed with $p(O_2)$ for $x = 0.16$, $x = 0.3$. The change in conductivity is due to the multivalent elements, Ce and Pr. Therefore, to fully comprehend the conduction mechanisms in (Ce,La,Pr,Sm,Y)$_{1-x}$Zr$_x$O$_{2-\delta}$, it is necessary to understand the defect interaction happening in the Pr doped ceria systems. Consequently, the defect interactions in Pr doped ceria will be discussed in the following subsection.
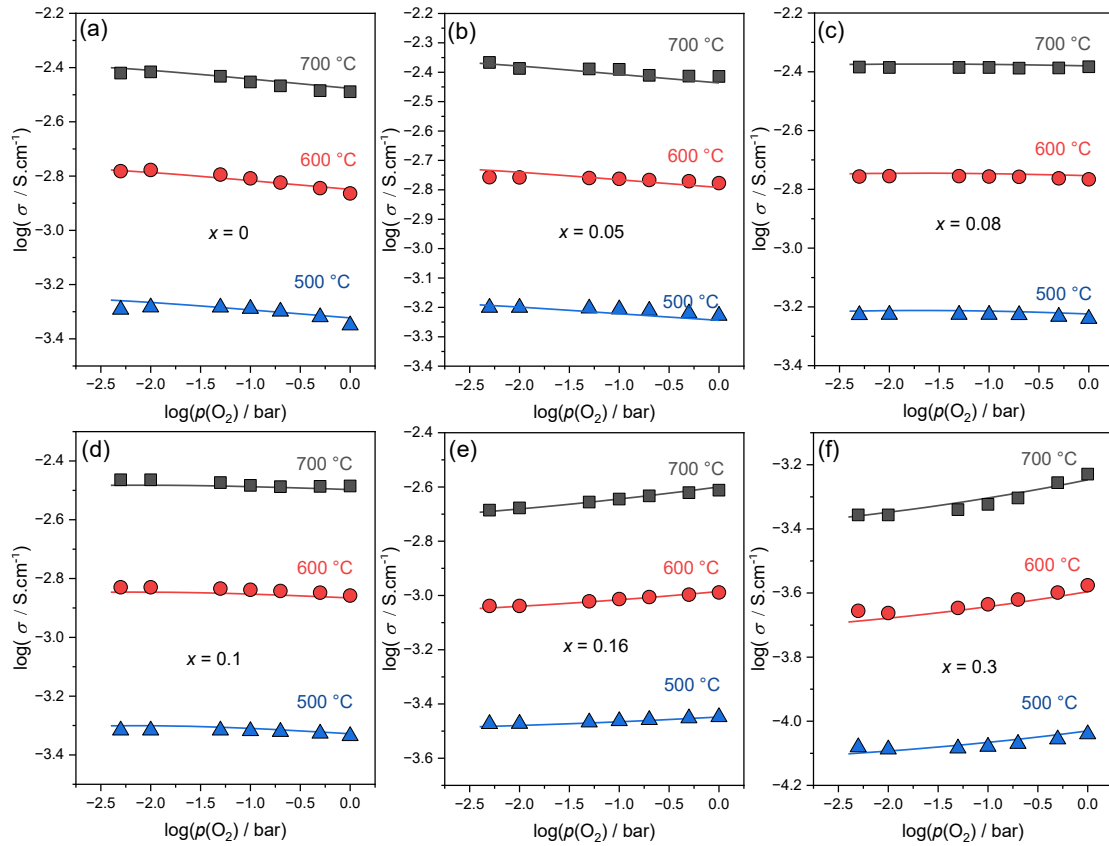
Figure 5-14 Conductivity vs partial pressure of oxygen of (Ce,La,Pr,Sm,Y)$_{1-x}$Zr$_x$O$_{2-\delta}$ (a) x = 0 (b) x = 0.05 (c) x = 0.08 (d) x = 0.1 (e) x = 0.16 and (f) x = 0.3.

5.1.5 Defect interactions in Pr doped Ceria

Pr and Ce are multivalent elements that can exhibit both +3 and +4 oxidation states. The multivalent elements like Ce, and Pr assist the polaron in hopping through the lattice, resulting in electronic conduction in the system. The changes in the oxidation state of Pr occur in oxidizing atmospheres ($10^{-5} – 10^0$ bar), whereas the changes in the oxidation states of Ce happen in reducing conditions ($10^{-30} – 10^{-20}$ bar)[13–22]. The environments investigated in this study are the oxidizing atmospheres ($10^{-5} – 10^0$ bar), and the EELS data indicate that the oxidation state of Ce is +4. There will be no changes in the oxidation state of Ce at current measurement conditions. Therefore, the effect of Ce on electronic conduction in the measured conditions is non-existent and not considered. However, the oxidation state of Pr changes in the measured conditions, and the observed conductivity changes are a consequence of the change in the oxidation state of Pr. The changes in oxidation state of Pr with the partial pressure of oxygen in Kröger-Vink notation can be written as

$$2Pr'_R + V_O^{\bullet\bullet} + \frac{1}{2}O_2 \rightleftharpoons 2Pr_R^\times + O_O^\times \qquad \textit{Reaction 5-1}$$
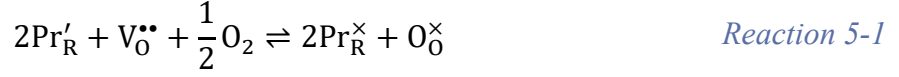
where Pr'_R is Pr^{+3}, $V_O^{\bullet\bullet}$ is the oxygen vacancy, $Pr_R^\times$ is Pr^{+4} and $O_O^\times$ is lattice oxygen. The equilibrium constant of *Reaction 5-1* is

$$K_1 = \frac{[Pr_R^\times]^2 \times [O_O^\times]}{[Pr'_R]^2 \times [V_O^{\bullet\bullet}] \times p(O_2)^{1/2}} \qquad \textit{Eq. 5-1}$$

The oxygen vacancies in fluorite structured oxides are introduced by +3 cations in the lattice. Consequently, the concentration of oxygen vacancies is dependent on the concentration of Pr in Pr doped ceria as

$$[V_O^{\bullet\bullet}] = 2[Pr'_R] \qquad \textit{Eq. 5-2}$$

Replacing $[V_O^{\bullet\bullet}]$ from *Eq. 5-1* to *Eq. 5-2* along with further modifications and considering the Brouwer approximation which considers $Pr_R^\times$ and $O_O^\times$ to be constant then *Eq. 5-1* can be changed to

$$[Pr'_R]^2 \times 2[Pr'_R] = \frac{constant}{K_1 \times p(O_2)^{1/2}} \qquad \textit{Eq. 5-3}$$

$$[Pr'_R] \propto p(O_2)^{-\frac{1}{6}} \qquad \textit{Eq. 5-4}$$

From *Eq. 5-4*, the concentration of Pr^{+3} is proportional to $p(O_2)^{-\frac{1}{6}}$. Furthermore, the electronic conduction depends on $[Pr'_R]$ with highest polaron propagation happening when $[Pr'_R]$ is 50% of Pr. As a result, the electronic conduction due to polaron hopping can be written as

$$\sigma_{elec} = e[Pr_R]x_{Pr}^{3+}(1 - x_{Pr}^{3+})\frac{\mu_{pol}^0}{T}\exp\left(-\frac{\Delta H_{mig}}{k_B T}\right) \qquad \textit{Eq. 5-5}$$

where x_{Pr}^{3+} is the mole fraction of Pr^{+3}, ΔH_{mig} is migration enthalpy for polaron hopping. The mole fraction of Pr^{+3} is dependent on the $p(O_2)$. Consequently, it has been observed in Pr doped ceria that an n-type conduction with partial pressure dependence of $p(O_2)^{-1/6}$ when $x_{Pr}^{3+}<0.5$ and a p-type dependence with partial pressure dependence of $p(O_2)^{1/6}$ when $x_{Pr}^{3+}>0.5$ [17,18,21,22,110,112,127]. The resultant polaron conduction can be written as

when $x_{Pr}^{3+} < 0.5$,

$$\sigma_{elec}^n = \sigma_{pol}^n \times p(O_2)^{-\frac{1}{6}} = \frac{\sigma_o^{n-pol}}{T}\exp\left(-\frac{E_A^{pol}}{k_B T}\right) p(O_2)^{-\frac{1}{6}} \qquad \textit{Eq. 5-6}$$

when $x_{\text{Pr}}^{3+} > 0.5$,

$$\sigma_{elec}^{p} = \sigma_{pol}^{p} \times p(O_2)^{\frac{1}{6}} = \frac{\sigma_{o}^{\text{p-pol}}}{T} \exp\left(-\frac{E_A^{\text{pol}}}{k_B T}\right) p(O_2)^{\frac{1}{6}} \qquad \text{Eq. 5-7}$$

here σ_{elec}^{n} is the n-type electronic conduction, σ_{elec}^{p} is the p-type electronic conduction observed. σ_{pol}^{n} and σ_{pol}^{p} are the oxygen partial pressure independent conductivity at a given temperature T for p-type and n-type conduction. The activation energy for polaron migration via Pr for a given material system is independent of the Pr^{+3} but is rather dependent on the material system. As a result, the activation energies are considered the same for both cases. The p-type conduction and n-type conduction happen in the same material system but at different oxygen partial pressures. Consequently, both conditions can be combined into a single electrical model in series or parallel. The electronic conductivity resulting from a combination in series or parallel can be written as

In parallel combination,

$$\sigma_{\text{elec}} = \sigma_{elec}^{n} + \sigma_{elec}^{p} \qquad \text{Eq. 5-8}$$

$$\sigma_{\text{elec}} = \left(\frac{\sigma_{o}^{\text{n-pol}}}{T} p(O_2)^{-\frac{1}{6}} + \frac{\sigma_{o}^{\text{p-pol}}}{T} p(O_2)^{\frac{1}{6}}\right) \exp\left(-\frac{E_A^{\text{pol}}}{k_B T}\right) \qquad \text{Eq. 5-9}$$

In serial combination,

$$\frac{1}{\sigma_{\text{elec}}} = \frac{1}{\sigma_{elec}^{n}} + \frac{1}{\sigma_{elec}^{p}} \qquad \text{Eq. 5-10}$$

$$\sigma_{\text{elec}} = \left(\frac{\sigma_{o}^{\text{n-pol}} \times \sigma_{o}^{\text{p-pol}}}{\sigma_{o}^{\text{n-pol}} p(O_2)^{-\frac{1}{6}} + \sigma_{o}^{\text{p-pol}} p(O_2)^{\frac{1}{6}}}\right) \frac{\exp\left(-\frac{E_A^{\text{pol}}}{k_B T}\right)}{T} \qquad \text{Eq. 5-11}$$

The total conductivity of a system is the sum of ionic and electronic conductivity of the system which can be written as

$$\sigma_{\text{total}} = \sigma_{\text{ion}} + \sigma_{\text{elec}} \qquad \text{Eq. 5-12}$$

Applying the *Eq. 2-19* on the ionic conductivity as well as assuming the ionic conductivity to be independent of the partial pressure of oxygen then the ionic conductivity can be written as

$$\sigma_{ion} = \frac{\sigma_o^{ion}}{T} \exp\left(-\frac{E_A^{ion}}{k_B T}\right) \qquad \text{Eq. 5-13}$$

where σ_o^{ion} is the pre-factor of the ionic conductivity and E_A^{ion} is the activation energy for ion migration. Replacing the ionic conductivity and electronic conductivity from *Eq. 5-9*, *Eq. 5-11* and *Eq. 5-13* into *Eq. 5-12* for two different electrical models for electronic conductivity gives the total conductivity as follows for the two cases

In parallel combination of electronic conductivity,

$$\sigma_{total} = \frac{\sigma_o^{ion}}{T} \exp\left(-\frac{E_A^{ion}}{k_B T}\right) + \left(\frac{\sigma_o^{n-pol}}{T} p(O_2)^{-\frac{1}{6}} + \frac{\sigma_o^{p-pol}}{T} p(O_2)^{\frac{1}{6}}\right) \exp\left(-\frac{E_A^{pol}}{k_B T}\right) \qquad \text{Eq. 5-14}$$

In serial combination of electronic conductivity,

$$\sigma_{total} = \frac{\sigma_o^{ion}}{T} \exp\left(-\frac{E_A^{ion}}{k_B T}\right) + \left(\frac{\sigma_o^{n-pol} \times \sigma_o^{p-pol}}{\sigma_o^{n-pol} p(O_2)^{-\frac{1}{6}} + \sigma_o^{p-pol} p(O_2)^{\frac{1}{6}}}\right) \frac{\exp\left(-\frac{E_A^{pol}}{k_B T}\right)}{T} \qquad \text{Eq. 5-15}$$

5.1.6 Ionic and electronic conduction in $(Ce,La,Pr,Sm,Y)_{1-x}Zr_xO_{2-\delta}$

The conductivity data measured at different temperatures and various oxygen partial pressures is fitted with the two possible models as per *Eq. 5-14* and *Eq. 5-15*, as shown in *Figure 5-15* and *Figure 5-16*, both models provide a good representation of the experimental data. However, for $x = 0$, $x = 0.05$, $x = 0.08$, and $x = 0.1$, it can be observed that the fits using the model of the parallel combination of the electronic conductivities (*Eq. 5-14*) in *Figure 5-15* show a parabolic curvature, whereas the fits corresponding to the model of the serial combination of electronic conductivities (*Eq. 5-14*) in *Figure 5-16* show an inverted parabolic curvature. On closer inspection, the data follows an inverted parabolic trend, suggesting the serial model is more suitable for these samples. Nevertheless, both models accurately fit the conductivity values of $x = 0.16$ and $x = 0.3$. The electronic and ionic conductivities extracted from both fits are comparable with slight differences as illustrated in *Figure 5-17*. The difference between both models is observed at $x = 0.3$. The parallel combination model results in higher electronic conduction, and the serial combination results in a lower electronic conduction. Nevertheless, both models suggest a predominant ionic conduction in these systems, as observed in *Figure 5-17*. The serial combination results in an inverted parabola and results in a better-suited model for the conductivities of all of the samples. Consequently, the

following discussions will consider the pre-factors, activation energies, and conductivities calculated from the serial combination.
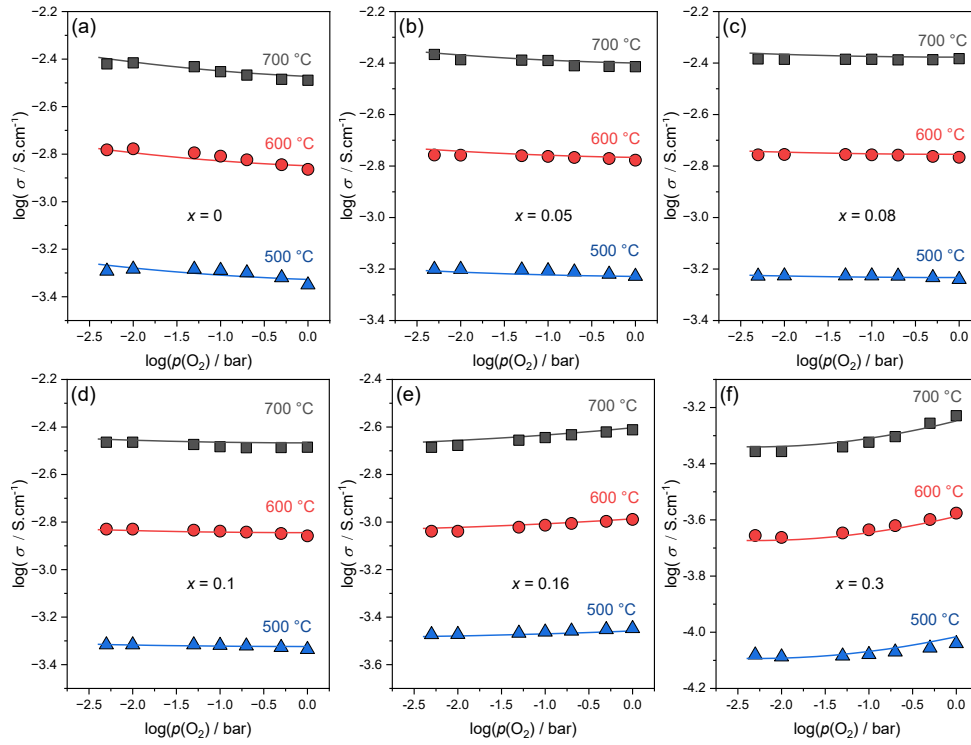
Figure 5-15 Conductivity vs. partial pressure of oxygen of (Ce,La,Pr,Sm,Y)$_{1-x}$Zr$_x$O$_{2-\delta}$ (a) x = 0 (b) x = 0.05 (c) x = 0.08 (d) x = 0.1 (e) x = 0.16 and (f) x = 0.3 fitted with Eq. 5-14 (parallel).
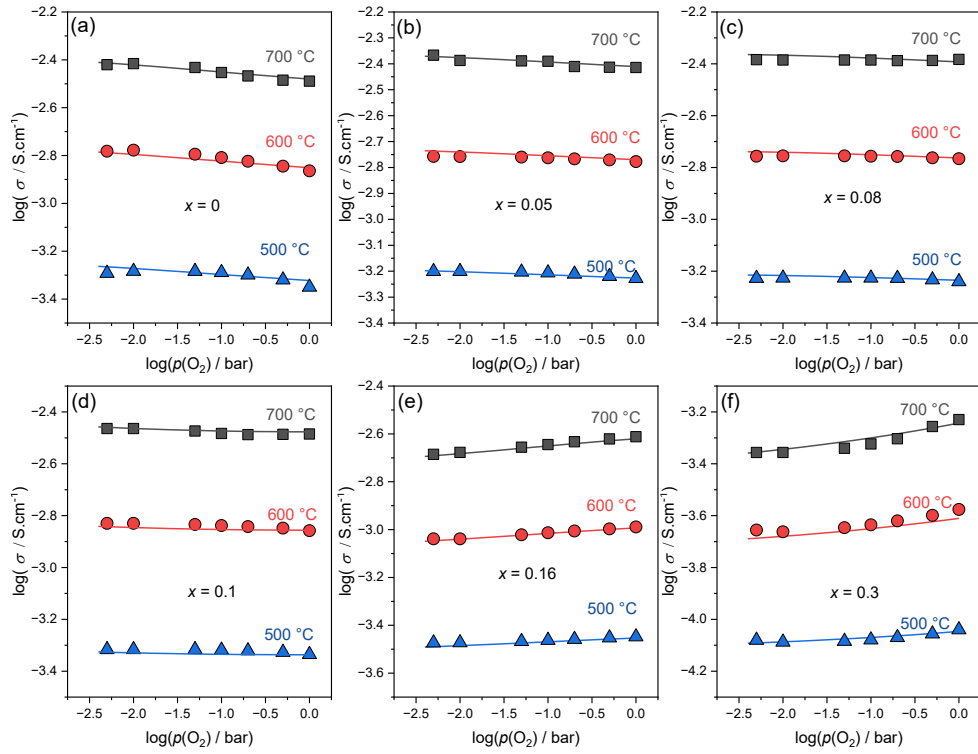
Figure 5-16 Conductivity vs partial pressure of oxygen of (Ce,La,Pr,Sm,Y)$_{1-x}$Zr$_x$O$_{2-\delta}$ (a) x = 0 (b) x = 0.05 (c) x = 0.08 (d) x = 0.1 (e) x = 0.16 and (f) x = 0.3 fitted with Eq. 5-15 (serial).
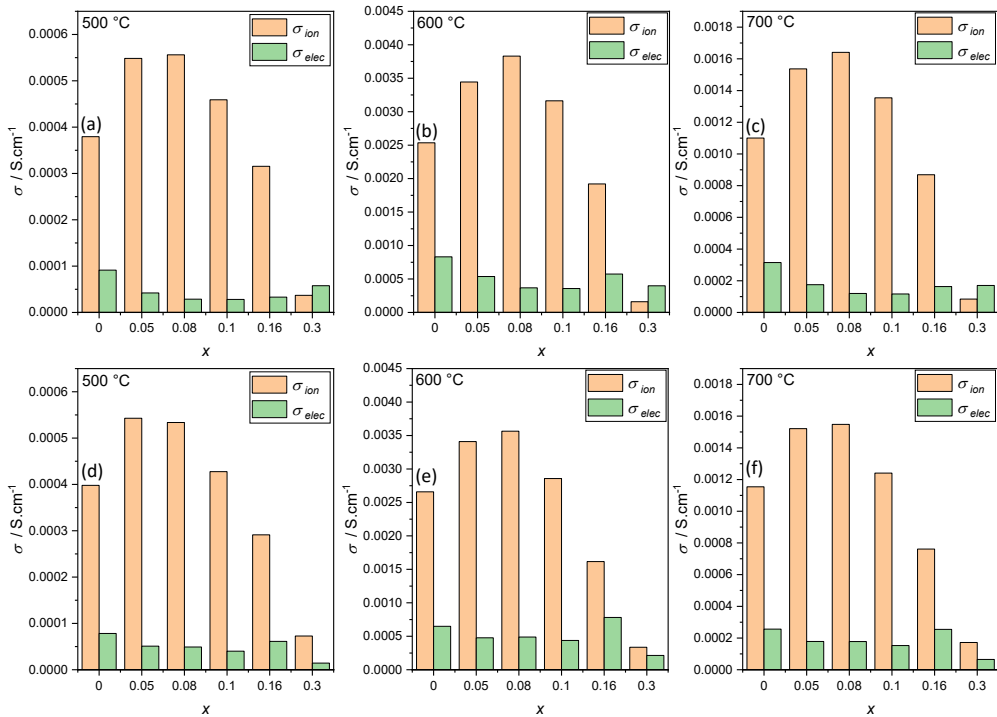
Figure 5-17 The ionic and electronic conductivities of (Ce,La,Pr,Sm,Y)$_{1-x}$ Zr$_x$O$_{2-\delta}$ with respect to x calculated from Eq. 5-14 (parallel) at temperatures of (a) 500 °C, (b) 600 °C, and (c) 700 °C as well as the ionic and electronic conductivities calculated from Eq. 5-15 (serial) at temperatures of (d) 500 °C, (e) 600 °C, and (f) 700 °C.

The dominant contribution from the ionic conduction to the total conduction is demonstrated in *Figure 5-17* and in *Figure 5-18(a)*. The electronic component in *Figure 5-18(a)* is in accordance with the expected changes in electronic conductivity from the defect chemistry of Pr doped ceria depicted in *Eq. 5-6* and *Eq. 5-7*. The maximum of the electronic conductivity is achieved when the content of Pr^{+3} in total Pr reaches 50% as seen the *Figure 5-18(a)*. The total calculated conductivity extracted by fitting the experimental data of $(Ce,La,Pr,Sm,Y)_{1-x}Zr_xO_{2-\delta}$ is extrapolated until $log(p(O_2)) = -8$ to predict the changes in conductivity with partial pressure of oxygen at 700 °C. The ionic conductivities are assumed to be constant over the extrapolated regions. The changes in conductivity are not significant in the cases of $x = 0.05$, 0.08 and 0.1 as observed in the predicted total conductivities in *Figure 5-18(b)*. However, the conductivities change over a few orders of magnitude for $x = 0$, 0.16 and 0.3, especially in $x = 0.16$ and 0.3. The predicted ionic conductivities in *Figure 5-18(c)* of $(Ce,La,Pr,Sm,Y)_{1-x}Zr_xO_{2-\delta}$ follows the same conductivity trend observed in *Figure 5-13(b)* and *Figure 5-17*. Furthermore, the ionic conductivity in ceria-based oxides is hugely dependent on the ionic radii of the dopant cations [124]. The highest ionic conductivities are observed in Sm doped CeO_2 in which Sm has an ionic radius of 1.079 Å[124]. The ionic conductivity decreases as the dopant's ionic radius deviates from 1.079 Å[124]. To understand the ionic conductivity trend in the high entropy oxides, all the elements other than Ce are assumed to be dopants in a Ce lattice. The effective ionic radii of the elements are calculated according to their concentrations and ionic radii (coordination number-8) [128]. These effective ionic radii are subtracted from 1.079 Å to give the difference in the ionic radii and the absolute value of the difference is plotted with respect to Zr content along with the ionic conductivity at 700 °C in *Figure 5-19*. It can be observed that the ionic conductivity is highest in $x = 0.08$ when the difference is close to 0. Furthermore, the absolute value of the difference follows the inversing trend of the conductivity. Therefore, the conductivity trend observed here is a consequence of the effective ionic radii of the dopant changing with the addition of Zr which reaches close to 1.079 Å at $x = 0.08$ at which the maximum conductivities are observed in ceria-based oxides and subsequently in high entropy oxide as well.

Unlike the total and ionic conductivity, the electronic conductivity is extrapolated over the range of $log(p(O_2)) = -8$ to $log(p(O_2)) = 4$ to understand the electronic conduction mechanism as well as the significance of the electronic conduction in the predicted range. The electronic conduction parabola observed in *Figure 5-18(d)* is observed to shift towards right (high oxygen partial pressure regions) with increasing Zr content. The shift in the electronic conduction towards the right signifies a difference in oxidation states of Pr in

(Ce,La,Pr,Sm,Y)$_{1-x}$Zr$_x$O$_{2-\delta}$ at an oxygen partial pressure of 210 mbar(log(p(O$_2$)) = -0.6). The conduction maximum for x = 0, 0.05, 0.08 and 0.1 is left to ambient pressure (log(p(O$_2$)) = -0.6) suggesting the content of Pr^{+3} to be less than 50%. Conversely, the conductivity maximum for x = 0.16, and 0.3 is right to ambient pressure (log(p(O$_2$)) = -0.6) suggesting the content of Pr^{+3} to be greater than 50%. The oxidation states predicted from the conductivity are further validated from the EELS data from *Figure 5-8*, which suggests that the content of Pr^{+3} is 40-50% of Pr content. Along with the shift in the parabola towards right, a decrease in the electronic conductivity is recorded with increasing Zr content in *Figure 5-18(d)*. The decrease in electronic conductivity can be a result of the decreasing concentrations of multivalent cations (Ce, Pr) in the systems with addition of Zr. Furthermore, in multicomponent systems like high entropy materials, the probability of finding a multivalent cation adjacent to a multivalent cation is lower when compared to traditional single or bi-component systems. This can limit the polaron propagation through the lattice. Consequently, adding an additional element (Zr) to a multicomponent system can further reduce the hopping probability of the polaron through the lattice and thereby increasing the activation energy for electron transport. Consequently, an increase in activation energy in the activation energies of the electronic conduction with increasing Zr content has been observed as seen in *Figure 5-20(a)*.
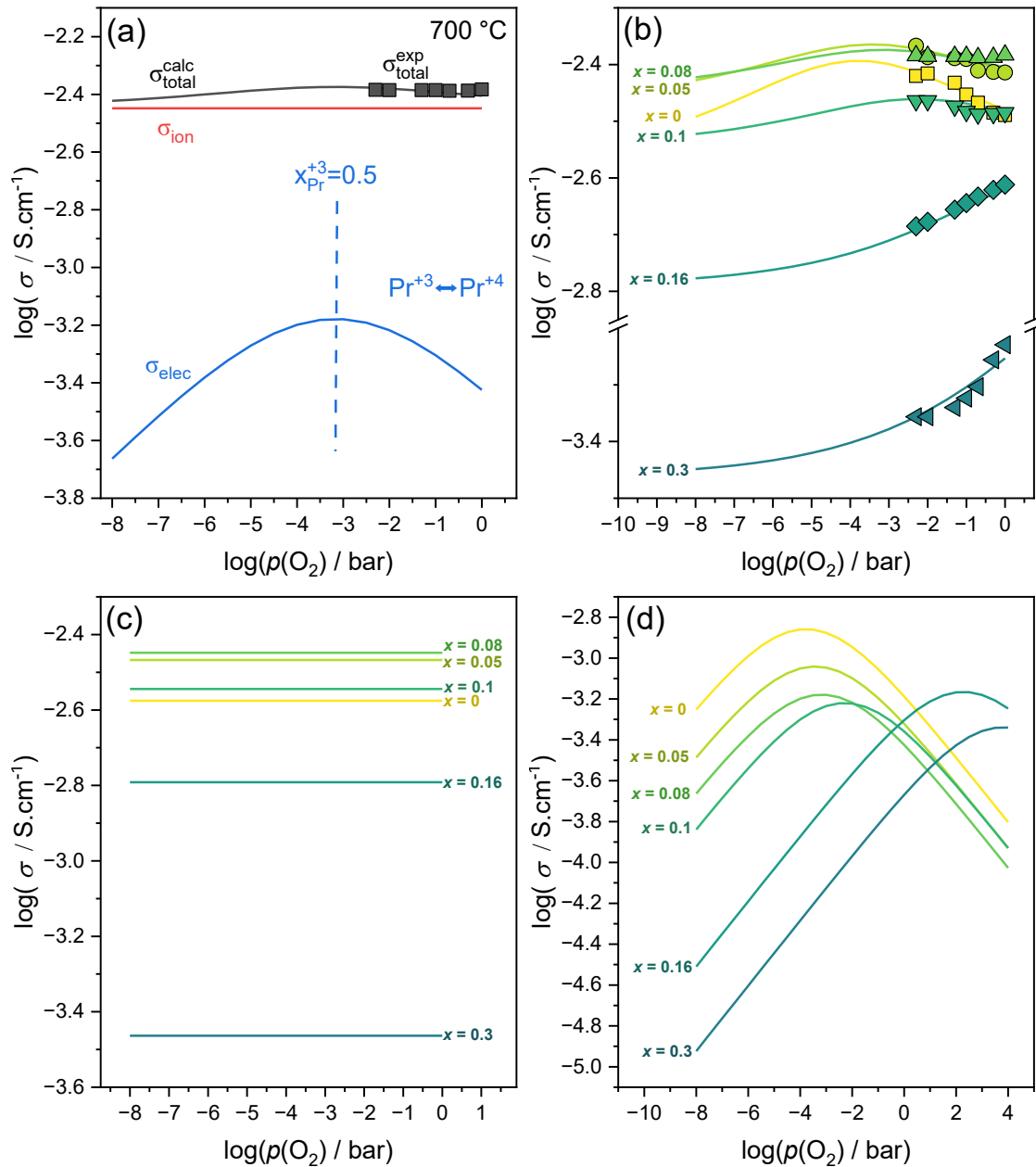
Figure 5-18 (a) Pressure dependence of conductivity depicting the contributions from ionic and electronic conduction to the total conduction calculated from Eq. 5-15 for $(Ce,La,Pr,Sm,Y)_{0.92}Zr_{0.08}O_{2-\delta}$ at a temperature of 700 °C. (b) Pressure dependence of total conductivity along with the calculated total conductivity from Eq. 5-15 for $(Ce,La,Pr,Sm,Y)_{1-x}Zr_{x}O_{2-\delta}$ at a temperature of 700 °C. (c) The calculated ionic conduction of $(Ce,La,Pr,Sm,Y)_{1-x}Zr_{x}O_{2-\delta}$ at a temperature of 700 °C. (d) The calculated electronic conduction of $(Ce,La,Pr,Sm,Y)_{1-x}Zr_{x}O_{2-\delta}$ at a temperature of 700 °C.
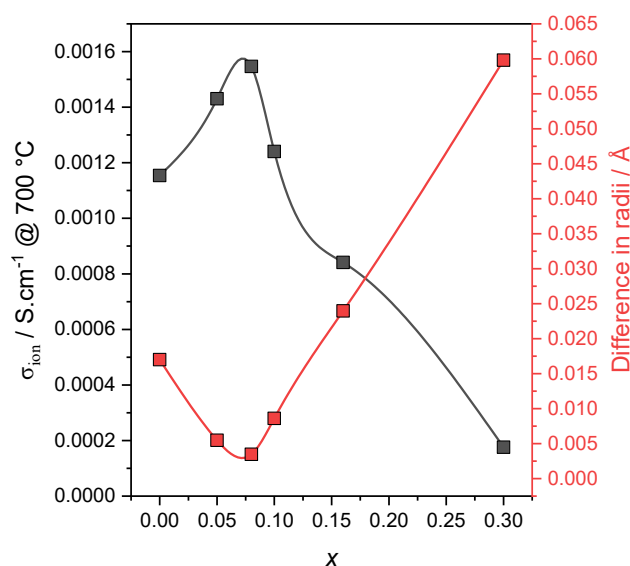
Figure 5-19 The ionic conductivity of (Ce,La,Pr,Sm,Y)$_{1-x}$Zr$_x$O$_{2-\delta}$ with Zr content at 700 °C along with the difference in ionic radii (effective ionic radii – 1.079Å).

The transference numbers of (Ce,La,Pr,Sm,Y)$_{1-x}$Zr$_x$O$_{2-\delta}$ at 500 °C, 600 °C, 700 °C and at 1 bar are presented in *Figure 5-20(b)*. The transference number increases with increasing Zr and reaches a maximum around $x = 0.08$. However, the transference number decreases with further addition of Zr even though the electronic conductivity with Zr is decreasing with addition of Zr. On closer inspection of the ionic and electronic conductivities, it can be seen that the ionic conductivities decrease over a magnitude of 10^{-1} and the electronic conductivity at 1 bar oxygen partial pressure decreases over a magnitude of $10^{-0.4}$. As a result, due to stronger decrease in ionic conductivity compared to the electronic conductivity at 1 bar, a decrease in transference numbers is observed at higher concentrations of Zr at 1 bar oxygen partial pressure.
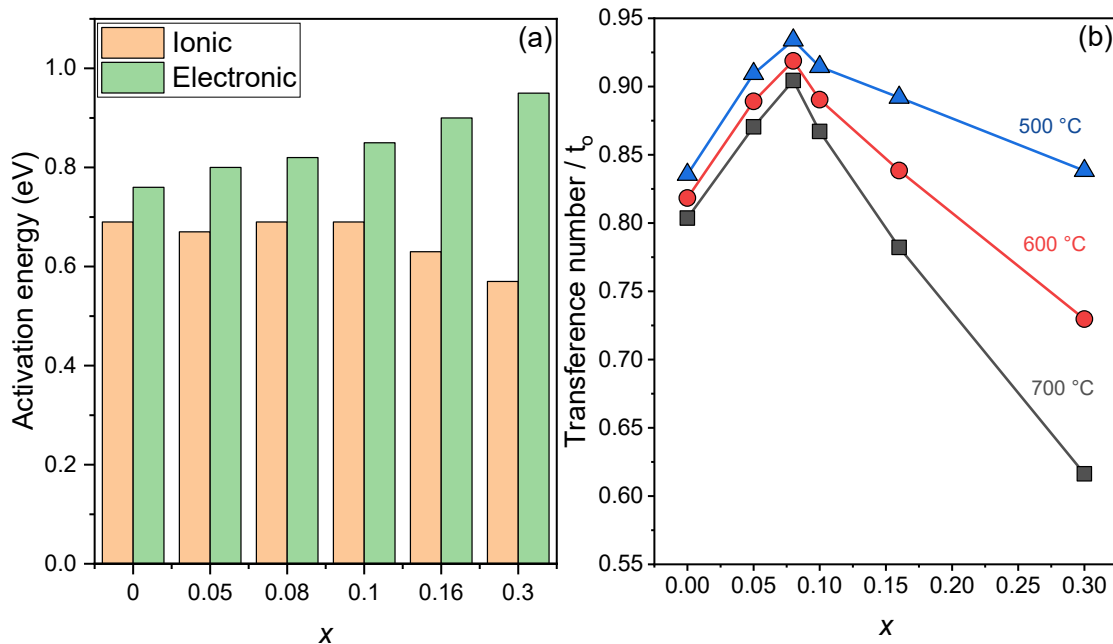
Figure 5-20 (a) The activation energies of ionic, electronic conduction for $(Ce,La,Pr,Sm,Y)_{1-x}Zr_xO_{2-\delta}$ estimated from the Eq. 5-15. (b) Transference number of $(Ce,La,Pr,Sm,Y)_{1-x}Zr_xO_{2-\delta}$ at 1 bar oxygen pressure estimated from the Eq. 5-15.

In the current study, $(Ce,La,Pr,Sm,Y)_{0.92}Zr_{0.08}O_{2-\delta}$ has the highest conductivity and predominant ionic conduction. Therefore, the conductivity of this HEO is compared to $Y_{0.08}Zr_{0.92}O_{1.96}$ (YSZ), a state-of-the-art oxygen ion conductor and the comparison is shown in *Figure 5-21*. The conductivity of $(Ce,La,Pr,Sm,Y)_{0.92}Zr_{0.08}O_{2-\delta}$ is higher than YSZ at lower temperatures along with lower activation energies. The conductivity of the fluorite structured ceria-based oxides is optimal when the dopant ionic radii closely match the ionic radii of the cerium ion [124]. The conductivity of the current high entropy oxide can be increased by strategically replacing bigger cations like La with a cation like Gd, which has an ionic radius closer to the cerium cation. Therefore, fluorite structured ceria-based high entropy oxides have the potential of having better ionic conductivities than yttria stabilized zirconia and lower electronic conductivities than traditionally doped ceria.
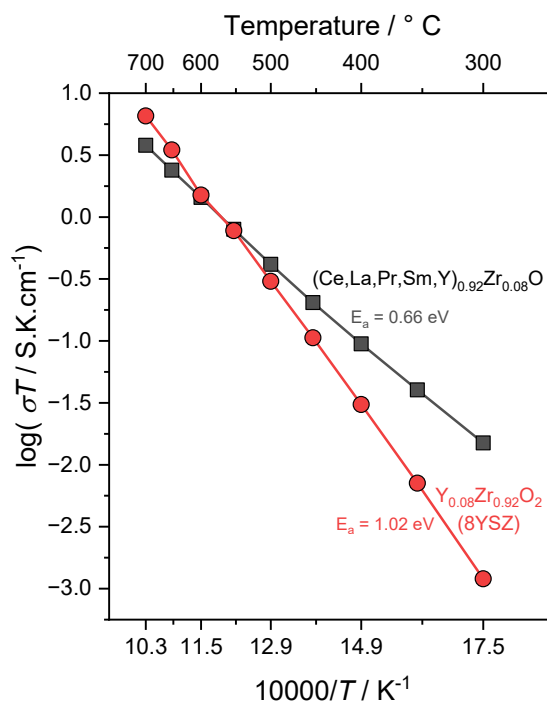
Figure 5-21 Comparison of conductivities with temperature of $(Ce,La,Pr,Sm,Y)_{0.92}Zr_{0.08}O_{2-\delta}$ and $Y_{0.08}Zr_{0.92}O_2$.

5.1.7 Conclusion and summary

In this study, Zr is added to $(Ce,La,Pr,Sm,Y)O_{2-\delta}$ to stabilize the fluorite structure. Powders of $(Ce,La,Pr,Sm,Y)_{1-x}Zr_xO_{2-\delta}$ were synthesized by ball milling and then consolidated into pellets via conventional sintering. Powders synthesized via ball milling exhibit a fluorite structure. The pellets consolidated by conventional sintering are heat treated at 1400 °C for 12 h, which resulted in a bixbyite structure for x = 0, 0.05, and 0.08. Nevertheless, further addition of Zr (x = 0.1, 0.16) resulted in fluorite structure even while heat treated at 1400 °C. However, at high concentrations of Zr (x = 0.3), the structure changes to pyrochlore due to the ordering of added Zr cations. Furthermore, local ordering on the nanometer scale of both fluorite and bixbyite structures has been observed for x = 0, 0.05, and 0.08. This local ordering into two phases disappears for x = 0.1, 0.16 but reappears at x = 0.3 as the local ordering of fluorite and pyrochlore structures. The chemical compositions are close to the nominal values, with slight changes in the distribution of elements on a nanometer scale. A multivalency has been observed for Pr, with the effective oxidation state decreasing with increasing Zr content. The conductivity of $(Ce,La,Pr,Sm,Y)_{1-x}Zr_xO_{2-\delta}$ increases with Zr addition, reaches a maximum around x = 0.05, and reduces with further addition of Zr. The ionic conductivities estimated from the changes in

conductivity with oxygen partial pressure follow the same trend as the total conductivities. However, the conductivity maximum for ionic conductivity is around $x = 0.08$. The electronic conductivity has been observed to decrease with increasing Zr content. Furthermore, the activation energy for electronic conduction reduces with increasing Zr. The ionic and electronic conductivity trends suggest that the highest transference number for oxygen ions is achieved at $x = 0.08$. The decreased electronic conductivity in the high entropy oxides due to the suppressed polaron hopping in these multicomponent systems can be a possible solution for mitigating the electronic conductivity in the ceria-based systems. Hence, ceria-based high entropy oxides with a fluorite structure are promising candidates for oxygen ion conductors.

5.2 Perovskite-type high entropy oxides - $(Gd_{0.2}La_{0.2}Nd_{0.2}Pr_{0.2}Sm_{0.2})_{1-x}Ca_xAlO_3$

Perovskite structured oxides are popular material systems known for their exceptional functional properties. Oxygen ion conduction in perovskite structured oxides is discussed in detail in chapter 2. Rare earth aluminates ($R_{1-x}M_xAlO_{3-x/2}$) represent one such perovskite-structured oxide. While it exhibits electronic contributions in oxidizing atmospheres, as observed in *Reaction 2-2*, it is particularly attractive due to its lower cost compared to $La_{1-x}Sr_xGa_{1-y}Mg_yO_{3-(x+y)/2}$. The electronic contribution due to *Reaction 2-2* can be a consequence of the structural transitions (orthorhombic➜rhombohedral/trigonal➜cubic) happening at high temperatures in $MAlO_3$ systems[129–132]. High entropy materials are conceptualized to have high structural stability at higher temperatures due to an increased entropy term ($T\Delta S_{mix}$) overcoming the enthalpy of mixing leading to negative Gibbs free energy of formation. Studies suggest that the application of the high entropy concept can enhance thermal stability, also in perovskite structured high entropy oxides[39,46,133,134]. As a result, the high entropy concept is introduced into rare earth aluminates aiming to stabilize the lattice avoiding the structural transition and exchange of oxygen thereby reducing the p-type conduction observed in doped rare earth aluminates. High entropy rare earth aluminate with a composition of $(Ga_{0.2}La_{0.2}Nd_{0.2}Pr_{0.2}Sm_{0.2})AlO_3$ was synthesized. Ca was doped into $(Ga_{0.2}La_{0.2}Nd_{0.2}Pr_{0.2}Sm_{0.2})AlO_3$ to introduce oxygen vacancies for oxygen ion migration. The compositions summarized in *Table 5-4* were investigated in this study.

Table 5-4 The compositions synthesized and explored in this study along with their corresponding notations

| Composition	Notation
$(Gd_{0.2}La_{0.2}Nd_{0.2}Pr_{0.2}Sm_{0.2})AlO_3$	$x = 0$
$(Gd_{0.2}La_{0.2}Nd_{0.2}Pr_{0.2}Sm_{0.2})_{0.95}Ca_{0.05}AlO_3$	$x = 0.05$
$(Gd_{0.2}La_{0.2}Nd_{0.2}Pr_{0.2}Sm_{0.2})_{0.9}Ca_{0.1}AlO_3$	$x = 0.1$
$(Gd_{0.2}La_{0.2}Nd_{0.2}Pr_{0.2}Sm_{0.2})_{0.85}Ca_{0.15}AlO_3$	$x = 0.15$
$(Gd_{0.2}La_{0.2}Nd_{0.2}Pr_{0.2}Sm_{0.2})_{0.8}Ca_{0.2}AlO_3$	$x = 0.2$

The powders of these compositions were synthesized using the Pechini process. The dried polymer precursor gels were heat treated at 1250 °C for 2 hours to form oxide powders. The

powders were then pressed into pellets at 500 MPa after which the green pellets were sintered at 1400 °C for 12 h. The resultant pellets were structurally, chemically, morphologically characterized and furthermore the transport properties of the pellets were investigated. Along with the examination of the high entropy oxide, corresponding single component Ca-doped rare earth aluminates were synthesized and characterized. The structure and properties of the high entropy oxides are compared to the single component Ca-doped rare earth aluminates to understand the significance of these novel materials.

5.2.1 Structural characterization

X-ray diffraction (XRD) was used for structural characterization of the powders and pellets. The XRD patterns of powder and surface of the pellets are depicted in *Figure 5-22*. The X-ray diffraction patterns of powders of $(Gd_{0.2}La_{0.2}Nd_{0.2}Pr_{0.2}Sm_{0.2})_{1-x}Ca_xAlO_3$ in *Figure 5-22(a)* suggest the structure to be orthorhombic perovskite with a space group of *Pbnm*. However, a small amount of secondary phase has been observed at $x = 0.2$. There is no change in the structure upon sintering the powder into pellets as observed from the XRD patterns of the pellets in *Figure 5-22(b)*, however a secondary phase appears at $x = 0.15$. This impurity might be a Ca-rich oxide phase as it appears at higher concentrations of Ca. The XRD reflections in the patterns of the pellets are narrower than the reflections in the patterns of the powders suggesting an increase in crystallite size after sintering. This increase in crystallite size is due to the grain growth at higher sintering temperatures used for densification. The XRD patterns of powders and pellets of single component rare earth aluminates ($La_{0.9}Ca_{0.1}AlO_3$, $Nd_{0.9}Ca_{0.1}AlO_3$, $Pr_{0.9}Ca_{0.1}AlO_3$, $Sm_{0.9}Ca_{0.1}AlO_3$, $Gd_{0.9}Ca_{0.1}AlO_3$) indicate an orthorhombic structure (*Pbnm*) which are shown in Figure 5-22(c) and *Figure 5-22(d)*. There is no change in the structure between the powders and the pellets with both exhibiting orthorhombic perovskite structure. Rietveld refinement was performed on the XRD patterns exhibiting single phases ($x = 0, 0.05$ and 0.1) with an orthorhombic perovskite (*Pbnm*) which can be seen in *Figure 5-23*. The structure fits the XRD patterns with minimal residue which further confirms the compositions to be a single-phase orthorhombic perovskite.
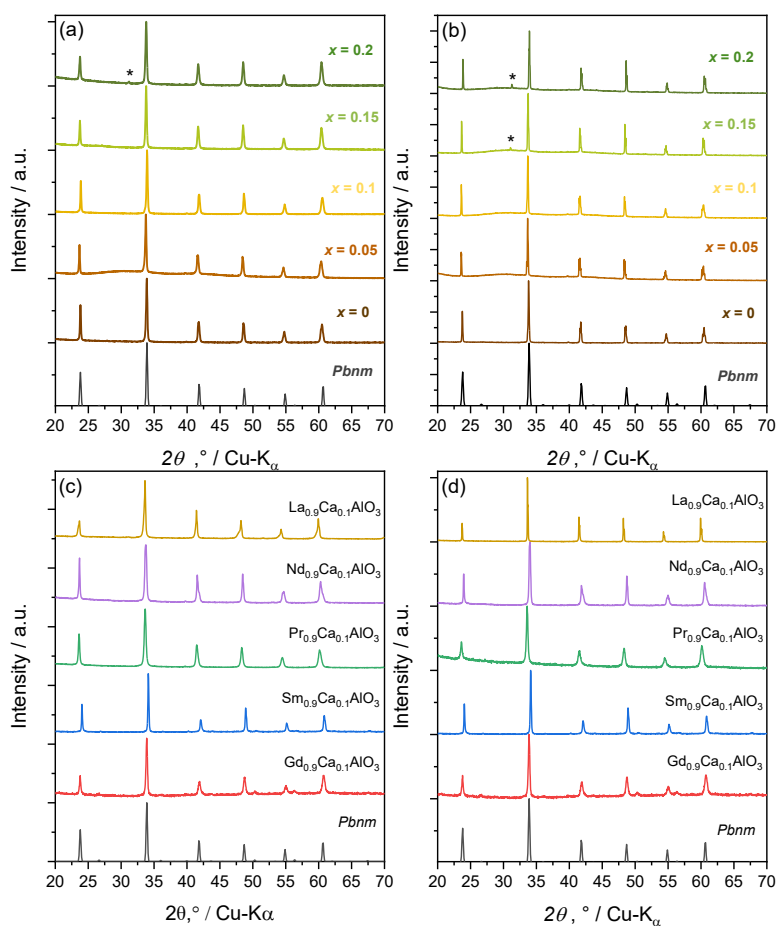
Figure 5-22 The X-ray diffraction patterns of (a) powders of $(Gd_{0.2}La_{0.2}Nd_{0.2}Pr_{0.2}Sm_{0.2})_{1-x}Ca_xAlO_3$, (b) surface of the sintered pellets of $(Gd_{0.2}La_{0.2}Nd_{0.2}Pr_{0.2}Sm_{0.2})_{1-x}Ca_xAlO_3$, (c) powders of single component Ca doped rare earth aluminates $(La_{0.9}Ca_{0.1}AlO_3, Nd_{0.9}Ca_{0.1}AlO_3, Pr_{0.9}Ca_{0.1}AlO_3, Sm_{0.9}Ca_{0.1}AlO_3, Gd_{0.9}Ca_{0.1}AlO_3)$ and (d) pellets of single component Ca doped rare earth aluminates.
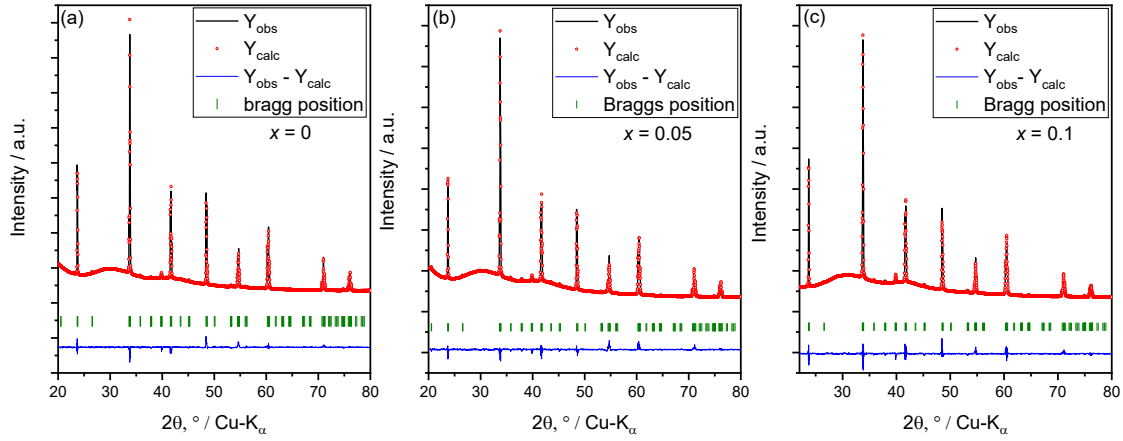
Figure 5-23 Rietveld refinements of $(Gd_{0.2}La_{0.2}Nd_{0.2}Pr_{0.2}Sm_{0.2})_{1-x}Ca_xAlO_3$ (a) x = 0, (b) x = 0.05 and (c) x = 0.1. Here Y_{obs} is the experimental data, Y_{calc} is the fit and Y_{obs}- Y_{calc} is the residue (difference between experimental data and the fit).

An ideal cubic perovskite structured oxide (ABO_3) is a primitive cubic lattice where lattice sites are occupied by A-site cations and the body center of the lattice is occupied by the B-site cation with the face center occupied by the oxygen ion. The unit cell of an ideal cubic perovskite structure is demonstrated in *Figure 5-24(a)*. The lattice parameter of the unit cell can be estimated from the ionic radii of the cations and anions from the structure of the unit cell. Consequently, the lattice parameter (a) of an ideal cubic perovskite lattice can be written as follows

$$a = \sqrt{2}\,(r_A + r_O) = 2(r_B + r_O) \qquad\qquad Eq.\ 5\text{-}16$$

here, r_A represent the ionic radii of the A-site cations, r_B is the ionic radii of the B-site cations and r_O is the ionic radius of the oxygen ion. The expression of lattice parameter in *Eq. 5-16* is only for the cubic lattice. However, not all perovskite materials are cubic. Various structures like orthorhombic, rhombohedral, hexagonal and tetragonal structures are possible in perovskite structured oxides. The structure of a perovskite-type oxide is strongly dependent on the ionic radii of the cations. Consequently, to identify the structure and deviations from the cubic structure, Victor Moritz Goldschmidt introduced a tolerance factor[134](t), which is written as follows [135]

$$t = \frac{(r_A + r_O)}{\sqrt{2}\,(r_B + r_O)} \qquad\qquad Eq.\ 5\text{-}17$$

If t = 1 then the structure is cubic which can be understood from *Eq. 5-16*. However, if t < 1 then the possible structures of the composition would be orthorhombic or rhombohedral. Whereas if t > 1 then the possible structures would be hexagonal or tetragonal.

The tolerance factors of the synthesized perovskite-type oxides are calculated and summarized in *Table 5-5*. The crystal structure of all the oxides in this study is orthorhombic perovskite. Consequently, the tolerance factor is calculated by considering a coordination number of 8. The values of the tolerance factors of the compositions investigated in this study are smaller than 1, suggesting the structure to be either orthorhombic or rhombohedral. Indeed, the orthorhombic structure is observed in *Figure 5-22* from XRD patterns. The tolerance factor as well as lattice parameters of $(Gd_{0.2}La_{0.2}Nd_{0.2}Pr_{0.2}Sm_{0.2})_{1-x}Ca_xAlO_3$ (HEO) increases slightly with increasing Ca content as Ca is a slightly bigger cation (1.18 Å) compared to average ionic radii of the rare earth cations (1.16 Å). The tolerance factor follows the following order Gd < Sm < HEO < Nd < Pr < La. Consequently, the lattice parameter follows the same trend as the tolerance factor because the lattice parameters increase with increasing ionic radii of A-site cation or tolerance factor. Furthermore, the volume of the unit cell of these aluminates increases as well with increasing ionic radii of A-site cation or tolerance factor which can be seen in *Figure 5-24(b).* The volume of the unit cell is directly proportional to the volume of atoms present in the unit cell. Hence, the volume of the unit cell is direct proportional to the cube of ionic radii of A-site cation. It can be noted that the volume of the unit cells follows a cubic relation with the ionic radii of A-site cation or tolerance factor.
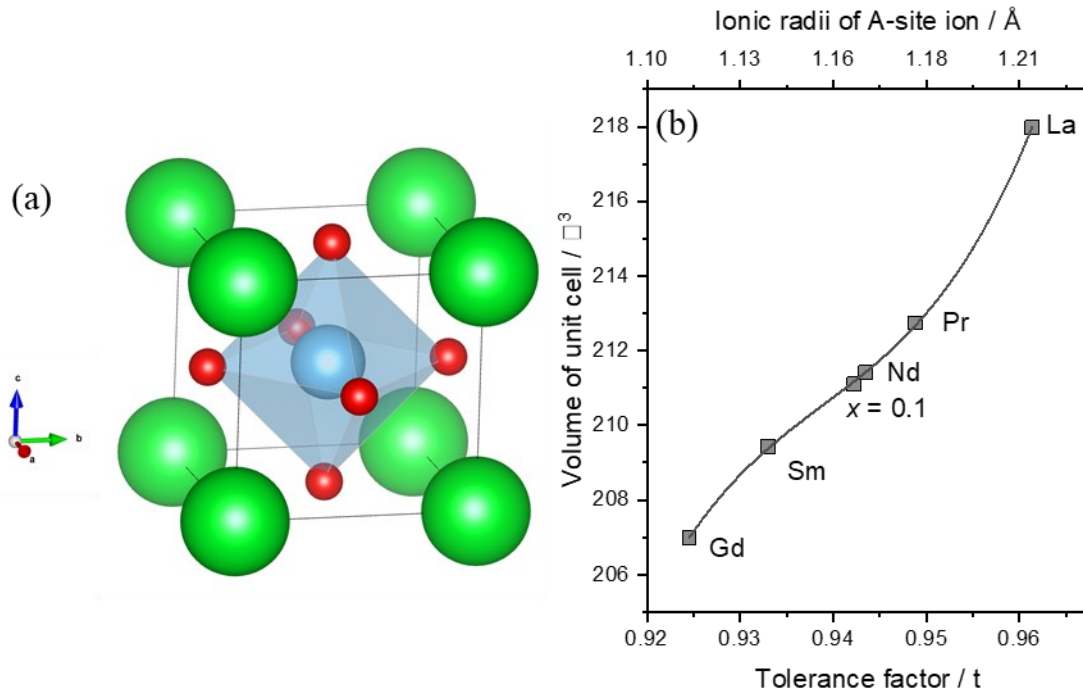
Figure 5-24(a) Unit cell of an ideal cubic perovskite, (b) volume of the unit cell vs. the tolerance factor (t), ionic radii of A-site of $(Gd_{0.2}La_{0.2}Nd_{0.2}Pr_{0.2}Sm_{0.2})_{0.9}Ca_{0.1}AlO_3$-x = 0.1, $La_{0.9}Ca_{0.1}AlO_3$-La, $Nd_{0.9}Ca_{0.1}AlO_3$-Nd, $Pr_{0.9}Ca_{0.1}AlO_3$-Pr, $Sm_{0.9}Ca_{0.1}AlO_3$-Sm and $Gd_{0.9}Ca_{0.1}AlO_3$.

Table 5-5 Composition, notation, Goldschmidt tolerance factor (t) considering ions having a coordination of 12 – t (12), Goldschmidt tolerance factor (t) considering ions having a coordination of 8 – t (8), lattice parameters (a,b,c) of $(Gd_{0.2}La_{0.2}Nd_{0.2}Pr_{0.2}Sm_{0.2})_{1-x}Ca_xAlO_3$, $La_{0.9}Ca_{0.1}AlO_3$, $Nd_{0.9}Ca_{0.1}AlO_3$, $Pr_{0.9}Ca_{0.1}AlO_3$, $Sm_{0.9}Ca_{0.1}AlO_3$, $Gd_{0.9}Ca_{0.1}AlO_3$. The ionic radii are taken from Shannon ionic radii website [128].

Composition	Notation	t (12)	t (8)	a	b	c
$Gd_{0.9}Ca_{0.1}AlO_3$	Gd	-	0.92456	5.265	5.284	7.44
$Sm_{0.9}Ca_{0.1}AlO_3$	Sm	0.975467	0.933	5.281	5.296	7.488
$(Gd_{0.2}La_{0.2}Nd_{0.2}Pr_{0.2}Sm_{0.2})AlO_3$	$x = 0$	0.968414	0.94148	5.299	5.324	7.494
$(Gd_{0.2}La_{0.2}Nd_{0.2}Pr_{0.2}Sm_{0.2})_{0.95}Ca_{0.05}AlO_3$	$x = 0.05$	0.970455	0.94186	5.295	5.323	7.491
$(Gd_{0.2}La_{0.2}Nd_{0.2}Pr_{0.2}Sm_{0.2})_{0.9}Ca_{0.1}AlO_3$	$x = 0.1$	0.972496	0.94225	5.296	5.319	7.494
$(Gd_{0.2}La_{0.2}Nd_{0.2}Pr_{0.2}Sm_{0.2})_{0.85}Ca_{0.15}AlO_3$	$x = 0.15$	0.974537	0.94264	5.292	5.311	7.499
$(Gd_{0.2}La_{0.2}Nd_{0.2}Pr_{0.2}Sm_{0.2})_{0.8}Ca_{0.2}AlO_3$	$x = 0.2$	0.976578	0.94302	5.296	5.324	7.491
$Nd_{0.9}Ca_{0.1}AlO_3$	Nd	0.985597	0.94346	5.288	5.322	7.512
$Pr_{0.9}Ca_{0.1}AlO_3$	Pr	-	0.94887	5.3	5.325	7.538
$La_{0.9}Ca_{0.1}AlO_3$	La	1.015986	0.96136	5.357	5.364	7.586

5.2.2 Microstructure and pellet density

The surface morphology of the pellets was investigated by SEM. The surface micrographs of $(Gd_{0.2}La_{0.2}Nd_{0.2}Pr_{0.2}Sm_{0.2})_{1-x}Ca_xAlO_3$ at 500 x magnification are depicted in *Figure 5-25*. It can be seen that at x = 0, the surface consists of a lot of open pores (Red dotted circles in *Figure 5-25* mark the open pores) which decrease with increasing Ca content. The least number of pores are observed at *x* = 0.1. At higher values of *x* open pores reappear. The presence of open pores is also reflected in the density measurements. The relative densities calculated from Archimedes principle are above 90%TD illustrated in *Table 5-6*. However, the geometric densities in *Table 5-6* vary between 80 and 95 %TD. The difference between these two relative densities provides information on the open pores. The difference in densities or open porosity decreases with increasing Ca content, reaches a minimum at x = 0.1 and increases with further addition. On closer inspection into the pores, the grains in the samples are visible in *Figure 5-26*. The grains are around 1-2 µm. The grain size is similar in all systems with undoped high entropy oxide having slightly higher grain sizes.

Table 5-6 The relative densities calculated from Archimedes principle and the dimensions of pellets along with the difference between these densities.

Composition	Relative density – Archimedes (%TD)	Geometric relative density (%TD)	Difference (%TD)
$(Gd_{0.2}La_{0.2}Nd_{0.2}Pr_{0.2}Sm_{0.2})AlO_3$	94	80	14
$(Gd_{0.2}La_{0.2}Nd_{0.2}Pr_{0.2}Sm_{0.2})_{0.95}Ca_{0.05}AlO_3$	96	94	2
$(Gd_{0.2}La_{0.2}Nd_{0.2}Pr_{0.2}Sm_{0.2})_{0.9}Ca_{0.1}AlO_3$	96	95	1
$(Gd_{0.2}La_{0.2}Nd_{0.2}Pr_{0.2}Sm_{0.2})_{0.85}Ca_{0.15}AlO_3$	92	86	6
$(Gd_{0.2}La_{0.2}Nd_{0.2}Pr_{0.2}Sm_{0.2})_{0.8}Ca_{0.2}AlO_3$	96	90	6
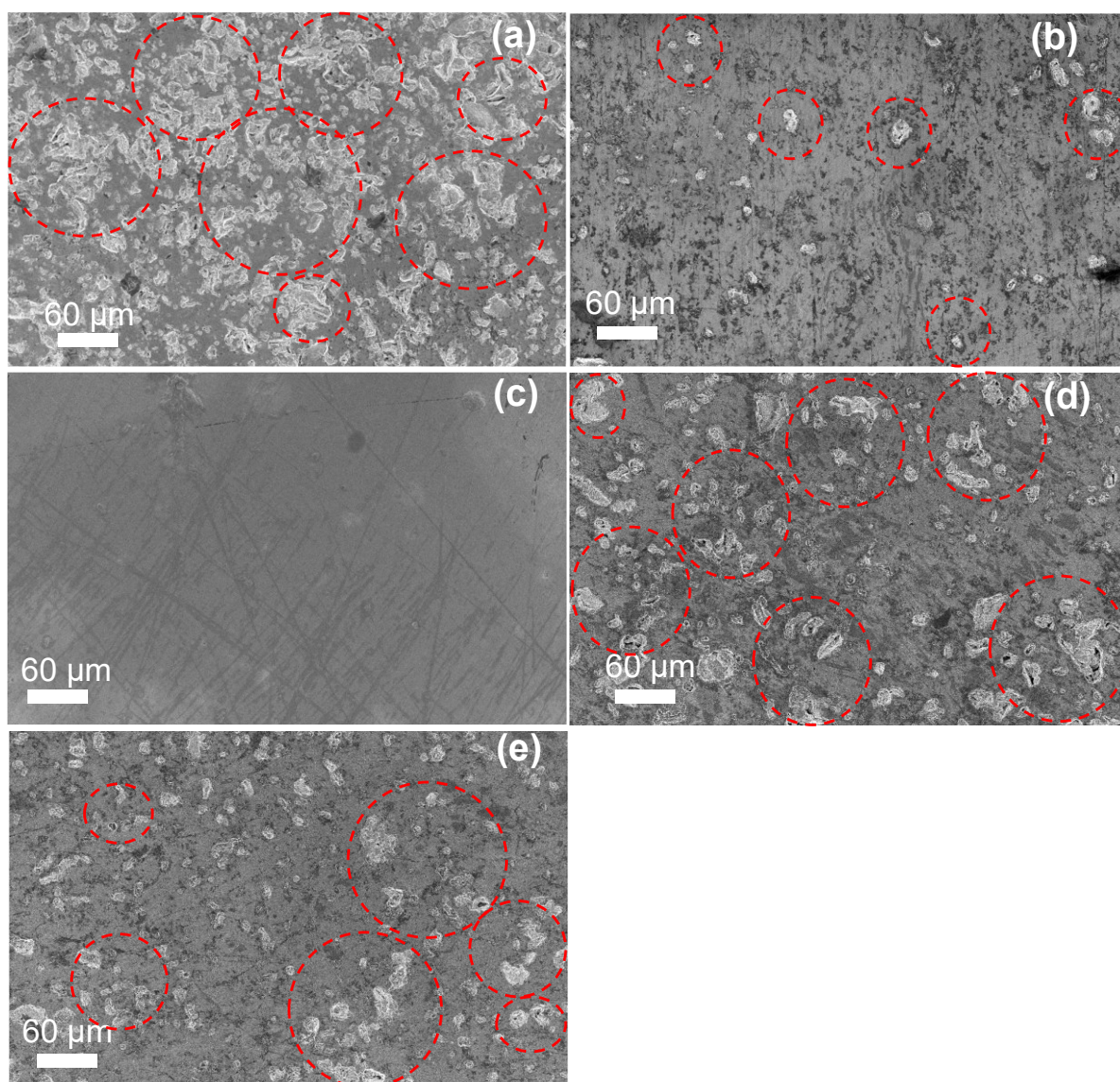
Figure 5-25 Scanning electron micrographs of $(Gd_{0.2}La_{0.2}Nd_{0.2}Pr_{0.2}Sm_{0.2})_{1-x}Ca_xAlO_3$ (a) x = 0 (b) x = 0.05 (c) x =0.1 (d) x = 0.15 (e) x=0.2 at a magnification of 500x. Red dotted circles highlight the open pores.
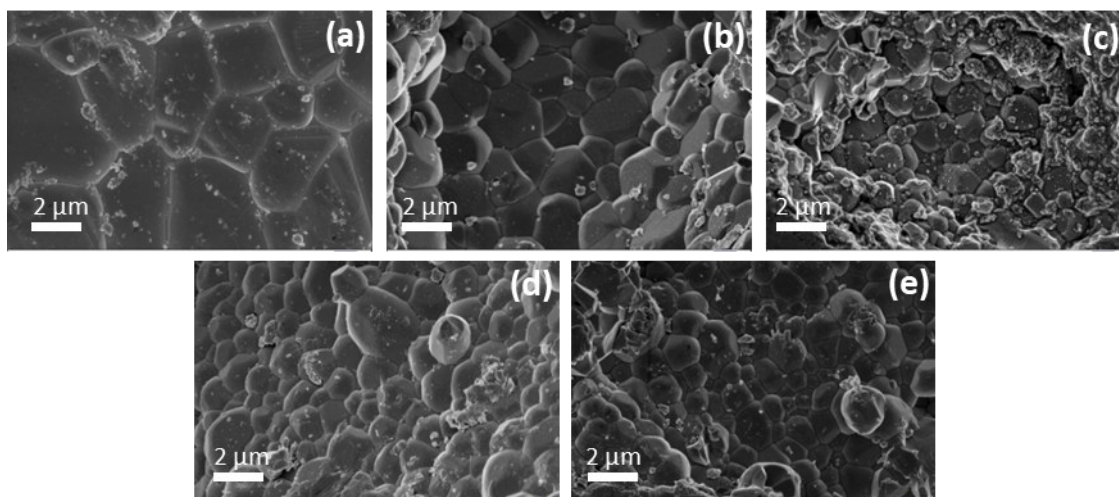
Figure 5-26 Scanning electron micrographs of $(Gd_{0.2}La_{0.2}Nd_{0.2}Pr_{0.2}Sm_{0.2})_{1-x}Ca_xAlO_3$ (a) x = 0 (b) x = 0.05 (c) x =0.1 (d) x = 0.15 (e) x=0.2 at a magnification of 30000x inside the pores on the surface.

5.2.3 Chemical composition and distribution

The chemical characterization of these compositionally complex oxides was performed using EDS at different magnifications in the scanning electron microscope and transmission electron microscope. The chemical compositions of the $(Gd_{0.2}La_{0.2}Nd_{0.2}Pr_{0.2}Sm_{0.2})_{1-x}Ca_xAlO_3$ is close to the nominal values, as shown in Figure 5-27. The rare earth elements are close to equiatomic ratio with slightly higher amounts of La and lower amounts of Pr. The Ca content is consistent with nominal values with a deviation of 1-2 at.%. The elemental distribution of the constituent elements are observed in the EDS maps in *Figure 5-28*. The EDS maps from SEM were conducted on the pellets while the EDS maps from TEM were conducted on the powders. EDS maps from SEM and TEM do not show any evidence of segregation. The elements are homogenously distributed on both micro- and nanoscale.
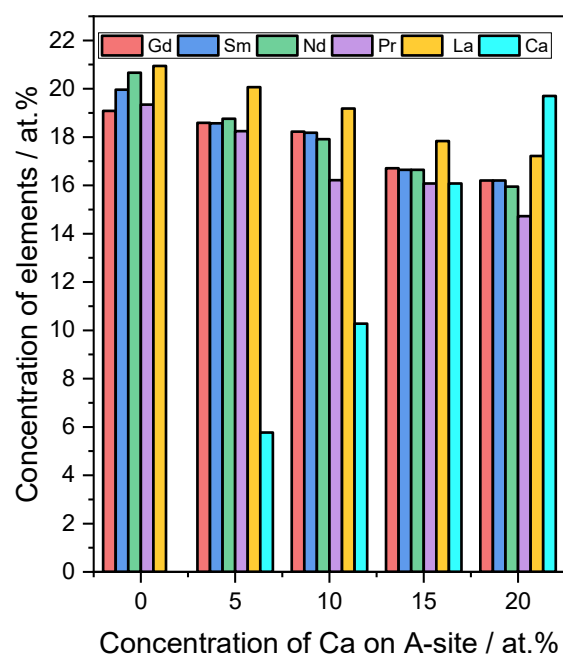
Figure 5-27 The chemical composition of $(Gd_{0.2}La_{0.2}Nd_{0.2}Pr_{0.2}Sm_{0.2})_{1-x}Ca_xAlO_3$.
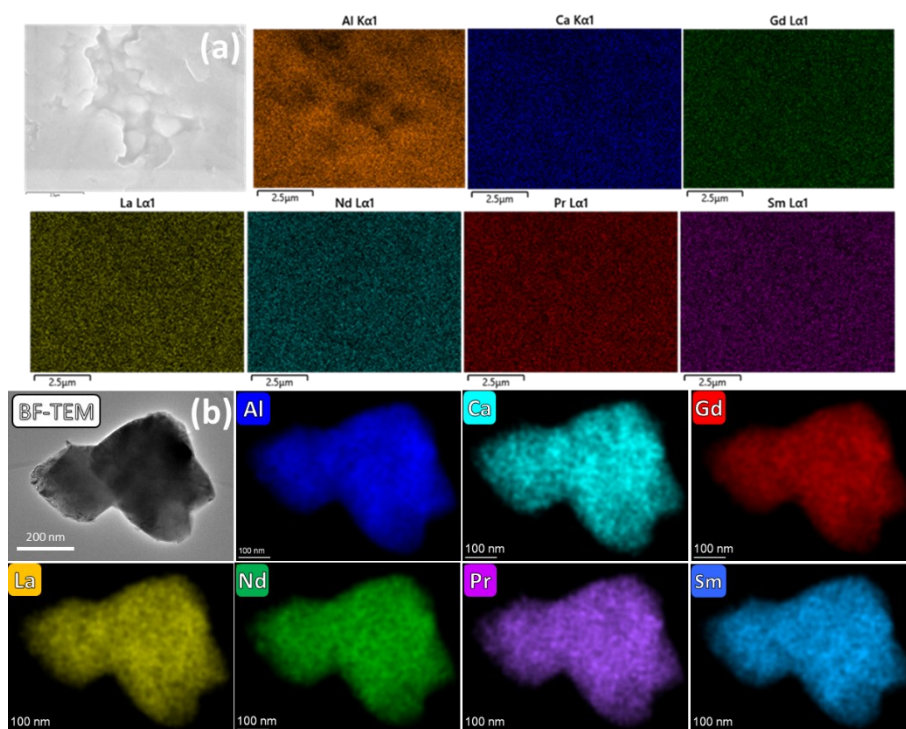
Figure 5-28 The elemental EDS maps of $(Gd_{0.2}La_{0.2}Nd_{0.2}Pr_{0.2}Sm_{0.2})_{0.9}Ca_{0.1}AlO_3$ at different magnifications imaged using a (a) scanning electron microscope and (b) transmission electron microscope.

5.2.4 Raman spectroscopy

Raman spectra measured on sintered pellets of the $(Gd_{0.2}La_{0.2}Nd_{0.2}Pr_{0.2}Sm_{0.2})_{1-x}Ca_xAlO_3$ are presented in *Figure 5-29*. In the undoped high entropy aluminate, a Raman band at 241 cm^{-1} has been observed. This peak corresponds to the internal vibration A_g mode of ReO_9 dodecahedra[136,137]. Additional bands around 514, 608, and 687 cm^{-1} appear upon Ca doping into $(Gd_{0.2}La_{0.2}Nd_{0.2}Pr_{0.2}Sm_{0.2})AlO_3$. These new Raman bands can be attributed to the B_{1g}, B_{2g}, and B_{3g} vibrational modes of the BO_6 octahedra in the $CaBO_3$ system [138,139]. These new peaks are the vibration modes due to Ca indicating the incorporation of Ca into the lattice. However, with further addition of Ca, there is no change in the Raman spectra. Raman spectra are a result of the vibrations, distortions and crystal symmetry of a crystal. In this study, all the $(Gd_{0.2}La_{0.2}Nd_{0.2}Pr_{0.2}Sm_{0.2})_{1-x}Ca_xAlO_3$ exhibit the same crystal symmetry and lattice parameters which can be seen in the XRD data shown in *Figure 5-22* and *Table 5-5*. No significant change in the Raman spectra is observed, as the structure and lattice parameters remain similar.
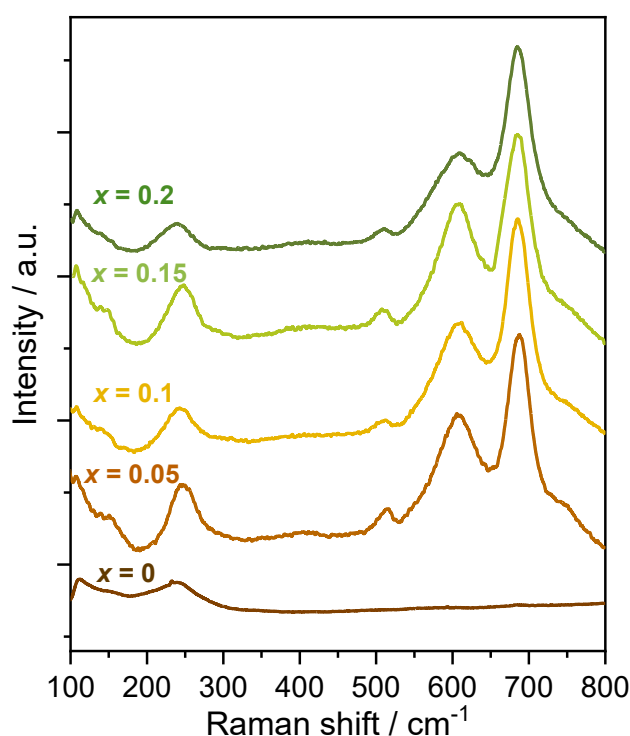
Figure 5-29 Raman spectra measured on sintered pellets of $(Gd_{0.2}La_{0.2}Nd_{0.2}Pr_{0.2}Sm_{0.2})_{1-x}Ca_xAlO_3$.

5.2.5 UV-Vis spectroscopy

UV-Vis spectroscopy was conducted to calculate the band gap of the material. In some materials, the band gap of the material can change depending on the oxidation state of the ions as it can lead to a change of the valence state thereby changing the band gap. Pr is one such multivalent element (+3,+4) which can influence the band gap of the material depending on its oxidation state. The effect of Pr multivalency on the band gap is very well known in the Pr containing rare earth oxides [44,111,119,140]. Band gaps were calculated to identify multivalency of Pr. In the literature, rare earth aluminates exhibit a direct band gap ranging from 4 to 5 eV[141-144]. The direct band was calculated via TAUC method and the corresponding plots (($\alpha h\nu)^2$ vs. hν) are shown in *Figure 5-30(a)*. The undoped high entropy aluminate shows a band gap of 3.6 eV. The band gap decreases below 2 eV upon the addition of Ca. This decrease in band gap can be a result of a change in oxidation state of Pr. Rare earth aluminates are doped with alkali earth metals like Ca to introduce oxygen vacancies as shown in the following equation.

$$CaO \xrightarrow{ReAlO_3} Ca'_{Re} + Al^x_{Al} + \frac{5}{2}O^x_O + \frac{1}{2}V^{\bullet\bullet}_O \qquad \textit{Reaction 5-2}$$
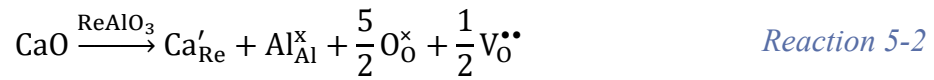
here, Ca'_{Re} is the calcium on the rare earth lattice site, Al^x_{Al} is the aluminum ion on the Al lattice site, O^x_O is lattice oxygen and $V^{\bullet\bullet}_O$ are oxygen vacancies in the system. In *Reaction 5-3*, it is considered that addition of Ca introduces oxygen vacancies. However, the presence of multivalent elements like Pr can provide another charge compensation mechanism for the charge imbalance created by Ca. Pr can change its oxidation state from +3 to +4 to compensate the charge imbalance created by Ca.

$$Pr^x_{Pr} + h^{\bullet} \rightarrow Pr^{\bullet}_{Pr} \qquad \textit{Reaction 5-3}$$

where Pr^x_{Pr} is Pr^{+3} and $Pr^{\bullet}_{Pr}$ is Pr^{+4}. In LaAlO$_3$, it has been observed by Szubka *et al.* that the band gap of LaAlO$_3$ is between the La 5d orbital forming the conduction band and O 2p is the valence band[145]. However, the presence of Pr can introduce an occupied 4f electron shell between 5d orbital of rare earth cation and the oxygen 2p orbital. As a result, the band gap in undoped high entropy rare earth aluminate (($Gd_{0.2}La_{0.2}Nd_{0.2}Pr_{0.2}Sm_{0.2}$)AlO$_3$) is between 4f orbital of Pr^{+3} and O 2p orbital. This is illustrated in the band structure in *Figure 5-30(a)*. However, there is a chance of Pr^{+4} formation upon addition of Ca. Furthermore, the presence of Pr^{+4} lower the 4f orbital thereby reducing the band gap. A drop in band gap has been observed

in *Figure 5-30(a)* with addition of Ca. Hence, the band gaps suggest the presence of Pr^{+4} and multivalency of Pr.
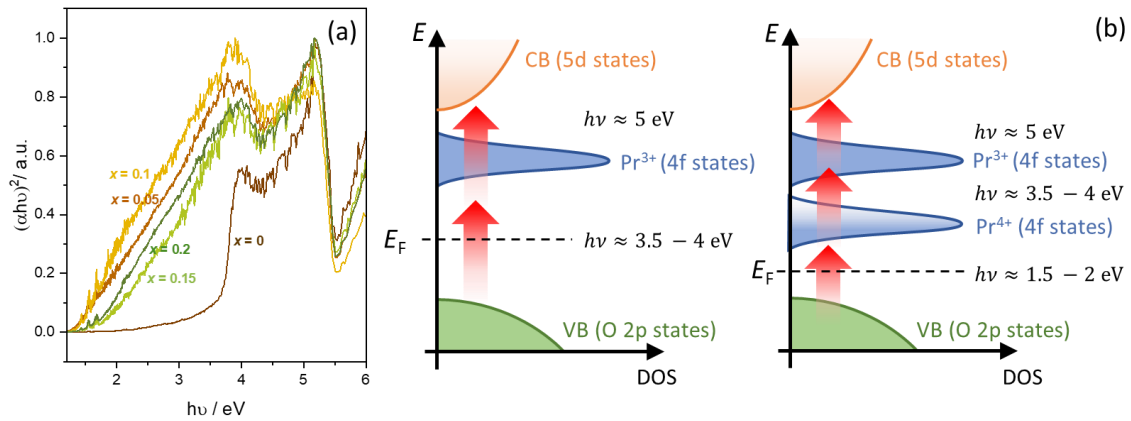
Figure 5-30 (a) TAUC plots derived from the UV-Vis spectra of pellets of $(Gd_{0.2}La_{0.2}Nd_{0.2}Pr_{0.2}Sm_{0.2})_{1-x}Ca_xAlO_3$ (b) A simple representation of band structure in rare earth oxides. Here VB is valence band, CB is conduction band, E_f is Fermi energy level and DOS is the density of states.

The fully dense single phase crystalline pellets of $(Gd_{0.2}La_{0.2}Nd_{0.2}Pr_{0.2}Sm_{0.2})_{1-x}Ca_xAlO_3$ were coated on both sides with silver paste along with a subsequent heat treatment to create electrodes for electrical characterization

5.2.6 Electrical characterization

The electrical properties of $(Gd_{0.2}La_{0.2}Nd_{0.2}Pr_{0.2}Sm_{0.2})_{1-x}Ca_xAlO_3$ were investigated using EIS. EIS was conducted at different temperatures (300 -700 °C) and at various oxygen partial pressures (1 mbar to 1 bar). The Nyquist plots of $(Gd_{0.2}La_{0.2}Nd_{0.2}Pr_{0.2}Sm_{0.2})_{0.9}Ca_{0.1}AlO_3$ at 350 and 600 °C in air are depicted in *Figure 5-31*. Three semicircles are observed in the Nquist plot of $(Gd_{0.2}La_{0.2}Nd_{0.2}Pr_{0.2}Sm_{0.2})_{0.9}Ca_{0.1}AlO_3$ at 350 °C in air see *Figure 5-31(a)*. The semicircles are at low frequency regime, medium frequency regime and high frequency regime. These semicircles in *Figure 5-31(a)* are observed to be depressed. A depressed semicircle can be fitted with a parallel combination of CPE element and resistance (R). As a result, the impedance data at 350 °C is fitted with three CPE//R elements. The values of CPE elements and the resistances estimated from the fits are summarized in *Table 5-7*. According to literature, the capacitance and resistances suggest the following

1) Semicircle at the high frequency regime is due to the contribution from the grain [85,123].

2) Semicircle at the mid frequency regime is due to the contribution from grain boundary [85,123].

3) Semicircle at the low frequency regime is due to the contribution from the electrolyte/ electrode interface [85,123].

The semicircle shifts to higher frequencies with increasing temperature as the resistance of the ionic conductors decreases ($Z = \frac{R}{1+(i\omega)^\alpha QR}$) which is observed in the impedance spectra at 600 °C in *Figure 5-31(b)*. Appropriately, the contributions from the grains shift to very high frequencies which cannot be measured by the available potentiostat and only two contributions from grain boundaries and electrolyte/electrode interfaces are observed. The observed capacitances and resistance derived by fitting two CPE//R elements are summarized in *Table 5-7*. These values indicate that the two semicircles are due to the contributions from grain and grain boundary [85,123]. The EIS data becomes less detailed with increasing temperature making it difficult to identify the resistances from the grains and grain boundaries. Therefore, the total resistance of the system is considered from this point onwards. The intersection of the EIS data with x-axis at very low frequencies was considered to be the total resistance of the system. The conductivities (σ) were then calculated from the total resistance of the system using the following equation

$$\sigma = \frac{1}{R}\frac{l}{A} \qquad\qquad \textit{Eq. 5-18}$$

Here, R is the total resistance of the system from EIS data, l is thickness of the pellet and A is area of the electrodes on the pellets.
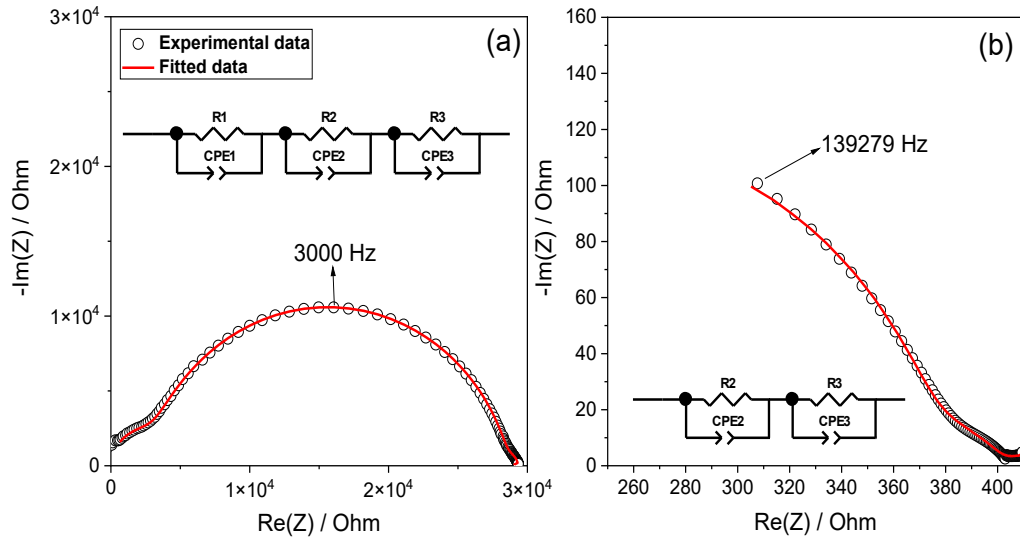
Figure 5-31 Impedance spectra of (Gd$_{0.2}$La$_{0.2}$Nd$_{0.2}$Pr$_{0.2}$Sm$_{0.2}$)$_{0.9}$Ca$_{0.1}$AlO$_3$ at different temperatures (a) 350 °C and (b) 600 °C along with fits. The impedance data was fitted with the equivalent circuit in the corresponding figures.

Table 5-7 The resistances, CPE parameters Q and α of (Gd$_{0.2}$La$_{0.2}$Nd$_{0.2}$Pr$_{0.2}$Sm$_{0.2}$)$_{0.9}$Ca$_{0.1}$AlO$_3$ at different temperatures (a) 350 °C and (b) 600 °C corresponding to different contributions. The fits were derived from the equivalent circuits shown in Figure 5-31. Error percentages are included in brackets.

Component	Values	350 ˚C (error%)	600 ˚C (error%)	Contribution
1	Q1 (F/s$^{(1-\alpha)}$)	$4.282 \cdot 10^{-10}$ (0.991)	-	Grain
	α1 (°)	1	-	
	R1 (Ω)	2682 (1.346)	-	
	C (F)	$4.282 \cdot 10^{-10}$		
2	Q2(F/s$^{(1-\alpha)}$)	$7.576 \cdot 10^{-9}$ (3.438)	$1.972 \cdot 10^{-8}$ (4.658)	Grain boundary
	α2(°)	0.86258 (0.402)	0.792 (0.419)	
	R2(ohm)	26229 (0.324)	381.1 (0.813)	
	C(F)	$1.948 \cdot 10^{-9}$	$8.896 \cdot 10^{-10}$	
3	Q3(F/s$^{(1-\alpha)}$)	$8.845 \cdot 10^{-6}$ (31.4)	$9.013 \cdot 10^{-5}$ (15.573)	Electrode
	α3(°)	1	0.659 (4.485)	
	R3(ohm)	586.2(18.8)	23.57 (3.509)	
	C(F)	$8.845 \cdot 10^{-6}$	$3.731 \cdot 10^{-6}$	

The total conductivities (grains + grain boundaries) of $(Gd_{0.2}La_{0.2}Nd_{0.2}Pr_{0.2}Sm_{0.2})_{1-x}Ca_xAlO_3$ are plotted vs. the Ca content at different temperatures which are shown in *Figure 5-32(a)*. The conductivity is the lowest in undoped high entropy aluminate (when $x = 0$). However, with addition of Ca, the conductivity increases over a few orders of magnitude. Nevertheless, the conductivity slightly decreases with the Ca content. In ionic conductors, the conductivity of the system ($\sigma_{ion}(T)$) can be written as follows

$$\sigma_{ion}(T) = 2e\mu_{ion}(T)[V_O^{\bullet\bullet}] \hspace{3cm} \textit{Eq. 5-19}$$

where $\mu_{ion}(T)$ is the mobility of the ions and $[V_O^{\bullet\bullet}]$ is the concentration of oxygen vacancies in the lattice. In undoped systems, there are no oxygen vacancies as the rare earth cations are +3 and Aluminum is +3. However, with addition of Ca^{+2}, a charge inequality is created which will be compensated by the creation of oxygen vacancies. This reaction is depicted in *Reaction 5-3*. As a result, an increase in conductivity is observed with addition of Ca as per *Eq. 5-19*. It should be noted here that the conductivity of the system not only depends on the concentration of the oxygen vacancies but also the mobility of the oxygen ions through those oxygen vacancies. It is observed in multiple oxygen ion conductors that the conductivity decreases at high dopant concentrations [5,124,146–154]. This decrease in conductivity is due to the decrease in mobility of the oxygen ions. The decrease in mobility is a result of defect interaction and/or the formation of dopant-defect associates (e.g., oxygen vacancies trapped at Ca^{+2})[105,116,120]. Therefore, a slight decrease in conductivity is observed above 5 at.% Ca. The conductivities are plotted versus temperature using Arrhenius representation ($\log(\sigma T)$ vs. $1/T$) depicted in *Figure 5-32(b)*. The Arrhenius plot of the undoped system ($x = 0$) shows three different activation energies (E_a). The slope changes at temperatures of 627 and 827 °C. The presence of three activation energies in $x = 0$ can be a result of structural transitions from orthorhombic to rhombohedral to cubic at higher temperatures[129,131,132]. The Ca doped counterparts show almost a linear relationship. However, on closer inspection, the Arrhenius plots of the doped systems exhibit two slopes or two activation energies with the transitional kink occurring at 500 °C. There are multiple reasons for the observed change in activation energy. It can be due to the different contributions of grains and grain boundaries or it can be due to breaking free of the defect associate ($V_O^{\bullet\bullet}$) with the dopant (Ca^{+2}) at high temperatures[120]. The activation energies of the Ca doped system vary between 0.89 to 1.01 eV. The conductivities of $x = 0.1$ are plotted against different oxygen partial pressures measured at different temperatures which are demonstrated in *Figure 5-32(c)*. The pressure dependence of conductivity of $x = 0.1$ at 400 and 500 °C is constant. which

suggests a dominant ionic conduction at these temperatures. However, the pressure dependence of conductivity changes at 600 and 700 °C to a p-type conduction, where the conductivity increases with increasing oxygen partial pressure. This p-type conduction is often observed in doped rare earth aluminates with a slope of ¼ [23,150,154–156]. In the case of high entropy oxide, very low slopes ($<\frac{1}{10}$) are observed.
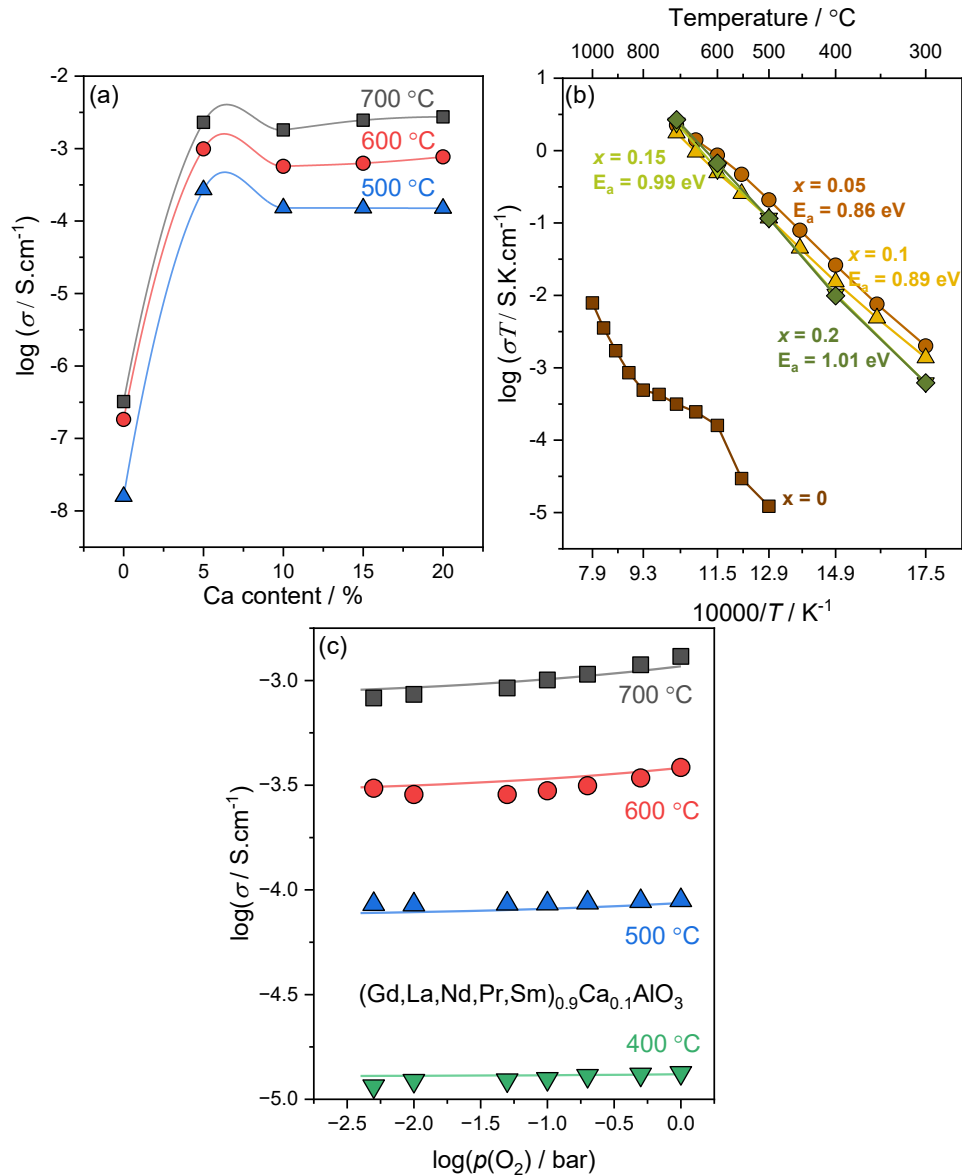
Figure 5-32 (a) Conductivity vs. Ca content at 500 °C, 600 °C and 700 °C in air. (b) Arrhenius representation of conductivities of $(Gd_{0.2}La_{0.2}Nd_{0.2}Pr_{0.2}Sm_{0.2})_{1-x}Ca_xAlO_3$ at different temperatures in air. The activation energies in the legend are derived from Arrhenius equation by linear fitting of the data. (c) Conductivity vs. partial pressure of oxygen ($p(O_2)$) at different temperatures. The scatter plot is the experimental data and the line plot is the fits extracted from Eq. 5-29 which will be discussed in the following section.

5.2.7 Correlation between high entropy oxide and single component oxides

Figure 5-33 shows the conductivities of $(Gd_{0.2}La_{0.2}Nd_{0.2}Pr_{0.2}Sm_{0.2})_{0.9}Ca_{0.1}AlO_3$ ($x = 0.1$) along with the single component doped rare earth aluminates ($La_{0.9}Ca_{0.1}AlO_3$, $Pr_{0.9}Ca_{0.1}AlO_3$, $Nd_{0.9}Ca_{0.1}AlO_3$, $Sm_{0.9}Ca_{0.1}AlO_3$, $Gd_{0.9}Ca_{0.1}AlO_3$). $Pr_{0.9}Ca_{0.1}AlO_3$ has the highest conductivity among the systems investigated in this study. The conductivities of the rest of the aluminates follow the following trend $\sigma_{(Gd,La,Nd,Pr,Sm)CaAlO_3} > \sigma_{LaCaAlO_3} > \sigma_{NdCaAlO_3} > \sigma_{SmCaAlO_3} > \sigma_{GdCaAlO_3}$. The conductivities of single component rare earth aluminates except $Pr_{0.9}Ca_{0.1}AlO_3$ follow the same trend as their unit cell volume (V) as in *Figure 5-24(b)* ($V_{La} > V_{Nd} > V_{Sm} > V_{Gd}$). The pathway for oxygen ion conduction opens up as the unit cell volume increases resulting in the conductivity trend observed. Whereas for $Pr_{0.9}Ca_{0.1}AlO_3$, the multivalent Pr can contribute to polaron hopping through the lattice. Consequently, the higher conductivities observed in Pr containing oxides might be due to the additional electronic contribution from the multivalent Pr.
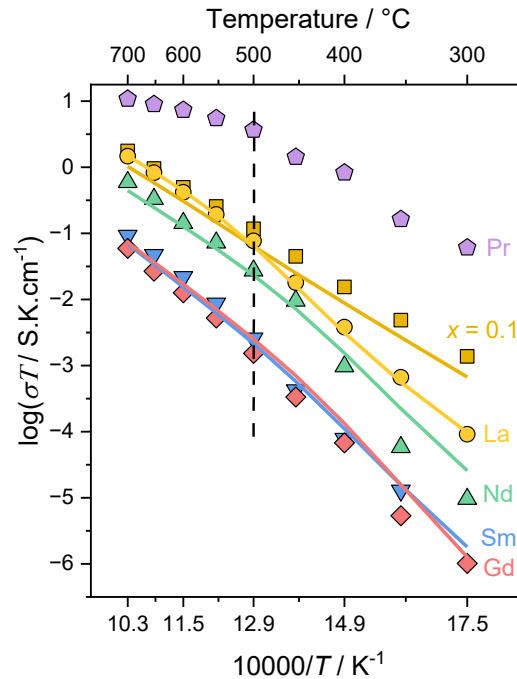
Figure 5-33 Arrhenius plot of conductivities with temperature of (Gd,La,Nd,Pr,Sm)$_{0.9}$Ca$_{0.1}$AlO$_3$ (x=0.1), La$_{0.9}$Ca$_{0.1}$AlO$_3$ (La), Pr$_{0.9}$Ca$_{0.1}$AlO$_3$ (Pr), Nd$_{0.9}$Ca$_{0.1}$AlO$_3$ (Nd), Sm$_{0.9}$Ca$_{0.1}$AlO$_3$ (Sm), Gd$_{0.9}$Ca$_{0.1}$AlO$_3$ (Gd) in air. The scatter plots are the experimental data and the line plot is the fits derived from Eq. 5-29.

Pr is multivalent in oxidizing atmospheres and changes its oxidation state between +3 and +4 depending on the change in oxygen partial pressures in oxidizing atmospheres.

Consequently, the conductivity of the system changes with the oxidation state of Pr. Therefore, the effect of Pr on the conductivity can be identified by measuring the conductivity at different oxygen partial pressures in the oxidizing regime. The conductivities of the doped rare earth aluminates at different oxygen partial pressures of oxygen can be seen *Figure 5-34*. The pressure dependence of conductivity of all the doped rare earth aluminates at 400 °C exhibits very low slopes suggesting predominantly ionic conduction. However, in the single component doped rare earth aluminates, the slopes become significant ($\frac{1}{4}$ to $\frac{1}{6}$) above 500 °C indicating a change in the conduction mechanism in the system. The Arrhenius plots of single component rare earth aluminates in *Figure 5-33* indicate a change in activation energy above 500 °C as a kink in the plot. The pressure dependence of conductivity above 500 °C is observed in multiple reports in the literature [23,150,154–156]. This pressure dependence is interpreted to be a result of the surface oxygen exchange with the atmosphere. This exchange generates holes in the system resulting in a p-type electronic conduction as illustrated in *Reaction 2-2*. The equilibrium constant of *Reaction 2-2* can be written as follows

$$K_{\text{ox}} = \frac{[V_O^{\bullet\bullet}]p(O_2)^{\frac{1}{2}}}{[O_O^x][h^\bullet]^2} \qquad\qquad Eq.\ 5\text{-}20$$

The initial oxygen vacancies in the system are created to balance the charge after Ca doping. As a result, the concentration of oxygen vacancies according to the Brouwer approximation is half of the dopant concentration i.e.

$$[V_O^{\bullet\bullet}] = \frac{[Ca_{Re}']}{2} \qquad\qquad Eq.\ 5\text{-}21$$

From *Eq. 5-21*, it is assumed that the concentration of oxygen vacancies are dependent on the Ca concentration and are independent of oxygen partial pressure in the atmosphere. Consequently, the concentration of holes and electronic conduction due to the holes from *Eq. 5-20* and *Eq. 5-21* can be written as

$$\sigma_{elec} \propto [h^\bullet] = \sqrt{\frac{[V_O^{\bullet\bullet}]}{[O_O^x]K_{\text{ox}}}}\, p(O_2)^{\frac{1}{4}} \qquad\qquad Eq.\ 5\text{-}22$$

Therefore, p-type electronic conductivity (σ_{elec}) of the systems is directly proportional to $p(O_2)^{\frac{1}{4}}$ and a slope of $\frac{1}{4}$ is expected in the $\log(\sigma)$ vs. $\log(p(O_2))$. The expected slope is observed in $La_{0.9}Ca_{0.1}AlO_3$, $Pr_{0.9}Ca_{0.1}AlO_3$, $Nd_{0.9}Ca_{0.1}AlO_3$ above 500 °C. Whereas, the slopes are lower for $Sm_{0.9}Ca_{0.1}AlO_3$ and $Gd_{0.9}Ca_{0.1}AlO_3$ showing a value of $\frac{1}{6}$.
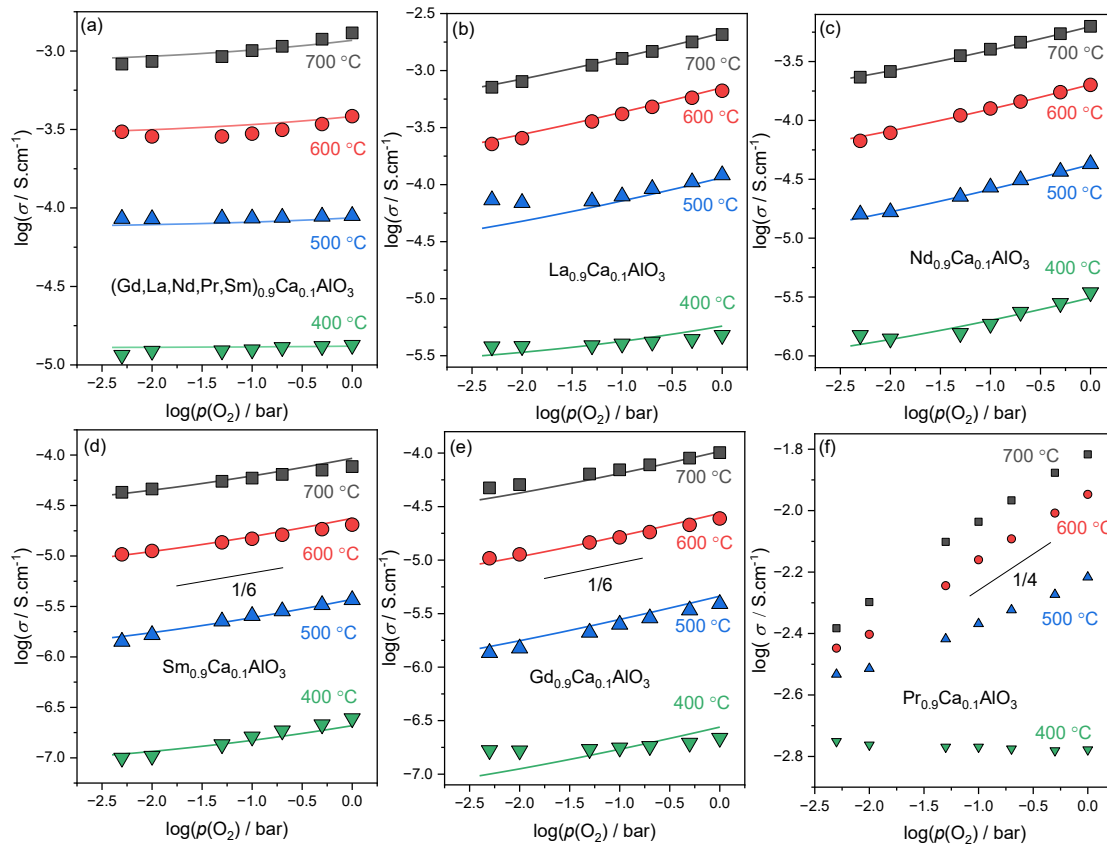
Figure 5-34 Conductivity of (a)(Gd,La,Nd,Pr,Sm)$_{0.9}$Ca$_{0.1}$AlO$_3$, (b)La$_{0.9}$Ca$_{0.1}$AlO$_3$, (c) Nd$_{0.9}$Ca$_{0.1}$AlO$_3$, (d)Sm$_{0.9}$Ca$_{0.1}$AlO$_3$, (e)Gd$_{0.9}$Ca$_{0.1}$AlO$_3$, (f)Pr$_{0.9}$Ca$_{0.1}$AlO$_3$, plotted versus partial pressure of oxygen at 400 °C, 500 °C, 600 °C and 700 °C. The scatter plot is the experimental data and line plot is the fits derived from the Eq. 5-29.

The largest slopes of conductivity vs. oxygen partial pressure are observed in Pr$_{0.9}$Ca$_{0.1}$AlO$_3$. The high slopes observed are due to the multivalency of Pr. This multivalency has been observed to occur in the oxidizing regimes. The oxygen partial pressures investigated in this study are within the oxidizing regime and holes created according to *Reaction 5-1* convert the Pr^{+3} (Pr$_R^{\times}$) to Pr^{+4} (Pr$_R^{\bullet}$). Consequently, *Reaction 5-1* in Pr$_{0.9}$Ca$_{0.1}$AlO$_3$ can be written as

$$2Pr_R^{\times} + V_O^{\bullet\bullet} + \frac{1}{2}O_2 \rightleftharpoons 2Pr_R^{\bullet} + O_O^{\times} \qquad \text{\textit{Reaction 5-4}}$$
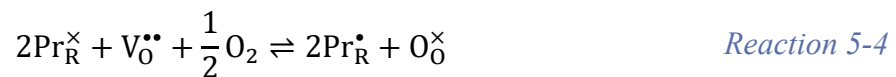
Multivalent Pr provides pathways for electron transport through the lattice via exchange of electrons from Pr^{+3} and Pr^{+4}. Consequently, a system with multivalent Pr can be an electronic conductor. The electronic conductivity resulting from Pr is given by [18,110,157,158]

$$\sigma_{elec} = \mathrm{e}[h^\bullet]\mu_{elec} = e[\mathrm{Pr_{Re}}]x_{\mathrm{Pr}}^{4+}(1 - x_{\mathrm{Pr}}^{4+})\frac{\mu_{pol}^0}{T}\exp\left(-\frac{\Delta H_{\mathrm{mig}}}{k_\mathrm{B}T}\right)p(\mathrm{O_2})^{\frac{1}{4}}$$

<div align="right">Eq. 5-23</div>

$$= \frac{\sigma_{elec,0}}{T}\exp\left(-\frac{E_\mathrm{A}}{k_\mathrm{B}T}\right)p(\mathrm{O_2})^{\frac{1}{4}}$$

Here μ_{elec} is the polaron mobility, $\sigma_{\mathrm{elec,0}}$ is the polaron conductivity pre-factor, $E_A = \Delta H_{\mathrm{mig}}$ is the activation energy or the migration enthalpy for the polaron hopping and $[h^\bullet]$ is the concentration of holes. The pressure dependence of conductivity resulting from Pr depends on the concentration of Pr^{+4} and the mobility of the polaron via Pr. EELS was performed to determine the oxidation states of Pr in these oxides. The EELS spectra of the $(\mathrm{Gd,La,Nd,Pr,Sm})_{0.9}\mathrm{Ca}_{0.1}\mathrm{AlO_3}$ and $\mathrm{Pr}_{0.9}\mathrm{Ca}_{0.1}\mathrm{AlO_3}$ are shown in *Figure 5-35(a)*. EELS is a suitable tool for understanding the oxidation state of Pr. The peak positions of M_4 and M_5 edges of $\mathrm{Pr}_{0.9}\mathrm{Ca}_{0.1}\mathrm{AlO_3}$ is higher than $(\mathrm{Gd,La,Nd,Pr,Sm})_{0.9}\mathrm{Ca}_{0.1}\mathrm{AlO_3}$. This suggests that the electron energy loss is higher in $\mathrm{Pr}_{0.9}\mathrm{Ca}_{0.1}\mathrm{AlO_3}$ which results due to a higher effective oxidation state of Pr in $\mathrm{Pr}_{0.9}\mathrm{Ca}_{0.1}\mathrm{AlO_3}$. Consequently, the peak positions indicate that the oxidation state of Pr is higher in $\mathrm{Pr}_{0.9}\mathrm{Ca}_{0.1}\mathrm{AlO_3}$ when compared to $(\mathrm{Gd,La,Nd,Pr,Sm})_{0.9}\mathrm{Ca}_{0.1}\mathrm{AlO_3}$. The intensity ratio between M_5 and M_4 (I_{M5}/I_{M4}) is calculated and can be seen in the legend of *Figure 5-35(a)*. $\mathrm{Pr}_{0.9}\mathrm{Ca}_{0.1}\mathrm{AlO_3}$ has a value of 1.4 and $(\mathrm{Gd,La,Nd,Pr,Sm})_{0.9}\mathrm{Ca}_{0.1}\mathrm{AlO_3}$ has 1.6. These values can provide approximate concentrations of Pr^{+4} by extrapolating the I_{M5}/I_{M4} values from literature. This was done in the previous chapter in section 5.1.2 in *Figure 5-8*. The interpolation in *Figure 5-8(c)* gives the concentrations of Pr^{+4} of $(\mathrm{Gd,La,Nd,Pr,Sm})_{0.9}\mathrm{Ca}_{0.1}\mathrm{AlO_3}$ and $\mathrm{Pr}_{0.9}\mathrm{Ca}_{0.1}\mathrm{AlO_3}$ as 20 % and 40 %, respectively. Therefore, $(\mathrm{Gd,La,Nd,Pr,Sm})_{0.9}\mathrm{Ca}_{0.1}\mathrm{AlO_3}$ shows lower conductivity with electronic contribution than $\mathrm{Pr}_{0.9}\mathrm{Ca}_{0.1}\mathrm{AlO_3}$ ($\sigma_{\mathrm{pol}} \propto x_{\mathrm{Pr}}^{4+}$). However, the electronic contribution observed from the oxygen partial pressure dependence of conductivity in *Figure 5-34(a)* is very low even though there is multivalent Pr with 20% Pr^{+4} present in the system.

The conductivity via polaron hopping depends mainly on the mobility of the polarons (μ_{elec}). *Figure 5-35(b)* shows the unit cell of the orthorhombic perovskite. It is double of the unit cell of the cubic perovskite from *Figure 5-24*. The propagation of polarons happens through Pr cations (A-site or R site in *Figure 5-35(b)*). The number of next nearest A sites to A-site ions are 6 along the sides. In $\mathrm{Pr}_{0.9}\mathrm{Ca}_{0.1}\mathrm{AlO_3}$, each Pr ion is surrounded by more than five next-nearest Pr ions. The Pr^{+4} content in $\mathrm{Pr}_{0.9}\mathrm{Ca}_{0.1}\mathrm{AlO_3}$ is 40%, which means that two of the next-nearest neighbor ions are Pr^{+4}. This provides a continuous pathway for polaron migration. However, in the case of $(\mathrm{Gd,La,Nd,Pr,Sm})_{0.9}\mathrm{Ca}_{0.1}\mathrm{AlO_3}$, the Pr ions are surrounded by multiple elements that decreases the number of Pr ions adjacent to Pr from 5 to 1. Furthermore, the

content of Pr^{+4} in $(Gd,La,Nd,Pr,Sm)_{0.9}Ca_{0.1}AlO_3$ is 20%, which reduces the number of Pr^{+4} ions adjacent to Pr^{+3} from 2 to 0.2. This breaks the pathway for polaron migration, thereby reducing the mobility of the polarons. Therefore, we hypothesize that the reduced electronic contribution observed in $(Gd,La,Nd,Pr,Sm)_{0.9}Ca_{0.1}AlO_3$ is a consequence of lower concentration of Pr^{+4} and lower mobility for polaron propagation. Consequently, the effect of Pr on the conductivity of $(Gd,La,Nd,Pr,Sm)_{0.9}Ca_{0.1}AlO_3$ is minimal. However, $Pr_{0.9}Ca_{0.1}AlO_3$ has a large electronic contribution due to Pr. Therefore, it's considered to be an electronic conductor and is not explored further in this study.
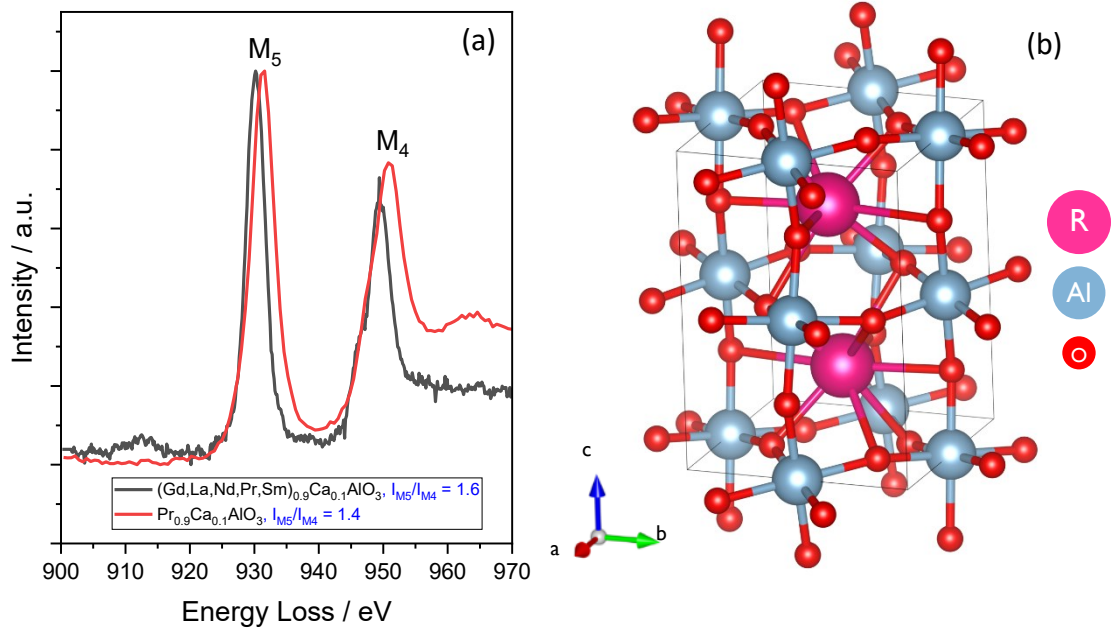
Figure 5-35 (a) Electron energy loss spectra of $(Gd,La,Nd,Pr,Sm)_{0.9}Ca_{0.1}AlO_3$ and $Pr_{0.9}Ca_{0.1}AlO_3$ and (b) Unit cell of an orthorhombic perovskite structure where R = La, Pr, Nd, Sm, Gd, and Ca.

All the other doped rare earth aluminates in this study predominantly show an ionic conduction and p-type electronic conduction from oxygen exchange under oxidizing conditions. The total conductivity $(\sigma_{tot}(T, p(O_2)))$ of these systems can be written as the sum of ionic and p-type electronic conduction which is

$$\sigma_{tot}(T, p(O_2)) = \sigma_{ion}(T) + \sigma_{elec}(T, p(O_2)) \qquad \text{Eq. 5-24}$$

Here $\sigma_{ion}(T)$ is the ionic conductivity and $\sigma_{elec}(T, p(O_2))$ is the p-type electronic conduction.

The ionic conduction is assumed to be constant over the oxygen partial pressures range used in this study. This assumption is valid because the conductivity reaches an ionic plateau

at $\log(p(O_2)) < -2$ as observed in *Figure 5-34*. However, from *Eq. 5-22*, the electronic conduction depends on the oxygen partial pressure. Consequently, the total conductivity can be written as

$$\sigma_{\text{tot}}\big(T, p(O_2)\big) = \sigma_{\text{ion}}(T) + \sigma_{elec}(T) \times p(O_2)^{\frac{1}{4}} \qquad\qquad \textit{Eq. 5-25}$$

Furthermore, a kink is observed in the Arrhenius plot in *Figure 5-33* at 500 °C indicating two different conduction mechanisms above and below 500 °C. The decrease in activation energy at high temperatures in the Arrhenius plot of oxygen ion conductors might be due to either different contributions from grains and grain boundaries or defect association with dopant at lower temperatures [16,120,121,159–162]. Therefore, multiple models are considered for the conductivity mechanism which are as follows

1) Grains and grain boundaries: The change in conduction mechanism is assumed to be a consequence of different ionic and electronic conduction mechanisms from grains and grain boundaries. In polycrystalline samples, it is reasonable to assume that the grains and grain boundaries are in series. A simple representation and the equivalent electrical circuit of such a model is presented in *Figure 5-36*. The total conductivity derived from the current model can be written as

$$\sigma_{\text{tot}} = \left(\left(\frac{1}{\sigma_{ion}^{Grain}} + \frac{1}{\sigma_{ion}^{GB}} \right)^{-1} + \left(\frac{1}{\sigma_{elec}^{Grain}} + \frac{1}{\sigma_{elec}^{GB}} \right)^{-1} \right)^{-1} \qquad \textit{Eq. 5-26}$$
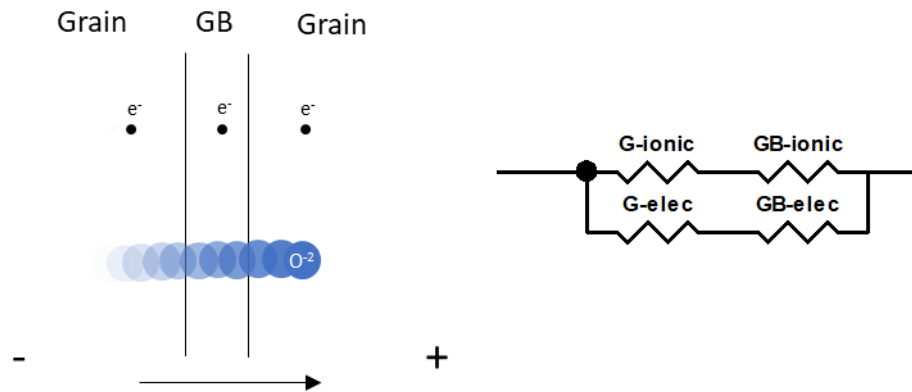
Figure 5-36 A simple representation of the grain and grain boundary model along with equivalent electrical circuit. Here GB is grain boundary, G is grain, ionic is the electrical element representing ionic conduction and elec is the electrical element representing the electronic conduction.

2) Defect association between oxygen vacancies and dopants: The defects in such systems are observed to localize near the dopants due to its lower charge and repulsive forces between the defects and the dopants compared to the lattice cations. This localization results in the formation of defect associates which reduce the mobility and increase the activation energy for migration of the charge carrier [16,120,121,159–162]. At higher temperatures, the defect associates dissociate thereby increasing the mobility and reducing the activation energy for migration of the charge carriers. The defect association can be between the dopant and the oxygen vacancies or holes. The total conductivities and corresponding equivalent circuits are summarized in *Table 5-8*. The total conductivities with different defect associate models are given by:
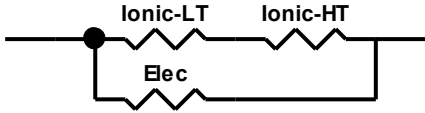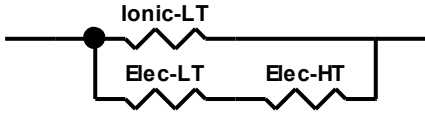
For $(Ca'_{Re}V_o^{\bullet\bullet})^x$,

$$\sigma_{\text{tot}} = \left(\frac{1}{\sigma_{ion}^{LT}} + \frac{1}{\sigma_{ion}^{HT}}\right)^{-1} + \sigma_{elec} \qquad \text{Eq. 5-27}$$

For $(Ca'_{Re}h^{\bullet})^x$,

$$\sigma_{\text{tot}} = \sigma_{ion} + \left(\frac{1}{\sigma_{elec}^{LT}} + \frac{1}{\sigma_{elec}^{HT}}\right)^{-1} \qquad \text{Eq 5-28}$$

Table 5-8 Defect association and corresponding equivalent circuit. Here LT is the conduction element at low temperature, HT is the conduction element at high temperature, ionic is the element corresponding to ionic conduction and elec is the element corresponding to the electronic conduction.

Defect association	Equivalent circuit
$Ca'_{Re} + V_o^{\bullet\bullet} \leftrightarrow (Ca'_{Re}V_o^{\bullet\bullet})^x$	
$Ca'_{Re} + h^{\bullet} \leftrightarrow (Ca'_{Re}h^{\bullet})^x$	

The models above were used to fit the data in *Figure 5-33* and *Figure 5-34*. The defect association model with dopant and holes forming an associate ($(Ca'_{Re}h^\bullet)^x$) is superior to the other models, since it allows fittings the data with the least number of parameters. Consequently, the total conductivity data is fitted with the $(Ca'_{Re}h^\bullet)^x$ model. Total conductivity from $(Ca'_{Re}h^\bullet)^x$ model after applying the Arrhenius equation and pressure dependence to oxygen partial pressure can be written as

$$\sigma_{tot}(T, p(O_2)) = \frac{\sigma_o^{ion}}{T}\exp\left(-\frac{E_A^{ion}}{k_BT}\right) + \frac{\sigma_{elec,0}^{LT}\sigma_{elec,0}^{HT}}{T}\left(\frac{\exp\left(-\frac{E_A^{LT}+E_A^{HT}}{k_BT}\right)}{\sigma_{elec,0}^{LT}\exp\left(-\frac{E_A^{LT}}{k_BT}\right)+\sigma_{elec,0}^{HT}\exp\left(-\frac{E_A^{HT}}{k_BT}\right)}\right)p(O_2)^{\frac{1}{4}} \qquad \textit{Eq. 5-29}$$

here, σ_o^{ionic} is the conductivity pre-factor for ionic conductivity, E_A^{ionic} is the activation energy for ion migration, $\sigma_{elec,0}^{LT}$ is the conductivity pre-factor for electronic conductivity at temperatures below 500 °C, $\sigma_{elec,0}^{HT}$ is the conductivity pre-factor for electronic conductivity at temperatures above 500 °C, E_A^{LT} is the activation energy for electron migration at temperatures below 500 °C and E_A^{HT} is the activation energy for electron migration at temperatures above 500 °C. The σ_o^{ionic}, $\sigma_{elec,0}^{LT}$ and $\sigma_{elec,0}^{HT}$ are conductivity pre-factors of different charge carriers which are a function of the charge carriers present in the system. In this case, the conductivity prefactors depend on the oxygen vacancies present in the system. Since all of them have the same Ca content (10 at.%), it is reasonable to assume that they have the same oxygen vacancy concentration and conductivity pre-factors. Therefore, the conductivity pre-factors were set to the same values for all samples fitted with the model: σ_o^{ionic}=20000, $\sigma_{elec,0}^{LT}$=15000, and $\sigma_{elec,0}^{HT}$=3.73 * 10^{-10}. The different contributions to the total conductivity are plotted in an Arrhenius representation and log(σ) vs. log ($p(O_2)$) for $La_{0.9}Ca_{0.1}AlO_3$ which can be seen in *Figure 5-37*. The model fits the data very well across the entire temperature range. The model also represents the kink as observed from *Figure 5-37(a)*. However, there is a slight misfit at low oxygen partial pressures in *Figure 5-37(b)*.
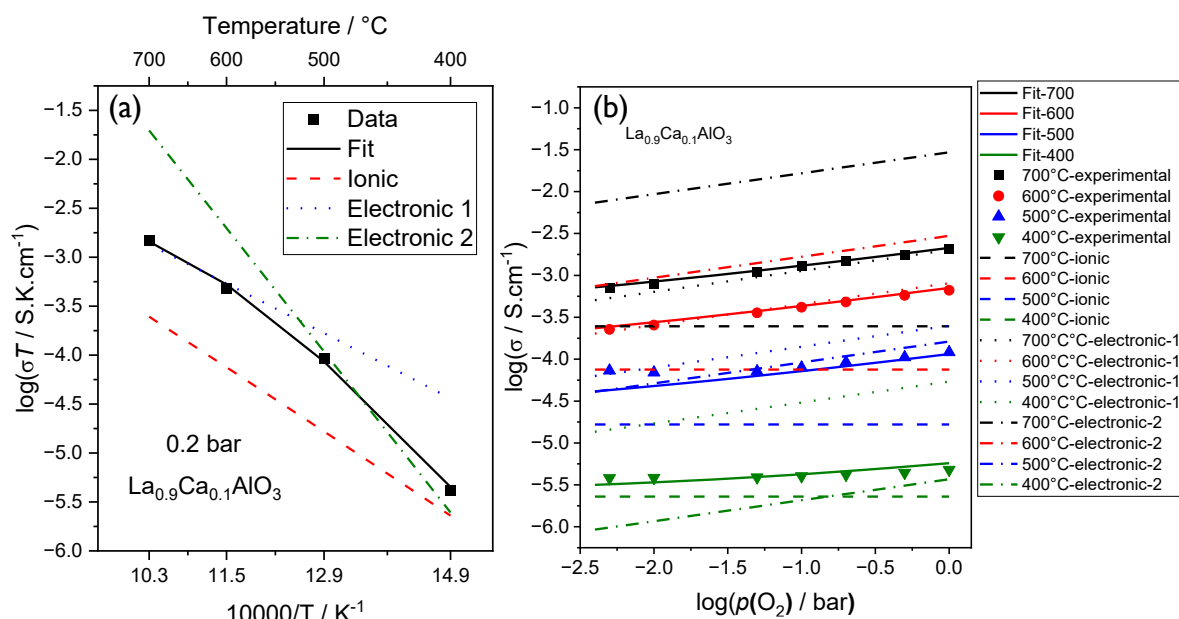
Figure 5-37 (a) Fit of the experimental data of La$_{0.9}$Ca$_{0.1}$AlO$_3$ using Eq. 5-29 at different temperatures and pressures with different ionic and electronic contributions. Here electronic 1 is the electronic contribution above 500 °C and electronic 2 is the electronic contribution below 500 °C.(b) Arrhenius representation of experimental data and the fits of La$_{0.9}$Ca$_{0.1}$AlO$_3$ with the help of Eq. 5-29 along with the three corresponding contributions. Here electronic 1 is the electronic contribution above 500 °C and electronic 2 is the electronic contribution below 500 °C.

The activation energies for ionic conduction and electronic conduction above and below 500 °C are calculated from the model. These values of the activation energy values are presented in the bar graph in *Figure 5-38*. The activation energies for ion propagation in all compositions are lower than of the electron migration below 500 °C. This indicates the ease of ion migration compared to electron migration. However, as the temperature increases above 500 °C, the dopant – hole defect associate $(Ca'_{Re}h^{\bullet})^x$ breaks down resulting in an increase in hole mobility. Consequently, the activation energies for the hole migration drop drastically and are lower than the activation energies for ion migration. As a result, the ease for hole migration is higher than the ion migration above 500 °C for all the single component doped rare earth aluminates (La$_{0.9}$Ca$_{0.1}$AlO$_3$, Nd$_{0.9}$Ca$_{0.1}$AlO$_3$, Sm$_{0.9}$Ca$_{0.1}$AlO$_3$, Gd$_{0.9}$Ca$_{0.1}$AlO$_3$). However, for the high entropy oxide, (Gd,La,Nd,Pr,Sm)$_{0.9}$Ca$_{0.1}$AlO$_3$, the activation energy for ions remains lower than the activation energy of the electrons above 500 °C. This indicates that the ease of ion migration is not affected by temperature and stays higher than the electron migration in the high entropy oxide. It should be noted that the ionic activation energy is lowest in the high

entropy oxide as well, indicating that the high entropy oxide might be a better ionic conductor than the single component doped rare earth aluminates.
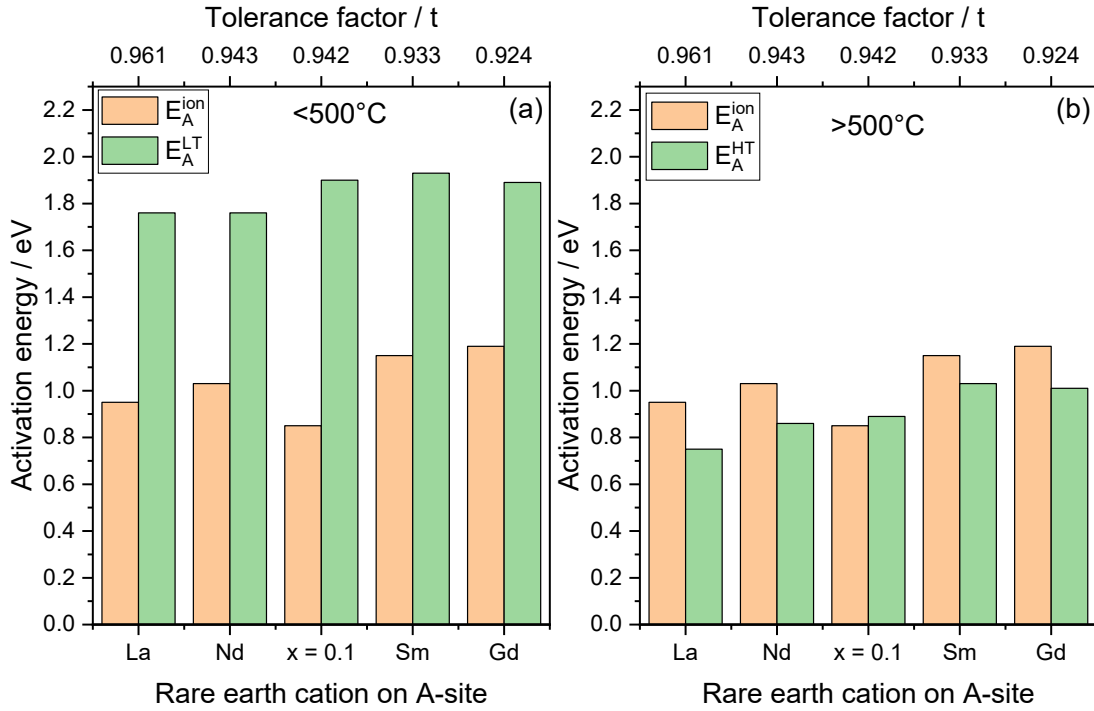
Figure 5-38 (a) Activation energies for ion migration (E_A^{ion}), electron migration below 500 °C (E_A^{LT}), and (b) Activation energies for ion migration (E_A^{ion}), electron migration above 500 °C (E_A^{HT}) of (Gd,La,Nd,Pr,Sm)$_{0.9}$Ca$_{0.1}$AlO$_3$ - x=0.1 , La$_{0.9}$Ca$_{0.1}$AlO$_3$ - La , Nd$_{0.9}$Ca$_{0.1}$AlO$_3$ - Nd, Sm$_{0.9}$Ca$_{0.1}$AlO$_3$ - Sm, Gd$_{0.9}$Ca$_{0.1}$AlO$_3$ – Gd along with the tolerance factors. The activation energies were calculated from the experimental data in Figure 5-33 and Figure 5-34 with the help of Eq. 5-29.

Nevertheless, for practical purposes, the ionic conductivity as well as the oxygen transference numbers are important and should be high for a good ionic conductor. The ionic conductivity and the oxygen transference number are plotted versus the tolerance factor and the ionic radii, which can be seen in *Figure 5-39*. The ionic conductivity in the single component rare earth aluminates is increasing with increasing tolerance factor. The observed increase is a consequence of the volume of unit cell becoming bigger with tolerance factor (*Figure 5-24(b)*) and ionic radii thereby facilitating the movement of the oxygen ions through the lattice and thus increasing the ionic conductivity. This correlation between the structure and ionic conductivity is often observed and well explored in the literature of oxygen ion conductors [5,23,124,146]. Even though, the high entropy oxide - (Gd,La,Nd,Pr,Sm)$_{0.9}$Ca$_{0.1}$AlO$_3$ has a tolerance factor between Nd$_{0.9}$Ca$_{0.1}$AlO$_3$ and Sm$_{0.9}$Ca$_{0.1}$AlO$_3$, it has the highest ionic conductivity as depicted in *Figure 5-39(a)*. The transference number is also highest in high entropy oxide -

$(Gd,La,Nd,Pr,Sm)_{0.9}Ca_{0.1}AlO_3$ in *Figure 5-39(b)*. Therefore, the high entropy oxide - $(Gd,La,Nd,Pr,Sm)_{0.9}Ca_{0.1}AlO_3$ is an ionic conductor with better ionic conduction and oxygen transference numbers than single component doped rare earth aluminates - $La_{0.9}Ca_{0.1}AlO_3$, $Nd_{0.9}Ca_{0.1}AlO_3$, $Sm_{0.9}Ca_{0.1}AlO_3$, $Gd_{0.9}Ca_{0.1}AlO_3$.
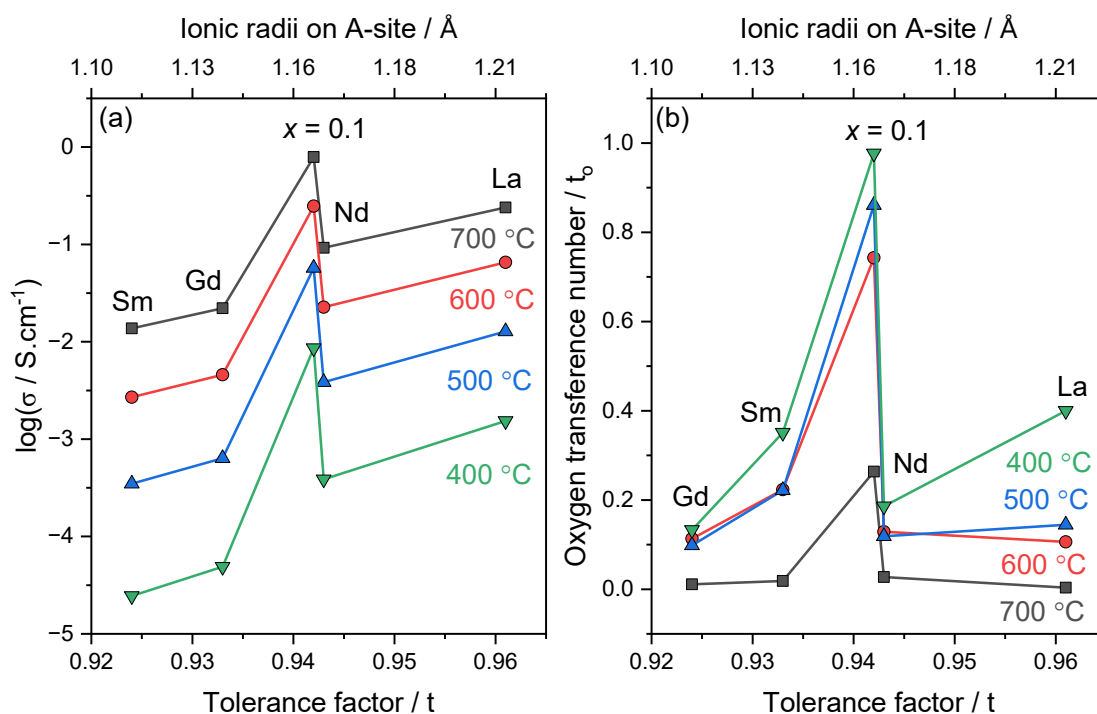
Figure 5-39 (a) Ionic conductivity and (b) Oxygen transference numbers of $(Gd,La,Nd,Pr,Sm)_{0.9}Ca_{0.1}AlO_3 - x = 0.1$, $La_{0.9}Ca_{0.1}AlO_3$ - La , $Nd_{0.9}Ca_{0.1}AlO_3$ - Nd, $Sm_{0.9}Ca_{0.1}AlO_3$ - Sm, $Gd_{0.9}Ca_{0.1}AlO_3 - Gd$ vs. the tolerance factors and ionic radii of A-site cation at 400, 500, 600 and 700 °C. The ionic conductivity and the oxygen transference numbers were calculated from the experimental data in Figure 5-33 and Figure 5-34 using Eq. 5-29 for fitting.

The conductivity of the high entropy oxide - $(Gd,La,Nd,Pr,Sm)_{0.9}Ca_{0.1}AlO_3$ is compared with the state of the art oxygen ion conductor – yttria stabilized zirconia (YSZ). The YSZ pellets were prepared using commercially available YSZ powders from Neyco, following the same sintering parameters as the high entropy oxide to achieve comparable grain size and density. The high entropy oxide has slightly lower conductivity than YSZ. However, the conductivity can be increased in future studies by double doping of the perovskite structure on both A-site and B-site as this is known to increase the conductivity in $RAlO_3$ and $RGaO_3$ [23,163]. To conclude, we introduced the high entropy concept as a potential strategy to mitigate the p-type conduction

observed in the doped rare earth aluminates by moving the surface exchange reaction causing the electronic contribution to higher temperatures.

5.2.8 Conclusions

Perovskite structured high entropy rare earth aluminates - $(Gd_{0.2}La_{0.2}Nd_{0.2}Pr_{0.2}Sm_{0.2})_{1-x}Ca_xAlO_3$ with different Ca content are synthesized and investigated for oxygen ionic conductivity. The powders of these high entropy oxides are synthesized by sol-gel (Pechini) method after which the powders are pressed into pellets and sintered. The pellets are characterized and ionic conductivity was investigated. XRD and Raman results indicate that these compositions crystallize in a single orthorhombic structure with minor secondary phases at a doping content of 15 at.% and 20 at.% of Ca. SEM shows a grain size of around 1-2 microns with the grain size independent of Ca content. EDX from SEM and TEM confirms the presence of all elements in stoichiometric amounts with a homogenous distribution in both micrometer and nanometer range. The EELS and UV-Vis suggest the presence of multivalent Pr. The conductivity increased by a few orders of magnitude with addition of Ca and saturates at a Ca content of 10 at.% with slight decrease with further addition of Ca. The high entropy oxides are compared with the corresponding single component doped rare earth aluminates ($La_{0.9}Ca_{0.1}AlO_3$, $Pr_{0.9}Ca_{0.1}AlO_3$, $Nd_{0.9}Ca_{0.1}AlO_3$, $Sm_{0.9}Ca_{0.1}AlO_3$, $Gd_{0.9}Ca_{0.1}AlO_3$). The high entropy oxide exhibits higher ionic conductivity and higher transference numbers with lower activation energy for ion migration than all of the single component doped rare earth aluminates. The activation energy for electronic conduction in the high entropy oxide is higher than the activation energy for ionic conduction, which is not the case for the single component doped rare earth aluminates. The high entropy approach in the rare earth aluminates resulted in the mitigation of the p-type electronic conduction observed in the rare earth aluminates. Therefore, high-entropy rare earth aluminates are promising candidates for oxygen ion conduction.

6 Anode for solid oxide electrolyzers – water splitting

6.1 Perovskite-type high entropy oxides – La(Co$_{0.2}$Cr$_{0.2}$Fe$_{0.2}$Mn$_{0.2}$Ni$_{0.2}$)O$_3$

In electrolyzer, water is converted into hydrogen and oxygen by application of an electric field. One of the important reactions in electrolysis is the oxygen evolution reaction (OER). It is a complex four step reaction which often suffers from extremely high overpotentials [27]. These overpotentials are due to the energy barriers for formation of the intermediates of the reaction and their respective transition states [26,164,165]. Therefore, to make electrolyzer efficient, it is essential to find materials with lower overpotentials for the OER [166]. One of such material systems known for their high OER catalytic activity are the perovskite-type transition metal oxides (ABO$_3$). They are known for their functional properties which can be carefully manipulated by doping on both A and B site [29,167–172]. Furthermore, State-of-the-art OER catalysts are oxides of expensive noble metals like IrO$_2$ or RuO$_2$ which are not perovskite. However, in the case of perovskite structured transition metal oxides, the noble metals can be eliminated thereby drastically reducing the cost of the catalyst. Nevertheless, the challenge of the high overpotentials for the OER still persists in these perovskite structured transition metal oxides. To overcome this issue, the high entropy concept was introduced into perovskite-type transition metal oxides. In high entropy oxides, multiple elements are substituted in a single lattice site of the structure. The presence of multiple elements in such close proximity can provide multiple active sites and a possible solution to reduce the energy barriers for formation of intermediates thereby reducing the overpotential. This might occur when different intermediates and their corresponding reactions take place at various available adsorption sites [166,173–176]. This theory has been investigated in high entropy alloys [173–176]. Transition metal high

entropy alloys with an oxide layer show very low overpotentials even lower than the standard state-of-the-art benchmarks such as IrO_2 [177]. Therefore, exploring compositional regime of high entropy oxides might provide an oxide composition with good OER activity. In fact, in recent studies on perovskite structured transition metal high entropy oxides, overpotentials lower than the standard state-of-the-art catalysts have been observed [82,178,179]. Although these studies have shown exceptional OER activity in high entropy oxides, systematic studies investigating the electrocatalytic activity by separating the complex powder morphologies and undefined surface areas have not yet been investigated.

In this section of the thesis, we explore the perovskite structured transition metal high entropy oxide - $La(Co_{0.2}Cr_{0.2}Fe_{0.2}Mn_{0.2}Ni_{0.2})O_3$ (PHEO). The OER activity of PHEO was systematically compared with the OER activity of the corresponding single component perovskite structured transition metal oxides. Jaramillo, Nørskov, Rossmeisl, and Markovic groups emphasized that comparing intrinsic activity across multiple compositions should occur using identical sample geometries and, ideally, single crystalline surfaces [26,180]. This approach becomes more critical for high entropy electrocatalysts, given the complexity in composition, structure and physical properties, which presents a significant challenge in understanding structure-activity relationships [181,182]. The oxides in this section were synthesized as epitaxial thin films to systematically compare the structure-property relationships between the high entropy oxide and the corresponding single component oxides. The epitaxial thin films were deposited by pulsed laser deposition on a (001)-oriented, TiO_2-terminated, and step-terraced Nb-$SrTiO_3$ substrate. The resultant thin films were characterized by X-ray reflectivity (XRR), high resolution X-ray diffraction (XRD), transmission electron microscopy (TEM), and X-ray photoemission spectroscopy (XPS). The characterized films were electrochemically tested for OER activity and ambient pressure XPS.

6.1.1 Structural, morphological and chemical characterization

High resolution X-ray diffraction (HRXRD) was conducted on epitaxial thin films of P-HEO on Nb: $SrTiO_3$ substrates. The HRXRD patterns are shown in *Figure 6-1(a)*. The Laue fringes from the epitaxial thin films can be identified in *Figure 6-1(a)*. The presence of Laue fringes suggests a highly crystalline epitaxial thin film of P-HEO. The width of the Laue fringes indicates a thickness of 11 nm. The (200) Bragg reflection resulting from the epitaxial film is very close and overlaps with the (200) Bragg reflection of the substrate Nb: $SrTiO_3$ as observed in *Figure 6-1(a)*. Furthermore, the out of plane lattice parameter of P-HEO is estimated to be

3.86 Å. The HRXRD pattern of single component perovskite-type oxides – $LaCrO_3$, $LaMnO_3$, $LaFeO_3$, $LaCoO_3$, $LaNiO_3$ are shown in *Figure 6-1(b),(c),(d),(e),(f)*. All the single component perovskite oxides show epitaxial thin film growth with good crystalline nature. The surface morphology of the thin films was investigated by atomic force microscopy. The atomic force micrographs are presented in *Figure 6-2*. All the epitaxial films of all the perovskite structured oxides exhibit a roughness below 200 pm. Due to the low roughness of the films, their surface area can be approximated as the geometric surface area.
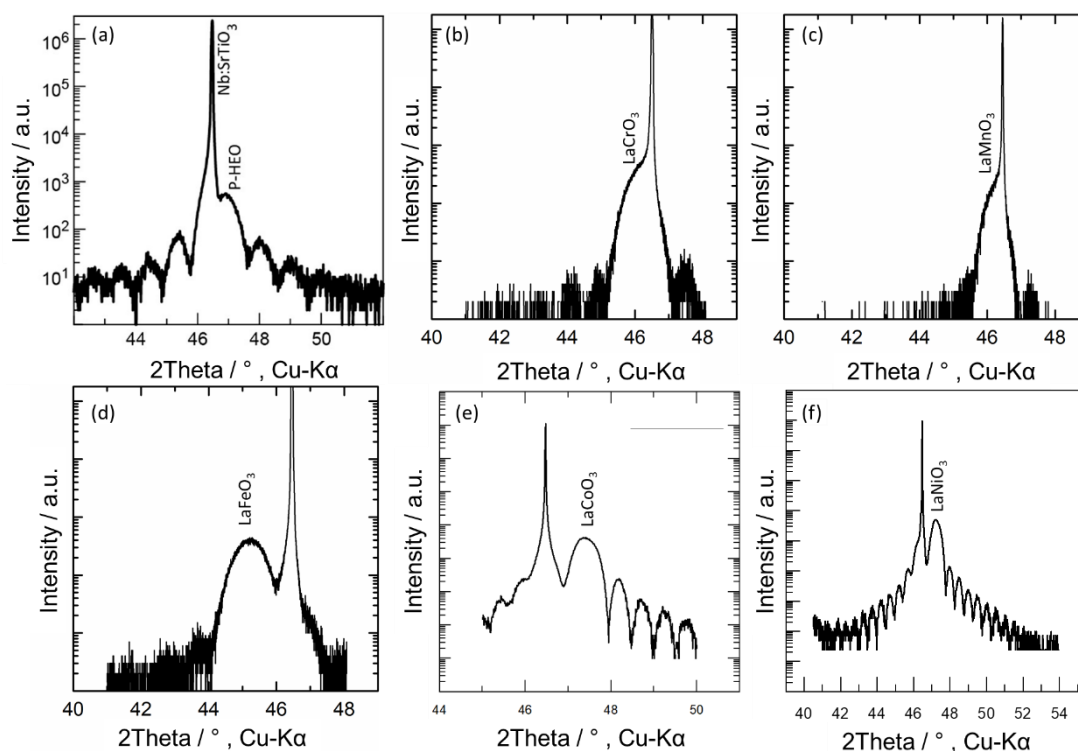
Figure 6-1 The high resolution X-ray diffraction patterns of epitaxial thin films of (a) $La(Co_{0.2}Cr_{0.2}Fe_{0.2}Mn_{0.2}Ni_{0.2})O_3$ – PHEO, (b) $LaCrO_3$, (c) $LaMnO_3$, (d) $LaFeO_3$, (e) $LaCoO_3$ and (f) $LaNiO_3$ deposited on Nb:STO substrate.
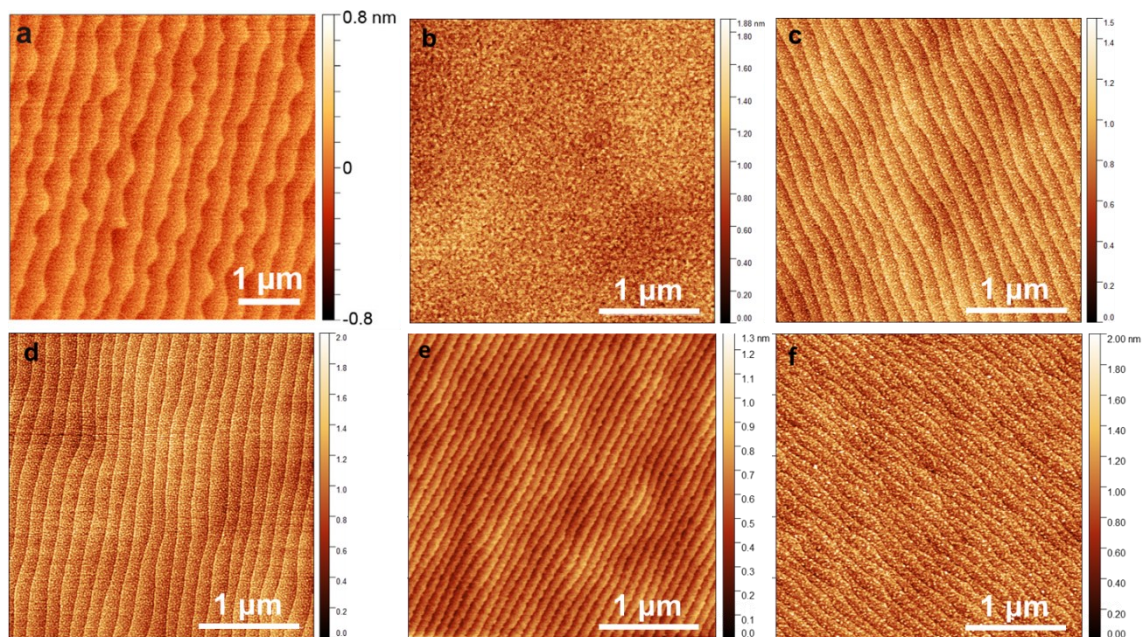
Figure 6-2 Atomic force microscopy images of (a) La(Co$_{0.2}$,Cr$_{0.2}$,Fe$_{0.2}$,Mn$_{0.2}$,Ni$_{0.2}$)O$_3$ – PHEO, (b) LaCrO$_3$, (c) LaMnO$_3$, (d) LaFeO$_3$, (e) LaCoO$_3$ and (f) LaNiO$_3$ deposited on Nb:STO substrate.

Transmission electron microscopy (TEM) was performed on the P-HEO film. The STEM image of the P-HEO epitaxial thin film can be seen in Figure 6-3*(a)*. The micrograph reveals a highly ordered atomic arrangement at the interface between the film and the substrate. The SAED pattern in *Figure 6-3(b)* reveals a single crystal confirming the crystalline nature and the epitaxy of the film. A closer inspection of the micrograph in *Figure 6-3(a)* is depicted in *Figure 6-3(c)* showing the stacking of A and B site consecutively where yellow spots are the A-site ions and red spots are the B-site ions. In the P-HEO film, La is on A-site (yellow spot) and the transition metal elements on the B-site (red spot) as depicted in *Figure 6-3(c)*. The energy dispersive X-ray spectroscopy (EDS) maps are presented in *Figure 6-3(d)* which show a homogenous distribution of transition metal elements and La with no hints of segregation. EDS maps can help clearly differentiate the substrate and the film as the Sr and Ti rich region is the substrate and the area with La, Co, Cr, Fe, Mn, Ni is the P-HEO epitaxial thin film. The chemical composition of the P-HEO extracted from the EDS maps can be in *Table 6-1*. The chemical composition shows a slight La deficiency.
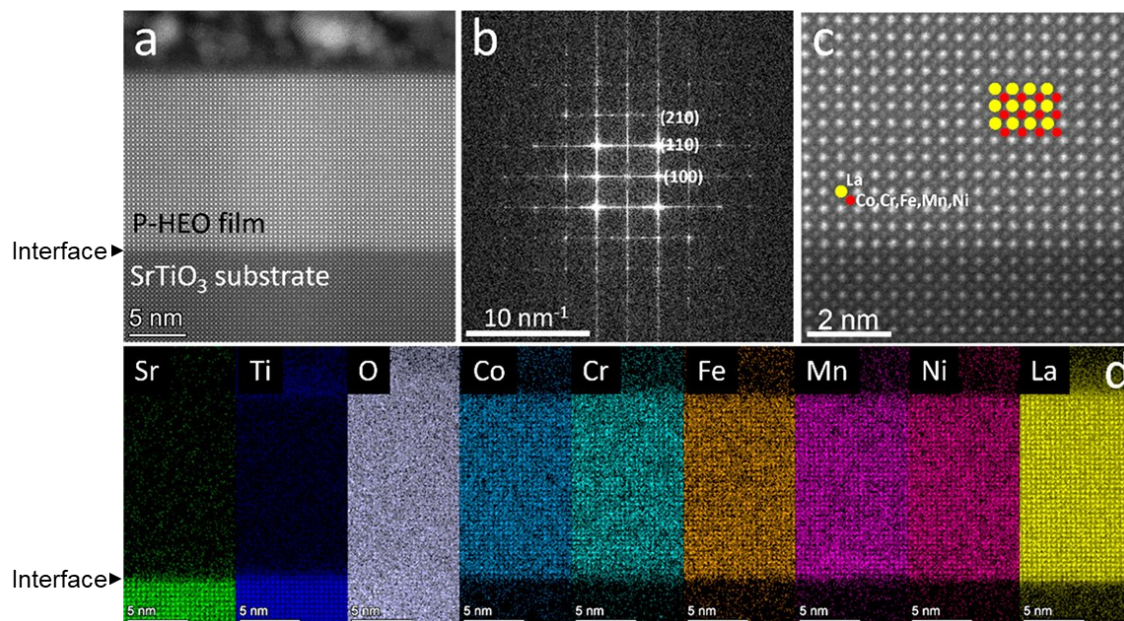
Figure 6-3 (a) Scanning transmission electron micrograph of cross-section of P-HEO epitaxial film. (b) Selected area electron diffraction pattern extracted from the Fast Fourier Transform of micrograph of the P-HEO epitaxial thin film. (c) Magnified image of the micrograph of cross-section of P-HEO, and (d) energy dispersive X-ray spectroscopy (EDS) maps along the cross-section of P-HEO epitaxial film.

Table 6-1 The chemical composition in atomic percentage of P-HEO epitaxial film extracted from the EDS maps in Figure 6-3(d).

Element	Content (at.%)	Nominal content (at.%)
La	46.3 ± 3	50
Cr	9.81 ± 0.8	10
Co	11.25 ± 1.6	10
Fe	11.1 ± 1.5	10
Mn	11.1 ± 1.4	10
Ni	10.3 ± 1.5	10

EELS was conducted in the TEM on the epitaxial thin film of P-HEO. EELS can provide valuable information on the valence state of the elements. The edge positions and intensity ratio of L_3 and L_2 edges of Cr, Mn, Fe, Co can provide information about the oxidation state of these elements. The EELS spectra of edges of all the elements except Ni present in P-HEO are shown in *Figure 6-4.* The EELS of Ni L edge was not possible to collect because the Ni L-edge and La M-edge coincide with each other making Ni L-edge harder to detect. The intensity ratio

between L_3 and L_2 (I_{L3}/I_{L2}) were calculated from the data in *Figure 6-4*. The intensity ratio and the edge positions of the L edges depicted in *Table 6-2*. The edge positions and I_{L3}/I_{L2} indicate that Cr and Fe show +3 oxidation state [183,184] whereas Co and Mn show a mixture of +2 and +3 oxidation states [184,185]. The M edge of La in *Figure 6-4(f)* suggests that La exhibits a +3-oxidation state corresponding to the stable ^{54}Xe inert gas configuration. However, a La deficiency is observed in *Table 6-1*, which is compensated by observed multivalency in Co and Mn.
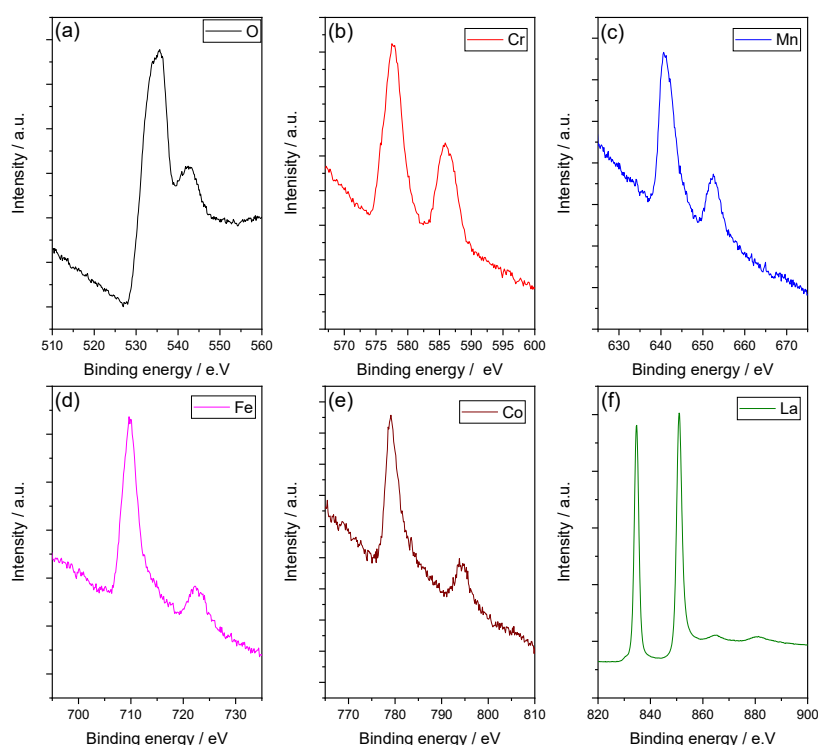
Figure 6-4 Electron Energy Loss Spectroscopy (EELS) spectra of P-HEO epitaxial film at (a) O edge (b) Cr edge (c) Mn edge (d) Fe edge (e) Co edge and (f) La edge.

Table 6-2 The edge position, Intensity ratio between L_3 and L_2 edge (I_{L3}/I_{L2}) and oxidation state of Cr, Fe, Mn and Co. These values were extracted from the EELS spectra in Figure 6-4.

Element	L₃ edge position	I_{L3}/I_{L2}	Oxidation state
Cr	577.3	1.8	+3[183]
Mn	641.4	2.6	+2/+3 mixture (66% - +3, 33% -+2)[184,185]
Fe	707.8	4.6	+3[185]
Co	778.9	3.9	+2/+3 mixture (66% - +2, 33% -+3)[184]
La	834.6 (M₅)	1	+3

6.1.2 Catalytic activity

Cyclic voltammetry was used to measure the OER activity of the films. The OER measurement was conducted in O_2 saturated 0.1 M KOH solution with a rotating disc electrode in a three-electrode configuration. The resistance resulting from the setup for different films can be calculated from the impedance spectroscopy measurements in *Figure 6-5(a)*. The resistances of the circuit are around 50 ohms except for $LaNiO_3$, which has a resistance of around 410 ohms. As a result, the cyclic voltammetry (CV) plots are generated by averaging cathodic and anodic scans as well as compensating for the system's resistance. The CV plots in *Figure 6-5(b)* summarizes the OER activity of P-HEO and its corresponding single component oxides. P-HEO exhibits way better OER activity than the corresponding single component oxides. Furthermore, in the current density at 1.68 V potential vs. reversible hydrogen electrode (RHE) in *Figure 6-5(c)*, current densities of P-HEO are 17 times higher than $LaNiO_3$ and $LaCoO_3$, approximately 45 times higher than $LaMnO_3$, 680 times higher than $LaCrO_3$ and $LaFeO_3$. The volcano trend predicted by density functional theory (DFT) [28] is portrayed as red transparent triangle in the background of *Figure 6-5(c)*. This predicted trend is a result of the increasing formation energy difference between the O^* and HO^* intermediates (X^* represents the ion, atom or molecule adsorbed on a surface or bound to a site) due to increasing electronegativity of the transition metal [26]. However, $LaFeO_3$ doesn't follow the trend predicted by DFT. The Tafel slopes extracted from Tafel plots in *Figure 6-5(d)* of P-HEO are 51 mV dec^{-1} which are lower than that of $LaNiO_3$ which has a Tafel slope of 128 mV dec^{-1} suggesting an efficient charge transfer at the interface in the P-HEO.
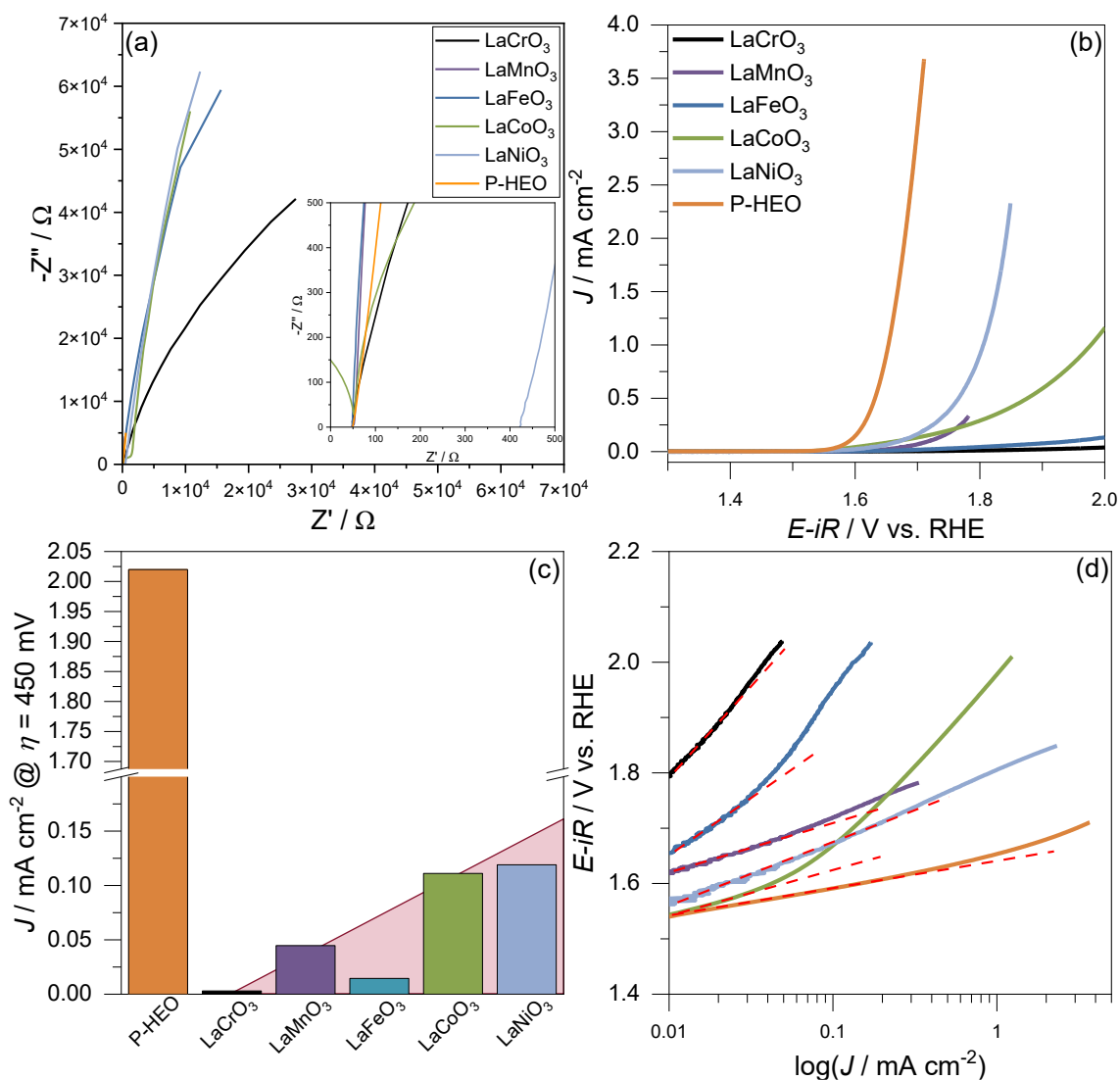
Figure 6-5 (a) Electrochemical impedance spectroscopy of the setup for OER reaction for each film. (b) Cyclic voltammetry of P-HEO and its corresponding single component transition metal perovskite oxide. (c) Comparison of current densities at an overpotential of 450 mV at 1.68 V. The red triangle in the background depicts the predicted OER activity volcano [28]. (d) Tafel plots extracted from Figure 6-5(b) and the red dotted lines indicate the linear portion of the graph depicting tafel slope..

The current density, i, can be transformed to capacitance, C_{dl}, by the following the relation for an ideal electrode:

$$i = C_{dl} \frac{dV}{dt}$$

Eq. 6-1

where i is current response, $\frac{dV}{dt}$ is the change in voltage or voltage scan rate. To determine the double layer capacitance, the cyclic voltammetry of the films is measured in a capacitive region at various voltage scan rates (10 – 500 mVs^{-1}), as shown in *Figure 6-6*. The height of the CV plot for a given scan rate provides the current response. Consequently, the double layer capacitance is the slope of current vs. scan rate and an example of such plot for P-HEO is presented in *Figure 6-7(a)*. The double layer capacitance calculated from *Eq. 6-1* can be seen in *Table 6-3*. All the films exhibit similar double layer capacitances except LaFeO$_3$, indicating a similar number of active sites on the electrode surface for the films contributing to the OER leading to a reasonable comparison of the catalytic activity among the compositions. The preliminary stability tests on P-HEO and LaNiO$_3$ show an enhanced stability in the high entropy oxide when compared to LaNiO$_3$, as observed in *Figure 6-7(b)*. The electrochemical studies show that P-HEO has better OER activity than the corresponding single component transition metal oxides. In order to further understand the enhanced OER activity of the high entropy oxide, valence band states and the oxidation states of the transition metals in different environments (air, O$_2$ and water vapor) were characterized by X-ray photoemission spectroscopy in the following section.
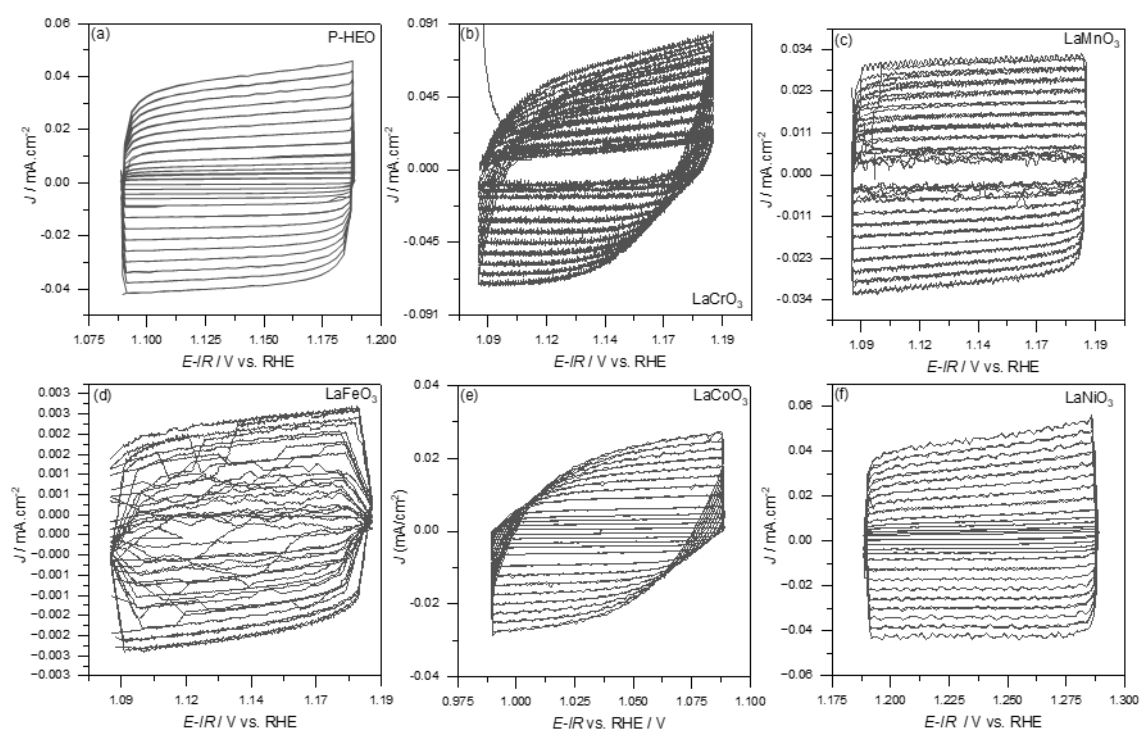
Figure 6-6 Cyclic voltammetry of (a) P-HEO and its corresponding single component oxides (b) LaCrO$_3$ (c) LaMnO$_3$ (d)LaFeO$_3$ (e) LaCoO$_3$ (f) LaNiO$_3$ measured in a potential range where no faradaic reaction occurs, with output current solely from the capacitance of the electrode.

Table 6-3 The double layer capacitances of all the compositions investigated in this study.

Composition	C_{dl} (µF)
$La(Co_{0.2},Cr_{0.2},Fe_{0.2},Mn_{0.2},Ni_{0.2})O_3$	3.478×10^{-5}
$LaCrO_3$	5.74×10^{-5}
$LaMnO_3$	2.26×10^{-5}
$LaFeO_3$	1.92×10^{-6}
$LaCoO_3$	1.93×10^{-5}
$LaNiO_3$	3.89×10^{-5}
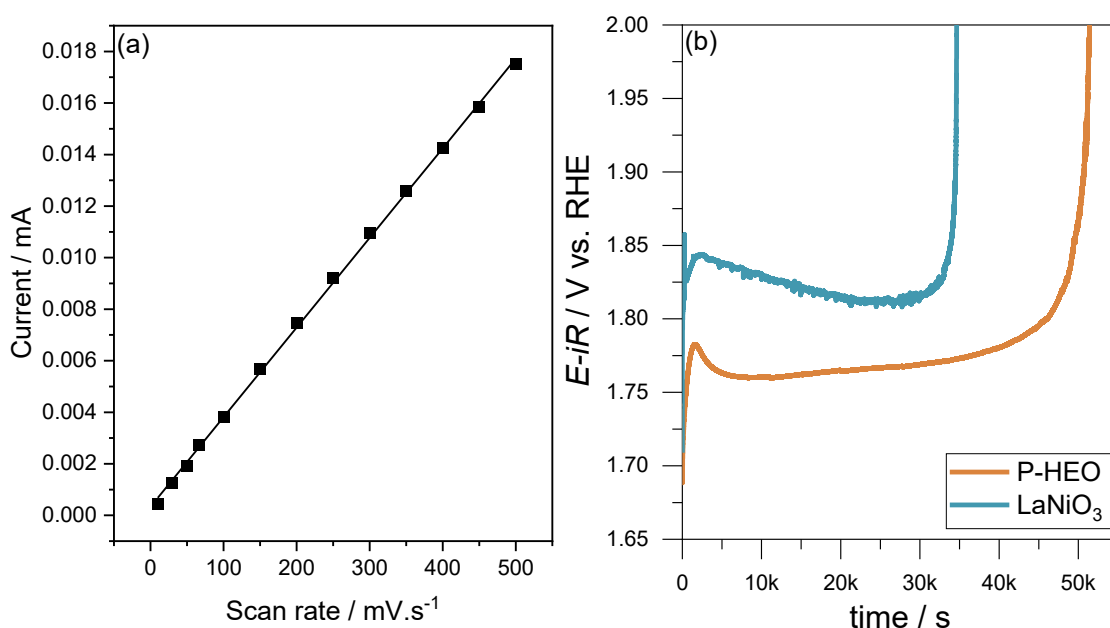
Figure 6-7(a) The current response of the electrode vs. the scan rate of the measurement of P-HEO and (b) chronopotentiometry of the P-HEO and LaNiO₃ at 1 mA cm⁻².

6.1.3 Mechanisms and spectroscopic studies

The valence band spectroscopy of all the films is investigated by X-ray photoemission spectroscopy at low binding energies (eV). The XPS spectra were calibrated using the C 1s peak at 285 eV. The low binding energies of the films can be observed in *Figure 6-8(a)*. The XPS spectra of the single component oxides is similar to the XPS spectra observed in a previous study [186]. The low binding energy XPS consists of three peaks, which are two O 2p peaks corresponding to bonding and non-bonding states and the third peak corresponding to the

unoccupied transition metal (TM) 3d orbital. The difference between the occupied O 2p and partially occupied TM 3d orbital (charge transfer energy) was used as activity descriptors in literature for perovskite-type OER electrocatalysts [187,188]. Therefore, the valence band spectra in *Figure 6-8(a)* was fitted using Voigt function with Shirley background. The current densities show a direct correlation with the energy of O 2p orbital w.r.t to Fermi energy level ($E_{O2p} - E_F$) for the single component transition metal oxides which can be seen in *Figure 6-8(b)*. Out of all the single component transition metal oxides, $LaNiO_3$ has the highest E_{O2p} consequently most OER activity as well as the gap between the unoccupied O 2p and TM 3d is the lowest. Furthermore, it can also be noted that the peak broadening occurs along with an increasing E_{O2p} energy level which leads to an overlap between the TM 3d and O 2p energy states suggesting an increase in covalency of the TM-O bond. The covalency of TM 3d-O 2p bond and the high energy of the unoccupied O 2p orbital is a possible reason for the activity trend observed in the perovskite structured single component transition metal oxides [170,189]. A simple representation of the valence band of $LaNiO_3$ estimated from the fits of *Figure 6-8(a)* can be seen *Figure 6-8(c)*. In contrast, the valence band of $LaCrO_3$ in *Figure 6-8(c)* shows lower E_{O2p} along with no overlap between the TM 3d and O 2p orbital further indicating the lowest covalency in this series. Consequently, the lowest activity is observed in $LaCrO_3$. Moreover, there are only a few densities of states near the Fermi energy level (Binding Energy = 0) of $LaCrO_3$, $LaFeO_3$ and $LaMnO_3$ leading to lower conductivities in these systems, which may further contribute to low OER activities. OER activity of $LaFeO_3$ in *Figure 6-5* does not follow the volcano trend. However, this can be explained by the valence band spectra. E_{O2p} is lower than for $LaMnO_3$. Consequently, $LaFeO_3$ shows lower activity than $LaMnO_3$ and similar to $LaCrO_3$. This might be due to the electronic configuration of Fe^{+3} which is $[Ar] 3d^5 4s^0$. The $3d^5$ configuration might increase the exchange stability leading to lowering of E_{O2p} and decrease in hybridization of the orbitals resulting in lower OER activity. Therefore, the activity trend observed in single component transition metal oxides can be explained by the valence band spectra. For P-HEO, the valence band configuration depicts a covalent nature and the E_{O2p} value is lower than $LaCoO_3$ and $LaNiO_3$ but higher than $LaCrO_3$, $LaFeO_3$ and $LaMnO_3$. According to the E_{O2p} and the covalency, the activity of the P-HEO should be lower than $LaCoO_3$, $LaNiO_3$ and higher than $LaCrO_3$, $LaFeO_3$ and $LaMnO_3$. As a result, the exceptionally high OER activities observed in the P-HEO cannot be explained by the valence band structure of the P-HEO.
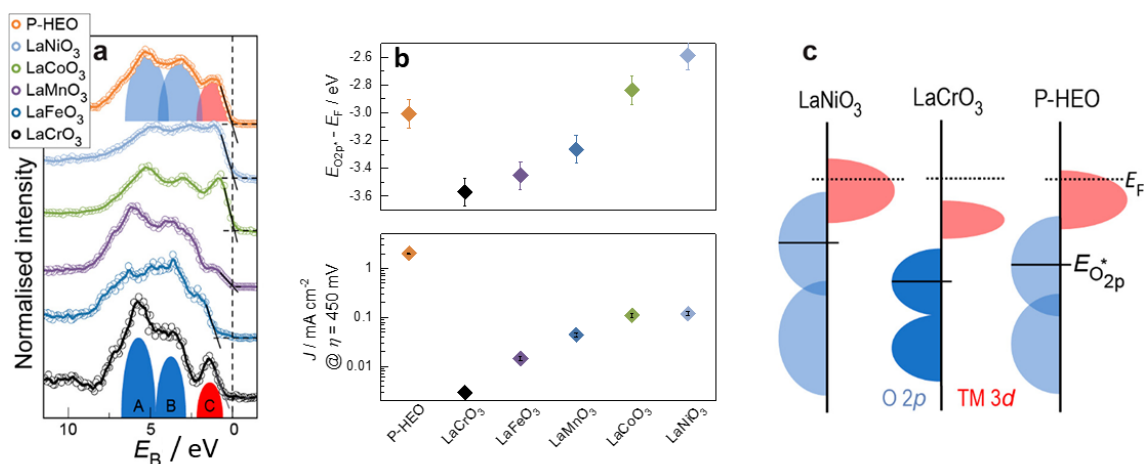
Figure 6-8 (a) Valence band spectra of P-HEO and its corresponding single component transition metal oxides. The peaks A, B in blue represent the O 2p states whereas the peak C in red represent the transition metal 3d states. The maximum of the valence band is represented from the intercept of the zero-photoemission intensity and the linear regression of the low-binding energy of the valence band spectra. (b) Difference between O2p binding energy and Fermi energy level for P-HEO and its corresponding single component oxides along with current density at 1.68 V vs. RHE for all the films. (c) Representation of the band diagrams for LaNiO₃, LaCrO₃ and P-HEO. The band diagrams are extracted from the peaks in Figure 6-8(a).

Alternatively, the synergistic effects of multiple elements on a single lattice site on the partial reactions of the four step OER reaction must be explored. Multiple different elements in the neighboring active sites can help stabilize the OER intermediates that are not favored on a single site and a given element. In P-HEO, there are multiple transition elements (Co,Cr,Fe,Mn,Ni) with different binding abilities which aids in adsorption of different reaction intermediates formed during the OER reaction thereby multiple active sites available for the reaction[190,191]. As a result, to understand the synergistic effects of multiple transition metals on the OER activity, a hypothetical pathway is assumed which can be seen in *Figure 6-9*. The OER mechanism consists of four steps and three reaction intermediates. The initial step of the reaction is the formation of a hydroxyl reaction intermediate (RI1) on the surface of the catalyst. The RI1 gets oxidized to a singlet oxygen (RI2) which is the second step of the OER reaction. This reaction might preferably happen on the strongly binding sites which are Cr and Mn. The RI2 hops onto the weakly binding sites of Co, Ni on which the 3rd and 4th step might occur with smaller potential steps reducing the overall overpotential of the system. It is important to note here that the model considered here is purely hypothetical and needs to be proven by advanced

characterization techniques. Investigation of the surface kinetics for the hydroxyl group as the first reaction of OER, that involves formation and adsorption of the hydroxyl on the surface, can provide more insight. To understand the interactions of the hydroxyl group on the surface of the films, X-ray spectroscopic techniques were used at ambient pressures of O_2, air and H_2O.
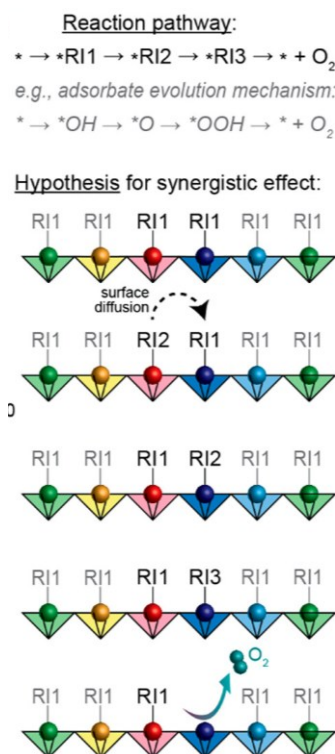
Figure 6-9 Presumed reaction mechanism involving the three intermediates of OER with surface diffusion between a strongly binding ions in red and weakly binding ions in blue.

Ambient Pressure X-ray photoemission spectroscopy (APXPS) and Ambient Press X-ray absorption spectroscopy (APXAS) were measured at ambient pressures under different atmospheres to investigate the binding of the hydroxyl group on the surface of the P-HEO. The samples are pretreated in-situ inside the XPS at 300 °C in O_2 ($p(O_2)$ = 75 mTorr) for cleaning the film of any residues. One more reason for heat treating the sample in an oxygen atmosphere is because the samples were annealed inside the PLD in an oxygen atmosphere. Therefore, this can be a good starting point for investigating the surface adsorption of the hydroxyl groups. The pretreated samples were exposed to water vapour ($p(H_2O)$ = 75 mTorr) at room temperature (25 °C). The pristine samples which are exposed to air during synthesis and transfer. The $p(H_2O)$ in air is assumed to be around 10 Torr as Karlsruhe has humidity levels of 50-75%. Therefore, the air exposed films have been exposed to higher water content than in-situ H_2O measurement. The APXPS of the P-HEO at these three different exposures are shown in *Figure*

6-10. The Cr 2p doublet in Figure 6-10*(a)* shows the presence of large amounts of Cr^{+6} on the sample that is heat treated in the O_2 atmosphere at 300 °C. This Cr^{+6} is reduced after exposure to H_2O and air. The Cr oxidation state decreases with increasing exposure to $p(H_2O)$ with the air exposed sample having the lowest Cr^{+6} and the O_2 annealed sample having the highest Cr^{+6} content. Furthermore, Cr^{+6} is not observed in $LaCrO_3$ annealed in O_2 atmosphere. The APXPS in *Figure 6-10(b)* was conducted at different mean escape depths by changing the X-ray source angle to grazing angles. Cr^{+6} is higher at lower mean escape depths, which suggests that Cr^{+6} is only observed on the surface of the P-HEO sample annealed in O_2. These results suggest surface Cr is more prone to changes in oxidation states in P-HEO than $LaCrO_3$. Along with oxidation of Cr with O_2 treatment, both Ni and Co also show little signs of oxidation as seen in the 3p XPS peak of Ni and Co in *Figure 6-10(c)*. The changes in oxidation state of Ni and Co are small and are around 10 % when compared to a change of 30 % in the case of Cr. The changes in oxidation state of Mn and Fe are not observed in the XPS data. The first step of the OER reaction involves the adsorption of hydroxyl groups on the surface of the catalyst. The adsorption of -OH onto the surface of P-HEO can be clearly observed in the O 2p peak in Figure 6-10*(d)*. The measurement done on the O_2 annealed P-HEO shows no signs of -OH on the surface, whereas the measurement done the H_2O exposed samples show clear signs of -OH on the surface of the film. These results are further explored by APXAS in the following paragraph.
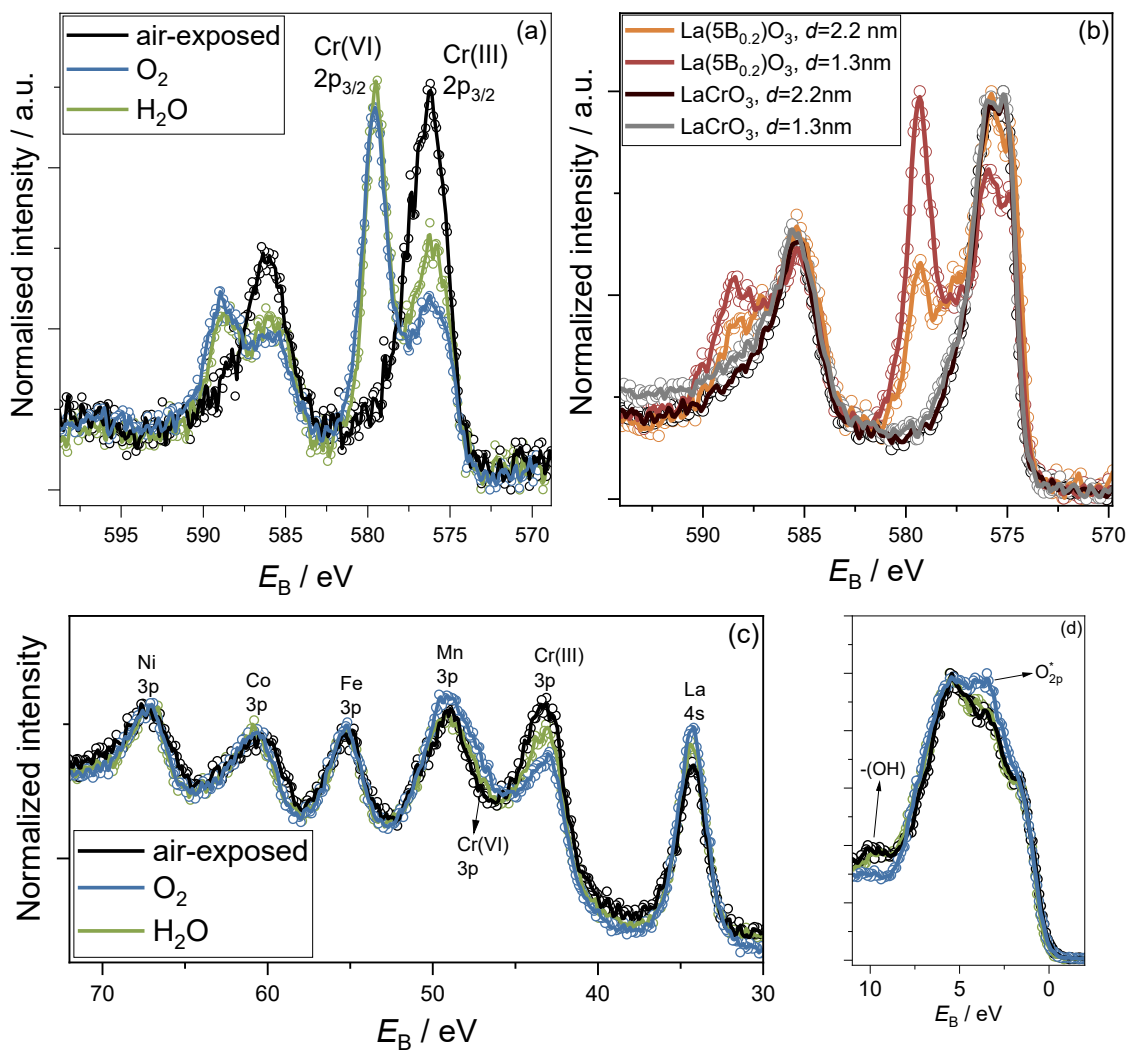
Figure 6-10 (a) APXPS spectra of Cr 2p orbital of P-HEO collected in different atmospheres (O₂, air and H₂O). (b) Comparison of APXPS spectra of Cr 2p orbital of P-HEO and LaCrO₃ collected at different mean escape depths and these measurements were conducted in O₂ atmosphere. (c) The APXPS spectra of TM 3p orbital and La 4s orbital of P-HEO collected in different atmospheres (O₂, air and H₂O). (d) The APXPS spectra of O 2p orbital of P-HEO collected in different atmospheres (O₂, air and H₂O). The scatter plot in the graphs are the experimental data and the line plots are the smoothed curves extracted from the experimental data.

The APXAS data is displayed in *Figure 6-11*. The XAS spectra of Cr L-edge in *Figure 6-11(a)* clearly show reduction of Cr with exposure to water as the Cr^{+6} (Cr(VI)) peak decreases with exposure. The lowest Cr^{+6} is observed in the air exposed sample with the in-situ H_2O measurement showing further decrease of Cr^{+6}. Moreover, reduction of Co is also observed in the L-edge of Co in *Figure 6-11(b)* as the peak shifts to lower energies. However, the oxidation

states of Fe and Mn can be probed from their corresponding L-edges which can be seen in *Figure 6-11(b)* and *Figure 6-11(c)*. No significant change in the spectra as well as oxidation state is observed for Fe and Mn. The oxidation state of Ni cannot be probed with APXAS because the Ni L-edge overlaps with the La M-edge in *Figure 6-11(e)*.
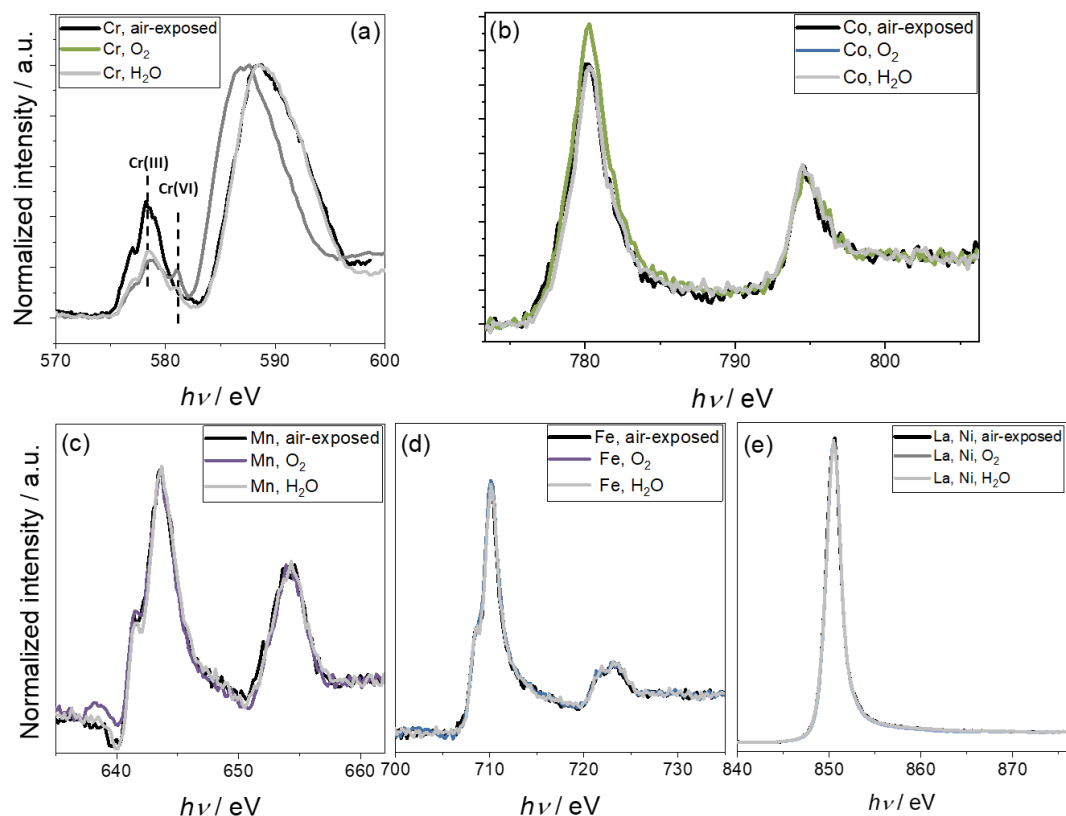
Figure 6-11 (a) The Cr edge of the APXAS spectra of P-HEO collected at different atmospheres (O_2, air and H_2O). (b) The Mn edge of the APXAS spectra of P-HEO collected at different atmospheres (O_2, air and H_2O). (c) The Fe edge of the APXAS spectra of P-HEO collected at different atmospheres (O_2, air and H_2O). (d) The Cr edge of the APXAS spectra of P-HEO collected at different atmospheres (O_2, air and H_2O). (e) The Cr edge of the APXAS spectra of P-HEO collected at different atmospheres (O_2, air and H_2O).

Both APXPS and APXAS results suggest that the oxidation states of Cr, Co and Ni can change readily at different atmospheres (oxidizing or reducing), while the oxidation states of Fe and Mn remain unchanged. The presence of Cr^{+6} is not observed in the single component $LaCrO_3$. As a result, the changes in oxidation states of the TM metals are only observed in the high entropy oxide. Furthermore, the change in oxidation states in different atmosphere is observed only on the top most layer (surface) of the film. It can be speculated that Cr, Co and Ni play an integral role in the OER mechanism in the P-HEO with easily oxidizable Cr in the

HEO matrix, specifically at the surface, contributing to high OER activity. The presence of other elements aids in keeping the structure intact and compensates for the charge imbalance while Cr, Ni and Co are oxidized. The presence of multiple elements with different electronegativities and easily oxidizable cations like Cr, Ni and Co possibly aids the initial step of the OER reaction (-OH formation and adsorption) as well as the following steps which result in the high OER activity observed in the high entropy oxide. According to Sabatier principle, optimum activity is achieved when reaction intermediates bind neither too weakly nor too strongly [26]. Therefore, one could speculate that Cr^{+6} ions may have a low thermodynamic barrier for the initial oxidation (HO* to O* in the adsorbate evolution mechanism), while Ni and Co have a lower thermodynamic barrier for additional oxidation steps (e.g., O* to HOO*). Additionally, Fe and Mn stabilize the structure leading to a synergistic effect among the TM elements of the P-HEO, as schematically depicted in *Figure 6-9*.

6.1.4 Conclusion

La($Co_{0.2}Cr_{0.2}Fe_{0.2}Mn_{0.2}Ni_{0.2}$)$O_3$, a perovskite structured high entropy oxide has been successfully synthesized as an epitaxial thin film by pulsed laser deposition. The epitaxial film exhibits good crystalline nature with surface roughness less than 200 pm. A La deficiency is observed in the films which leads to changes in oxidation states of some transition metal elements. La($Co_{0.2}Cr_{0.2}Fe_{0.2}Mn_{0.2}Ni_{0.2}$)$O_3$ is a highly active OER catalysts. La($Co_{0.2},Cr_{0.2},Fe_{0.2},Mn_{0.2},Ni_{0.2}$)$O_3$ outperforms all of its single component perovskite structured transition metal oxides. The single component perovskite structured transition metal oxides follow the OER behavior expected from the binding energy of the occupied O 2p, energy gap or covalency of the occupied O 2p and partially filled TM 3d shells, and the activity trends predicted by DFT. The valence band analysis indicates covalency in the high entropy oxide which is beneficial for the OER reaction. However, the OER activity is exceptionally higher than the trends expected from the above electronic structure depicters. Transition metal ions especially Cr is observed to readily oxidize or reduce depending on the environment in the high entropy oxide. These changes in valence state are only confined to the surface of the film. However, it is interesting to note that the change in oxidation state of Cr is not observed in $LaCrO_3$. Consequently, the flexibility in the oxidation state of transition metal ions while maintaining the structure in different environments in the high entropy oxide leads to synergistic effects in binding the surface adsorbates by creating multiple active sites, thereby possibly enhancing the OER catalytic activity.

7 Concluding remarks and outlook

7.1 Concluding remarks

In this dissertation, high entropy materials are explored as oxygen ion conductors and catalysts for oxygen evolution reaction.

Synthesis of high entropy oxides

Chapter 4 of the dissertation focuses on synthesizing high entropy oxides in the form of powders, thin films, and dense pellets. The methods employed for fabricating powders include reverse co-precipitation, the Pechini process, and mechanochemical synthesis. These methods yield powders that exhibit a single-phase fluorite structure. The powders are subsequently used to consolidate and densify pellets through conventional sintering. However, due to the high sintering temperatures, the pellets display a mixture of fluorite and bixbyite phases. Thin films are produced using the Pechini process and Pulsed Laser Deposition. All the resulting thin films demonstrate a fluorite structure. Notably, three distinct morphologies are observed for the thin films deposited by Pulsed Laser Deposition: polycrystalline, columnar and epitaxial. The pellets and thin films exhibit a uniform distribution of elements, with stoichiometry closely matching the nominal values. These fabrication methods are applied to various high entropy oxides to investigate their oxygen ion conductivity and electrocatalytic activity for the oxygen evolution reaction (OER).

Oxygen-ion conductivity in high entropy oxides

The transport of oxygen ions in fluorite-type and perovskite-type high entropy oxides is investigated in this thesis. The fluorite-structured high entropy oxide examined here is $(Ce,La,Pr,Sm,Y)_{1-x}Zr_xO_{2-\delta}$ where x ranges from 0 to 0.3. Zr is doped into $(Ce,La,Pr,Sm,Y)O_{2-\delta}$ to stabilize the fluorite structure at elevated temperatures. As Zr is added, the structure transitions from a mixture of fluorite and bixbyite to a single fluorite phase and eventually to a mixture of fluorite and pyrochlore. The rare earth cations are homogeneously distributed, and their chemical compositions closely align with the nominal values. Praseodymium (Pr) exhibits multivalency, with an approximate oxidation state between +3.4 and +3.5. The conductivity improves with the introduction of Zr, reaching a maximum at $x = 0.05$, but decreases with further incorporation of Zr. Notably, the ionic conductivity and oxygen transference number

are highest at $x = 0.08$. Additionally, electronic conduction, due to the multivalent Pr, is suppressed in the fluorite-type high entropy oxides.

The perovskite-type high entropy oxides studied in this thesis are $(Gd_{0.2}La_{0.2}Nd_{0.2}Pr_{0.2}Sm_{0.2})_{1-x}Ca_xAlO_3$, where the value of x varies between 0 and 0.2. All these perovskite-type high entropy oxides exhibit an orthorhombic perovskite structure with no significant changes in lattice parameters. The constituent elements adhere to the nominal stoichiometry and are uniformly distributed on micro- and nanoscale. The introduction of Ca increases conductivity, which reaches its maximum at $x = 0.05$ but slightly decreases with further additions of Ca. While p-type electronic conduction is expected in single-component rare earth aluminates, it is suppressed in the high entropy oxides. Furthermore, the perovskite-type high entropy oxides demonstrate superior conductivities, ionic conductivities, and oxygen transport numbers compared to single-component rare earth aluminates.

The fluorite-type and perovskite-type high entropy oxides exhibit high ionic conductivities, with minimal electronic conduction compared to their single-component counterparts. Additionally, these high entropy oxides display conductivities comparable to the state-of-the-art electrolyte YSZ, with fluorite-structured high entropy oxides achieving higher conductivities at lower temperatures.

Catalysts for oxygen evolution reaction

The perovskite structured high entropy oxide - $La(Co_{0.2}Cr_{0.2}Fe_{0.2}Mn_{0.2}Ni_{0.2})O_3$ is investigated as catalyst for oxygen evolution reaction. Epitaxial thin films are explored to reduce surface area effects on the catalytic activity. A high ordered, crystalline epitaxial film with a thickness of 11 nm is deposited on Nd doped $SrTiO_3$ substrate using pulsed laser deposition. An enhanced catalytic activity for $La(Co_{0.2}Cr_{0.2}Fe_{0.2}Mn_{0.2}Ni_{0.2})O_3$ is observed when compared to single component perovskite oxides. The current densities at an overpotential of 450 mV and 1.68 V vs. RHE are 17 times higher than $LaNiO_3$ and $LaCoO_3$, approximately 45 time higher than $LaMnO_3$ and 680 times higher than $LaFeO_3$ and $LaCrO_3$. A change in oxidation states of Cr, Ni, Co is observed on the surface in different atmospheres in the high entropy oxide which is not observed in its single component counterparts. APXPS analysis demonstrated that the adsorption of reaction intermediates induces a valence change in several transition metals, pointing to a synergistic effect in the binding of surface adsorbates, which may contribute to the enhanced OER activity.

7.2 Outlook

Oxygen ion conductivity in high entropy oxides - The current work is one of the few studies that delve into the oxygen ion transport in high entropy oxides. In this dissertation, the conduction behavior of the different high entropy oxides is investigated in the oxidizing regime, however, the nature of conduction in the reducing regime is equally important to investigate the applicability of the material as an oxygen ion conductor. Especially in the case of $(Ce,La,Pr,Sm,Y)_{1-x}Zr_xO_{2-\delta}$ as Ce exhibits multivalency in reducing atmospheres leading to an electronic contribution to the total conductivity in Ce-based systems. While in the case of rare earth aluminates, according to literature, the conduction behavior observed in reducing atmospheres is constant and this might hold true for the high entropy oxide. Nevertheless, the conduction behavior in reducing atmosphere needs to be investigated to confirm the mitigation of electronic conduction in a wide oxygen partial pressure regime for all high entropy oxides. Furthermore, the conductivities in the fluorite structured high entropy oxides can be increased further by strategically selecting the constituent elements with lower size mismatch with an average ionic radius close to 1.079 Å. While for the perovskite structured high entropy aluminates, the conductivity can be increased by simultaneous doping on both rare earth- and Al-sites with +2 cations. Oxygen ion conductors are commercially used as electrolytes in solid oxide cells, oxygen ion pumps and oxygen sensors. This dissertation discusses only the ionic and electronic conduction of the high entropy oxides. For potential electrolyte materials for an industrial application, there are other properties that are important to consider for their applicability as electrolytes such as

1) High densities with very low open continuous pores – gas tightness to prevent interflow of gases between electrodes
2) Thermal and chemical stability at high temperatures over a long period of time in both oxidizing and reducing atmospheres.
3) The cost of the electrolyte should be evaluated.
4) Matching the thermal expansion coefficient with the electrode materials.

In this dissertation, the relative densities of $(Ce,La,Pr,Sm,Y)_{1-x}Zr_xO_{2-\delta}$ and $(Gd_{0.2}La_{0.2}Nd_{0.2}Pr_{0.2}Sm_{0.2})_{1-x}Ca_xAlO_3$ are high and the percentage of open porosity for some of the compositions is very low indicating a gas tight material. Nevertheless, further investigations are needed to find and optimize scalable synthesis techniques for fabricating high entropy oxides with high densities and gas tightness. The second important property in the abovementioned list is the thermal stability at high temperatures over wide ranges of oxygen

partial pressure. According to the first core effect in high entropy materials, these materials are thermodynamically stable at high temperatures due to the high configurational entropy. Therefore, the high entropy oxides have the potential to be thermally stable at higher temperatures over wide ranges of oxygen partial pressures and further investigations in this area are necessary. One of the important advantages of high entropy materials is the compositional flexibility in these multicomponent systems. This compositional flexibility enables researchers to substitute an expensive element with a relatively inexpensive element, while considering environmental aspects, without compromising the materials' functionality. Furthermore, the compositional flexibility of these materials can help in finding a composition with thermal expansion coefficient close to that of the desired electrodes. Therefore, high entropy oxides show promise as potential electrolyte materials, and further research is necessary to investigate scalability of these materials.

Catalysts for oxygen evolution reaction – Since the introduction of high entropy oxides, many articles reported the catalytic activity for oxygen evolution reaction in high entropy oxides. Most of the high entropy oxides have shown enhanced OER activity compared to the single component oxides as well as the state-of-the-art oxide catalysts like IrO_2 and RuO_2. This dissertation investigates such a perovskite structured high entropy oxide for its catalytic activity for oxygen evolution reaction. The observed enhancement of catalytic activity is due to the synergy among the constituent elements, also known as cocktail effects, which offers limitless compositional possibilities. Therefore, strategically narrowing down the compositional space of high entropy oxides for experimentation, using theoretical calculations, activity descriptors, or combinatorial and high-throughput methods, is essential for advancing high entropy oxides. One of the biggest drawbacks of the traditional OER catalyst such as IrO_2 and RuO_2 are their high cost and their low abundance. The high entropy oxides provide a cheaper and more abundant alternative. Even though the high entropy oxide explored in this dissertation contains earth abundant transition metals and lanthanum, cobalt is toxic to the environment. Consequently, compositions without Co should be explored to avoid the toxicity and humanitarian impact of cobalt mining. Furthermore, to date the mechanism behind the enhanced catalytic activity is not clear and this dissertation attempts to reveal the underlying mechanisms. However, more in-situ studies are necessary for a better understanding of the enhanced catalytic activity due to the cocktail effect in the high entropy oxides. Additionally, in this dissertation, epitaxial thin films are investigated for a systematic comparison of catalytic activity among the different oxides. While this is a suitable model system, for industrial

applications, the epitaxial films are not ideal and a morphology with highest surface area is needed. Therefore, exploring different synthesis routes to achieve a morphology with maximum surface area is vital for introducing high entropy oxides for industrial application.

List of figures

List of tables

List of abbreviations

AC	Alternating current
AEM	Adsorbate evolution mechanism
APXAS	Ambient pressure X-ray Absorption spectroscopy
APXPS	Ambient pressure X-ray Photoemission spectroscopy
DC	Direct current
CN	Co-ordination number
CPE	Constant Phase element
CS	Conventional sintering
CV	Cyclic voltammetry
ECSA	Electrochemical Surface Area
EDS	Energy-Dispersive X-ray spectroscopy
EIS	Electrochemical Impedance Spectroscopy
EELS	Electron Energy Loss spectroscopy
eV	electron volt
GIXRD	Grazing Incidence X-ray Diffraction
HRXRD	High Resolution X-ray Diffraction
FHEO	Fluorite type High Entropy Oxide
HEO	High Entropy Oxide
HT	Conduction element at High Temperature (>500 °C)
LOM	Lattice oxygen evolution mechanism
LT	Conduction element at Low Temperature (<500 °C)
MC	Mechanochemical synthesis
OER	Oxygen Evolution Reaction
PLD	Pulsed Laser Deposition
RCP	Reverse co-precipitation
SAED	Selected Area Electron Diffraction
SEM	Scanning Electron Microscopy
STEM	Scanning Transmission Electron Microscopy
TEM	Transmission Electron Microscopy
XPS	X-ray Photoelectron Spectroscopy
XRD	X-ray Diffraction
YSZ	Yttria Stabilized Zirconia

List of symbols

R	Universal gas constant
σ_t	Total conductivity
σ_{ion}	Ionic conductivity
σ_{elec}	Electronic conductivity
μ_{ion}, μ_{elec}	Mobilities of the ions and electrons respectively
t_{ion}, t_{elec}	Transference numbers of the ions and electrons respectively
c_{ion}, c_{elec}	Concentration of the ions and electrons respectively
Δg_m	Migration free energy
p	Probability of a jump of charge carrier
k	Boltzmann constant
T	Temperature
q	Charge on the carrier
j	Attempt frequency
γ	Geometric factor
Δh_m	Enthalpy of migration
Δs_m	Entropy of migration
σ_o	Conductivity pre-factor
E_a	Activation energy
HO^*	Adsorbed OH – Reaction Intermediate 1 – RI1
O^*	Adsorbed O – Reaction Intermediate 1 – RI2
HOO^*	Adsorbed HOO – Reaction Intermediate 1 – RI3
ΔG	Gibbs free energy of a reaction
F	Farad
E_{meas}^{RHE}	Potential measured w.r.t reversible hydrogen electrode
E_{meas}	Potential measured w.r.t reference electrode
E_{RE}^{RHE}	Standard electrode potential of the reference electrode w.r.t RHE
η	Overpotential
α	Charge transfer coefficient
C_{dl}	Double layer capacitance
C_s	Specific capacitance
O	Oxygen

P	Number of phases
C	Number of constituents
F	Degrees of freedom
S_{config}	Configurational entropy
x	Mole fraction
ΔG_{mix}	Gibbs free energy of formation of a solid solution
ΔH_{mix}	Enthalpy of formation of a solid solution
ΔS_{mix}	Entropy of formation of a solid solution
V_o	Oxygen vacancies
W	Work function
BE	Binding energy
KE	Kinetic energy
h	Planck's constant
ν	Frequency
r	Radius
h	Height
$V(t)$	Voltage
$I(t)$	Current
R	Resistance
ω	Angular frequency
ϕ	Phase difference
$Re(Z')$	Real part of impedance
$Im(Z'')$	Imaginary part of impedance
Å	Angstroms
$Cu\text{-}K_\alpha$	X-ray source is copper K_α
at%	Atomic percentage
a	Lattice parameter
I_{M5}	Intensity of M_5 edge
I_{M4}	Intensity of M_4 edge
μm	Micrometer
nm	Nanometer
TD	Theoretical density
$p(O_2)$	Partial pressure of oxygen

μ_{pol}^{0}	Mobility of polaron
σ_{elec}^{n}, σ_{o}^{n-pol}	Conductivity and conductivity pre-factor for n-type electronic conduction
σ_{elec}^{p}, σ_{o}^{p-pol}	Conductivity and conductivity pre-factor for p-type electronic conduction
E_{A}^{pol}	Activation energy for polaron hopping
E_{A}^{ion}	Activation energy for ion hopping
t	Goldschmidt tolerance factor
σ_{elec}^{LT}, $\sigma_{elec,0}^{LT}$	Conductivity and conductivity pre-factor for electronic conduction <500 °C
σ_{elec}^{HT}, $\sigma_{elec,0}^{HT}$	Conductivity and conductivity pre-factor for electronic conduction >500 °C
E_{A}^{LT}, E_{A}^{HT}	Activation energies for electronic conduction below and above 500 °C
t_{o}	Oxygen transference number
E_{F}	Fermi energy level
E_{O2p}	Energy level of Oxygen 2p orbital

Acknowledgements

First and foremost, I would like to express my deepest gratitude to my supervisor, Prof. Horst Hahn, for granting me the incredible opportunity to pursue my doctorate under his guidance. I am sincerely grateful for his unwavering support, insightful advice, and encouragement throughout my PhD journey. His mentorship provided me with the independence and confidence to explore new ideas, fostering both my academic and personal growth.

I am deeply indebted to my group leader, Dr. Miriam Botros, for her continuous support throughout my doctorate. She was always available whenever I faced challenges during my PhD, providing invaluable guidance and insightful ideas. Her connections introduced me to brilliant researchers, helping me expand my network and further enrich my research journey.

I am thankful for Dr. Leonardo Velasco Estrada for providing me guidance for the initial years of my PhD journey. I would like to thank him for suggesting and encouraging me to pursue the doctoral position after my masters.

I would like to express my sincere gratitude to my co-referee, Prof. Jan Philipp Hofmann, and the esteemed members of my doctoral examination committee, Prof. Wolfgang Donner and Prof. Christina Roth, for their valuable time and effort in evaluating my work.

I am deeply grateful to Prof. S.S. Bhattacharya for providing me with the opportunity to pursue my master's dissertation in Germany. His unwavering support and guidance throughout both my master's and doctoral studies have been invaluable.

I am fortunate to have had the opportunity to collaborate with Dr. Christoph Bäumer, Dr. Simon Schweidler, and Dr. Matthias Elm. Their expertise, support, and insightful guidance have been instrumental in my research and publications.

I would like to sincerely thank Boya Ajai Raj Lakshmi Nilayam for his efforts in measuring TEM for my samples. I truly appreciated our discussions and the weekends spent together at INT.

I would like to thank my officemate, Boya Ramin Shadkam for his support in UHV lab. We had a lot of fun discussing everything. I truly enjoyed our running sessions together

I am also deeply grateful to my bros—Dr. Arun Kumar Jaiswal, Dr. Surya Abhishek, Dr. Abhishek Sarkar, Dr. Praneeth Chilakalpudi, Dr. Sri Harsha Nandam, and Anurag Dinesh Khandelwal—for their unwavering support and for the unforgettable moments we shared in Karlsruhe. I would like to express my heartfelt gratitude to my colleagues, Dr. Robert Kruk and Dr. Evgeniy Boltynjuk, for the countless enjoyable conversations about politics, sports, and all things in between.

A special thanks to Alaa Alsawaf, Yanyan Cui, Anurag Dinesh Khandelwal, Zhibo Zhao, Gleb Iankevich, David Stenzel, Yan Liu, Robert Wang, Yueyue he and Ling Lin for the wonderful time we shared, the fun discussions, and the camaraderie that made this journey both intellectually stimulating and enjoyable.

I would like to express my deepest gratitude to my family and friends for their unwavering support and understanding throughout this journey. A special mention goes to my parents, Kante Venkata Lakshmi and Kante Srinivasarao, whose endless sacrifices, love, and encouragement have been the foundation of my success.

Curriculum Vitea

Education

September 2020 – Present	Doctoral student at the Insitute of Nanotechnology; TU Darmstadt and Karlsruhe Institute of Technology; Supervisor: Prof. Dr. -Ing. Horst Hahn
July 2018 – June 2020	Masters of Technology in Metallurgical and Materials Engineering; Indian Institute of Technology, Madras, and Karlsruhe Institute of Technology, Germany; Grade: 8.8/10
August 2014 – May 2018	Bachelors of Technology Metallurgical Engineering; National institute of Technology, Raipur; Grade: 7.5/10

Research Experience

September 2020 – Present	Karlsruhe Institute of Technology, Karlsruhe, Germany Supervised by Prof. Dr.-Ing. Horst Hahn Oxygen-ion transport and electrocatalysis in high entropy oxides (PhD work).
July 2019 – June 2020	Indian Institute of Technology, Madras, and Karlsruhe Institute of Technology, Germany; Supervised by Prof. Dr. Subramshu Shekar Bhattacharya and Prof. Dr.-Ing. Horst Hahn; A study of structure and magnetism in hole doped high entropy rare earth orthomanganites.
August 2018 – July 2019	Indian Institute of Technology, Madras; Supervised by Prof. Dr. Tiju Thomas; Calculation of bond valence parameters of Na-O, Ba-O, Ti-O using GAMESS software.
July 2017 – May 2018	National institute of Technology, Raipur; Supervised by Dr. Manoranjan Kumar Manoj; Investigated the mechanical properties of Similar and Dissimilar welded steels.

1) **Mohana V Kante**, Horst Hahn, Subramshu S Bhattacharya, Leonardo Velasco; Synthesis and characterization of dense, rare-earth based high entropy fluorite thin films; J Alloys Compd. 2023 Jun 25; DOI: 10.1016/J.JALLCOM.2023.169430.

2) **Mohana V Kante**, Moritz L Weber, Shu Ni, Iris C G van den Bosch, Emma van der Minne, Lisa Heymann, Lorenz J Falling, Nicolas Gauquelin, Martina Tsvetanova, Daniel M. Cunha, Gertjan Koster, Felix Gunkel, Slavomír Nemšák, Horst Hahn, Leonardo Velasco Estrada, and Christoph Baeumer; A High-Entropy Oxide as High-Activity Electrocatalyst for Water Oxidation; ACS Nano 2023 17;
DOI: 10.1021/acsnano.2c08096

3) **Mohana V Kante**, Ajai R Lakshmi Nilayam, Kosova Kreka, Horst Hahn, Subramshu S Bhattacharya, Leonardo Velasco, Albert Tarancón, Christian Kübel, Simon Schweidler, and Miriam Botros; Influence of Zr-doping on the structure and transport properties of rare earth high-entropy oxides; Journal of Physics: Energy, 2024;
DOI:10.1088/2515-7655/ad423c.

4) **Mohana V Kante**, L. Ajai R Lakshmi Nilayam, Horst Hahn, Subramshu S Bhattacharya, Matthias T Elm, Leonardo Velasco, and Miriam Botros; Elucidation of the Transport Properties of Calcium-Doped High Entropy Rare Earth Aluminates for Solid Oxide Fuel Cell Applications; Small, 2024; DOI:10.1002/smll.202309735.

5) Leonardo Velasco, Juan S Castillo, **Mohana V Kante**, Jhon J Olaya, Pascal Friederich, Horst Hahn; Phase–Property Diagrams for Multicomponent Oxide Systems toward Materials Libraries; Advanced Materials, 2021; DOI:10.1002/adma.202102301.

6) David Stenzel, Bei Zhou, Chukwudalu Okafor, **Mohana V Kante**, Ling Lin, Georgian Melinte, Thomas Bergfeldt, Miriam Botros, Horst Hahn, Ben Breitung, and Simon Schweidler; High-entropy spinel-structure oxides as oxygen evolution reaction electrocatalyst; Frontiers in Energy Research, 2022; DOI:10.3389/fenrg.2022.942314.

7) Abhishek Sarkar, Di Wang, **Mohana V Kante**, Luis Eiselt, Vanessa Trouillet, Gleb Iankevich, Zhibo Zhao, Subramshu S. Bhattacharya, Horst Hahn, Robert Kruk; High Entropy Approach to Engineer Strongly Correlated Functionalities in Manganites; Advanced Materials, 2022; DOI:10.1002/adma.202207436.

8) Mukesh Kumbhakar, Anurag Khandelwal, Shikhar Krishn Jha, **Mohana V Kante**, Pirmin Keßler, Uli Lemmer, Horst Hahn, Jasmin Aghassi-Hagmann, Alexander

Colsmann, Ben Breitung, Leonardo Velasco, and Simon Schweidler; High-Throughput Screening of High-Entropy Fluorite-Type Oxides as Potential Candidates for Photovoltaic Applications; Advanced Energy Materials, 2023; DOI:10.1002/aenm.202204337.

9) Ling Lin, Ziming Ding, Guruprakash Karkera, Thomas Diemant, **Mohana V. Kante**, Daisy Agrawal, Horst Hahn, Jasmin Aghassi-Hagmann, Maximilian Fichtner, Ben Breitung, and Simon Schweidler; High-Entropy Sulfides as Highly Effective Catalysts for the Oxygen Evolution Reaction; Small Structures, 2023; DOI:10.1002/sstr.202300012.

10) Matthew Wells, Kosova Kreka, **Mohana V Kante**, Miriam Botros, Ozden Celikbilek, Jan Pieter Ouweltjes, Federico Baiutti, Simon Fairclough, Caterina Ducati, Albert Tarancón, Judith MacManus-Driscoll; Reducing critical raw material use in commercial solid oxide fuel cells using vertically aligned thin-film cathodes with enhanced long-term stability; Energy & Environmental Materials, 2025; DOI:10.22541/au.172518318.87990984/v1.

11) Evgeniy Boltynjuk, Claudia P Mejía V, **Mohana V Kante**, Carlos M. Garzón, Jhon J Olaya, Horst Hahn, Leonardo Velasco; Effect of zirconium addition on the microstructure and mechanical properties of TiSiN films fabricated by reactive magnetron sputtering; Submitted.

12) Mahsa Kalantari Saghafi, **Mohana V Kante**, Ramin Shadkam, Evgeniy Boltynjuk, Simon Schweidler, Ben Breitung, Michael Hirtz, Jasmin Aghassi-Hagmann, Gabriel Cadilha Marques; Optimizing the Performance of Printed Indium Oxide Thin-Film Transistors Through Gallium Incorporation; Submitted.

Conferences

1) Effect of citric acid to ethylene glycol (CA:EG) ratio on the particle size and OER catalytic activity of perovskite-type high entropy oxides; CHEAC summer school, Copenhagen, Denmark, 15 – 18 August 2023, Poster.
2) High entropy oxides as electrolyte for solids oxide fuel cells; Microstructural functionality at the nanoscale III, Venice, Italy, June 8-9, 2023, Oral presentation.
3) Study of oxygen ion conductivity in high entropy oxides; European materials research society, Strasbourg, France, May 29 – June 2, 2023, Oral presentation.
4) Study of conductivity in Ca-doped high-entropy aluminates $(Gd,La,Nd,Pr,Sm)_{1-x}Ca_xAlO_3$; KIT Materials day, Karlsruhe, Germany, June 21, 2022, Poster.

References

1. Oliveira, A. M., Beswick, R. R. & Yan, Y. A green hydrogen economy for a renewable energy society. *Curr Opin Chem Eng* 33, 100701 (2021).

2. Kreith, F. & West, R. Fallacies of a Hydrogen Economy: A Critical Analysis of Hydrogen Production and Utilization. *J Energy Resour Technol* 126, 249–257 (2004).

3. Fichtner, M. Hydrogen storage. *The Hydrogen Economy: Opportunities and Challenges* 9780521882163, 309–321 (2009).

4. Shinnar, R. The hydrogen economy, fuel cells, and electric cars. *Technol Soc* 25, 455–476 (2003).

5. Singhal, S. C. & Kendall, K. High-temperature Solid Oxide Fuel Cells: Fundamentals, Design and Applications. *High-temperature Solid Oxide Fuel Cells: Fundamentals, Design and Applications* 1–405 (2003).

6. Inaba, H. & Tagawa, H. *Ceria-Based Solid Electrolytes. Solid State Ionics* vol. 83 (1996).

7. Andersson, D. A., Simak, S. I., Skorodumova, N. V., Abrikosov, I. A. & Johansson, B. Optimization of ionic conductivity in doped ceria. *Proc Natl Acad Sci U S A* 103, 3518–3521 (2006).

8. Omar, S., Wachsman, E. D. & Nino, J. C. Higher ionic conductive ceria-based electrolytes for solid oxide fuel cells. *Appl. Phys. Lett* 91, 144106 (2007).

9. Omar, S., Wachsman, E. D. & Nino, J. C. Higher conductivity Sm3+ and Nd3+ co-doped ceria-based electrolyte materials. *Solid State Ion* 178, 1890–1897 (2008).

10. Zajac, W. & Molenda, J. Electrical conductivity of doubly doped ceria. *Solid State Ion* 179, 154–158 (2008).

11. Dholabhai, P. P., Adams, J. B., Crozier, P. A. & Sharma, R. In search of enhanced electrolyte materials: a case study of doubly doped ceria. *J Mater Chem* 21, 18991–18997 (2011).

12. Kasse, R. M. & Nino, J. C. Ionic conductivity of SmxNdyCe0.9O2−δ codoped ceria electrolytes. *J Alloys Compd* 575, 399–402 (2013).

13. Navarro, L., Marques, F. & Frade, J. n-Type Conductivity in Gadolinia-Doped Ceria. *J Electrochem Soc* 144, 267–273 (1997).

14. Wang, S., Kobayashi, T., Dokiya, M. & Hashimoto, T. Electrical and Ionic Conductivity of Gd-Doped Ceria. *J Electrochem Soc* 147, 3606 (2000).

15. Gopal, C. B. & Haile, S. M. An electrical conductivity relaxation study of oxygen transport in samarium doped ceria. *J Mater Chem A Mater* 2, 2405–2417 (2014).

16. Celik, E., Ma, Y., Brezesinski, T. & Elm, M. T. Ordered mesoporous metal oxides for electrochemical applications: correlation between structure, electrical properties and device performance. *Physical Chemistry Chemical Physics* 23, 10706–10735 (2021).

17. Michel, K., Bjørheim, T. S., Norby, T., Janek, J. & Elm, M. T. Importance of the Spin-Orbit Interaction for a Consistent Theoretical Description of Small Polarons in Pr-Doped CeO2. *Journal of Physical Chemistry C* 124, 15831–15838 (2020).

18. Bishop, S. R., Stefanik, T. S. & Tuller, H. L. Defects and transport in Pr xCe 1-xO 2-δ: Composition trends. *J Mater Res* 27, 2009–2016 (2012).

19. Bishop, S. R., Stefanik, T. S. & Tuller, H. L. Electrical conductivity and defect equilibria of Pr0.1Ce 0.9O2-δ. *Physical Chemistry Chemical Physics* 13, 10165–10173 (2011).

20. Tuller, H. L. *et al.* Praseodymium doped ceria: Model mixed ionic electronic conductor with coupled electrical, optical, mechanical and chemical properties. *Solid State Ion* 225, 194–197 (2012).

21. Nicollet, C., Kalaev, D. & Tuller, H. L. Mixed conductivity and oxygen surface exchange kinetics of lanthanum-praseodymium doped cerium dioxide. *Solid State Ion* 331, 96–101 (2019).

22. Stefanik, T. S. 1973-. Electrical properties and defect structures of praseodymium-cerium oxide solid solutions. (2003).

23. Lybye, D., Poulsen, F. W. & Mogensen, M. Conductivity of A- and B-site doped LaAlO3, LaGaO3, LaScO3 and LaInO3 perovskites. *Solid State Ion* 128, 91–103 (2000).

24. Xie, X. *et al.* Oxygen Evolution Reaction in Alkaline Environment: Material Challenges and Solutions. *Adv Funct Mater* 32, (2022).

25. Anantharaj, S. *et al.* The reference electrode dilemma in energy conversion electrocatalysis: "right vs. okay vs. wrong". *J Mater Chem A Mater* 11, 17699–17709 (2023).

26. Man, I. C. *et al.* Universality in Oxygen Evolution Electrocatalysis on Oxide Surfaces. *ChemCatChem* 3, 1159–1165 (2011).

27. Fabbri, E. & Schmidt, T. J. Oxygen Evolution Reaction - The Enigma in Water Electrolysis. *ACS Catal* 8, 9765–9774 (2018).

28. Yoo, J. S., Rong, X., Liu, Y. & Kolpak, A. M. Role of Lattice Oxygen Participation in Understanding Trends in the Oxygen Evolution Reaction on Perovskites. *ACS Catal* 8, 4628–4636 (2018).

29. Bockris, J. O. & Otagawa, T. The Electrocatalysis of Oxygen Evolution on Perovskites. *J Electrochem Soc* 131, 290–302 (1984).

30. Rossmeisl, J., Logadottir, A. & Nørskov, J. K. Electrolysis of water on (oxidized) metal surfaces. *Chem Phys* 319, 178–184 (2005).

31. Kim, D. *et al.* Perovskite-based electrocatalysts for oxygen evolution reaction in alkaline media: A mini review. *Frontiers in Chemistry* vol. 10 (2022).

32. Suntivich, J., May, K. J., Gasteiger, H. A., Goodenough, J. B. & Shao-Horn, Y. A perovskite oxide optimized for oxygen evolution catalysis from molecular orbital principles. *Science (1979)* 334, 1383–1385 (2011).

33. Cantor, B., Chang, I. T. H., Knight, P. & Vincent, A. J. B. Microstructural development in equiatomic multicomponent alloys. *Materials Science and Engineering: A* 375–377, 213–218 (2004).

34. Yeh, J. W. *et al.* Nanostructured High-Entropy Alloys with Multiple Principal Elements: Novel Alloy Design Concepts and Outcomes. *Adv Eng Mater* 6, 299–303 (2004).

35. Sarkar, A., Kruk, R. & Hahn, H. Magnetic properties of high entropy oxides. *Dalton Transactions* 50, 1973–1982 (2021).

36. Sarkar, A. *et al.* High-Entropy Oxides: Fundamental Aspects and Electrochemical Properties. *Advanced Materials* 31, 1806236 (2019).

37. Schweidler, S. *et al.* High-entropy materials for energy and electronic applications. *Nature Reviews Materials 2024 9:4* 9, 266–281 (2024).

38. Lee, C. *et al.* Lattice-Distortion-Enhanced Yield Strength in a Refractory High-Entropy Alloy. *Advanced Materials* 32, 2004029 (2020).

39. Rost, C. M. *et al.* Entropy-stabilized oxides. *Nat Commun* 6, (2015).

40. Bérardan, D., Franger, S., Dragoe, D., Meena, A. K. & Dragoe, N. Colossal dielectric constant in high entropy oxides. *physica status solidi (RRL) – Rapid Research Letters* 10, 328–333 (2016).

41. Kante, M. V., Hahn, H., Bhattacharya, S. S. & Velasco, L. Synthesis and characterization of dense, rare-earth based high entropy fluorite thin films. *J Alloys Compd* 947, 169430 (2023).

42. Djenadic, R. *et al.* Multicomponent equiatomic rare earth oxides. *Mater Res Lett* 5, 102–109 (2017).

43. Velasco, L. *et al.* Phase–Property Diagrams for Multicomponent Oxide Systems toward Materials Libraries. *Advanced Materials* 33, 2102301 (2021).

44. Sarkar, A. *et al.* Multicomponent equiatomic rare earth oxides with a narrow band gap and associated praseodymium multivalency. *Dalton Transactions* 46, 12167–12176 (2017).

45. Kante, M. V *et al.* Influence of Zr-doping on the structure and transport properties of rare earth high-entropy oxides. *Journal of Physics: Energy* 6, 035001 (2024).

46. Sarkar, A. *et al.* Rare earth and transition metal based entropy stabilised perovskite type oxides. *J Eur Ceram Soc* 38, 2318–2327 (2018).

47. Kante, M. V. *et al.* A High-Entropy Oxide as High-Activity Electrocatalyst for Water Oxidation. *ACS Nano* 17, 5329–5339 (2023).

48. Dąbrowa, J. *et al.* Synthesis and microstructure of the (Co,Cr,Fe,Mn,Ni)3O4 high entropy oxide characterized by spinel structure. *Mater Lett* 216, 32–36 (2018).

49. Nguyen, T. X., Patra, J., Chang, J. K. & Ting, J. M. High entropy spinel oxide nanoparticles for superior lithiation–delithiation performance. *J Mater Chem A Mater* 8, 18963–18973 (2020).

50. Zhao, J., Yang, X., Huang, Y., Du, F. & Zeng, Y. Entropy Stabilization Effect and Oxygen Vacancies Enabling Spinel Oxide Highly Reversible Lithium-Ion Storage. *ACS Appl Mater Interfaces* 13, 58674–58681 (2021).

51. Matović, B. *et al.* Fabrication and characterization of high entropy pyrochlore ceramics. *Boletín de la Sociedad Española de Cerámica y Vidrio* (2021).

52. Teng, Z. *et al.* Synthesis and structures of high-entropy pyrochlore oxides. *J Eur Ceram Soc* 40, 1639–1643 (2020).

53. Jiang, B. *et al.* Probing the Local Site Disorder and Distortion in Pyrochlore High-Entropy Oxides. *J Am Chem Soc* 143, 4193–4204 (2021).

54. Kumbhakar, M. *et al.* High-Throughput Screening of High-Entropy Fluorite-Type Oxides as Potential Candidates for Photovoltaic Applications. *Adv Energy Mater* 13, 2204337 (2023).

55. Sarkar, A. *et al.* Determining role of individual cations in high entropy oxides: Structure and reversible tuning of optical properties. *Scr Mater* 207, (2022).

56. Sarkar, A. *et al.* Role of intermediate 4f states in tuning the band structure of high entropy oxides. *APL Mater* 8, 051111 (2020).

57. Kumbhakar, M. *et al.* High-Throughput Screening of High-Entropy Fluorite-Type Oxides as Potential Candidates for Photovoltaic Applications. *Adv Energy Mater* 13, 2204337 (2023).

58. Chen, K. *et al.* A five-component entropy-stabilized fluorite oxide. *J Eur Ceram Soc* 38, 4161–4164 (2018).

59. Bonnet, E. *et al.* On the ionic conductivity of some zirconia-derived high-entropy oxides. *J Eur Ceram Soc* 41, 4505–4515 (2021).

60. Gild, J. *et al.* High-entropy fluorite oxides. *J Eur Ceram Soc* 38, 3578–3584 (2018).

61. Zhang, F. *et al.* Preparation and electrical conductivity of (Zr, Hf, Pr, Y, La) O high entropy fluorite oxides. *J Mater Sci Technol* 105, 122–130 (2022).

62. Dąbrowa, J. *et al.* Stabilizing fluorite structure in ceria-based high-entropy oxides: Influence of Mo addition on crystal structure and transport properties. *J Eur Ceram Soc* 40, 5870–5881 (2020).

63. Luo, X., Huang, S., Xu, C., Hou, S. & Jin, H. Rare-earth high-entropy aluminate-toughened-zirconate dual-phase composite ceramics for advanced thermal barrier coatings. *Ceram Int* 49, 766–772 (2023).

64. Zhao, Z. *et al.* High-entropy (Y0.2Nd0.2Sm0.2Eu0.2Er0.2)AlO3: A promising thermal/environmental barrier material for oxide/oxide composites. *J Mater Sci Technol* 47, 45–51 (2020).

65. Zhao, Z. *et al.* High-entropy (Nd0.2Sm0.2Eu0.2Y0.2Yb0.2)4Al2O9 with good high temperature stability, low thermal conductivity, and anisotropic thermal expansivity. *Journal of Advanced Ceramics* 9, 595–605 (2020).

66. Li, Z. *et al.* A Promising High-Entropy Thermal Barrier Material with the Formula (Y0.2Dy0.2Ho0.2Er0.2Yb0.2)3Al5O12. *Materials 2022, Vol. 15, Page 8079* 15, 8079 (2022).

67. Albedwawi, S. H., AlJaberi, A., Haidemenopoulos, G. N. & Polychronopoulou, K. High entropy oxides-exploring a paradigm of promising catalysts: A review. *Mater Des* 202, 109534 (2021).

68. Gao, Y., Liu, Y., Yu, H. & Zou, D. High-entropy oxides for catalysis: Status and perspectives. *Appl Catal A Gen* 631, 118478 (2022).

69. Pan, Y., Liu, J. X., Tu, T. Z., Wang, W. & Zhang, G. J. High-entropy oxides for catalysis: A diamond in the rough. *Chemical Engineering Journal* 451, 138659 (2023).

70. Wang, D. *et al.* Low-temperature synthesis of small-sized high-entropy oxides for water oxidation. *J Mater Chem A Mater* 7, 24211–24216 (2019).

71. Abdelhafiz, A., Wang, B., Harutyunyan, A. R. & Li, J. Carbothermal Shock Synthesis of High Entropy Oxide Catalysts: Dynamic Structural and Chemical Reconstruction

Boosting the Catalytic Activity and Stability toward Oxygen Evolution Reaction. *Adv Energy Mater* (2022).

72. Zhao, S. *et al.* Preparation and electrocatalytic properties of (FeCrCoNiAl0.1)Ox high-entropy oxide and NiCo-(FeCrCoNiAl0.1)Ox heterojunction films. *J Alloys Compd* 868, 159108 (2021).

73. Hooch Antink, W. *et al.* High-Valence Metal-Driven Electronic Modulation for Boosting Oxygen Evolution Reaction in High-Entropy Spinel Oxide. *Adv Funct Mater* 34, 2309438 (2024).

74. Triolo, C. *et al.* Evaluation of electrospun spinel-type high-entropy (Cr 0.2 Mn 0.2 Fe 0.2 Co 0.2 Ni 0.2) 3 O 4 , (Cr 0.2 Mn 0.2 Fe 0.2 Co 0.2 Zn 0.2) 3 O 4 and (Cr 0.2 Mn 0.2 Fe 0.2 Ni 0.2 Zn 0.2) 3 O 4 oxide nanofibers as electrocatalysts for oxygen evolution in alkaline medium. *Energy Advances* 2, 667–678 (2023).

75. Stenzel, D. *et al.* High-entropy spinel-structure oxides as oxygen evolution reaction electrocatalyst. *Front Energy Res* 10, 942314 (2022).

76. Zhang, Y., Dai, W., Zhang, P., Lu, T. & Pan, Y. In-situ electrochemical tuning of (CoNiMnZnFe)3O3.2 high-entropy oxide for efficient oxygen evolution reactions. *J Alloys Compd* 868, 159064 (2021).

77. Kim, K. H. & Choi, Y. H. Effect of constituent cations on the electrocatalytic oxygen evolution reaction in high-entropy oxide (Mg0.2Fe0.2Co0.2Ni0.2Cu0.2)O. *Journal of Electroanalytical Chemistry* 922, 116737 (2022).

78. Nguyen, T. X., Liao, Y. C., Lin, C. C., Su, Y. H. & Ting, J. M. Advanced High Entropy Perovskite Oxide Electrocatalyst for Oxygen Evolution Reaction. *Adv Funct Mater* 31, 1–10 (2021).

79. Ji, X. *et al.* Highly active and durable La0.6Ca0.4(CrMnFeCo2Ni)O3 high entropy perovskite oxide as electrocatalyst for oxygen evolution reaction in alkaline media. *J Mater Sci Technol* 168, 71–78 (2024).

80. Wei, R., Fu, G., Qi, H. & Liu, H. Tuning the high-entropy perovskite as efficient and reliable electrocatalysts for oxygen evolution reaction. *RSC Adv* 14, 18117–18125 (2024).

81. Tang, L. *et al.* High Configuration Entropy Activated Lattice Oxygen for O2 Formation on Perovskite Electrocatalyst. *Adv Funct Mater* 32, 2112157 (2022).

82. Schweidler, S. *et al.* Synthesis of perovskite-type high-entropy oxides as potential candidates for oxygen evolution. *Front Energy Res* 10, (2022).

83. Nguyen, T. X. *et al.* Advanced High Entropy Perovskite Oxide Electrocatalyst for Oxygen Evolution Reaction. *Adv Funct Mater* 31, 2101632 (2021).

84. Makuła, P., Pacia, M. & Macyk, W. How To Correctly Determine the Band Gap Energy of Modified Semiconductor Photocatalysts Based on UV-Vis Spectra. *Journal of Physical Chemistry Letters* 9, 6814–6817 (2018).

85. McNealy, B. E. & Hertz, J. L. On the use of the constant phase element to understand variation in grain boundary properties. *Solid State Ion* 256, 52–60 (2014).

86. Fleig, J. The grain boundary impedance of random microstructures: numerical simulations and implications for the analysis of experimental data. *Solid State Ion* 150, 181–193 (2002).

87. Sarkar, A. *et al.* Nanocrystalline multicomponent entropy stabilised transition metal oxides. *J Eur Ceram Soc* 37, 747–754 (2017).

88. Chen, H. *et al.* Mechanochemical Synthesis of High Entropy Oxide Materials under Ambient Conditions: Dispersion of Catalysts via Entropy Maximization. *ACS Mater Lett* 1, 83–88 (2019).

89. Biesuz, M., Spiridigliozzi, L., Dell'Agli, G., Bortolotti, M. & Sglavo, V. M. Synthesis and sintering of (Mg, Co, Ni, Cu, Zn)O entropy-stabilized oxides obtained by wet chemical methods. *J Mater Sci* 53, 8074–8085 (2018).

90. Mao, A. *et al.* Solution combustion synthesis and magnetic property of rock-salt (Co0.2Cu0.2Mg0.2Ni0.2Zn0.2)O high-entropy oxide nanocrystalline powder. *J Magn Magn Mater* 484, 245–252 (2019).

91. Kante, M. V. *et al.* Elucidation of the Transport Properties of Calcium-Doped High Entropy Rare Earth Aluminates for Solid Oxide Fuel Cell Applications. *Small* 2309735, 1–15 (2024).

92. Song, B. *et al.* Microstructure and mechanical properties of microwave sintered (MgCoNiCuZn)O high-entropy ceramics. *Ceram Int* 50, 22232–22242 (2024).

93. Yan, N. *et al.* Reactive Flash Sintering of High-Entropy Oxide (Mg, Co, Ni, Cu, Zn)1−xLixO at Room Temperature. *Materials 2022, Vol. 15, Page 3836* 15, 3836 (2022).

94. Dupuy, A. D., Wang, X. & Schoenung, J. M. Entropic phase transformation in nanocrystalline high entropy oxides. *Mater Res Lett* 7, 60–67 (2019).

95. Tyagi, P. K. & Jha, S. K. Flash sintering improves the densification and mechanical properties of high entropy oxides used in anodic applications. *Materialia (Oxf)* 33, 101967 (2024).

96. Guo, H., Wang, X., Dupuy, A. D., Schoenung, J. M. & Bowman, W. J. Growth of nanoporous high-entropy oxide thin films by pulsed laser deposition. *J Mater Res* (2022) doi:10.1557/s43578-021-00473-2.

97. Khan, N. A. *et al.* Nanostructured AlCoCrCu0.5FeNi high entropy oxide (HEO) thin films fabricated using reactive magnetron sputtering. *Appl Surf Sci* 553, 149491 (2021).

98. Kante, M. V., Horst Hahn, Subramshu S. Bhattacharya & Leonardo Velasco. Synthesis and characterization of dense, rare-earth based high entropy fluorite thin films. *J Alloys Compd*.

99. Mazor, A., Srolovitz, D. J., Hagan, P. S. & Bukiet, B. G. Columnar growth in thin films. *Phys Rev Lett* 60, 424–427 (1988).

100. Adachi, G. Y. & Imanaka, N. The binary rare earth oxides. *Chem Rev* 98, 1479–1514 (1998).

101. Pianassola, M. *et al.* Tuning the melting point and phase stability of rare-earth oxides to facilitate their crystal growth from the melt. *Journal of Advanced Ceramics* 11, 1479–1490 (2022).

102. Sinclair, R., Lee, S. C., Shi, Y. & Chueh, W. C. Structure and chemistry of epitaxial ceria thin films on yttria-stabilized zirconia substrates, studied by high resolution electron microscopy. *Ultramicroscopy* 176, 200–211 (2017).

103. Pergolesi, D., Fronzi, M., Fabbri, E., Tebano, A. & Traversa, E. Growth mechanisms of ceria- and zirconia-based epitaxial thin films and hetero-structures grown by pulsed laser deposition. *Mater Renew Sustain Energy* 2, (2013).

104. Li, Z. P. *et al.* Structural phase transformation through defect cluster growth in Gd-doped ceria. *Phys Rev B Condens Matter Mater Phys* 84, 1–5 (2011).

105. Coduri, M., Checchia, S., Longhi, M., Ceresoli, D. & Scavini, M. Rare earth doped ceria: The complex connection between structure and properties. *Front Chem* 6, 1–23 (2018).

106. Małecka, M. A. *et al.* Structure and phase stability of nanocrystalline Ce 1-x Ln x O 2-x/2-δ (Ln = Yb, Lu) in oxidizing and reducing atmosphere. *Journal of Nanoparticle Research* 11, 2113–2124 (2009).

107. Ou, D. R. *et al.* Microstructures and electrolytic properties of yttrium-doped ceria electrolytes: Dopant concentration and grain size dependences. *Acta Mater* 54, 3737–3746 (2006).

108. Coduri, M., Scavini, M., Allieta, M., Brunelli, M. & Ferrero, C. Defect structure of Y-doped ceria on different length scales. *Chemistry of Materials* 25, 4278–4289 (2013).

109. Artini, C., Pani, M., Carnasciali, M. M., Plaisier, J. R. & Costa, G. A. Lu-, Sm-, and Gd-Doped Ceria: A Comparative Approach to Their Structural Properties. *Inorg Chem* 55, 10567–10579 (2016).

110. Bishop, S. R., Stefanik, T. S. & Tuller, H. L. Electrical conductivity and defect equilibria of $Pr_{0.1}Ce_{0.9}O_{2-\delta}$. *Physical Chemistry Chemical Physics* 13, 10165–10173 (2011).

111. Kim, J. J., Bishop, S. R., Chen, D. & Tuller, H. L. Defect Chemistry of Pr Doped Ceria Thin Films Investigated by in Situ Optical and Impedance Measurements. *Chemistry of Materials* 29, 1999–2007 (2017).

112. Chatzichristodoulou, C., Park, W. S., Kim, H. S., Hendriksen, P. V. & Yoo, H. I. Experimental determination of the Onsager coefficients of transport for $Ce_{0.8}Pr_{0.2}O_{2-\delta}$. *Physical Chemistry Chemical Physics* 12, 9637–9649 (2010).

113. Fortner, J. A. & Buck, E. C. The chemistry of the light rare-earth elements as determined by electron energy loss spectroscopy. *Appl Phys Lett* 68, 3817–3819 (1996).

114. Garvie, L. A. J. & Buseck, P. R. Determination of Ce4+/Ce3+ in electron-beam-damaged CeO2 by electron energy-loss spectroscopy. *Journal of Physics and Chemistry of Solids* 60, 1943–1947 (1999).

115. Artini, C., Costa, G. A., Pani, M., Lausi, A. & Plaisier, J. Structural characterization of the CeO 2/Gd 2O 3 mixed system by synchrotron X-ray diffraction. *J Solid State Chem* 190, 24–28 (2012).

116. Minervini, L., Zacate, M. O. & Grimes, R. W. Defect cluster formation in M2O3-doped CeO2. *Solid State Ion* 116, 339–349 (1999).

117. Žguns, P. A., Ruban, A. V. & Skorodumova, N. V. Phase diagram and oxygen–vacancy ordering in the CeO2–Gd2O3 system: a theoretical study. *Physical Chemistry Chemical Physics* 20, 11805–11818 (2018).

118. Sugar, J., Brewer, W. D., Kalkowski, G., Kaindl, G. & Paparazzo, E. Photoabsorption by the 3d shell in Ce, Pr, Ho, and Er: Observations and calculations. *Phys Rev A (Coll Park)* 32, 2242–2248 (1985).

119. Alaydrus, M. *et al.* Praseodymium Doped Ceria: The Role of 4f-Electrons of Pr Dopant in Doped Ceria. *ECS Trans* 68, 369–373 (2015).

120. Ahamer, C., Opitz, A. K., Rupp, G. M. & Fleig, J. Revisiting the Temperature Dependent Ionic Conductivity of Yttria Stabilized Zirconia (YSZ). *J Electrochem Soc* 164, F790–F803 (2017).

121. Gregori, G., Merkle, R. & Maier, J. Ion conduction and redistribution at grain boundaries in oxide systems. *Prog Mater Sci* 89, 252–305 (2017).

122. Lasia, A. The Origin of the Constant Phase Element. *Journal of Physical Chemistry Letters* 13, 580–589 (2022).

123. Fleig, J. The grain boundary impedance of random microstructures: numerical simulations and implications for the analysis of experimental data. *Solid State Ion* 150, 181–193 (2002).

124. Koettgen, J. *et al.* Understanding the ionic conductivity maximum in doped ceria: trapping and blocking. *Physical Chemistry Chemical Physics* 20, 14291–14321 (2018).

125. Kilner, J. A. Fast oxygen transport in acceptor doped oxides. *Solid State Ion* 129, 13–23 (2000).

126. Butler, V., Catlow, C. R. A., Fender, B. E. F. & Harding, J. H. Dopant ion radius and ionic conductivity in cerium dioxide. *Solid State Ion* 8, 109–113 (1983).

127. Tuller, H. L. & Nowick, A. S. Small polaron electron transport in reduced CeO2 single crystals. *Journal of Physics and Chemistry of Solids* 38, 859–867 (1977).

128. Shannon, R. D. & IUCr. Revised effective ionic radii and systematic studies of interatomic distances in halides and chalcogenides. *urn:issn:0567-7394* 32, 751–767 (1976).

129. Lehnert, H. *et al.* A powder diffraction study of the phase transition in LaAlO3. *Zeitschrift fur Kristallographie* 215, 536 (2000).

130. Ohon, N., Vasylechko, L., Prots, Y. & Schmidt, M. Phase and structural behavior of SmAlO3–RAlO3 (R = Eu, Gd) systems. *Mater Res Bull* 50, 509–513 (2014).

131. Basyuk, T. *et al.* Crystal structures, thermal expansion and phase transitions of mixed Pr1–xLaxAlO3 perovskites. *physica status solidi c* 6, 1008–1011 (2009).

132. Yoshikawa, A., Saitow, A., Horiuchi, H., Shishido, T. & Fukuda, T. Orthorhombic to trigonal phase transition of perovskite-type (Ndx,Sm1−x)AlO3. *J Alloys Compd* 266, 104–110 (1998).

133. Jiang, S. *et al.* A new class of high-entropy perovskite oxides. *Scr Mater* 142, 116–120 (2017).

134. Dewangan, S. K. *et al.* A review on High-Temperature Applicability: A milestone for high entropy alloys. *Engineering Science and Technology, an International Journal* 35, (2022).

135. Goldschmidt, V. M. Die Gesetze der Krystallochemie. *Naturwissenschaften* 14, 477–485 (1926).

136. Liu, B., Li, L., Liu, X. Q. & Chen, X. M. Structural evolution of SrLaAl1−x(Zn0.5Ti0.5)xO4 ceramics and effects on their microwave dielectric properties. *J Mater Chem C Mater* 4, 4684–4691 (2016).

137. Liu, B. M. *et al.* X-ray-activated, UVA persistent luminescent materials based on Bi-doped SrLaAlO4 for deep-Seated photodynamic activation. *J Appl Phys* 129, 120901 (2021).

138. Kojitani, H. *et al.* Raman spectroscopy and heat capacity measurement of calcium ferrite type MgAl 2 O 4 and CaAl 2 O 4. doi:10.1007/s00269-003-0332-4.

139. McMillan, P. & Ross, N. The Raman spectra of several orthorhombic calcium oxide perovskites. *Phys Chem Miner* 16, 21–28 (1988).

140. Kim, J. J., Bishop, S. R., Thompson, N., Kuru, Y. & Tuller, H. L. Optically derived energy band gap states of Pr in ceria. *Solid State Ion* 225, 198–200 (2012).

141. Remya, G. R., Solomon, S., Thomas, J. K. & John, A. Optical properties of PrAlO3 nano ceramic. *AIP Conf Proc* 1576, 102 (2015).

142. Remya, G. R., Solomon, S., Thomas, J. K. & John, A. Optical and Dielectric Properties of Nano GdAlO3. *Mater Today Proc* 2, 1012–1016 (2015).

143. Sandeep *et al.* Band-gap engineering of La1−xNdxAlO3 (x = 0, 0.25, 0.50, 0.75, 1) perovskite using density functional theory: A modified Becke Johnson potential study*. *Chinese Physics B* 25, 067101 (2016).

144. de Oliveira Neto, B. B. *et al.* Experimental and theoretical characterization of SmAlO3 perovskite synthesized by mechanical alloying. *J Solid State Chem* 298, 122097 (2021).

145. Szubka, M., Talik, E., Molak, A., Turczyński, S. & Pawlak, D. A. Electronic structure of Prx La1-xAlO3 solid solution. *Crystal Research and Technology* 45, 1309–1315 (2010).

146. Skinner, S. J. & Kilner, J. A. Oxygen ion conductors. *Materials Today* 6, 30–37 (2003).

147. Fergus, J. W. Electrolytes for solid oxide fuel cells. *J Power Sources* 162, 30–40 (2006).

148. Subbarao, E. C. & Maiti, H. S. Solid electrolytes with oxygen ion conduction. *Solid State Ion* 11, 317–338 (1984).

149. Ishihara, T., Matsuda, H. & Takita, Y. Oxide Ion Conductivity in Doped NdAlO3 Perovskite-Type Oxides. *J Electrochem Soc* 141, 3444–3449 (1994).

150. Nguyen, T. L., Dokiya, M., Wang, S., Tagawa, H. & Hashimoto, T. The effect of oxygen vacancy on the oxide ion mobility in LaAlO3-based oxides. *Solid State Ion* 130, 229–241 (2000).

151. Lybye, D., Poulsen, F. W. & Mogensen, M. Conductivity of A- and B-site doped LaAlO3, LaGaO3, LaScO3 and LaInO3 perovskites. *Solid State Ion* 128, 91–103 (2000).

152. Park, J. Y. & Choi, G. M. Electrical conductivity of Sr and Mg doped LaAlO3. *Solid State Ion* 154–155, 535–540 (2002).

153. Fabián, M. *et al.* Ionic and electronic transport in calcium-substituted LaAlO3 perovskites prepared via mechanochemical route. *J Eur Ceram Soc* 39, 5298–5308 (2019).

154. Park, J. Y. & Choi, G. M. The effect of Ti addition on the electrical conductivity of Sr- and Mg-doped LaAlO3. *Solid State Ion* 176, 2807–2812 (2005).

155. Fabián, M. *et al.* Ionic and electronic transport in calcium-substituted LaAlO3 perovskites prepared via mechanochemical route. *J Eur Ceram Soc* 39, 5298–5308 (2019).

156. Park, J. Y. & Choi, G. M. Electrical conductivity of Sr and Mg doped LaAlO3. *Solid State Ion* 154–155, 535–540 (2002).

157. Michel, K. *et al.* Combining two redox active rare earth elements for oxygen storage – electrical properties and defect chemistry of ceria–praseodymia single crystals. *Physical Chemistry Chemical Physics* 19, 17661–17669 (2017).

158. Tuller, H. L. & Nowick, A. S. Small polaron electron transport in reduced CeO2 single crystals. *Journal of Physics and Chemistry of Solids* 38, 859–867 (1977).

159. Guo, X. & Waser, R. Space charge concept for acceptor-doped zirconia and ceria and experimental evidences. *Solid State Ion* 173, 63–67 (2004).

160. Guo, X., Sigle, W. & Maier, J. Blocking Grain Boundaries in Yttria-Doped and Undoped Ceria Ceramics of High Purity. *Journal of the American Ceramic Society* 86, 77–87 (2003).

161. Duncan, K. L., Wang, Y., Bishop, S. R., Ebrahimi, F. & Wachsman, E. D. The role of point defects in the physical properties of nonstoichiometric ceria. *J Appl Phys* 101, 31 (2007).

162. Tilley, R. J. D. *Defects in Solids*. *Encyclopedia of Inorganic Chemistry* (2005). doi:10.1002/0470862106.ia062.

163. Huang, P. & Petric, A. Superior Oxygen Ion Conductivity of Lanthanum Gallate Doped with Strontium and Magnesium. *J Electrochem Soc* 143, 1644–1648 (1996).

164. Rossmeisl, J., Logadottir, A. & Nørskov, J. K. Electrolysis of water on (oxidized) metal surfaces. *Chem Phys* 319, 178–184 (2005).

165. She, Z. W. *et al.* Combining theory and experiment in electrocatalysis: Insights into materials design. *Science (1979)* 355, (2017).

166. Kulkarni, A., Siahrostami, S., Patel, A. & Nørskov, J. K. Understanding Catalytic Activity Trends in the Oxygen Reduction Reaction. *Chem Rev* 118, 2302–2312 (2018).

167. Wang, L. *et al.* Tuning Bifunctional Oxygen Electrocatalysts by Changing the A-Site Rare-Earth Element in Perovskite Nickelates. *Adv Funct Mater* 28, 1803712 (2018).

168. Bockris, J. O. M. & Otagawa, T. Mechanism of oxygen evolution on perovskites. *Journal of Physical Chemistry* 87, 2960–2971 (1983).

169. Baeumer, C. *et al.* Tuning electrochemically driven surface transformation in atomically flat LaNiO3 thin films for enhanced water electrolysis. *Nature Materials 2021 20:5* 20, 674–682 (2021).

170. Wang, L. *et al.* Understanding the Electronic Structure Evolution of Epitaxial LaNi1-xFexO3Thin Films for Water Oxidation. *Nano Lett* 21, 8324–8331 (2021).

171. Risch, M. *et al.* La0.8Sr0.2MnO3-δ decorated with Ba0.5Sr0.5Co0.8Fe0.2O 3-δ: A bifunctional surface for oxygen electrocatalysis with enhanced stability and activity. *J Am Chem Soc* 136, 5229–5232 (2014).

172. Yang, C.-Y. *et al.* Trends of epitaxial perovskite oxide films catalyzing the oxygen evolution reaction in alkaline media. *Journal of Physics: Energy* 2, 032003 (2020).

173. Löffler, T., Ludwig, A., Rossmeisl, J. & Schuhmann, W. What Makes High-Entropy Alloys Exceptional Electrocatalysts? *Angewandte Chemie International Edition* 60, 26894–26903 (2021).

174. A Batchelor, T. A. *et al.* Complex-Solid-Solution Electrocatalyst Discovery by Computational Prediction and High-Throughput Experimentation**. *Angewandte Chemie International Edition* 60, 6932–6937 (2021).

175. Batchelor, T. A. A. *et al.* High-Entropy Alloys as a Discovery Platform for Electrocatalysis. *Joule* 3, 834–845 (2019).

176. Banko, L. *et al.* Unravelling Composition–Activity–Stability Trends in High Entropy Alloy Electrocatalysts by Using a Data-Guided Combinatorial Synthesis Strategy and Computational Modeling. *Adv Energy Mater* 12, 2103312 (2022).

177. Trotochaud, L., Ranney, J. K., Williams, K. N. & Boettcher, S. W. Solution-cast metal oxide thin film electrocatalysts for oxygen evolution. *J Am Chem Soc* 134, 17253–17261 (2012).

178. Nguyen, T. X. *et al.* Advanced High Entropy Perovskite Oxide Electrocatalyst for Oxygen Evolution Reaction. *Adv Funct Mater* 31, 2101632 (2021).

179. Tang, L. *et al.* High Configuration Entropy Activated Lattice Oxygen for O2 Formation on Perovskite Electrocatalyst. *Adv Funct Mater* 32, 2112157 (2022).

180. Stamenkovic, V. R., Strmcnik, D., Lopes, P. P. & Markovic, N. M. Energy and fuels from electrochemical interfaces. *Nature Materials 2017 16:1* 16, 57–69 (2016).

181. Wang, L., Hossain, M. D., Du, Y. & Chambers, S. A. Exploring the potential of high entropy perovskite oxides as catalysts for water oxidation. *Nano Today* 47, 101697 (2022).

182. Yang, X. *et al.* Engineering high-entropy materials for electrocatalytic water splitting. *Int J Hydrogen Energy* 47, 13561–13578 (2022).

183. Daulton, T. L. & Little, B. J. Determination of chromium valence over the range Cr(0)– Cr(VI) by electron energy loss spectroscopy. *Ultramicroscopy* 106, 561–573 (2006).

184. Wang, Z. L., Yin, J. S. & Jiang, Y. D. EELS analysis of cation valence states and oxygen vacancies in magnetic oxides. *Micron* 31, 571–580 (2000).

185. Tan, H., Verbeeck, J., Abakumov, A. & Van Tendeloo, G. Oxidation state and chemical shift investigation in transition metal oxides by EELS. *Ultramicroscopy* 116, 24–33 (2012).

186. Hong, W. T. *et al.* Probing LaMO3 metal and oxygen partial density of states using X-ray emission, absorption, and photoelectron spectroscopy. *Journal of Physical Chemistry C* 119, 2063–2072 (2015).

187. Hong, W. T. *et al.* Charge-transfer-energy-dependent oxygen evolution reaction mechanisms for perovskite oxides. *Energy Environ Sci* 10, 2190–2200 (2017).

188. Grimaud, A. *et al.* Double perovskites as a family of highly active catalysts for oxygen evolution in alkaline solution. *Nature Communications 2013 4:1* 4, 1–7 (2013).

189. Heymann, L. *et al.* Separating the Effects of Band Bending and Covalency in Hybrid Perovskite Oxide Electrocatalyst Bilayers for Water Electrolysis. *ACS Appl Mater Interfaces* 14, 14129–14136 (2022).

190. Miyahara, Y., Fukutsuka, T., Abe, T. & Miyazaki, K. Dual-Site Catalysis of Fe-Incorporated Oxychlorides as Oxygen Evolution Electrocatalysts. *Chemistry of Materials* 32, 8195–8202 (2020).

191. Halck, N. B., Petrykin, V., Krtil, P. & Rossmeisl, J. Beyond the volcano limitations in electrocatalysis – oxygen evolution reaction. *Physical Chemistry Chemical Physics* 16, 13682–13688 (2014).